

DYMAT Hopkinson Centenary Conference

Commemorate the ground-breaking
invention of Bertram Hopkinson

9-11 September, 2014
Cambridge, United Kingdom



Hopkinson Centenary Conference Cambridge, UK

Stefan Hiermaier (ed.)

Hopkinson Centenary Conference Cambridge, UK

Editor Prof. Dr.-Ing. habil. Stefan Hiermaier

Contact:

Fraunhofer Institute for High-Speed Dynamics,
Ernst-Mach-Institut, EMI
Eckerstrasse 4
79104 Freiburg, Germany
www.emi.fraunhofer.de

ISBN: 978-3-00-046739-4

Freiburg, 2014

Printing and bindery:

Omniprint GmbH
Gewerbestr. 106
79194 Gundelfingen

Printed on acid-free and chlorine-free bleached paper.

© Fraunhofer Institute for High-Speed Dynamics, Ernst-Mach-Institut, EMI

All rights reserved

No part of this publication may be translated, reproduced, stored in a retrieval system, or transmitted in any form or by any means, electronic, mechanical, photocopying, recording or otherwise, without the written permission of the publisher. Many of the designations used by manufacturers and sellers to distinguish their products are claimed as trademarks. The quotation of those designations in whatever way does not imply the conclusion that the use of those designations is legal without the consent of the owner of the trademark.

Preface

DYMAT, the European Association for research into the dynamic behaviour of materials and its applications, organized a special international conference to celebrate the centenary of an epoch-making invention by Bertram Hopkinson (1874–1918). With his 1914 seminal paper, "A method of measuring the pressure produced in the detonation of high explosives or by the impact of bullets" *Phil. Trans. R. Soc. Lond.* A213 437-456, Bertram Hopkinson pioneered the development of an experimental set-up which even nowadays seems to be in greater demand than ever.

The Hopkinson Centenary Conference was intended to commemorate this ground-breaking invention and to reflect the most recent scientific developments in the area of Hopkinson bar type tests for dynamic material testing. In addition, presentations on other dynamic test methodologies (e.g. Taylor impact, blast and shock experiments) were given. A special issue of the *Philosophical Transactions of the Royal Society of London, Series A* was printed as a peer reviewed record of this meeting. In addition, this book of additional contributions submitted as conference papers is printed as proceedings.

With Cambridge University as the place where Bertram Hopkinson studied at Trinity College and where he was Professor for Mechanisms and Applied Mechanics, a perfect location was identified for the Centenary Conference organized on September 9–11, 2014.

Content

Quasi-static and high-strain-rate experiments on sand under one dimensional compression	1
A. D. Barr, S. D. Clarke, M. Petkovski, A. Tyas, J. Warren.....	1
1.1 Introduction.....	1
1.2 Material properties	2
1.3 Dynamic methodology.....	4
1.3.1 Test procedure.....	5
1.4 Quasi-static methodology	7
1.4.1 Test procedure.....	9
1.5 Results and discussion.....	11
1.5.1 Moisture effects.....	11
1.5.2 Strain-rate effects	12
1.6 Conclusions.....	13
1.7 Acknowledgements.....	14
1.8 References.....	14
Non-Dispersive Response of a Hopkinson Bar to Shock Loading ..	16
Dennis W. Baum	16
1.1 Abstract.....	16
1.2 Introduction.....	16
1.3 Description of analytic problem	19
1.3.1 Lateral surface loading.....	19
1.3.2 Shear Stress Loading.....	23
1.3.3 Mathematical summary	24
1.4 Experimental configuration.....	26
1.5 Comparison of experiment and theory.....	31
1.6 Summary.....	34
1.7 References.....	35
Application of gas-gun testing stand for experimental and theoretical studies of dynamic tensile and failure of hat-shaped specimens.....	37
V.G. Bazhenov, M.S. Baranova, E.V.Nagornykh	37
1.1 Introduction.....	37
1.2 The study of one-dimensional wave processes in the rod and tube	37

1.3	Experimental and numerical study of the tensile deformation process of hat-shaped specimens on the gas-gun testing stand	39
1.4	Investigation of the influence of geometrical parameters on the gas-gun testing stand in the tensile process	43
1.5	Scheme of gas-gun testing stand and testing methodology by direct impact method	45
1.6	Verification of methodology	46
1.7	Conclusion	49
1.8	Acknowledgments	49
1.9	References	50

A combined approach to dynamic testing of structural materials. 51

A. M. Bragov, L. A. Igumnov, A. Yu. Konstantinov, A. K. Lomunov	51	
1.1	Abstract	51
1.2	Introduction	51
1.3	Pulse shaper	52
1.4	The direct impact method	54
1.5	The experimental stand	58
1.6	Numerical investigation of the direct impact method	60
1.7	Conclusions	65
1.8	References	66

Use of Hopkinson method and its modifications in the USSR and Russia. 69

A. M. Bragov, L. A. Igumnov, A. Yu. Konstantinov, A. K. Lomunov, S. Yu. Linvinchuk	69	
1.1	Introduction	69
1.2	Using the SHB for studying shock compressibility and shear resistance of soft soils	72
1.3	Modification of the Kolsky method for studying properties of low-density materials under high-velocity cyclic strain	77
1.4	Determining dynamic friction using a modified Kolsky method	83
1.5	Determining the dynamic hardness	86
1.6	Experimental devices for studying the strain rate history effects	87
1.7	Investigation of Bauschiger effect	90
1.8	Ensuring constant strain rate	93
1.9	The methodology of complex experimental-numerical researches	94
1.10	Acknowledgements	97
1.11	References	97

Numerical simulation of the 45 steel deformation under Taylor impact	101
Chen Gang, Huang Xicheng.....	101
1.1 Abstract.....	101
1.2 Introduction.....	101
1.3 Material behaviors and model description.....	103
1.4 Numerical simulations on the Taylor impact deformation	106
1.5 Numerical simulations on the specimen failure under Taylor impact	110
1.6 Summary	113
1.7 References.....	114
Concrete under biaxial impact loading	117
M. Curbach, M. Quast	117
1.1 Introduction.....	117
1.2 Concrete properties	117
1.2.1 Concrete under impact.....	118
1.2.2 Concrete under multi-axial loading	120
1.3 HOPKINSON-Bar experiments on concrete	120
1.3.1 Hopkinson-Bar tension tests on concrete	121
1.3.2 Hopkinson-bar compression tests on concrete	125
1.4 The biaxial split-Hopkinson-bar	128
1.4.1 The test setup.....	128
1.4.2 The specimen	129
1.5 Experimental results.....	130
1.6 Conclusions	135
1.7 Acknowledgements	135
1.8 References.....	135
The joint time-frequency analysis of wave propagation in SHPB by means of wavelet transform	141
Roman Gieleta	141
1.1 Introduction.....	141
1.2 Why wavelet transform?.....	142
1.3 The fundamentals of the wavelet transform.....	142
1.4 Wavelet transform versus Fourier transform	146
1.5 Experimental setup and tests	148
1.6 Wave dispersion in elastic and viscoelastic bars	151
1.7 Next steps.....	157
1.8 Conclusions	158
1.9 Acknowledgement	159

1.10	References.....	159
------	-----------------	-----

Mechanical Characterization and Modelling of Reactive Polymeric Materials with the SHPB 163

N. Heider ¹ , H. Aurich ² , A. Steinbrenner ¹ , M. Salk ²	163
1.1	Introduction	163
1.2	Split Hopkinson Pressure Bar SHPB.....	164
1.2.1	Fundamental principles and signal analysis.....	164
1.2.2	SHPB facility with PMMA bars.....	166
1.2.3	SHPB facility with aluminum bars.....	167
1.3	Material behaviour – viscoelasticity and damage	169
1.4	Material characterization of KS-32	172
1.4.1	Characterization of the mechanical behaviour	172
1.4.2	Thermal loading of SHPB samples	176
1.4.3	Damage analysis with computer tomography	177
1.5	Determination of material parameters	177
1.6	Summary	182
1.7	References.....	183

An automatic SHPB pulses delimitation method with a novel optimization..... 185

Gueraiche Larbi ^{1,2} , Tarfaoui Mostapha ² , Osmani Hocine ¹ and Aboulghit El Malki Alaoui ²	185
1.1	Abstract.....	185
1.2	Introduction	186
1.3	Split Hopkinson pressure bar test set	187
1.4	Assumptions for a valid SHPB test.....	189
1.5	Data acquisition.....	190
1.6	Basic SHPB governing equations	192
1.7	Data processing	195
1.7.1	Starting and end times of pulses.....	195
1.7.2	Dispersion correction	202
1.8	Experimental results.....	203
1.9	Conclusions.....	206
1.10	References.....	207

Initial Development of Microdamage in a Zr-BMG under Plate Impact Loading 211

Zhong Ling ¹ , Xin Huang ² and Lanhong Dai ¹	211
1.1	Abstract.....	211
1.2	Introduction	211

1.3	Experimental procedure.....	214
1.3.1	Developed short stress duration technique.....	214
1.3.2	Plate-impact experiments.....	215
1.4	Experimental results.....	217
1.4.1	Micro-observations to BMG samples.....	217
1.4.2	Analysis and discussion.....	219
1.5	Conclusions.....	221
1.6	Acknowledgements.....	222
1.7	References.....	222

Dynamic Tensile Properties of Bioplastic Polymer Blends and Fracture Surface..... 225

Masahiro Nishida.....	225	
1.1	Introduction.....	225
1.2	Experimental setup.....	225
1.3	Experimental results.....	227
1.3.1	PLA/PBAT polymer blends.....	227
1.3.2	PA11/nanoparticle composite materials blends.....	230
1.4	Conclusions.....	232
1.5	References.....	233

Comparative study of damage kinetics and energy absorption of 2D and 3D glass/vinylester composite materials under dynamic compression..... 235

M. Tarfaoui ^{1, a} , C. Bouery ^{1, b}	235	
1.1	Abstract.....	235
1.2	Introduction.....	235
1.3	Experimental study.....	236
1.3.1	Composite specimen.....	236
1.3.2	Split Hopkinson pressure bar testing.....	238
1.4	Results and discussions for in-plane tests.....	239
1.4.1	Dynamic response.....	239
1.4.2	Energy dissipation.....	241
1.4.3	Failure modes.....	243
1.5	Conclusion.....	245
1.6	Acknowledgements.....	246
1.7	References.....	246

Experimental and numerical investigation of glass/epoxy composite materials under in-plane dynamic compression..... 249

M. Tarfaoui ^{1, a}	249
1.1 Abstract.....	249
1.2 Introduction	250
1.3 Materials	251
1.4 Dynamic compression loading	252
1.4.1 Data processing procedure	252
1.4.2 Strain rate dependencies of dynamic mechanical properties....	253
1.5 Finite element analysis	256
1.5.1 Dynamic compression without damage	256
1.5.2 Results and discussion	257
1.6 Conclusion	261
1.7 Acknowledgements.....	261
1.8 References.....	262

Quasi-static and high-strain-rate experiments on sand under one dimensional compression

A. D. Barr, S. D. Clarke, M. Petkovski, A. Tyas, J. Warren
Department of Civil and Structural Engineering, The University of Sheffield, Sheffield,
South Yorkshire, UK

S. Kerr
Defence Science and Technology Laboratory, Porton Down, Wiltshire, UK

This paper investigates the effect of strain rate on the behaviour of dry and partially-saturated sand at very high stresses, seeking to clarify the existence of a strain-rate dependence and how this is affected by changes in moisture content. Dynamic one-dimensional compression tests on a fine quartz sand have been carried out to axial stresses of 400 MPa using a split Hopkinson pressure bar, alongside quasi-static tests to 800 MPa using the mac^{2T} multi-axial test rig at The University of Sheffield. Specimens were prepared at moisture contents of 0.0 %, 2.5 % and 5.0 %, and were laterally confined using a steel ring or steel loading box to ensure one-dimensional test conditions. Lateral stresses were recorded to allow the three-dimensional stress state of the specimens to be analysed. The results show that knowledge of both the axial and radial stresses is important for understanding the response of sand at higher strain rates, where an increase in stiffness is observed axially when compared to the quasi-static results.

1.1 Introduction

This research is part of the Dstl-sponsored and QinetiQ-led Force Protection Engineering (FPE) research programme, which investigates protective materials and structures that can be used by military fortifications designers [1]. The FPE programme is split into applied and underpinning research, where the goal of the underpinning research is to enhance the understanding of how protective materials used in FPE perform under a wide range of loading conditions.

In order to make accurate predictions of the response of soils to blast and impact events, it is vital to have an understanding of the soil behaviour at very high pressures, and over a wide range of strain rates and ground conditions. While the effect of strain rate is of particular interest, the existing literature is inconsistent in its conclusions. Work by Farr [2] used a uniaxial strain device to test a variety of partially-saturated sandy soils at strain rates of 10^{-4} – 10^3 s^{-1} , where it was found that the axial stiffness of the soil increased with strain rate in all cases. In contrast, Song et al. [3] performed tests on a dry quartz sand using a quasi-static device and a split Hopkinson pressure bar (SHPB), and concluded that there was no strain-rate effect between 10^{-4} – 10^3 s^{-1} , while Bragov et al. [4] tested dry quartz sand using a SHPB and plate impact experiments, and reported no change in stiffness between 10^3 – 10^6 s^{-1} . Bragov et al. recorded radial stresses in the SHPB tests, and the relationship between axial and radial stresses was used to estimate the mean stress in the plate impact experiments.

Current work at The University of Sheffield seeks to clarify the effects of strain rate on dry and partially-saturated quartz sand through quasi-static and dynamic one-dimensional compression to very high stresses. Quasi-static tests (10^{-3} s^{-1}) have been performed to axial stresses of 800 MPa using the mac^{2T} test rig, alongside dynamic tests (10^3 s^{-1}) to axial stresses of 400 MPa using a SHPB. In both cases the sand was confined and the axial and lateral response was recorded, so that the three-dimensional stress state could be derived.

1.2 Material properties

The material tested was a light brown–orange uniform fine quartz sand. A sieve analysis of the sand was carried out to assess the particle size distribution, the results of which are presented in Figure 1. A summary of material properties is provided in Table 1. Specimens were tested at moisture contents of 0.0 %, 2.5 % and 5.0 % in both the quasi-static and dynamic tests, where moisture content, w , is the ratio of the mass of water, M_w , to the mass of dry sand, M_s . All specimens were carefully oven-dried before testing, and wet specimens were mixed well to ensure an even distribution of water. A summary of the test variables is shown in Table 2.

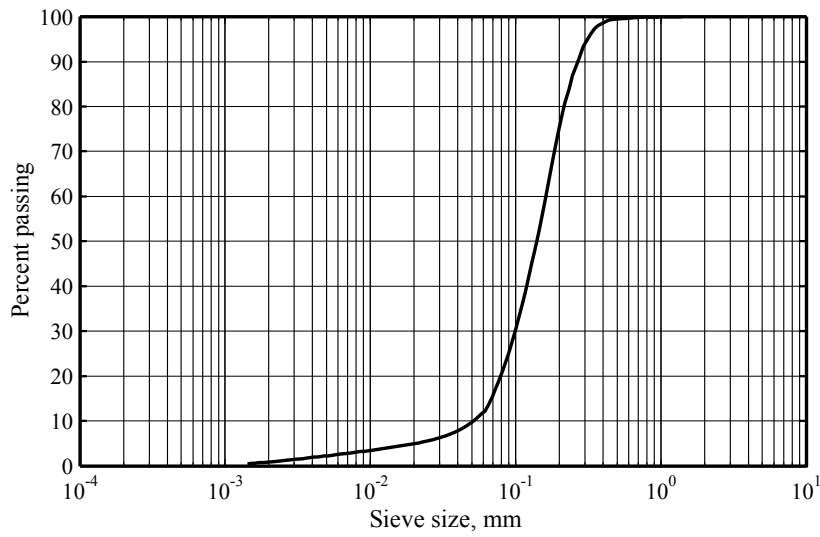


Figure 1: Initial particle size distribution.

Table 1: Initial sand properties

Specific gravity	2.66
D_{10}	50 μm
D_{50}	130 μm
D_{60}	150 μm
Uniformity coefficient, C_u	3.0
Min. dry density	1.35 Mg/m^3
Max. dry density	1.87 Mg/m^3

Table 2: Summary of test variables

Peak strain rate [s^{-1}]	Peak axial stress [MPa]	Moisture content [%]	Number of tests
10^{-3} (mac ^{2T})	800	0.0	3
		2.5	3
		5.0	3
10^3 (SHPB)	400	0.0	6
		2.5	5
		5.0	5

1.3 Dynamic methodology

The dynamic tests were performed using a split Hopkinson pressure bar, with a confining ring to contain the sand specimens. The stainless steel incident and transmitter bars are each 25 mm in diameter and 1500 mm in length, while the striker bar is 25 mm in diameter and 400 mm in length. Semi-conductor strain gauges on both bars were arranged to ensure that only longitudinal waves were recorded.

Sand specimens were held in a steel confining ring with a 25 mm internal diameter and 35 mm external diameter over a length of 5 mm, as depicted in Figure 2. A strain gauge located on the outside surface of the ring enabled the circumferential strain of the ring to be measured and, using thick walled pipe theory, the average internal pressure in the sample could be related to the circumferential strain using the expression

$$P_i = \frac{R_o^2 - R_i^2}{2R_i^2} E \epsilon_\theta$$

where P_i is the internal radial pressure exerted on the specimen by the confining ring, E is the Young's modulus of the ring, ϵ_θ is the circumferential strain measured on the outside of the ring and R_o and R_i are the outer and inner radii of the ring respectively [5]. To take into account the significant change in specimen length during the test, the average internal pressure deduced from the circumferential strain was factored by the length of the confining ring divided by the varying sample length.

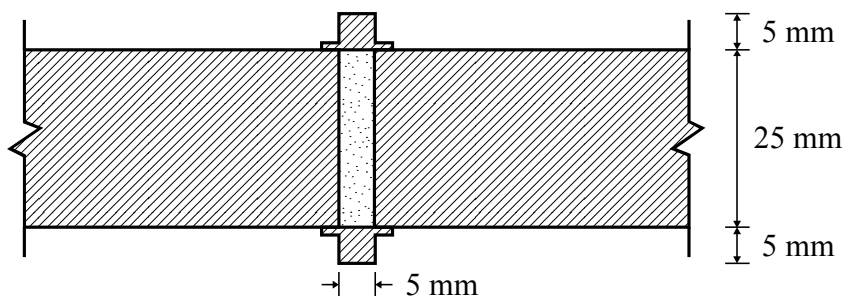


Figure 2: Detail of steel confining ring showing confinement of sand sample and ring dimensions.

1.3.1 Test procedure

To prepare a sand specimen, the confining ring was held vertically and a set mass of sand poured and compacted into the ring to achieve a density of approximately 1.5 Mg/m^3 . A thin ($10 \text{ }\mu\text{m}$) disk of aluminium foil and a small amount of cyanoacrylate adhesive were used to hold the specimen in place while the ring was arranged between the Hopkinson bars. During the test, the strength and mass (0.01g) of the foil could be considered to be negligible.

Small specimen lengths are required to achieve stress equilibrium in soil specimens, and so careful measurement of the initial length is needed to ensure the accuracy of density calculations. The incident and transmitter bars were each marked with a pair of perpendicular lines using a sharp blade, and the distance between the inside edges of these lines was measured using a travelling microscope fitted with a digital dial gauge (Figure 3). Comparison of the measurements before and after the sand specimen was inserted provided the initial specimen length with an accuracy of $\pm 10 \text{ }\mu\text{m}$.

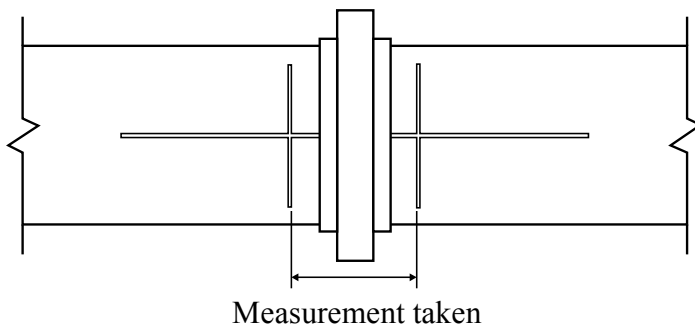


Figure 3: A travelling microscope fitted with a digital dial gauge was used to find the pre-test length of the sand specimen by measuring between lines marked on the pressure bars.

Stress pulses were applied by firing the striker bar using a gas gun, which was set up in a consistent manner to ensure a similar peak axial stress and strain rate in each test. This setup provided peak axial stresses in the specimen of approximately 400 MPa and peak strain rates of approximately 4800 s^{-1} . The stresses and strain observed in a typical test are shown in Figure 4 and Figure 5. The care taken in the setup of the apparatus and in the measurement of the specimens results in high repeatability, as shown in Figure 6.

The oscillations in Figure 4 show evidence of dispersion of the stress waves as they propagate along the bars: while dispersion correction has not been applied to the current test series, it is intended to include this in future work.

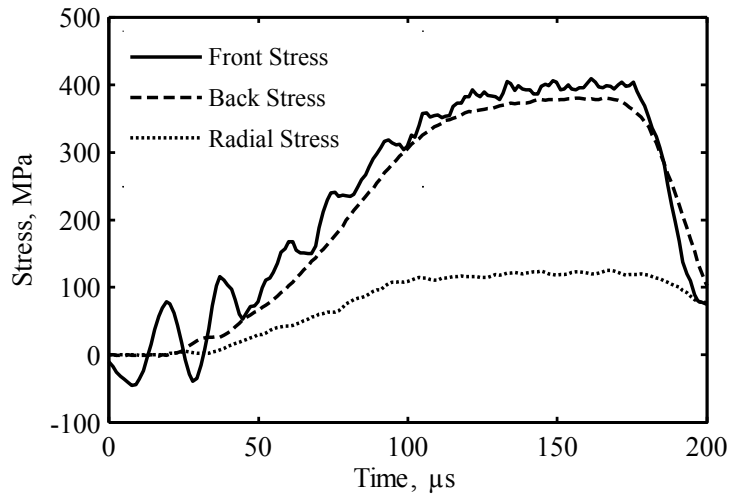


Figure 4: Typical axial and radial stress development in a SHPB test on dry sand.

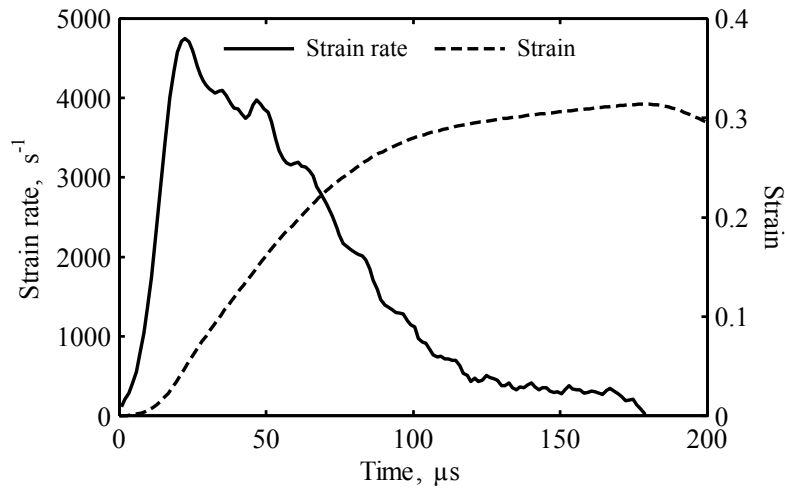


Figure 5: Typical development of strain and strain rate in a SHPB test on dry sand.

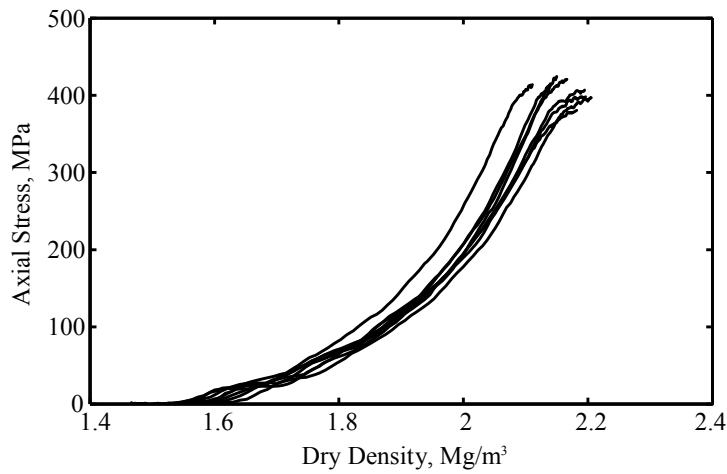


Figure 6: Repeatability of SHPB tests on dry sand.

1.4 Quasi-static methodology

The quasi-static tests were carried out in mac^{2T}, the University of Sheffield's test rig for Multi-Axial Compression of Concrete at Elevated Temperatures, which is shown in Figure 7. This rig allows specimens to be tested in true multi-axial compression ($\sigma_x \neq \sigma_y \neq \sigma_z$) to high stresses, with independent control of loads or displacements in the x-, y- and z-axes [6].

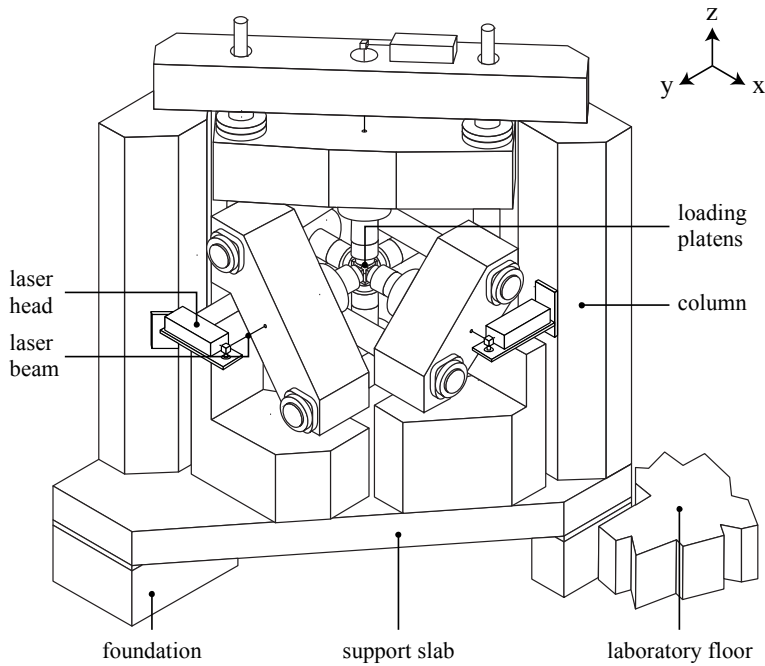


Figure 7: mac^{2T} test rig.

In its original application, mac^{2T} is used to test cubes of concrete under multi-axial loading conditions, where the strains involved are very small and concrete cubes are simply placed between the test rig platens. To allow the testing of cohesionless sand to high strains, a loading box was fabricated to contain the specimen. The test box is made up of six steel blocks, which are arranged to form an interior cube which accommodates the specimen, as shown in Figure 8. In the one-dimensional tests, the x-axis (or 'active') blocks are actively loaded by the rig while the others are held at zero strain, so that any stresses in the y- and z-axes (or 'passive') blocks are generated passively by the x-axis loading.

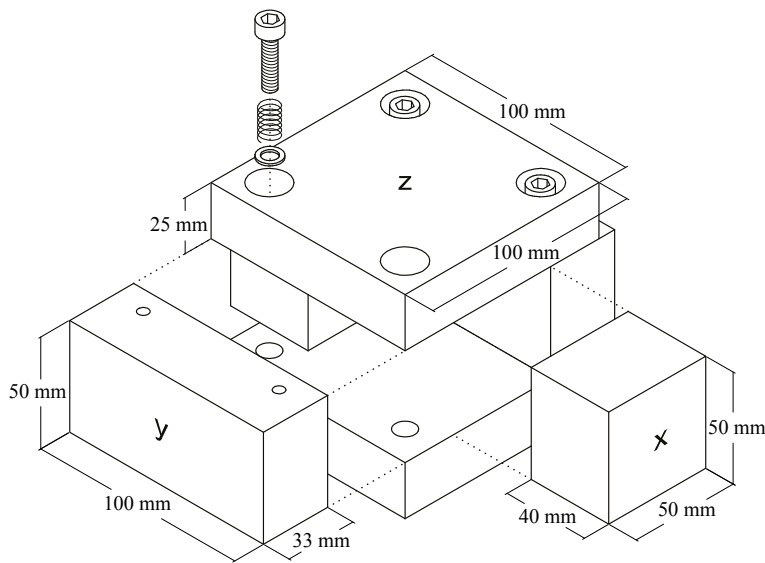


Figure 8: Sand loading box used in mac2T.

1.4.1 Test procedure

To prepare a specimen for testing, five of the six test box blocks were loosely bolted together so that only the topmost face of the box was open, then the sand specimen was poured into the void and the final block inserted. The sand was compacted using a series of hammer drops until the protrusion of the x-axis blocks indicated that the specimen had achieved a dry density of 1.5 Mg/m^3 .

During the test the box was nominally loaded on all three axes so that the load cell registered a small force of approximately 7 kN. The passive platens were then switched to displacement control with zero displacement, fixing the size of the specimen cross-section: from this point any loading in these axes was generated passively due to the loading in the x-axis. The load on the x-axis was varied cyclically to a maximum of 2000 kN (800 MPa) at a strain rate of approximately 10^{-3} s^{-1} .

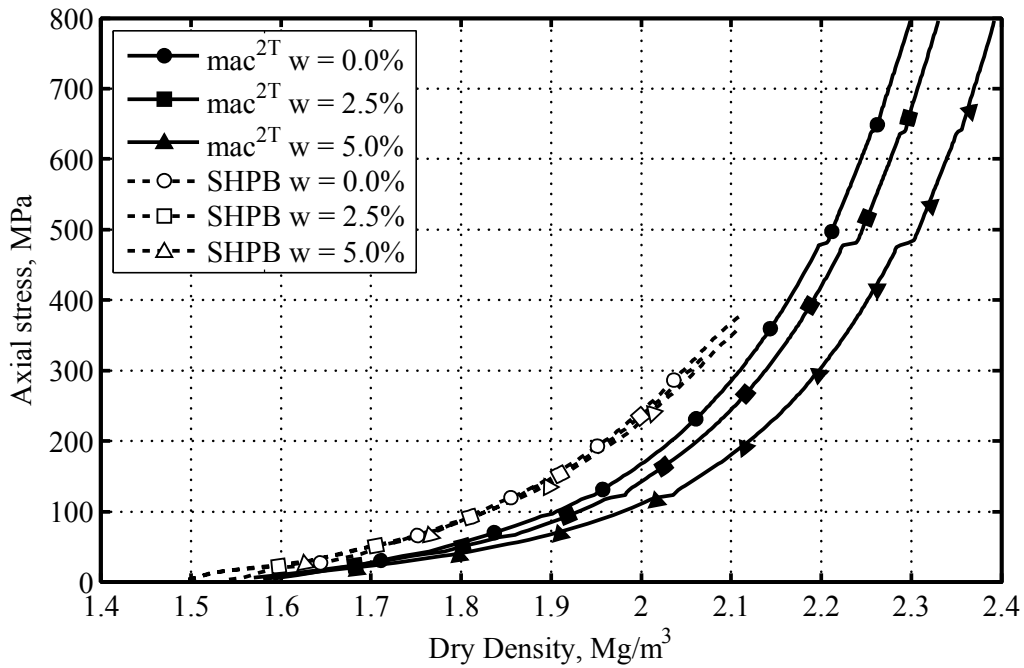


Figure 9: Axial stress–dry density data for mac^{2T} and SHPB tests with varying moisture content. Mean results are presented and unloading omitted for clarity.

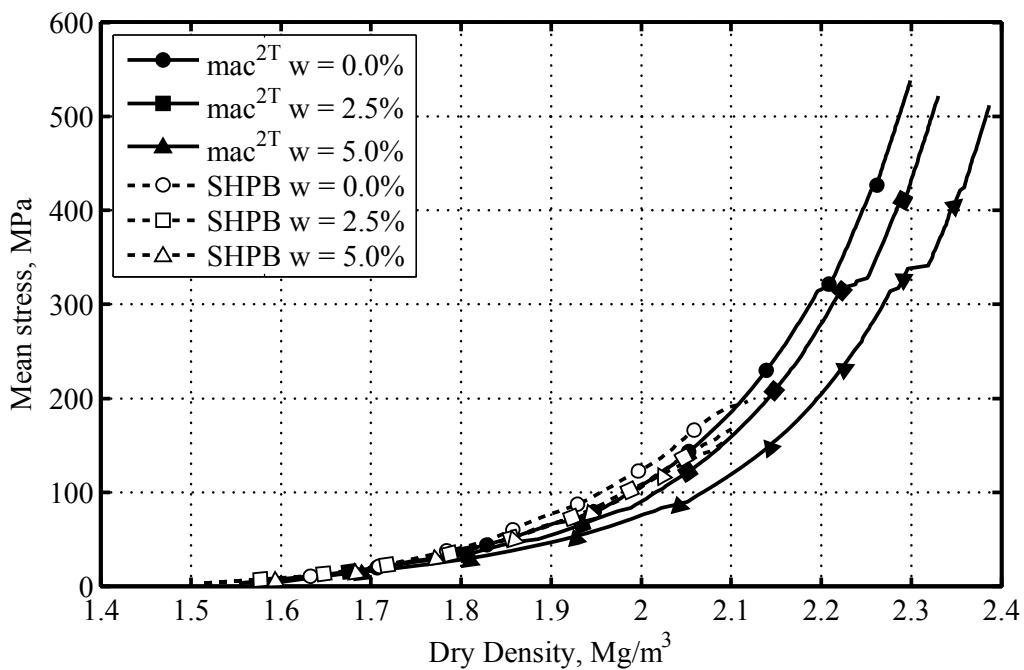


Figure 10: Mean stress–dry density data for mac^{2T} and SHPB tests with varying moisture content. Mean results are presented and unloading omitted for clarity.

1.5 Results and discussion

Data from the quasi-static mac^{2T} tests was readily converted into stress-strain data for further examination, and in the SHPB tests the response of the sand specimen was calculated using one-dimensional elastic wave propagation theory, which is well reported elsewhere and will not be repeated here [7]. One-dimensional conditions were assumed in the specimen, and the strains recorded in the steel confining ring confirmed that this assumption was valid: the maximum radial strain in the sand specimen was 0.05%, compared to axial strains of over 30%. Axial stress–dry density and mean stress–dry density data are presented in Figure 9 and Figure 10 for the quasi-static mac^{2T} tests and dynamic SHPB tests, where dry density, ρ_d , is the ratio of the dry mass of the soil to its volume. Unloading has been omitted for clarity. All of the specimens tested follow the expected pattern for sands in one-dimensional compression: at low stresses the particles in the sand roll and slide over each other into a denser configuration, then as the voids are filled this compaction mechanism becomes more difficult, with further compaction achieved through particle crushing.

1.5.1 Moisture effects

In the quasi-static tests the addition of water leads to a reduction in the stiffness of the sand specimen, with the 2.5% moisture content specimens behaving less stiffly than the dry specimens, and the 5.0% moisture content specimens less stiff than the 2.5% moisture content specimens. This is indicated by the higher dry densities achieved by the wet specimens for a given stress in Figure 9 and Figure 10. As reported by Martin et al. [8], this reduction in stiffness is likely due to the lubricating effect of the water between the sand particles, reducing inter-particle friction and facilitating the rolling and sliding mechanism which leads to compaction.

In contrast, the dynamic tests show no significant change in stiffness with changing moisture content, except at low stresses: while the mean results in Figure 10 appear to show a small decrease in stiffness with increasing moisture content, the individual tests overlap each other significantly. If it is assumed that the main effect of moisture in the quasi-static tests is in aiding particle rearrangement by rolling and sliding, the lack of effect in

the dynamic tests could indicate that the compression of the sand at higher strain rates is dominated more by particle crushing than by particle rearrangement; however, this contradicts previous work, such as that by Farr [2], which showed that sandy materials exhibited less particle breakage at higher strain rates. An alternative explanation could be that at the higher strain rate the moisture does assist in the rearrangement of particles as in the quasi-static tests, but that another mechanism, such as localised loading of pore water, increases the stiffness of the specimen, resulting in little net change in stiffness.

It is worth noting that none of the tests display the rapid stiffening associated with significant loading of pore water, such as that observed by Hendron et al. [9] and Veyera [10]. Full saturation is only encountered in the 5 % moisture content mac^{2T} tests at axial stresses of 600 MPa and above, where the drained conditions permit the excess pore water to be expelled from the specimen rather than sustain load.

1.5.2 Strain-rate effects

Figure 9 shows the relationship between axial stress and dry density, where the dynamically-tested specimens consistently exhibit an increase in stiffness over those tested quasi-statically. This effect is particularly evident at low stresses where the strain rate is at its peak, and is reduced as the strain rate decreases throughout the test. While the dynamic specimens display little change in stiffness with increasing moisture content, the quasi-static specimens become less stiff, so that the increase in axial stiffness due to strain rate appears to increase with moisture content. It is noted that while the mac^{2T} tests were fully drained, the loading of the SHPB specimens more closely resembled undrained conditions, with little opportunity for the escape of pore air. The resulting compression of pore air contributes to the stiffness of the specimen at higher strains, but a calculation based on ideal gas behaviour in undrained conditions estimates that the compression of air observed at 2.1 Mg/m^3 would require an additional pressure of 190 kPa, a tiny fraction of the 80 MPa mean increase in stress observed in the dry sand at 2.1 Mg/m^3 compared to the quasi-static tests.

While an apparent strain-rate effect is observed when considering one-dimensional stresses and strains, examination of the full three-

dimensional stress state reveals a much reduced effect, which is clear in comparison of Figure 9 and Figure 10, where use of mean stress instead of axial stress causes the dry quasi-static and dynamic series to overlap. This indicates that, for a certain dry density, the dynamically-tested sand specimens generated higher axial stresses but lower radial stresses when compared to the quasi-static specimens, so that there was a smaller change in the overall stiffness. Lower radial stresses may be the result of radial confinement in the sand specimen, which would enable the specimen to sustain the higher axial stresses seen in Figure 9.

1.6 Conclusions

Using the mac^{2T} test rig, quasi-static one-dimensional compression tests on fine quartz sand were carried out to axial stresses of 800 MPa, alongside dynamic tests using a split Hopkinson pressure bar to axial stresses of 400 MPa. In both test series lateral stresses and strains were also recorded.

Specimens were prepared at moisture contents of 0.0 %, 2.5 % and 5.0 %. In the quasi-static tests the specimens became increasingly less stiff with the addition of water, while in the dynamic tests the water appeared to have little effect on the overall stiffness at the moisture contents tested.

Between peak strain rates of 10^{-3} s^{-1} and 10^3 s^{-1} a significant increase in axial stiffness was observed, but this effect was greatly reduced when mean stresses were considered. The data presented suggests that the increase in axial stiffness observed between the quasi-static and dynamic tests is not due to an inherent strain-rate dependence in the sand, but rather is the result of increased confinement due to the radial inertia of the SHPB specimens.

Many of the previous studies on soils at high strain rates, including those by Farr [2] and Song et al. [3], presented only axial stress and strain results, and so this data highlights the importance of understanding the full three-dimensional stress state of the soil. The variation in radial stresses with strain rate also serves to warn against assumptions of consistent stress ratio with changing strain rate.

1.7 Acknowledgements

The authors wish to thank Dstl for funding this research, which is part of the QinetiQ-led Force Protection Engineering (FPE) research programme [1].

1.8 References

- [1] Warren, J., et al., *Briefing: UK Ministry of Defence Force Protection Engineering Programme*. Proceedings of the ICE - Engineering and Computational Mechanics, 2013. **166**(3): p. 119-123.
- [2] Farr, J.V., *Loading rate effects on the one-dimensional compressibility of four partially saturated soils*, 1986, US Army Engineer Waterways Experiment Station: Vicksburg, MS.
- [3] Song, B., W. Chen, and V. Luk, *Impact compressive response of dry sand*. Mechanics of Materials, 2009. **41**: p. 777-785.
- [4] Bragov, A.M., et al., *Determination of physicommechanical properties of soft soils from medium to high strain rates*. International Journal of Impact Engineering, 2008. **35**.
- [5] Stephens, R.C., *Strength of materials: theory and examples*. 1970: Hodder Arnold.
- [6] Petkovski, M., R.S. Crouch, and P. Waldron, *Apparatus for Testing Concrete under Multiaxial Compression at Elevated Temperature (mac2T)*. Experimental Mechanics, 2006. **46**: p. 387-398.
- [7] Gray III, G.T., *Classic split-Hopkinson pressure bar testing*, in *ASM Handbook Vol. 8: Mechanical Testing and Evaluation*, H. Kuhn and D. Medlin, Editors. 2000, ASM International.
- [8] Martin, B.E., et al., *Moisture effects on the high strain-rate behavior of sand*. Mechanics of Materials, 2009. **41**: p. 786-798.
- [9] Hendron, A.J., M.T. Davisson, and J.F. Parola, *Effect of degree of saturation on compressibility of soils from the Defence Research Establishment Suffield*, 1969, US Army Engineer Waterways Experiment Station: Vicksburg, MS.

- [10] Veyera, G.E., *Uniaxial stress-strain behavior of unsaturated soils at high strain rates*, 1994, Wright Laboratory Flight Dynamics Directorate, AFMC: Tyndall AFB, FL.

Non-Dispersive Response of a Hopkinson Bar to Shock Loading

Dennis W. Baum

Lawrence Livermore National Laboratory

1.1 Abstract

This paper is intended to draw attention to a unique aspect of the Hopkinson bar, which while not new, has not been exploited by the blast wave measurement community. The nearly 50-year-old work referenced herein established a solid theoretical basis for realizing a highly resolved temporal measurement of blast wave pressure profiles. The referenced work also compares the calculated bar response with shock tube experiments producing a step-function loading profile on a bar, mounted internal to and co-axial with the shock tube. Within the fidelity of the instrumentation and recording equipment, the experiments verified both the qualitative and quantitative analytical analysis of bar response. This paper respectfully revisits prior work on this centenary occasion as a fulfilment of the original intent of Hopkinson to measure blast waves and impactor effects.

1.2 Introduction

For the last 100 years and up to the present day, the Hopkinson bar technique¹ has been an important laboratory tool to study the response of materials to dynamic loads. In practice, the Hopkinson bar technique has been applied primarily in the moderate strain rate regime, rather than for the measurement of blast and impactor effects as envisioned by Hopkinson. Three fundamental papers provide the theoretical foundation for the response of a bar to dynamic loading and thus are the key to understanding the limitations and therefore applications of a Hopkinson bar.

The first two are the early theoretical work of Pochhammer² and Chree³ that proved that sinusoidal waves traveling in an infinite bar with a

condition of zero stress at the lateral surface leads to an equation connecting phase velocity and frequency of the waves. This conclusion is important because this phase velocity and frequency relationship requires that a pulse, which can be described in the frequency domain as a composition of Pochhammer-Chree (PC) waves of many frequencies, would be expected to change shape during travel. This inherent dispersive nature of wave propagation in a bar presents a fundamental limitation on the frequency response of a bar and thus limits its utility to moderate frequencies pulses and strain rates. A third paper by Folk, Fox, Shook, and Curtis⁴ examined the common end-loading usage of a bar and provided an exact solution to the problem of calculating the strain due to time-dependent end-loading of a semi-infinite bar. This work concerned calculating the amplitude of the resulting oscillations in the bar, the relative importance of the various possible modes of vibration, and the dependence of pulse shape on the conditions of loading. A method was presented for calculating the elastic strain produced by the sudden application of pressure to the end of a semi-infinite cylindrical bar with a stress-free lateral surface. The exact solution is expressed as a sum of Fourier integrals whose integrands have the form of Pochhammer–Chree waves, which can be evaluated to obtain asymptotic solutions valid at large distances from the end of the bar. These solutions take the form of an Airy⁵ function, shown in Fig. 1, which is a wave form consisting of a low frequency rise followed by a series of higher frequency waves of diminishing amplitude and increasing frequency. These findings explain the limitation of the Hopkinson bar to response regimes of moderate strain rates.

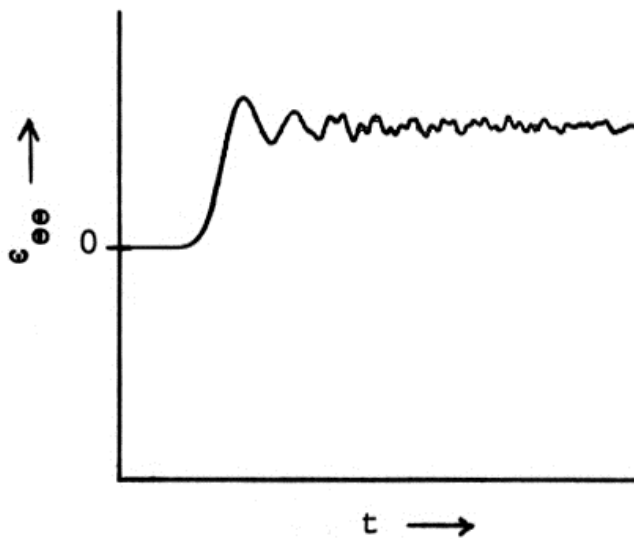


Fig. 1: Strain observed on surface of a cylindrical bar subject to step-function end-loading [ref. 4].

The “current” 50-year-old referenced work by Baum⁵ builds on these prior papers and uses the same theoretical approach for calculating the time-dependent response of a bar subject to a traveling lateral surface load. Within the same asymptotic solution conditions, there is found an additional non-dispersive term in addition to the Pochhammer-Chree waves. This additional finding enables a high-fidelity time-resolved response of a bar to a time-varying load.

This paper reviews the approach to the analysis described in Ref. 5 and the significant results, but refers back to Ref. 5 for detailed descriptions of the analysis. Copies of the original data records from the Baum thesis⁶, which verify the analysis, are contained herein and suggest the potential utilization of the Hopkinson bar for high resolution blast wave and shock tube pressure measurements. The included figures are referenced to their original sources.

1.3 Description of analytic problem

1.3.1 Lateral surface loading

The problem to be solved is the determination of the elastic strain in a cylindrical bar of radius a , subject to a step function in stress, τ_{rr} , traveling at velocity V , applied normal to the lateral surface, and subject to zero stress, τ_{zz} , and radial displacement, u_r , on the end of the bar. These boundary conditions are illustrated in Fig. 2.

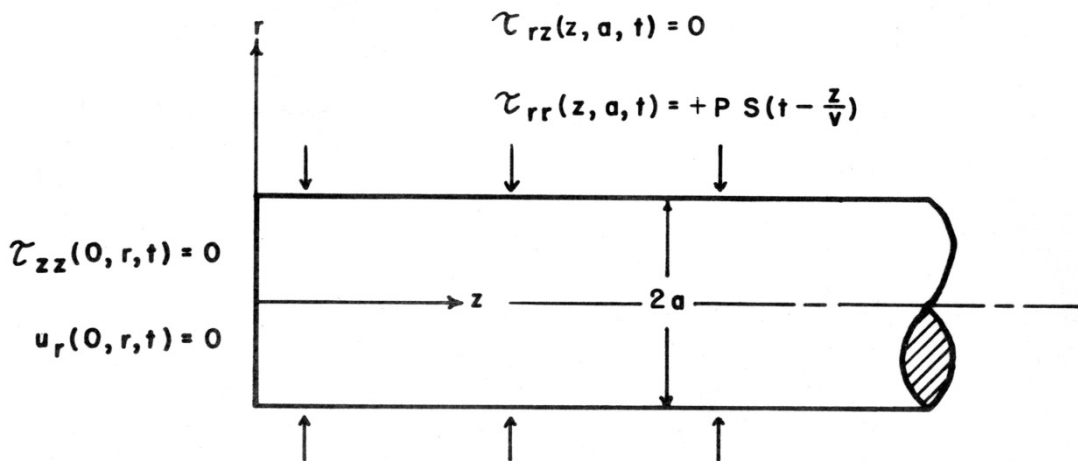


Fig. 2: Boundary conditions for constant velocity normal stress loading on the lateral surface of a bar [ref. 5].

This is a mixed-end condition problem (one component of stress and one component of displacement, specified on the end of the bar). The end conditions chosen allow the use of the double transform method of solution presented by Folk et al. The assumption regarding the value of the end displacement is relatively unimportant for strains at large distances from the end of the bar and serves to enable the solution technique.

The equations of motion for a bar having cylindrical symmetry and the coordinates as shown in Fig. 2 are:

$$\rho \frac{\partial^2 u_r}{\partial t^2} = (\lambda + 2\mu) \frac{\partial \Delta}{\partial r} + 2\mu \frac{\partial \Omega}{\partial z} \quad (1)$$

$$\rho \frac{\partial^2 \mathbf{u}_z}{\partial t^2} = (\lambda + 2\mu) \frac{\partial \Delta}{\partial z} - \frac{2\mu}{r} \frac{\partial(r\Omega)}{\partial r} \quad (2)$$

$$\Delta = \frac{1}{r} \frac{\partial(r\mathbf{u}_r)}{\partial r} + \frac{\partial \mathbf{u}_z}{\partial z} \quad (3)$$

$$\Omega = \frac{1}{2} \left(\frac{\partial \mathbf{u}_r}{\partial z} - \frac{\partial \mathbf{u}_z}{\partial r} \right) \quad (4)$$

In these equations t is time, u_r and u_z are radial and axial displacements respectively, ρ is the density and λ and μ are the Lamé elastic constants. Δ and Ω are defined by equations (3) and (4).

Solutions to these equations must satisfy the following initial and boundary conditions:

(a) the initial conditions at $t = 0$,

$$\mathbf{u}_r = \mathbf{u}_z = \frac{\partial \mathbf{u}_r}{\partial t} = \frac{\partial \mathbf{u}_z}{\partial t} = \mathbf{0} \quad (5)$$

(b) the boundary conditions on the lateral surface,
 $r = a$,

$$\begin{aligned} \tau_{rr}(\mathbf{z}, \mathbf{a}, \mathbf{t}) &= PS \left(\mathbf{t} - \frac{\mathbf{z}}{\mathbf{v}} \right) \\ \tau_{rz}(\mathbf{z}, \mathbf{a}, \mathbf{t}) &= \mathbf{0} \end{aligned} \quad (6)$$

(c) the boundary conditions at the end of the bar,
 $z = 0$,

$$\begin{aligned} \tau_{zz}(\mathbf{0}, \mathbf{r}, \mathbf{t}) &= \mathbf{0} \\ \mathbf{u}_r(\mathbf{0}, \mathbf{r}, \mathbf{t}) &= \mathbf{0} \end{aligned} \quad (7)$$

P represents the amplitude of the applied normal stress, V is the loading velocity, and $S \left(t - \frac{z}{v} \right)$ is a step function in time moving at speed V . In addition, the stress components τ_{rr} , τ_{rz} , and τ_{zz} are related to the displacements by the stress-strain equations.

$$\tau_{zz} = \frac{\lambda}{r} \frac{\partial(ru_r)}{\partial r} + (\lambda + 2\mu) \frac{\partial u_z}{\partial z} \quad (8)$$

$$\tau_{rr} = (\lambda + 2\mu) \frac{\partial u_r}{\partial r} + \frac{\lambda u_r}{r} + \lambda \frac{\partial u_z}{\partial z} \quad (9)$$

$$\tau_{rz} = \mu \left(\frac{\partial u_r}{\partial z} + \frac{\partial u_z}{\partial r} \right) \quad (10)$$

Equations (1) through (10) completely specify the problem.

Asymptotic solutions to the equations of motion valid at a long distance from the loaded end of the bar were obtained. These solutions predict time-dependent strain, which may be described as the superposition of several waves each of which propagates with a characteristic velocity. The strain produced by a positive normal loading of the lateral surface consists of a radial expansion followed by a radial compression. The initial radial expansion has the form of an Airy function and propagates at the bar velocity $C_o = \sqrt{Y/\rho}$. This wave is dispersive and its amplitude is a function of V , the elastic constants for the bar material, and the normal stress P . It is analogous to the pulse emanating from end-loading of the bar. The subsequent radial compression pulse is non-dispersive and can have several components traveling at the surface loading velocity and is best understood from the Pochhammer-Chree solutions in the Ω, Γ plane, where $\Omega = \omega/C_s$ and $\Gamma = Ya$, where the shear wave velocity $C_s = (\mu/\rho)^{1/2}$, as shown in Fig. 3.

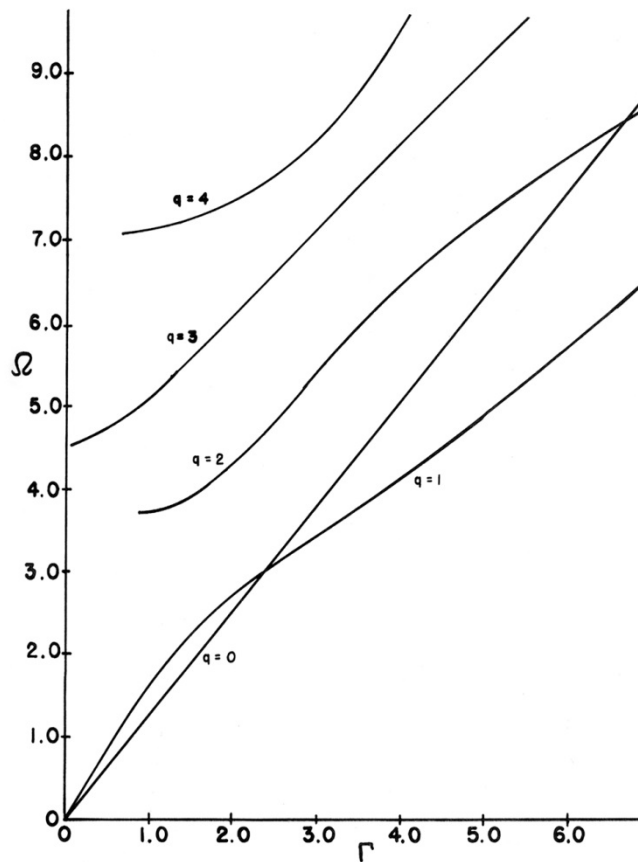


Fig. 3: Pochhammer-Chree dispersion curves for a bar having a Poisson's ratio of $\sigma = 0.35$ [ref. 4].

The curves in Fig. 3 having mode $q > 0$ represent allowable propagation frequencies and wave speeds according to PC, expressed in terms of elastic bar properties. The slope of the curves at any given point describes the propagation velocity of waves at the corresponding frequency. Thus, it can be readily seen that there are discrete relationships between wave propagation speed and wave frequency. With end-loading of the bar, the PC curves for $q > 0$ prescribe the only allowable propagation speeds of elastic waves of a given frequency. The result of this dispersive frequency propagation speed relationship prescribes the pulse shape in Fig. 1, where low frequency waves at the head of the pulse are traveling faster than the high frequency waves, which arrive later in time.

Of particular significance in this paper is the additional zeroth mode, $q = 0$, resulting from the lateral surface loading and is a straight line

indicating that particular mode allows propagation of all frequencies at the same speed, which corresponds to the surface loading speed V , i.e., it is a non-dispersive mode. Note that its slope (propagation speed) is directly proportional to the loading velocity, whereas all the higher PC modes are dependent only on bar parameters. For a given bar material and size, along with an assumed loading speed and pressure amplitude, the compressive bar response to step-function compressive loading has been calculated.⁵ An understanding of Fig. 2 provides a description of the response of a bar to both end-loading and lateral surface loading.

For all modes higher than the first ($q > 1$), the phase velocity in the high frequency limit is the shear velocity C_s . The high frequency limit phase velocity of the first mode ($q = 1$) is the Rayleigh surface wave velocity. The minimum phase velocity of the first mode C_{min} , is only slightly less than the Rayleigh velocity.

For loading velocities less than C_{min} , (roughly three-fourths of the elastic shear wave velocity C_s) the zeroth mode line does not intersect any PC mode curves and so wave propagation speed is constant at the loading speed V , for all wave frequencies. This zeroth mode result allows, in theory, a bar to respond to a lateral loading pulse with exquisitely faithful reproduction of the loading pulse. Of course limitations will arise from the finite dimensions of sensors employed to detect bar response, which will be discussed later.

For all loading velocities greater than or equal to C_{min} , there is at least one intersection of the zeroth mode and one or more of the PC modes. The intersection of the zeroth mode and a higher order mode will result in the zeroth mode non-dispersive response, followed by the singular frequency wave corresponding to the higher order PC mode intersect point.

1.3.2 Shear Stress Loading

An additional loading condition on the lateral surface of the bar is associated with a gas dynamic shock wave loading. The boundary layer flow behind a shock wave propagating along the lateral surface of a cylindrical bar exerts a shear stress on the surface of the bar. In order to establish the qualitative nature of the resulting strain, the equations of motion, Eqs. 1-4, were again solved using the method of Folk et al. The

same initial conditions and end conditions were used, but the boundary conditions on the lateral surface were assumed to be zero radial stress and a step-function shear stress traveling at the loading speed V . In reality, the shear stress should decrease with distance behind the shock, but as our intent here is only to understand the character of shear stress loading on bar response, the shear stress was assumed constant behind the shock.

The results of the double transform inversion technique predict that at time $t = z/C_0$, a positive shear stress produces a strain, which rises linearly with time. With the arrival of the loading shock at $t = z/V$ a linearly decreasing strain is added to the first so that the total shear strain decrease linearly with time.

1.3.3 Mathematical summary

Figure 4 illustrates bar response to lateral surface loads of two different speeds. Note that for all loading speeds there is an initial Airy function expansion pulse traveling down the bar at the bar velocity C_0 , followed by a compression load associated with and traveling at the loading speed V . The final strain in the bar is the sum of these two pulses and reduces to the static solution for radial compressive strain = $(P/E)(1-\sigma)$ and is independent of loading speed.

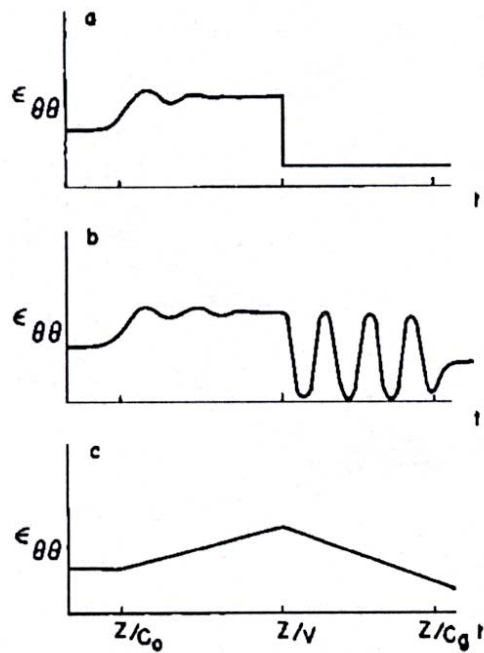


Fig. 4: Circumferential strain time profiles for a bar. (a) Normal stress loading, $V < C_{\min}$; (b) normal stress loading, $C_{\min} < V < C_o$; (c) shear stress loading, $V < C_{\min}$ [ref. 5].

For $V < C_{\min}$, total circumferential strain consists of an Airy function strain signal propagating in the bar with the bar velocity C_o followed by a negative step strain propagating with the loading velocity V , as shown in Fig. 4(a).

For $C_o > V > C_{\min}$, circumferential strain consists of the Airy function strain signal and the negative step strain of the previous case. The sinusoidal oscillations predicted by the intersection of the zeroth and first mode of the PC curves begin immediately following the negative step strain and continue until arrival of similar oscillations traveling with the group velocity. These two oscillations have the same frequency but are out of phase so they cancel exactly as shown in Fig. 4(b), and the strain in the bar is at its equilibrium value under the load P . The circumferential strain induced in a cylindrical bar by a transient shear step stress traveling with the shock speed consists of a linearly increasing ramp, which arrives at a time $t = z/C_o$, followed by a linearly decreasing ramp, which begins at a time $t = z/V$, as shown in Fig. 4(c).

An additional phenomenon not considered here is the thermal loading of the bar, which can further complicate bar and gage response intended solely to measure pressure induced circumferential strain.

1.4 Experimental configuration

The experiment designed to verify the preceding predictions for time-dependent strain in a bar required: A normal step-function stress loading of constant magnitude and loading velocity, strain measurements on a time scale allowing convenient comparison with the predictions, and use of a bar of sufficient length to allow completion of strain measurements before the arrival of strain waves reflected from the downstream end of the bar.

A conventional constant diameter bursting diaphragm shock tube, which had a 3.8 cm diameter by 1.5 m long driver section and a 7.0 m driven section, was used to produce a well characterized step-function loading pulse of shocked air. The driver section was pressurized with helium (2,000-lb/in.² maximum), and produced shock waves of desired speed and magnitude in the driven section. The shock velocity V was determined by recording the shock transit time between a pair of glow-discharge gages, placed 86 cm apart. Shock velocities were believed accurate to $\pm 2\%$. Shock pressure was computed from normal shock tables using the measured values of V , the initial pressure and temperature of the air in the driven section. The resulting shock pressure jump $-P$ loading the bar were believed accurate to $\pm 3\%$. The loading pressure ranged from 0.2 bar for fast shocks to 2.5 bar for slow shocks.

The driven section of the shock tube was modified to accommodate a long instrumented bar, co-axial with the shock tube, allowing the shocked air to establish an annular flow that progressively enveloped the lateral surface of the bar. The Plexiglas measuring bar was 0.95 cm in diameter and 2.9 m long. Plexiglas was chosen because its relatively low Young's modulus produces a larger strain than common metals such as Al or steel. A complication associated with the use of Plexiglas is its visco-elastic behavior, which was observed in the experiments. To aid in the development of a smooth region of annular flow along the bar, a lead-in bar of the same diameter and 350 cm long was mounted upstream of the instrumented bar. A second but important role of the lead-in bar was to

eliminate a reflected shock end-loading of the instrumented bar. To accomplish these goals, a small gap was adjusted between bars allowing the shocked gas to rapidly fill and equilibrate to the shocked gas pressure. A gap of <2 mm was found to accomplish both purposes. The Plexiglas bar has a low bar velocity, $C_0 = 2.08$ km/sec, compared with metals, and its length allows an observation time of more than 2 msec before arrival of elastic waves reflected from the end of the bar. The low C_0 also allows the bar to be studied over a broad range of loading velocities relative to the PC response modes portrayed and discussed in Fig. 3. Fine copper wires spaced at 90 cm intervals supported the bars and were adjustable to center the bars coaxial with the shock tube. No support was within 30 cm of either strain gage and no effect of the supports was observed on the experimental records.

A schematic of the shock tube, bar assembly, and instrumentation is shown in Fig. 5.

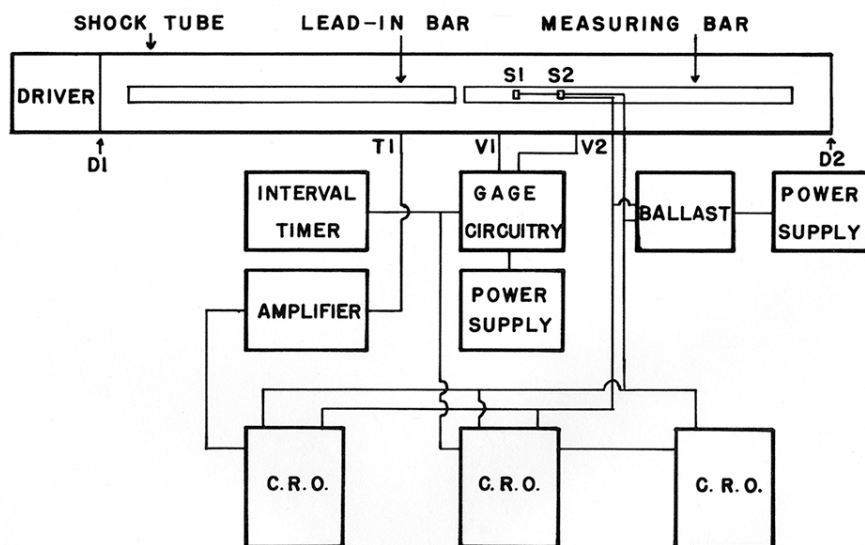


Fig. 5: Block diagram of the experiment setup [ref. 6].

V1 and V2 were glow discharge gages used to measure the average shock speed along the instrumented section of the bar. S1 and S2 are strain gages embedded beneath the surface of the bar to measure circumferential strain of the bar while being isolated from direct contact with the shocked gas. The gages were 30 cm apart. Gages S1 and S2 each consisted of four thin-film metal strain gages connected in series

and placed symmetrically on the measuring bar. This arrangement provided negligible sensitivity to flexural waves while providing maximum sensitivity to circumferential strain. A constant 10.0 mA current powered the gages and a gage voltage change of 0.3 mV resulted from a typical shock-produced strain of 10^{-5} . Shock transit times across the 0.185cm width of the strain gages ranged between 1 and 3 μ sec in these experiments. The signals were recorded on Tektronix type 555 and 585 oscilloscopes equipped with type D amplifiers.

Figures 6 and 7 are data records of circumferential strain vs time representative of different regimes of shock velocities studied. Strain is positive upward and time progresses from left to right.

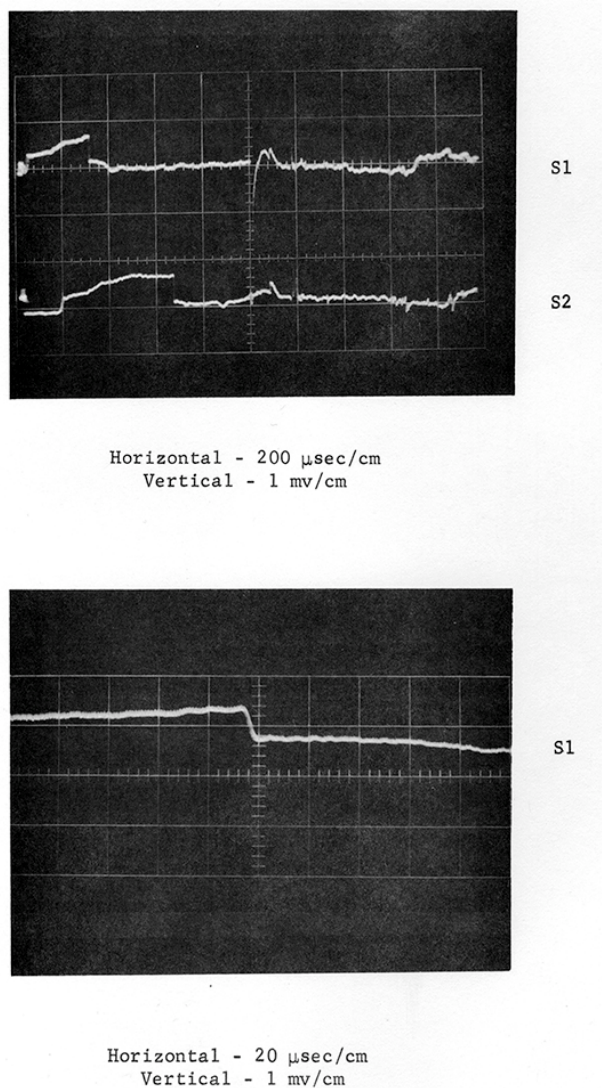
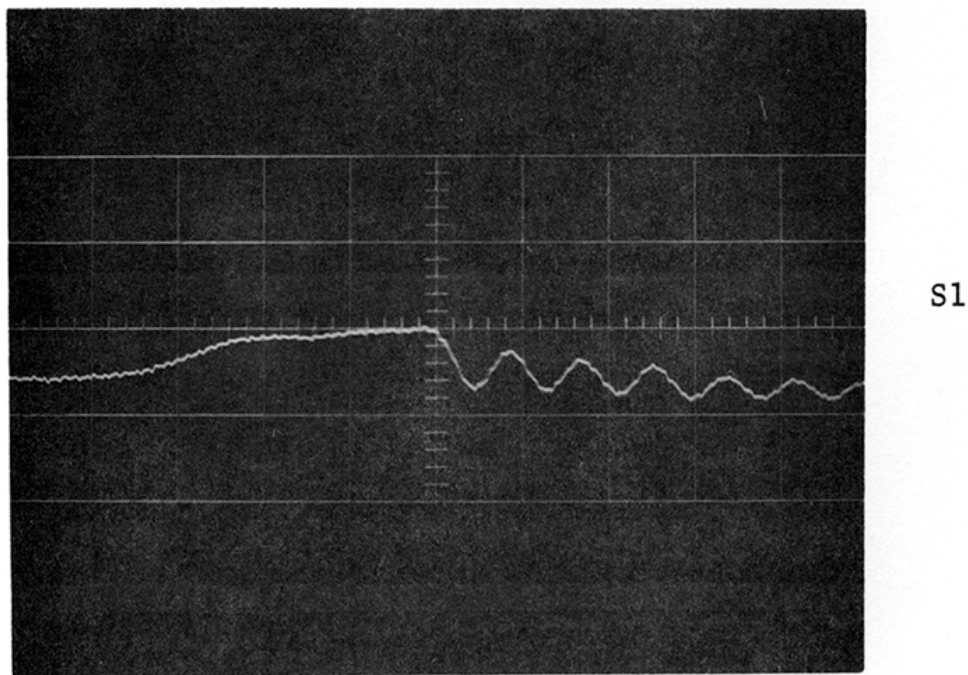


Fig. 6: S1 and S2 strain gage records for shock velocity $V=0.877 \times 10^5$ cm/sec [ref. 6].

Figure 6 shows a representative data record of S1 and S2 strain gage voltages versus time. Increases in strain are positive on the vertical axis and time increases from left to right. The shock velocity ($V = 0.877 \times 10^5$ cm/sec) is less than the minimum phase velocity of the first PC mode ($C_{\min} = 1.184 \times 10^5$ cm/sec). The first signal on the left travels with the bar velocity C_0 and is produced both by the loading of the lateral surface and by the filling of the gap between the lead-in and measuring bars. The slowly rising ramp signal has the qualitative features predicted for shear loading on the lateral surface (a thermally produced surface stress could show similar behavior). The negative step on the

records coincides with the loading shock arrival and represents the rapid compression of the bar resulting from the shock passing directly over the strain gages. The lower record of S1 is the same S1 gage response at a faster recording speed and shows a smooth negative response of the bar, corresponding with the 4 μsec transit time of the shock over the S1 gage width. Note the clean response of the bar to the shock loading and the absence of any associated overshoot and ringing. This response corresponds with the calculated response for the velocity conditions shown in Fig. 4(a). Figure 7 shows a similar record for strain gage output for a shock velocity ($V = 1.79 \times 10^5 \text{ cm/sec}$) greater than C_{min} . Oscillations follow the arrival of the shock as predicted by the theory, but they are damped because of the visco-elastic behavior of the Plexiglas.



Horizontal - 10 $\mu\text{sec/cm}$
Vertical - 1 mv/vm

Fig. 7: S1 strain gage record for shock velocity $V=1.79 \times 10^5 \text{ cm/sec}$ [ref. 6].

1.5 Comparison of experiment and theory

Comparisons of experiment and theory were based on measurements taken from oscilloscope traces similar to those shown in Figs. 6 and 7, the measured shock velocity V , and the measured initial temperature and pressure of the gas. The pressure jump $-P$ across the shock was calculated from normal shock tables⁸ and the applied lateral surface stress $\tau_{zz}(z, a, t)$ was taken to be $PS(t-z/V)$.

The experimental strain-time data were plotted along with the calculated strain histories. Only the strain wave traveling with the shock velocity is considered in this quantitative time-dependent strain comparison. Figures 8 and 9 show both calculated and experimental strain responses of the measuring bar to passage of the traveling air shock. The zero for the time coordinate used in the comparison occurs when the shock passes over the center of the strain gage. As data records did not contain an absolute indicator showing the arrival for the shock at the center of the gage, the experimental and calculated curves were aligned in time to obtain a best fit. The calculated strain data were averaged over a time interval τ corresponding to the transit time of the shock front across the width of the strain gage. This transit time in microseconds is indicated by a horizontal flag in each of Figs. 8 and 9. The possible data error in reducing the gage record to numerical data is shown by a vertical flag in each figure.

The values of the elastic bar parameters used in the calculations are

$C_s = 1.27 \times 10^5$ cm/sec	shear velocity,
$C_o = 2.08 \times 10^5$ cm/sec	bar velocity,
$C_d = 2.64 \times 10^5$ cm/sec	dilatational velocity,
$\Sigma = 0.35$	Poisson's ratio,
$E = 5.22 \times 10^{10}$ dyn/cm ²	Young's modulus

The values were taken from Meitzler⁹, whose measured values for the dilatational wave velocity in Plexiglas agreed within an experimental error of ± 2 % with ultrasonic measurements.

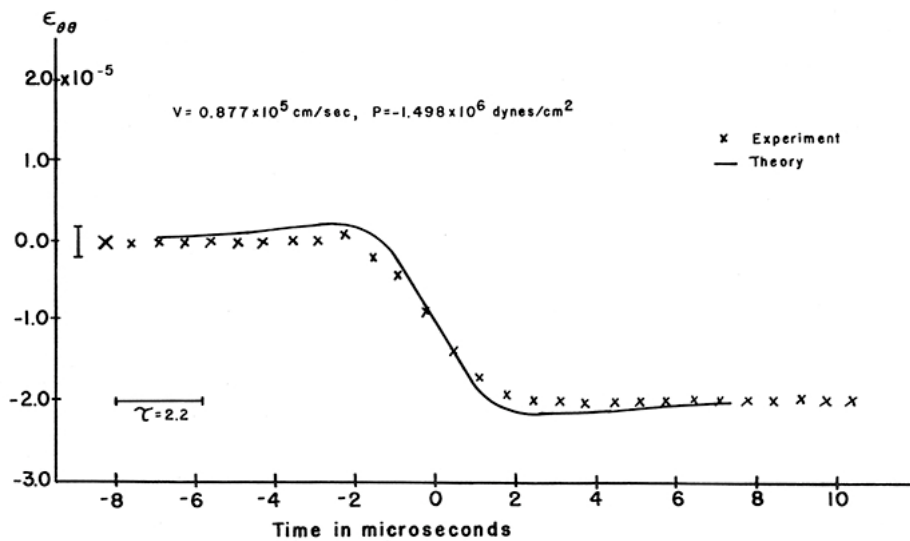


Fig. 8: Comparison of theory and experiment for strains produced by shock loading, $V = 0.887 \times 10^5$ cm/sec, $P = -1.498 \times 10^6$ dyn/cm² [ref. 6].

Figure 8 shows the simple behavior of the bar typical of speeds $V < \frac{3}{4}C_s$. The numerical data were taken from the S1 record in Fig. 6, converting the vertical scale from units of voltage to units of strain. The pressure jump across the shock front was 1.50×10^6 dyn/cm². A point-by-point comparison of experiment and theory in Fig. 8 shows the deviation of the two curves is less than the width of the oscilloscope trace. A correction for the high-frequency electrical response of the gage circuitry was not required.

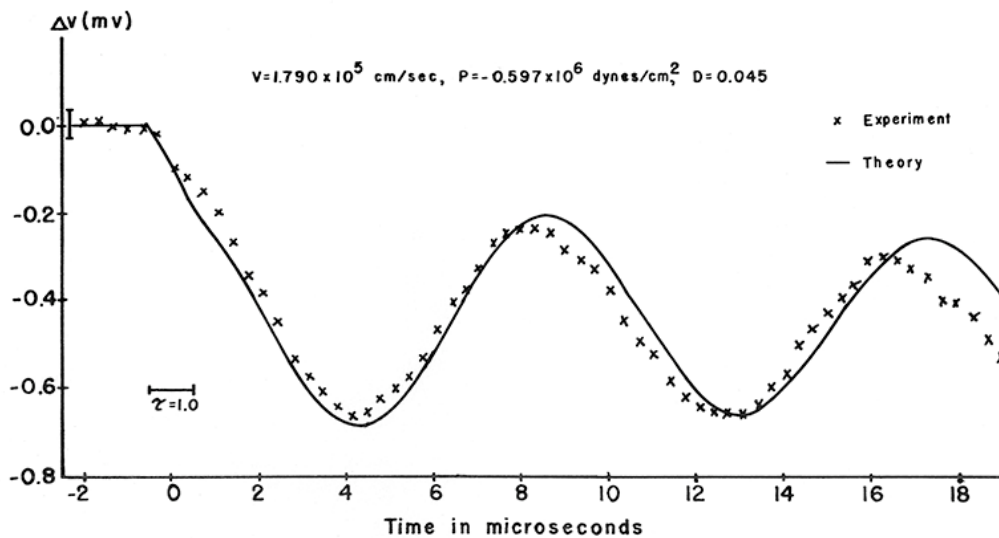


Fig. 9: Comparison of theory and experiment for strains produced by shock loading, $V = 1.79 \times 10^5 \text{ cm/sec}$, $P = -0.597 \times 10^6 \text{ dyn/cm}^2$ [ref. 6].

Figure 9 compares experiment and theory in the higher velocity regime where oscillations follow shock arrival. While the agreement is good, there is a slight discrepancy between calculated and measured frequencies. It is noted that the PC oscillation frequency is determined by the intersection of the $q = 0$ and $q = 1$ mode in Fig. 3 and the slope of the curves is such that a small change in characteristic material velocities or shock velocity will result in a larger change in the intercept point and thus predicted oscillation frequency. An example of the sensitivity is seen in Fig. 10, which is a comparison of the same data in Fig. 9, but with the elastic parameters adjusted by 2 %.

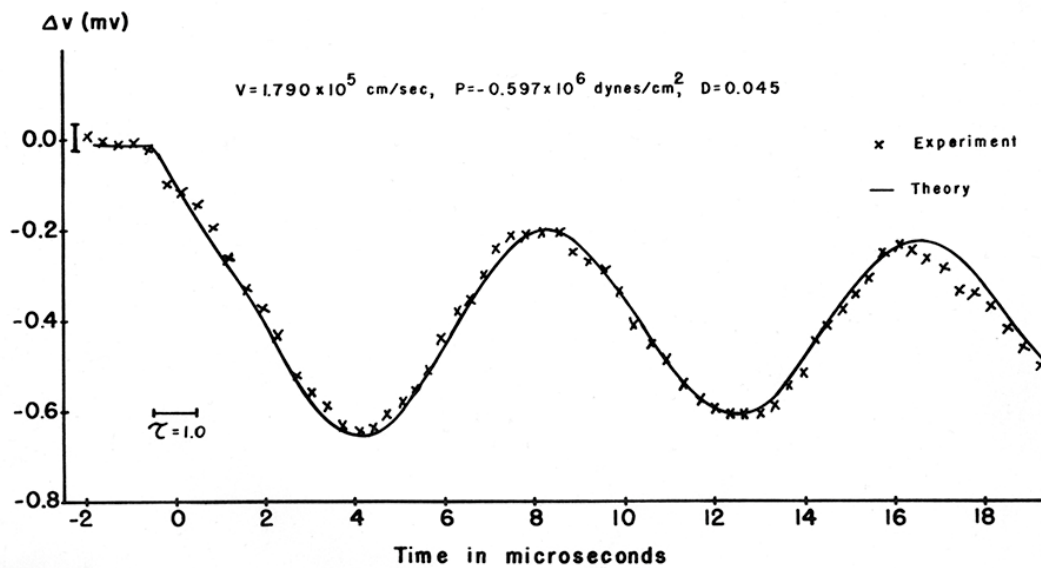


Fig. 10: Comparison of theory and experiment for strains produced by shock loading, $V = 1.79 \times 10^5 \text{ cm/sec}$, $P = -0.597 \times 10^6 \text{ dyn/cm}^2$, adjusted parameters [ref. 6].

The improved agreement seen in Fig. 10 resulted from an increase in C_s , C_o , C_d of 2 %. Note that values of these parameters were taken from Ref. 9 and were not independently measured for our bar material. With this small adjustment in parameters, the agreement with experiment is within the measurement error bars.

1.6 Summary

Prior work has been reviewed and referenced, which collectively provides a rigorous theoretical and experimental basis for realizing a non-dispersive response mode in a Hopkinson bar configuration. The configuration requires a lateral surface exposure to a shock loading pulse, which is consistent with the pencil probe geometry and orientation for measurement of blast waves. To realize the non-dispersive behavior, the blast wave speed must be less than $\frac{3}{4}$ of the shear wave velocity of the bar material. In this lateral loading mode, the frequency response of the bar is not limited and thus the time resolution obtainable from the bar is determined by the strain sensor response and the transit time of the shock over the strain sensor in the bar. Additional considerations on bar design in addition to elastic parameters include material properties and

surface finish to minimize effects of boundary layer drag and thermal conduction from shocked gas to the bar.

This collective of work demonstrates a capability through both theory and validating experiments for the direct utilization of a Hopkinson bar to faithfully reproduce a shock wave loading profile without the overshoot or ringing associated with the response of pressure transducers.

1.7 References

- [1] Hopkinson, B.: *Phil. Trans. R. Soc. Lond.* A213 437-456 (1914).
- [2] Pochhammer, L.: *J. Math. (Crelle)* **81**, 324 (1876).
- [3] Chree, C.: *J. Math.* **21**, 287 (1886).
- [4] Folk, R., Fox, G., Shook, C. A., and Curtis, C. W.: *J. Acoust. Soc. Amer.* **30**, 552-558 (1958).
- [5] Baum, D. W.: *J. Acoust. Soc. Amer.* **52**, 5 (part 2), 1421-1428, (1972).
- [6] Baum, D. W.: Thesis, Lehigh University, 1967.
- [7] Values for the Airy function are tabulated by M. C. P. Miller, *The Airy Integral* (Cambridge University Press, New York, 1946).
- [8] *Handbook of Supersonic Aerodynamics* (U. S. GPO, Washington, D. C., 1953).
- [9] Meitzler, A. H.: Thesis, Lehigh University, 1955.

This work performed under the auspices of the U.S. Department of Energy by Lawrence Livermore National Laboratory under Contract DE-AC52-07NA27344.

Application of gas-gun testing stand for experimental and theoretical studies of dynamic tensile and failure of hat-shaped specimens

V.G. Bazhenov, M.S. Baranova, E.V.Nagornykh

Research Institute of Mechanics, Lobachevsky State University of Nizhni Novgorod,
Pr. Gagarina 23, 603950 Nizhni Novgorod, Russia
Phone: +78314656611, Fax: +78314656611, email: mari.baranova18@gmail.com

1.1 Introduction

All known tensile testing techniques of hat-shaped specimens are based on the Hopkinson's scheme and Kolsky's method (Lindholm, U. [1], Mohr, D. [2], Gary, G. [2], Nicholas, T. [3] etc.). It is difficult to implement the strain rate in the order of 100 sec^{-1} in these apparatuses at horizontal configuration of rods. Experimental studies of the characteristics of failure by a direct impact method to the hat-shaped specimens on the vertical gas-gun testing stand are unknown to authors. Also there isn't analysis of the advantages and disadvantages of using a solid or tubular supported and measuring elements as a measuring rod.

1.2 The study of one-dimensional wave processes in the rod and tube

Solid or tubular rods is used by different researchers as support measuring elements in the testing of hat-shaped specimens. To estimate the accuracy of the experimental measurements of strain in these rods numerical investigations of wave process under impact loading of tubes and rods are conducted using application package "Dynamics - 2" [4] in axisymmetric formulation.

Measuring rods are considered as perfectly elastic mechanical characteristics $K = 1,7917 \cdot 10^5 \text{ MPa}$, $G = 8,269 \cdot 10^4 \text{ MPa}$, $\rho = 7,8 \cdot 10^3 \text{ kg/m}^3$. Rod lengths $L = 0,65 \text{ m}$, the outer radius of the tube $R_1 = 0,03 \text{ m}$, internal - $R_2 = 0,0217 \text{ m}$.

Solid rods are taken in two diameters: the first rod radius equal to the outer tube radius, the radius of the second rod $R_2 = 0,0207$ m, its cross section is equal to the cross sectional area of the tube.

For $t > 0$ constant axial velocity $V = 9.6$ m/s is set at the impacted end. Axial velocity is zero at the opposite end. Friction is not taken into account. Strain gages, recording deformation, are positioned at a distance of 15 cm from the impacted and supported ends. Calculations are performed on a square of the difference grid having 198 cells in length and 9 and 6 cells at the radius of the first and second rods and 2 cells at thickness of the tube. Smoothing of discontinuous solutions is applied to eliminate unphysical oscillations.

Fig. 1 - 3 shows a comparison of the axial strain in the locations of the strain gages on the tube, the first and second rods, respectively, in a one-dimensional (curves 1 and 2) and an axisymmetric (curves 3 and 4) formulations of the problem. e^A - axial strain near the impacted end of the rod, e^B - axial strain near the supported end.

Travel time of wave on tube (rod) is defined by $T = L/c$ where c - velocity of dimensional waves propagation in the tube (rod).

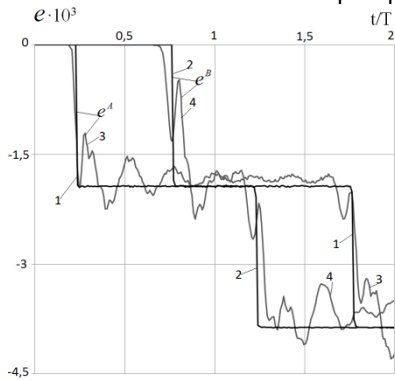


Fig.1: Axial strain in the locations of the strain gages on the tube.

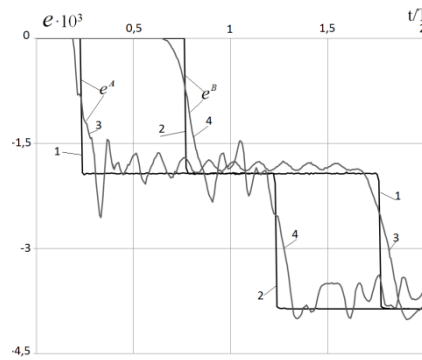


Fig.2: Axial strain in the locations of the strain gages on the first rod.

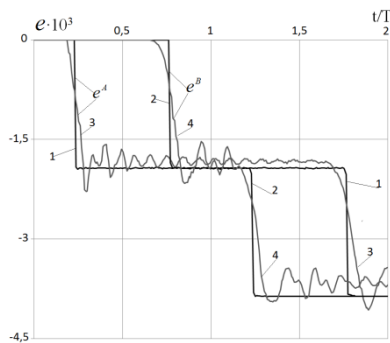


Fig.3: Axial strain in the locations of the strain gages on the second rod.

In axisymmetric formulation, unlike the one-dimensional formulation, oscillation amplitudes of longitudinal strain are observed, It is caused of transverse oscillations of tube and rods.

Analysis of numerical results shows that the amplitude and period of the oscillations of strain in the tube is greater than in the rods. Due to the discontinuity of displacement rate under impact loading at $t = 0$, the first peak is physically invalid, since it is exerted by dispersion of numerical solution. Later oscillations are damped slowly because of the conservative smoothing of numerical solutions. Numerical results are agreed well with the fact in experiment and theory - the thinner rod, the smaller the amplitude of transverse oscillations relative to the level of strain in the one-dimensional theory of longitudinal waves. Therefore, the amplitudes of oscillation of longitudinal strain are 2-3 times greater than a solid rod of the same cross section in the tube always.

1.3 Experimental and numerical study of the tensile deformation process of hat-shaped specimens on the gas-gun testing stand

Gas dynamic vertical test machine (vertical gas-gun testing stand) is developed in Research Institute of Mechanics Lobachevsky State University of Nizhni Novgorod.

This is a vertical impact machine with falling weight (hammer head) having pneumodynamic velocity device connected to the barrel. The

range of impact velocities is from 3 m / s to 60 m / s. The range of striker mass is from 3 kg to 10 kg.

The main elements of the gas-gun testing stand are striker, specimen and measuring rod. Scheme: 1 - striker, 2 - transmitting tube, 3 – hat-shaped specimen, 4 – measuring rod is used in the numerical simulation of wave process in the system striker - specimen - measuring rod in tensile process. This scheme is shown in Fig. 4 Oz - the axis of symmetry. The striker is moved at a predetermined velocity V_0 . Transmitting tube contacts with a flange of the specimen. Tension force is applied to the flange of the specimen after impact on the transmitting tube.

Strain gages record pulse of axial strain. It is located at a distance of 20 cm from the impacted end of the measuring rod.

Geometric dimensions, with which the calculations are performed, are shown in Fig. 4 (in centimeters). Mass striker - 7.5 kg.

The striker, the transmitting tube and the measuring rod are deform elastically, the specimen is deform elastoplastically. Mechanical characteristics of the elements of testing stand are shown in Table 1.

Tab.1: Mechanical characteristics of the elements of testing stand

Nr of subdoma in(fig.4)	Striker	Tube	Specimen	Measuring rod
Material	Steel 20	Steel 20	D16	Steel 35HGSA
K, MPa	$1,77 \cdot 10^5$	$1,77 \cdot 10^5$	$6,25 \cdot 10^5$	$1,79 \cdot 10^5$
G, MPa	$8,15 \cdot 10^4$	$8,15 \cdot 10^4$	$2,89 \cdot 10^5$	$8,27 \cdot 10^4$
ρ , kg/m ³	$7,8 \cdot 10^3$	$7,8 \cdot 10^3$	$2,8 \cdot 10^3$	$7,8 \cdot 10^3$
σ_T , MPa	$4,5 \cdot 10^2$			

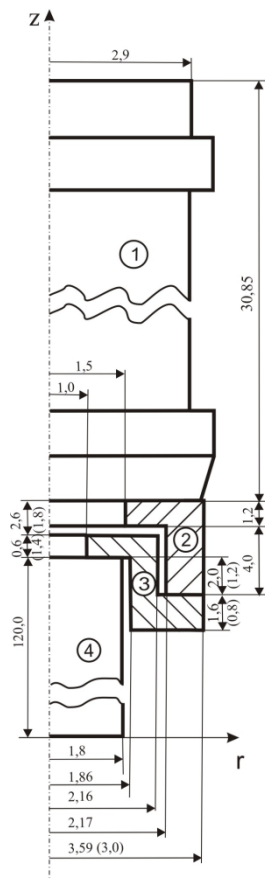


Fig.4: Gas-gun testing stand scheme.

The true stress-strain diagram of the material D16 (Fig. 5) which is obtained from dynamic compression experiments of tablets specimen as described in [5]. is used in calculations. Material was not sensitive to strain rate.

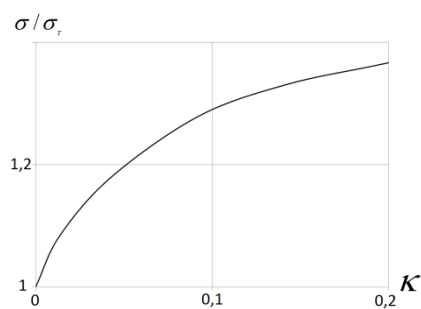


Fig.5: True stress-strain diagram of the D16 alloy.

"Bending" of the meridian section of the specimen is observed in the process of deformation at an impact velocity $V_0 = 30,7 \text{ m / s}$. At the same

time there is a partial separation of the contact surfaces of specimen and measuring rod. During deformation the outer surface of the specimen come into contact with the inner surface of the transmitting tube. Because of this, there is a significant nonuniformity of the stress-strain state of the test portion of the specimen. Therefore, it is advisable to change the geometrical dimensions of the specimen. These dimensions are shown in Fig. 4 in parenthesis. Test portion length is reduced from 2 cm to 1.2 cm; thickness bottoms increased from 0.6 cm to 1.4 cm; radius of the flange and the transmitting tube is reduced from 3.59 cm to 3 cm

Calculation with changed dimensions shows that separation of bottom from the measuring rod on the line of contact does not happen, and the stress-strain state of the test portion of the specimen become more homogeneous.

According to the second considered scheme, specimens are prepared. In the experiment, the initial axial velocity of the impact 9,6 m / s. Mass of striker - 5kg. Fig. 6 shows the time dependence of the axial force in the strain gage, which is located at a distance of 0.3 m from the the impacted end of measuring rod. - There is good agreement between the values of stresses in the experiment (curve 1) and calculation (curve 2). Here T - travel time of wave on measuring rod $F_r = \sigma_r S$, σ_r - yield stress, S - cross-sectional area of the test portion of the specimen.

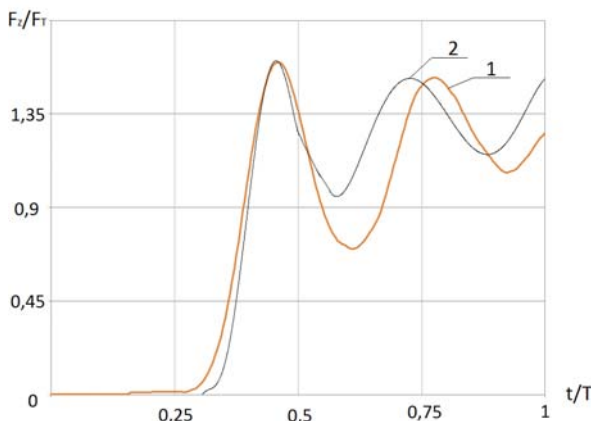


Fig.6: Axial force in the strain gauge.

The average strain of the test portion of specimen is about 4 %.

1.4 Investigation of the influence of geometrical parameters on the gas-gun testing stand in the tensile process

Analysis of the influence of the length of the striker, length and thickness of the test portion of the specimen, length and thickness of the supported tube on the velocity and degree of strain is done in modeling of the tensile process of the specimen in the gas-gun testing stand. The following scheme is considered (Fig. 7): the striker (1) measuring rod (2), hat-shaped specimen (3), tube (4).

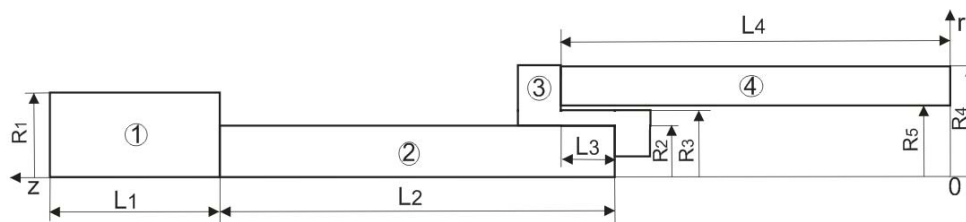


Fig. 7. Gas-gun testing stand scheme.

Geometrical parameters of the gas-gun testing stand are shown in Table 2. $m_1 = 10$ kg, $R_1 = 0,0364$ m, $l_1 = 0,3085$ m, $R_2 = 0,018$ m, $L_2 = 0,65$ m, $l_3 = 0,006$ m, $h_3 = R_3 - R_2 = 0,001$ m, $R_4 = 0,03$ m, $R_5 = 0,0217$ m, $l_4 = 0,325$ m Initial velocity of striker is 3 m / s.

Tab. 2: Mechanical characteristics of the elements of testing stand

Nr	Mass of striker m_1	Length of striker L_1	Length of test portion of specimen L_3	Thickness of test portion of specimen H_3	Length of tube L_4
1	m_1	$2l_1$	l_3	$3h_3$	$2l_4$
2	$2m_1$	$2l_1$	$4l_3$	h_3	l_4
3	$2m_1$	$2l_1$	$4l_3$	h_3	$2l_4$
4	m_1	l_1	$4l_3$	h_3	l_4
5	m_1	l_1	$2l_3$	h_3	$2l_4$
6	m_1	l_1	$4l_3$	h_3	$2l_4$
7	m_1	l_1	$4l_3$	$3h_3$	$2l_4$
8	$2m_1$	$2l_1$	$2l_3$	h_3	$2l_4$

In Figure 8, curves 1-8 are time dependences of conditional strain in the test portion of specimen, and Fig. 9 - time dependences of the strain rates (curves 1-8). Numbers of curves are corresponded to the number of rows in the table 2 in Fig. 8 and Fig. 9.

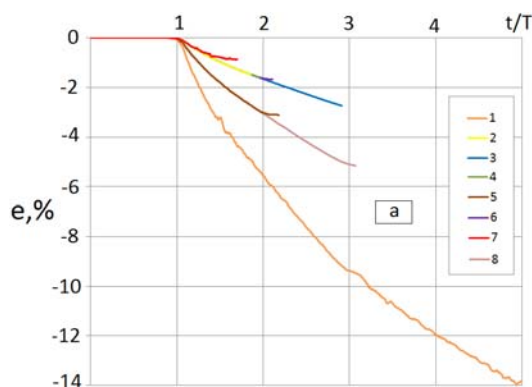


Fig. 8: Conditional strain in the test portion of specimen.

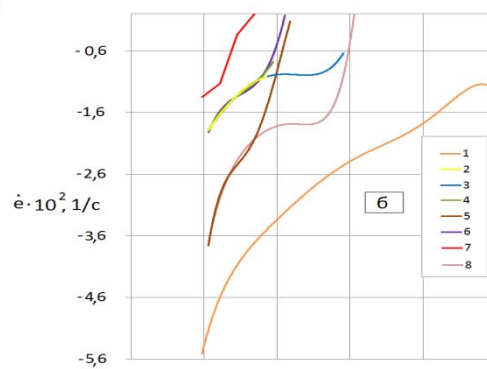


Fig.9: Strain rates.

The highest degree of strain of the order of 14% is achieved on the curve 1 at the $5,5 \cdot 10^{21} / s$ strain rate in the case $L_1 = 2l_1$, $L_3 = l_3$, $H_3 = 3h_3$, $L_4 = 2l_4$, $m_1 = 10$ kg.

The lowest strain rate is $1,5 \cdot 10^2$ 1 / s in the case of $L_1 = l_1$, $L_3 = 4l_3$, $H_3 = 3h_3$, $L_4 = 2l_4$, $m_1 = 10$ kg (curve 7).

1.5 Scheme of gas-gun testing stand and testing methodology by direct impact method

Gas-gun testing stand for tensile testing by direct impact method (Figure 10) contains the following elements: supported measuring rod (marked 1), hat-shaped specimen (2), transfer ring (3), striker (4).

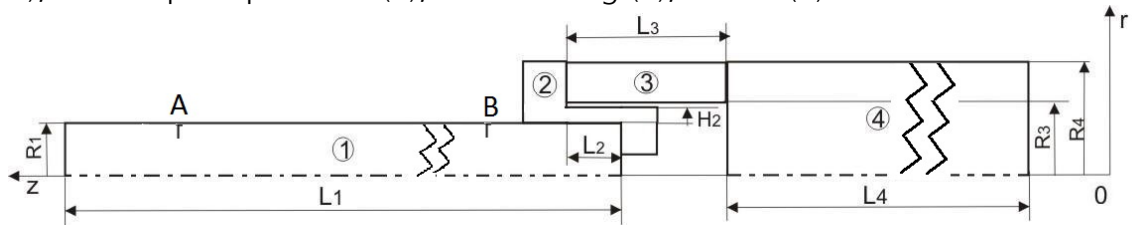


Fig. 10: Scheme of gas-gun testing stand for testing by direct impact method.

Geometric parameters of the elements of gas-gun testing stand are: radius and length of measuring rod $R_1 = 1,8 \cdot 10^{-2}$ m and $L_1 = 1,2$ m, the thickness and length of the test portion of the specimen $H_2 = 1 \cdot 10^{-3}$ m and $L_2 = 0,6 \cdot 10^{-2}$ m, the inner radius of the ring and the length of $R_3 = 2,17 \cdot 10^{-2}$ m and $L_3 = 5 \cdot 10^{-2}$ m, radius and length of the striker $R_4 = 3,45 \cdot 10^{-2}$ m and $L_4 = 30,85 \cdot 10^{-2}$ m. Material of striker, tube and measuring rod is steel 20, the mechanical characteristics: $K = 1,7917 \cdot 10^5$ MPa, $G = 8,269 \cdot 10^4$ MPa, $\rho = 7,8 \cdot 10^3$ kg/m³. Specimen material - D16T alloy, mechanical characteristics: $K = 6,25 \cdot 10^4$ MPa, $G = 2,885 \cdot 10^4$ MPa, $\rho = 2,8 \cdot 10^3$ kg/m³, yield stress $\sigma_T = 190$ MPa.

The initial velocity V_0 of the striker is recorded in the experiment. Strain gages are located in sections A and B at a distance $l_A = l_B = 0,3$ m (Figure 10) of the measuring rod. It registers the strain pulse $e_z^A(t)$, $e_z^B(t)$ at the ends of the rod in dependence on the time.

The procedure of recovery of the wave process using two strain gages is considered in [6]. Based on the methodology in [6] stress $\sigma_z^1(t)$ and

velocity $\dot{u}_z^1(t)$ on impacted end of measuring rod are reversed. Axial force on the impacted end of the measuring rod is given by

$$F_z^1 = \pi R_1^2 \sigma_z^1 \quad (5.1)$$

Displacement is given by

$$u_z^1 = \int_0^t \dot{u}_z^1(t) dt \quad (5.2)$$

And axial forces F_z^1 and F_z^3 on the contact surfaces of the specimen and measuring rod, specimen and transfer ring, are equal.

Displacement of the contact surface of the specimen and the ring is determined by integrating the equations of motion striker with given initial conditions

$$m\ddot{u}_z^3 = F_z^3, \quad \dot{u}_z^3|_{t=0} = V_0, \quad u_z^3|_{t=0} = 0 \quad (5.3)$$

where m - the total mass of the striker.

Thus, forces, velocities of displacement and displacements at the impacted end of measuring rod and at the contact surface of the transfer ring can be determined using registering strain by two strain gages in the rod.

In the future, the strain registration by strain gages in a physical experiment is replaced to registration of strain in mathematical experiments.

Numerical simulation of wave process in the "striker - transfer ring - specimen – measuring rod" in axisymmetric formulation is done using SPT "Dynamics - 2".

1.6 Verification of methodology

For verification of methodology numerical simulation of wave process in the "striker - transfer ring - specimen – measuring rod" in axisymmetric formulation is done using "Dynamics - 2".

Fig. 11 - 14 shows the results of calculations at impact velocities ($V_0 = 3$ and $V_0 = 5$ m / s) in an axisymmetric formulation (curves 1) and a one-dimensional model (curve 2). Scheme and geometric parameters of the testing stand are presented in Figure 10. The data from two strain gages are taken from calculations in axisymmetric formulation.

Fig. 11 shows the dimensionless time dependence of the axial force on the impacted end of the measuring rod which obtained from the one-dimensional and axisymmetric calculation. Dimensionless time $\hat{t} = t/T$, where $T = 68$ msec - time of propagation an elastic wave on the total length of the striker $L_4 = 0,3$ m and rings $L_3 = 0,05$ m.

Fig. 12 shows the dimensionless time dependence of displacements on the impacted end of measuring rod, obtained by integrating the formula (5.2) and the axisymmetric calculation. Fig. 13 shows the dimensionless time dependence on the displacement velocities on the contact surface of transfer ring and specimen obtained by integrating the equations of motion of the striker and the ring (5.3) and axisymmetric calculation. Figure 14 shows the dimensionless time dependence of $\Delta l / L_2 \sim \hat{t}$. Where $\Delta l = u_z^3 - u_z^1$.

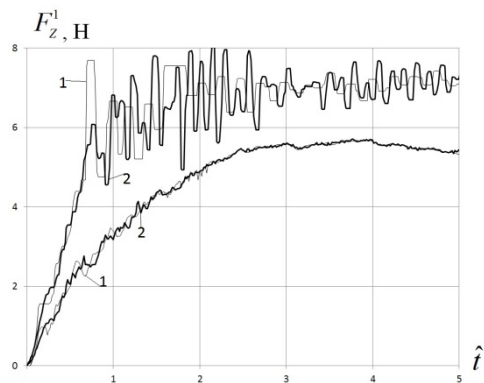


Fig.11: Axial force on the impacted end of the measuring rod.

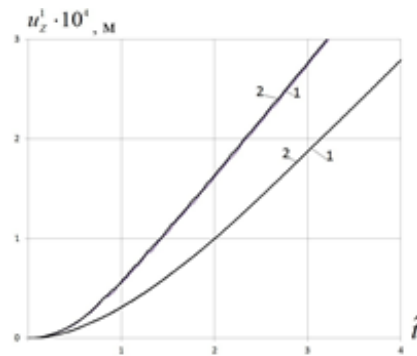


Fig.12: Displacements on the impacted end of measuring rod.

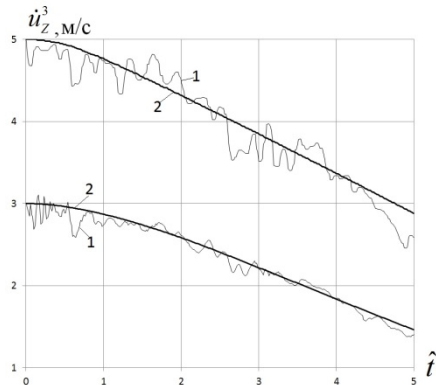


Fig.13: Displacement velocities or the contact surface of transfer ring and specimen.

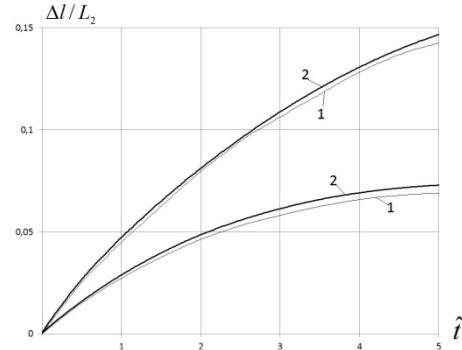


Fig.14: $\Delta l / L_2 \sim \hat{t}$.

Differences of calculating axial forces and displacement velocity in axisymmetric and one-dimensional formulations do not exceed 5%, and the strains and displacements are no more than 2%. Therefore, in analyzing the results of the physical experiment basic inaccuracy depends on the accuracy of the initial registration of the impact velocity and strain by strain gages in the measuring rod.

When comparing schemes dynamic test materials by a split Hopkinson bar method and a direct impact using gas-gun testing stand, it should be noted that each of these schemes has its own advantages and disadvantages. In the experiments based on Hopkinson method the loading pulse is nearly rectangular, and hence the strain rate is close to constant in the test specimen. This scheme is difficult to implement in the gas-gun testing stand due to a large length of rods. The direct impact method, due to the presence of only one measuring rod has a lower accuracy in determining the values of force and displacement velocities at the contact surfaces of the specimen, but provides higher impact energy and, consequently, the degree of strain at low and high impact velocities. So it preferred using two strain gages for tension-compression testing at considerable strains and more time of deformation process until fracture. The accuracy of the estimates of the parameters of processes of deformation is high enough, since the time of establishment of the wave process in the test specimen is small to negligible.

1.7 Conclusion

Numerical and physical modeling of the deformation process of the hat-shaped specimen for tensile process on the gas-gun testing stand are performed. It has been established that the strain amplitude of the oscillations in the supported tube is much larger than the equivalent of cross-sectional rods. With the increase in the diameter of the rod or tube growth oscillation amplitudes are observed.

The influence of the gas-dynamic parameters: mass, length, and the initial velocity of the striker, length and thickness of the test portion of the specimen is analyzed in the tensile process. It is shown that the achievable strain rates are order $1,5 \cdot 10^2$ 1 / s (and more) with degrees of strain sufficient to ductile failure of specimens with stress concentrators. Range of strain rates of the order of 10^2 is currently difficult to implement on the horizontal test machines such as Hopkinson bar.

A numerical simulation of the deformation process of the hat-shaped specimens in tension on the gas-gun testing stand with transfer ring is performed. It has been established that the test scheme in the case where the transfer ring, which transmits force to the test specimen and moves together with the striker, is more preferable as compared with a scheme where the ring is at rest, since the wave stage of process is reduced by time.

By comparing the results of the calculation process in axisymmetric impact and dimensional performances is shown that the error recovery efforts, displacement velocity and displacement in the test specimen on the basis of a one-dimensional model does not exceed 5 %.

Concluded that the application of a direct impact method is preferably at low impact velocities and (or) at large strains to failure.

1.8 Acknowledgments

The authors thank their colleagues from the Research Institute of Mechanics of Lobachevsky State University of Nizhni Novgorod, Zhegalov,

D.V., Kazakov, D.A., Korobov, V.B. for their help in conducting the experiments.

The research was financially supported by the Russian Ministry under the federal target program "Research and development on priority directions of scientific-technological complex of Russia in 2014 - 2020 years." Unique identifier project RFMEFIBBB14X0148.

1.9 References

- [1] Lindholm, U.S., Yeakley, L.M.: *High strain-rate testing: tension and compression*. Exp. Mech., Vol. 8, N 1, 1–9, 1968.
- [2] Mohr, D., Gary, G.: *High strain rate tensile testing using a split Hopkinson pressure bar apparatus*. J.Phys IV, Vol.134, 617-622, 2006.
- [3] Nicholas T.: *Tensile testing of materials at high rates of strain*. Exp.Mech. Vol.21, N 5,177-195, 1981.
- [4] Bazhenov, V.G., Zefirov, S.V., Kochetkov A.V., *Application Program Package "Dynamic -2"*, Problems of strength and plasticity. Research and optimization of constructions. Gorkovsky university. 4-13, 1987.
- [5] Bazhenov, V.G., Baranova, M.S., Pavlenkova, E.V.: *Development and verification of the direct impact method for identifying viscoplastic properties of materials in experiments on a gas dynamic vertical test stand*. Problems of resistance and plasticity, N.Novgorod, Stare university, 71, 184-192. 2009.
- [6] Bazhenov, V.G., Baranova, M.S., Pavlenkova, E.V.: *A method for research viscoplastic characteristics of materials using a vertical gas-gun stand*. 10th International Conference on the Mechanical and Physical Behaviour of Materials under Dynamic Loading, September 2-7, Fraunhofer EMI, Freiburg, Germany, EDP Sciences, 01059-p-1 - 01059-p-4, 2012.

A combined approach to dynamic testing of structural materials

A. M. Bragov, L. A. Igumnov, A. Yu. Konstantinov, A. K. Lomunov

1.1 Abstract

An idea of a combined approach to dynamically testing materials in the strain-rate range of $2 \cdot 10^2 \div 10^4 \text{ s}^{-1}$ is presented. In the approach, a scheme for forming a constant strain rate, the direct impact method and Kolsky method using Split Hopkinson Pressure Bar (SHPB) are combined in the same experiment. Examples are given illustrating the potential of the present approach.

1.2 Introduction

Dynamic tests of structural materials using traditional Kolsky method [[1]] are known to be conducted with a varying strain rate. Griffiths [[2]] was the first to use loading SHPB through an additional bar and a specimen. In this case, a pulse of increasing amplitude is formed in the SHPB system, its amplitude being determined by the nature of strengthening of the additional specimen. The tested specimen is deformed with a practically constant strain rate.

As back as in the middle of the 80-ies of the last century, the present authors proposed loading the SHPB system through an additional specimen situated at the left end of the transmitting bar [[3]-[5]]. A similar scheme for loading SHPB was later introduced by Nemat-Nasser [[6]] and then discussed in detail in Chen [[7],[8]]. Unfortunately, our works were published in Russian-language literature, which is hard to work with for foreign researchers.

Hauser [[9]] presented a methodology for determining dynamic properties of materials for the strain rates of 10^3 - 10^4 s^{-1} , called the *direct impact method*. This method was substantially developed in the works by Klepaczko [[10]]. The present paper describes combined use of Kolsky

method, the direct impact method and pulse shaping technique in the same experiment for dynamically testing materials in the strain-rate range of $10^2 \div 10^4 \text{ s}^{-1}$.

1.3 Pulse shaper

As was mentioned above, in traditional versions of Kolsky method for testing highly strengthening materials, the strain rate at the stage of plastic deformation under a trapeze-shaped loading pulse decreases considerably. This effect is qualitatively illustrated in Fig. 1. As strain rate is proportional to pulse ϵ^R reflected from the specimen which, in its turn, is equal to the difference between incident pulse ϵ^I and transmitted pulse ϵ^T , the strain rate decreases considerably, which is evident in Fig.1. To maintain a constant or nearly constant strain rate, it is necessary to apply a loading pulse with an increasing amplitude. To this end, we proposed loading the SHPB system with a pulse formed by an impact of a striker through a pulse shaper. A tablet of the same material that the tested specimen, or of some other material, could be used.

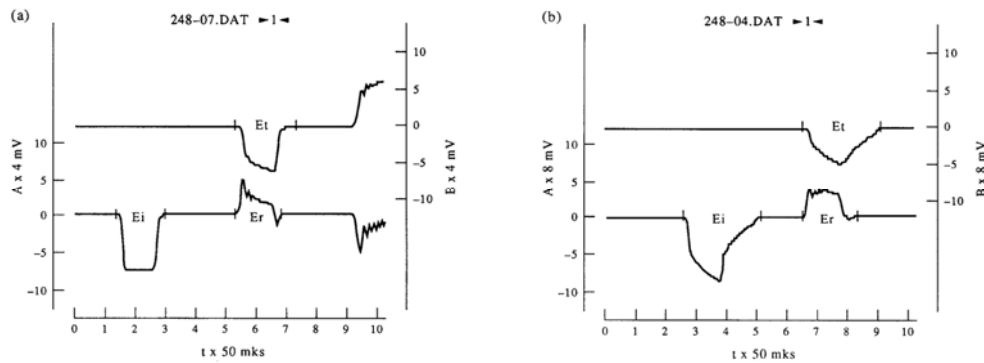


Fig. 1. Strain pulses in SHPB: traditional (a) and with pulse shaper (b).

The effect of varying the strain rate on the form of the deformation diagram is demonstrated in Fig. 2, based on the results of testing the AMg6M aluminum-magnesium alloy.

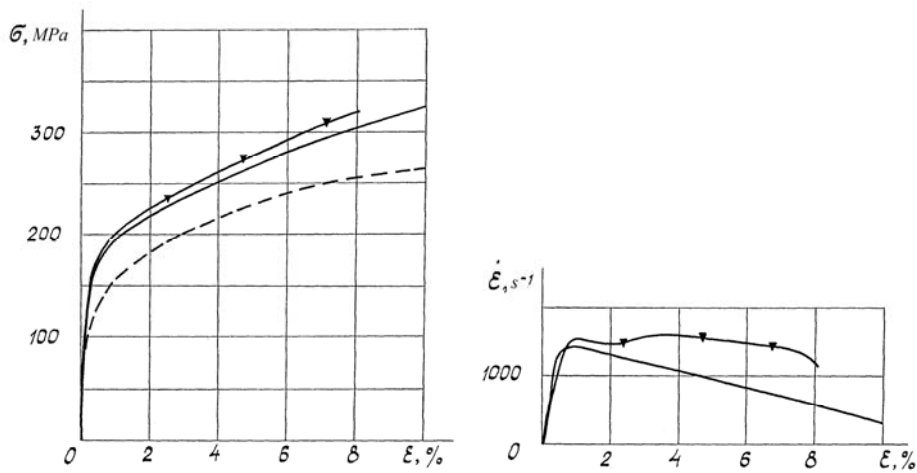


Fig. 2: Stress-strain curves of AMg6M alloy without shaper and with one.

As the pulse shaper undergoes considerable plastic deformations in the process of loading the SHPB, we proposed constructing its dynamic diagram using the direct impact method. Thus in one and the same experiment using SHPB, a pulse shaper and the direct impact method theory, it is possible to determine dynamic deformation diagrams of two different materials or of one material for different strain rates. As an example, Fig. 3a shows a diagram of a pulse-shaping specimen (made of steel), computed using the direct impact method and a diagram of an aluminum alloy D16T specimen constructed using Kolsky method.

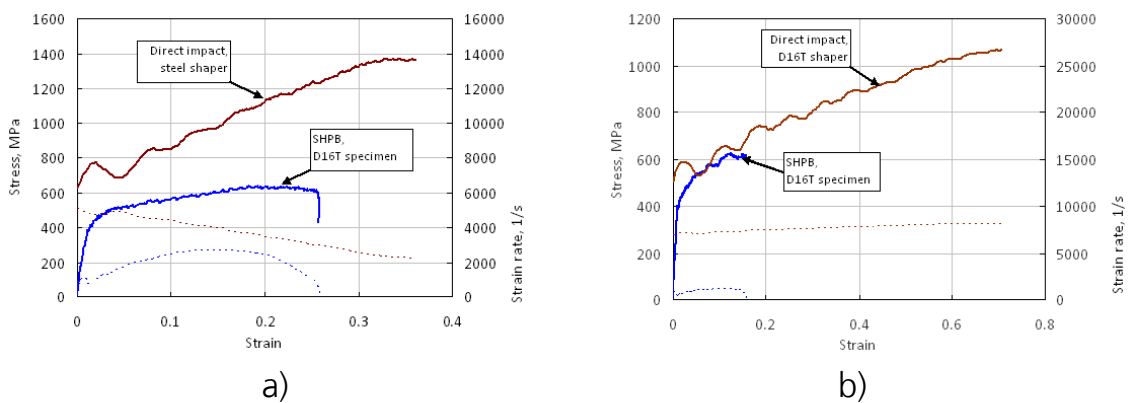


Fig. 3: Stress-strain curves of shaper and main specimen.

Kolsky method has been thoroughly studied both analytically and numerically, the scope of its applicability has been assessed, and the

effect of friction and inertia forces on the obtained diagram has been found. A similar study of the direct impact method is not available. Due to this, in the present paper, the main attention is paid to studying the homogeneity of the stressed-strained state (SSS) of the specimen and inertia and friction forces.

1.4 The direct impact method

As the direct impact method predetermines homogeneity and one-dimensional nature of SSS, and properties determined using this method can be affected by inertia effects and friction forces, it became necessary to thoroughly analyze this method. To this end, results of realistic and numerical experiments were used in this work.

There are two versions of the direct impact method (Fig. 4) [[10]]. In the first one, a massive striker is used, which has the stored kinetic energy many times as much as the work of elastic-plastic deformation of the specimen (Fig. 4a). In this case, the velocity of the striker is considered constant or slowly varying during the entire deformation process of the specimen. The loading of the specimen is of the inertial nature. In the second version, a striker of a considerably lower mass and of the same diameter as the measuring bar is used (Fig. 4b). The loading process here is of the wave nature.

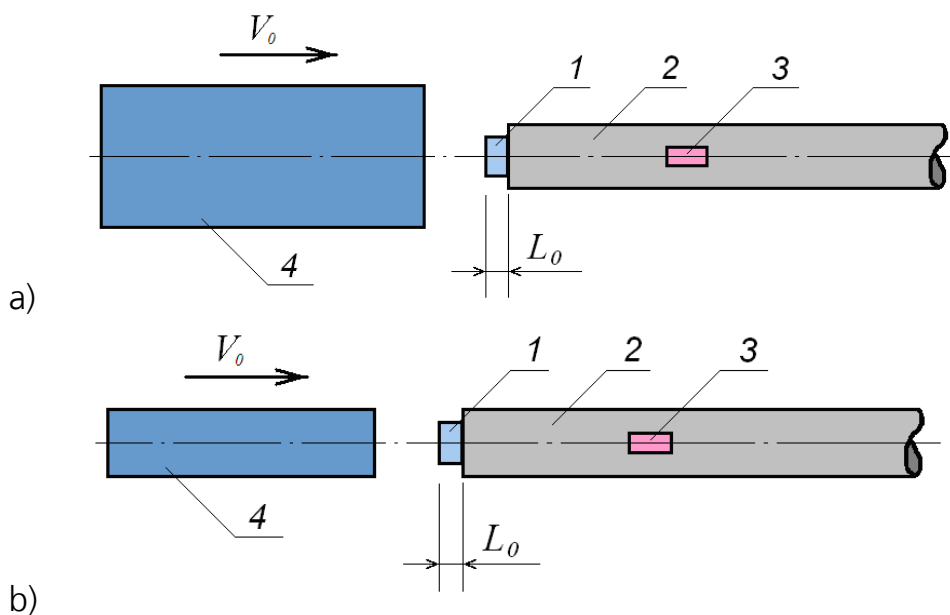


Fig. 4: Two versions of the direct impact method scheme.

In both versions of the direct impact method, the tested specimen (1) of the length of L_0 is placed at the end of a long and thin measuring bar (2) having a high yield limit, and is struck by a striker (4) 100÷500-mm long at a speed of V_0 from several meters per second to several tens meters per second. In the process of testing using strain gauges (3), a strain pulse is registered over a certain section of the measuring bar, which makes it possible to determine the stress in the specimen.

Impact velocity is also measured in this method. When constructing deformation diagrams using the direct impact method, as well as in other dynamic testing methods, the stressed and strained states in the specimen in the process of loading are assumed to be homogeneous and one-dimensional. This assumption may not hold due to the absence of friction between the specimen, the striker and the measuring bar, as well as due to the forces of axial and radial inertia arising in the specimen at high strain rates.

The basic relations for the first version of the direct impact method have the following form.

The velocity of the contact boundary of the specimen and of the supporting bar is determined, as in the case of using SHPB, after the strain gauge registers elastic strain pulse $\varepsilon_T(t)$ in the measuring bar:

$$V_1(t) = c_0 \varepsilon_T(t). \quad (1)$$

If L_0 is initial length of the specimen, then the average strain rate in the specimen can be written as:

$$\dot{\varepsilon}_n(t) = \frac{1}{L_0} (V_0 - V_1(t)). \quad (2)$$

Average engineering strain in the specimen, after integrating expression (2), is expressed as:

$$\varepsilon_n(t) = \frac{1}{L_0} (V_0 t - c_0 \int_0^t \varepsilon_T(\theta) d\theta). \quad (3)$$

Average technical stress in the specimen $\sigma_n(t)$ can be obtained as a function of time in the assumption of equality of forces at the ends of the specimen during the entire deformation process. After registering an

elastic strain pulse $\varepsilon_T(t)$ in the supporting bar by a strain gauge, stress in the specimen is found similarly to the traditional SHPB method:

$$\sigma_n(t) = E \left(\frac{D_b}{D_s} \right)^2 \varepsilon_T(t), \quad (4)$$

where D_b and D_s are diameters of the supporting bar and the specimen, respectively, E is Young's modulus of the measuring bar. After eliminating time as a parameter, relations $\sigma_n \sim \varepsilon_n$ and $\dot{\varepsilon}_n \sim \dot{\varepsilon}_T$ are constructed.

It should be kept in mind that, when testing high-strength materials, the direct impact method gives considerable evaluating strains in the specimen, especially over the initial portion of the diagram (up to 5-7%). To avoid this drawback, J. Klepaczko introduced the methodology of registering the displacements of the striker-specimen interface, using an optical sensor. In the recent years, experimental schemes have been developed that make it possible to register the velocity of the striker in the course of the experiment, which substantially improves the informative component of the method and increases its accuracy [[10]].

In the second version of the direct impact method which we analyze in the present paper, the experimental conditions are chosen such that the striker and the measuring bar are deformed elastically. This condition is provided, on the one hand, by the fact that the cross-section areas of the striker and the measuring bar are considerably larger than that of the specimen and, on the other hand, by the fact that elastic limit of the striker is higher than yield limit of the material of the specimen. After the impact, the wave propagating in the striker is the same as in the measuring bar. This makes it possible to determine the average velocity of the change of the specimen length, based on the strain pulse $\varepsilon_T(t)$ registered in the measuring bar, using the following formula. [[10]]:

$$V_s = V_0(t) - 2c_0\varepsilon_T(t), \quad (5)$$

where c_0 is sound velocity in the measuring bar. Thus, average strain rate in the specimen is

$$\dot{\varepsilon}_n(t) = \frac{1}{L_0} (V_0 - 2c_0\varepsilon_T(t)). \quad (6)$$

Then, average engineering strain in the specimen $\varepsilon_n(t)$ can be found as follows:

$$\varepsilon_n(t) = \frac{1}{L_0} (V_0 t - 2c_0 \int_0^t \varepsilon_T(\theta) d\theta). \quad (7)$$

Average engineering stress in the specimen $\sigma_n(t)$, as in the previous version, is calculated using formula (4).

The present version of the direct impact method is designed for analyzing characteristics of materials at elevated strain rates (above 10^3 s^{-1}), thus, when processing the results of dynamic tests using the direct impact method, it is necessary to take into account inertial stresses in the specimen, as well as stresses due to friction forces along the contact interface.

Effects of friction, of radial and axial inertia in a cylindrical specimen are analyzed in detail in Z. Malinowsky and J. Klepaczko [[12]]. The authors show that radial stress σ_r is not constant along the radius of the specimen and has its maximum at $R = 0$, i.e. along the axis of the specimen. In [[9]], the authors propose using their maximum values when evaluating radial stresses, i.e.

$$\sigma_{r \max}(t) = \frac{\rho \cdot R(t)^2}{4 \cdot L(t)(1 - \varepsilon_n(t))^2} \left[\frac{3V_x^2}{2L(t)(1 - \varepsilon_n(t))} + \frac{dV_x}{dt} \right], \quad (8)$$

where $\frac{dV_x}{dt} = c_0 \frac{d\varepsilon_T(t)}{dt}$, $V_x = V_0 - c_0 \cdot \varepsilon_T(t)$, ρ is density of the specimen material, $R(t)$ and $L(t)$ are current radius and length of the specimen, respectively.

There also exist other relations for evaluating σ_r , which yield close results. Thus, in [[12]], the following expression for evaluating the radial component of the stress is given:

$$\sigma_r(t) = \frac{3}{8} \rho (R_0 V / L_0)^2 (1 - \varepsilon_n(t))^{-2} \quad (9)$$

Stress due to axial inertia, following [[12]], is described by the following relation:

$$\sigma_{axial} = \frac{\rho D_s^2}{12} \left(S^2 - \frac{3}{16} \right) (\dot{\varepsilon}^2 + \ddot{\varepsilon}) + \frac{3\rho D_s^2}{64} \ddot{\varepsilon}, \quad (10)$$

where $S = \frac{L}{D_s}$, $\dot{\varepsilon}$ and $\ddot{\varepsilon}$ are strain rate of the specimen and its time derivative.

Computations showed [[11]] that the inertial component of the axial stress is within ~1 % for strain rates of up to $\sim 5 \cdot 10^3 \text{ s}^{-1}$ and can be neglected, whereas at the strain rates above $5 \cdot 10^3 \text{ s}^{-1}$ inertial components of stresses must be accounted for, using formula (10).

1.5 The experimental stand

Fig. 5 depicts a scheme of the experimental stand implementing the present combined method of testing dynamic properties of materials. Specimens are loaded by a 20mm-caliber gas gun. Impact velocity is measured with a light velocit Comparison of the dynamic diagrams obtained using different methods: dotted line – Kolsky method, solid line – direct impact method y meter. 20mm-dia 1.5m-long measuring bars are made of Martens-aging steel with the yield limit of ~2500 MPa. Strikers 50 to 500mm-long are made of the same steel. Strain pulses are measured with small-base strain gauges glued on the surface of the measuring bar. Impact velocity and strain pulses are registered using National Instruments PXI-5112 high-speed two-channel oscillographic modules. To construct dynamic diagrams, the experimental information is processed using specialized programs.

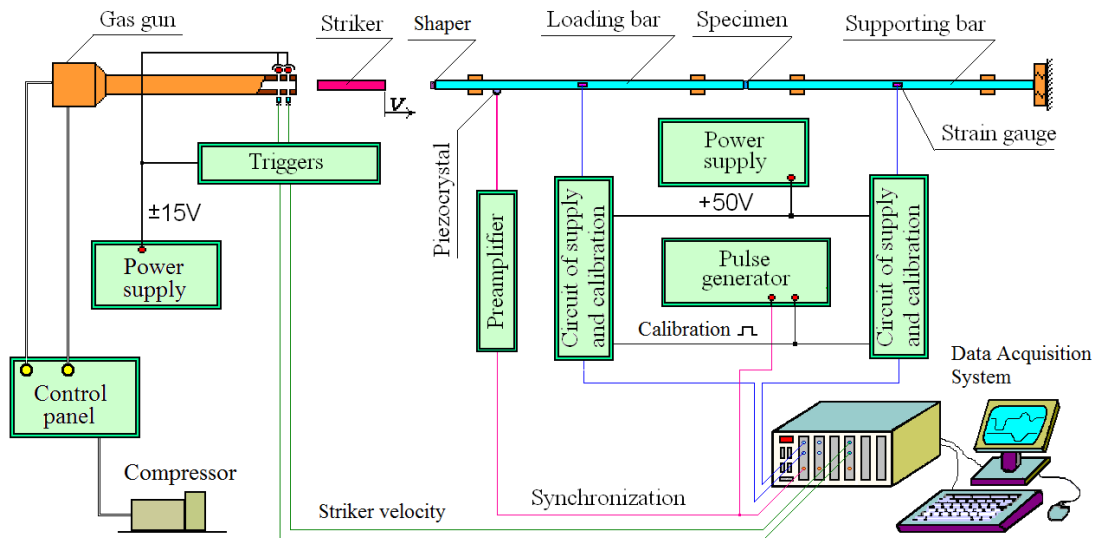


Fig. 5: Experimental stand implementing the combined method.

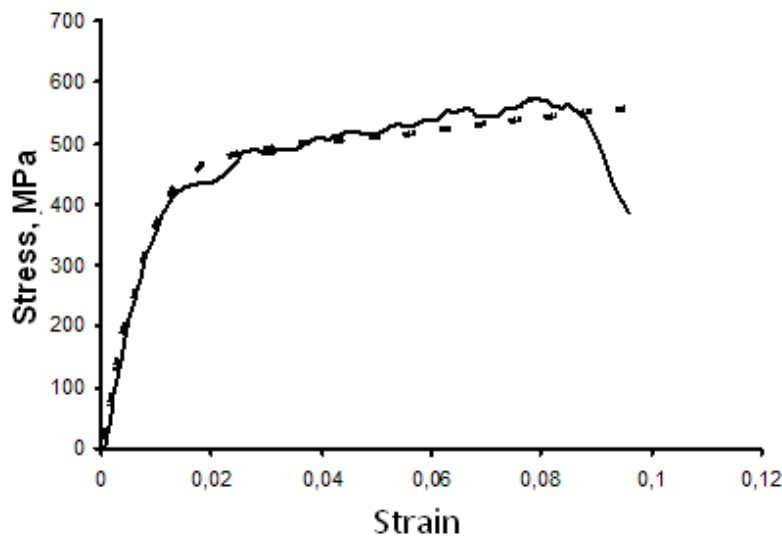


Fig. 6: Comparison of the dynamic diagrams obtained using different methods: dotted line – Kolsky method, solid line – direct impact method.

Using the direct impact method, we determined the deformation diagram of D16T aluminum alloy for $\dot{\epsilon}=10^3 \text{ s}^{-1}$. This diagram was compared against the diagram obtained using traditional Kolsky method for the same strain rate (Fig. 6). The diagrams obtained using the different methods agree well enough.

1.6 Numerical investigation of the direct impact method

To assess the effect of friction and inertia forces, as well as the degree of homogeneity and one-dimension nature of the stressed-strained state of the specimens, the direct impact method was numerically modeled [[13]]. The computational scheme for modeling the present experiment is shown in Fig. 7.

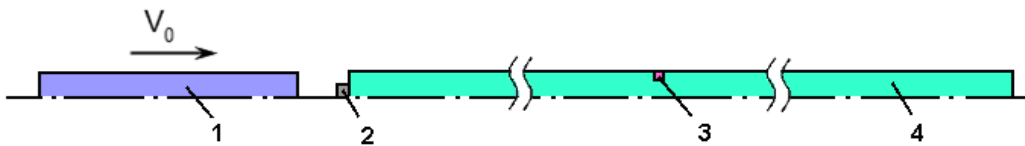


Fig. 7: A scheme of modeling the experiment based on the direct impact method.

The problem was analyzed in an axisymmetric formulation. The behavior of striker 1 and measuring bar 4 was described by a linear-elastic model. To describe the behavior of the specimen material 2, a bilinear elastic-plastic model with isotropic hardening and yield surface radius independent of the strain rate was used in all the numerical experiments. In the nodes of the finite-element model of the striker, initial conditions were prescribed in the form of axial velocity. In the measuring bar, a final sensor-element 3 was chosen, where strain was recorded in the process of computation. Comparison of the strain pulses in the measuring bar (Fig. 8) obtained in realistic and numerical experiments, as well as their good agreement, show that the numerical scheme can model the process of impact deformation of specimens with a good accuracy.

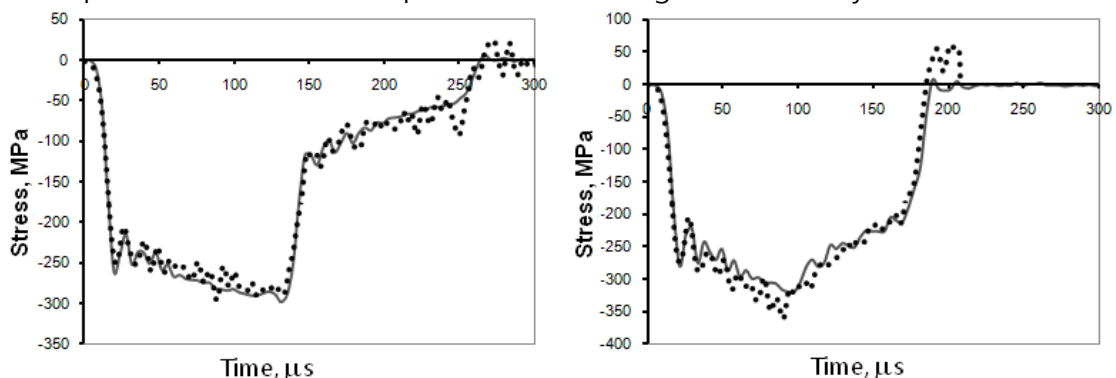


Fig. 8: Comparison of the results of realistic (dots) and numerical (solid line) experiments: left – 300mm-long striker, velocity 20 m/s; right – 200mm-long striker, velocity 30 m/s.

The data acquired in the numerical experiment and the initial velocity of the striker were used to construct a deformation diagram of the specimen (following formulas 4-7). Then the diagram used in computations was compared with the diagram determined using the strain pulse in the measuring bar. The specimen was made of the D16 aluminum alloy, the length of the striker is 200 mm, the measuring bar was made of steel.

Fig. 9a shows, for the specimen of the D16 aluminum alloy, time history of the radial component of stress tensor σ_r arising due to radial inertia, computed using formula (8) – dotted line, and formula (9) – solid line, as well as deformation diagrams computed using pulses in the measuring bar with and without taking into account this correction (Fig. 9b).

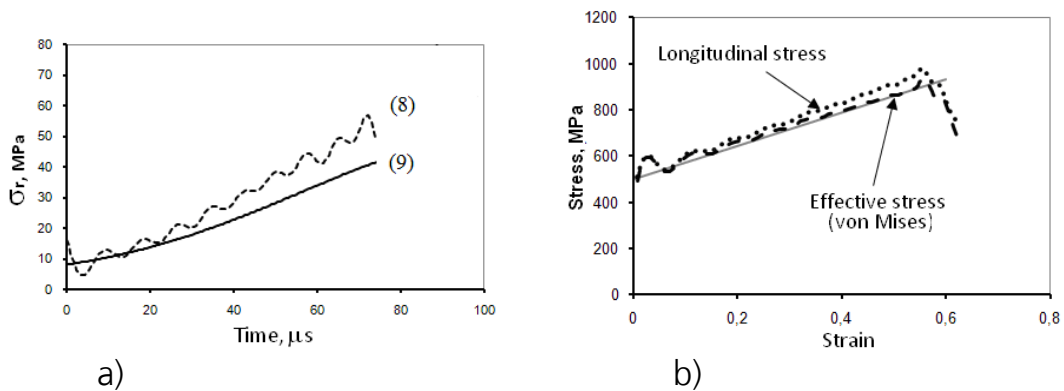


Fig. 9: Effect of inertia on the result of processing the experiment.

It is evident from the figures that taking into account the inertial correction makes a certain contribution into the results of processing the experimental data (in the example given, the difference between the diagrams constructed with and without taking account of this correction amounts to $\sim 10\%$ for $\dot{\epsilon} \sim 5000 \text{ s}^{-1}$). That is why it is necessary to account for inertial forces when determining stresses using the direct impact method.

It is worth noting that formula (3) allows one to correctly determine strain in the specimen only along the time interval corresponding to the double run of the elastic wave along the striker, i.e. up to time $t_{2L} = \frac{2L}{c}$ (vertical line in Fig. 10), where L is striker length, c is sound velocity in the specimen. Further, the velocity of the striker-specimen interface will be determined by the superposition of elastic waves: one entering the striker

from the specimen, and another, reflected from the free end of the striker. Formal use of formula (3) for times bigger than t_{2L} results in overestimating the strain in the specimen (Fig. 10).

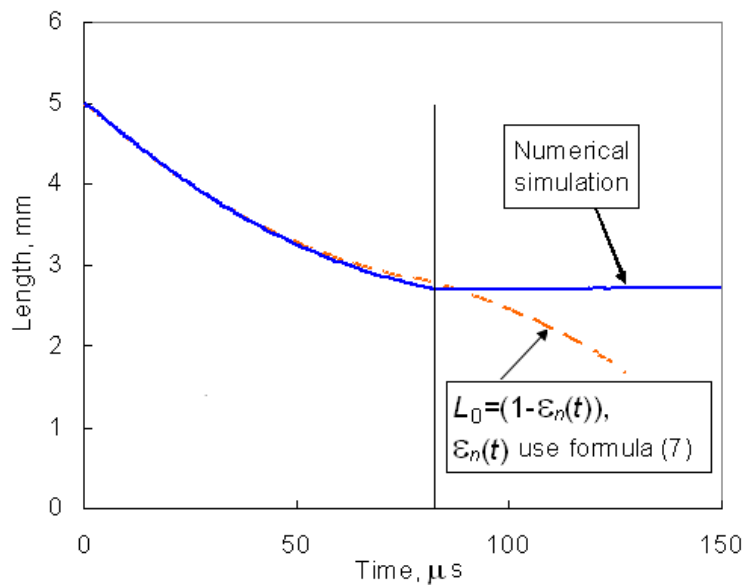


Fig. 10: Limits of applicability of formula (3).

The calculations show that strain rate is not constant in this type of testing, which is also characteristic of other methods of dynamic testing (Fig. 11). However, it should be kept in mind that strain-rate history can substantially affect the resulting dynamic properties.

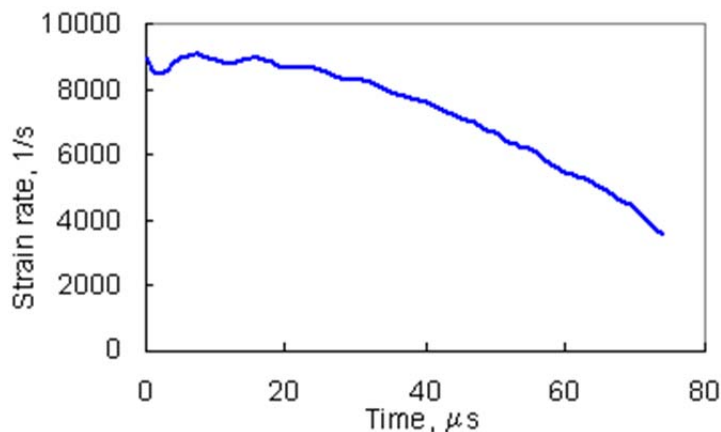


Fig. 11: Strain rate in the specimen in the course of testing.

It is common knowledge that friction between the striker, the specimen and the measuring bar, leading to constraining the deformation of the specimen, significantly affects the type of stressed-strained state of the specimen and, hence, the results of processing the experimental data. To assess the homogeneity and uniaxiality of SSS of the specimen in the presence of friction forces, its high-rate deformation was numerically modeled.

The following figures present the computed time histories of stresses (axial and radial) in various points of the specimen in the course of impact. It is evident that, in the absence of friction (Fig. 12), the stressed state of the specimen is homogeneous and uniaxial, whereas in the presence of friction (friction coefficient $\mu=0.1$), homogeneity of the axial stress along the radius of the specimen is lost, and a radial component of the stress appears (Fig. 13), i.e. the deformation process becomes constrained.

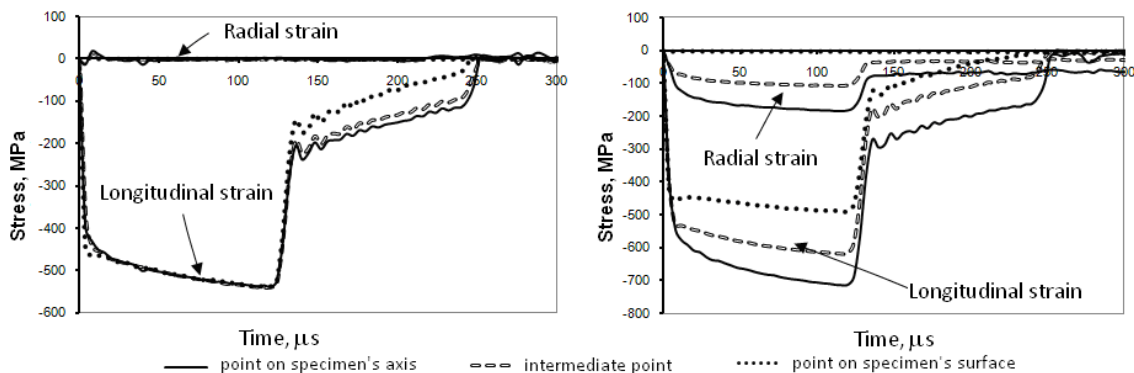


Fig. 12: Stress in different points of the specimen (friction coefficient $\mu = 0$).

Fig. 13: Stress in different points of the specimen (friction coefficient $\mu = 0.1$).

A similar situation is with strain fields (Fig. 14-15).

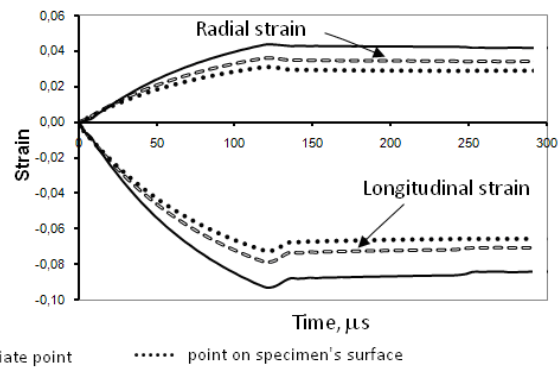
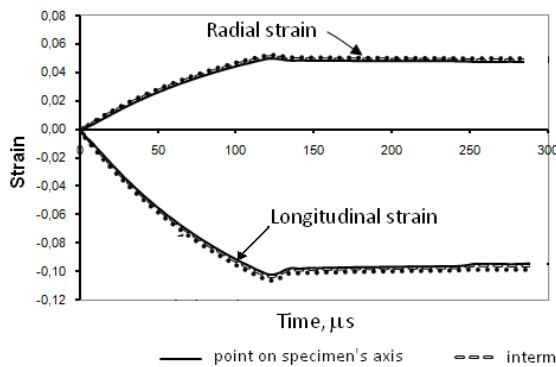


Fig. 14: Strain in various points of the specimen (friction coefficient $\mu = 0$).

Fig. 15: Strain in various points of the specimen (friction coefficient $\mu = 0.1$).

To assess the effect of friction forces on the resulting diagram, numerical experiments were done with various friction coefficients. Fig. 16 compares the deformation diagram used in calculations with the diagrams reconstructed from a strain pulse in the measuring bar. The strain pulse in the measuring bar was found by numerically modeling the experiment with various friction coefficients.

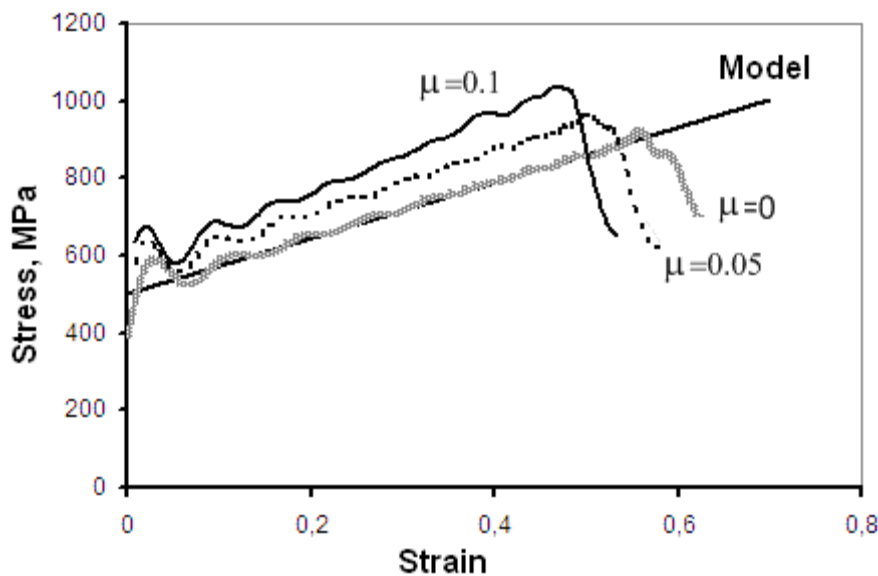


Fig. 16: Effect of friction on the diagrams.

It is evident from the figure that, in the absence of friction forces, the deformation diagram of the specimen material reconstructed from the pulse in the measuring bar follows the diagram used in the calculations. Whereas in the presence of friction with coefficients $\mu=0,05$ and $\mu=0,1$, the estimates according to the diagram reconstructed using the above

described methodology are 10 % and 21 % higher than those used in the calculations, respectively (for 40 % deformation).

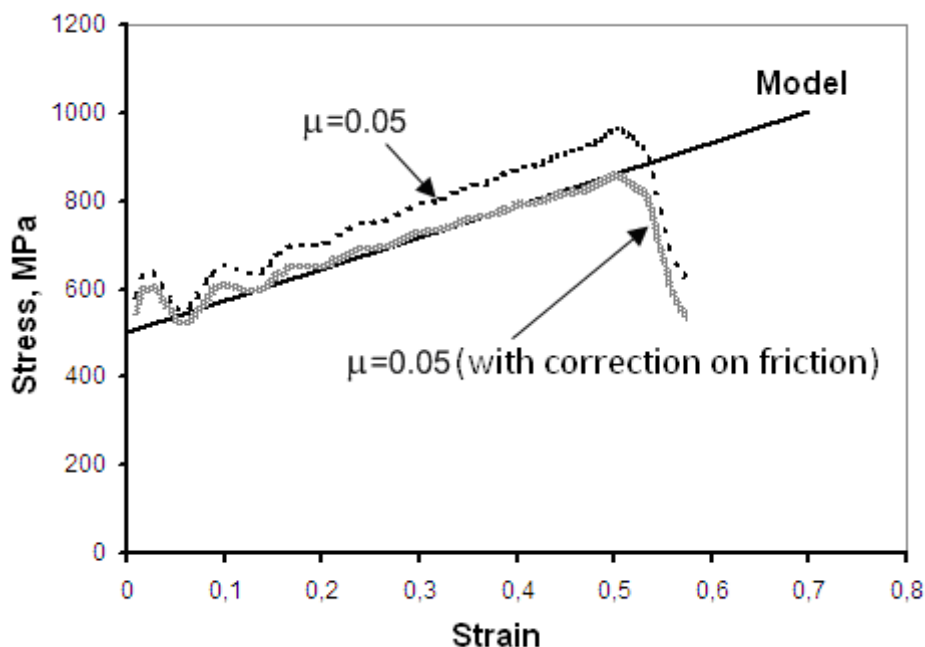


Fig. 17: Diagram accounting for the correction for friction.

To account for friction, simple relations are introduced that make it possible to determine the deformation diagram of the material using the direct impact method in the presence of friction too. Besides, to minimize friction effects, the surfaces of the specimen and the measuring bars should be greased and polished.

1.7 Conclusions

1. A novel idea is presented about determining dynamic properties of two different or similar materials in the same experiment with SHPB, using the direct impact method in combination with Kolsky methodology. Special attention in the paper is paid to the analysis of the direct impact method.
2. The paper presents the numerical-experimental analysis of the direct impact method for determining dynamic properties of materials for strain rates of 10^3 - 10^4 s⁻¹.

3. The effect of both inertia and friction forces on the properties studied is demonstrated. Ways of accounting for such forces in constructing dynamic deformation diagrams are described.
4. It is noted that a combined use of experimental and computational methods makes it possible to gain deep insight into the effect of various factors on the obtained dynamic diagram.

The study of the pulse shaper was done in the framework of fulfilling the governmental task from the Ministry of Education and Science of Russia (Project 7.846.2014K); the numerical study of the direct impact method was done with financial support from RFFI (Grants 13-08-00862 and 13-01-90406).

1.8 References:

- [1] Kolsky H. An investigation of the mechanical properties of material at very high rates of loading // Proc. Phys. Soc. (London), Vol. 62B, 1949, pp.676-700.
- [2] Ellwood S., Griffiths L.J. and Parry D.J. Material Testing at High Constant Strain Rates. // J. Phys. E: Scientific Instruments 15, 280-282 (1982).
- [3] Bragov A.M., Lomunov A.K. Special features of constructing deformation diagrams using Kolsky method // Applied problems of strength and plasticity: All-Union Inter-Univer. Collection / Gorky University, Gorky. -1984. -Issue.28., P.125-137.
- [4] Lomunov A.K. A methodology of studying processes of viscoplastic deformation and material properties using Split Hopkinson Bar. Cand. Theses, Gorky, 1987.
- [5] Bragov A.M., Lomunov A.K. Methodological aspects of studying dynamic material properties using Kolsky method // Int. J. Impact. Engng. 1995. Vol.16, No2, p.321-330.
- [6] Nemat-Nasser S., Isaacs, J.B., and Starrett, J.E. Hopkinson Techniques for Dynamic Recovery Experiments, Proceedings of the Royal Society of London A, 435, 371-391 (1991).
- [7] Weinong Chen, Bo Song Split Hopkinson (Kolsky) Bar: Design, Testing and Applications (Mechanical Engineering Series). Springer, 2010, 388 p.

- [8] Frew D.J., Forrestal M.J., Chen W. Pulse Shaping Techniques for Testing Elastic-plastic Materials with a Split Hopkinson Pressure Bar. *Experimental Mechanics*, 45(2), 2005, p.186-195.
- [9] Dharan C.K.H., Hauser F.E. Determination of stress-strain characteristics at very high strain rates // *Exp.Mech.* 1970. Vol.10. P.370-376.
- [10] Klepaczko J. Advanced experimental techniques in materials testing // "New Experimental Methods in Material Dynamics and Impact", Trends in Mechanics of Materials, eds. W.K.Nowacki, J.R.Klepaczko, Warsaw, 2001, p.1-58.
- [11] Bertholf L.D., Karnes C.H. Two-dimensional analysis of the split Hopkinson-pressure bar system // *J.Mech. Phys. Solids.* 1975. Vol.I, N 23. P.1-19.
- [12] Klepaczko J., Malinowski Z. Dynamic frictional effects as measured from the split Hopkinson pressure bar // *Proc. IUTAM Symp.*, ed.K.Kawata, Springer Verlag. 1977. P.403- 416.
- [13] Konstantinov A.Yu. An experimental-computational investigation of the behavior of structural materials under dynamic loading // PhD Theses, N.Novgorod, 2007.

Use of Hopkinson method and its modifications in the USSR and Russia

A. M. Bragov, L. A. Igumnov, A. Yu. Konstantinov, A. K. Lomunov, S. Yu.
Linvinchuk

Research Institute of Mechanics, Nizhny Novgorod Lobachevski State University

1.1 Introduction

Hopkinson's idea of using a pressure bar to measure loading pulses was revolutionary for dynamic testing methods. Unfortunately, it was not widely used in the USSR and Russia directly. More extensively it was used by Professor G. Stepanov [14] at the Institute of Problems of Strength (Kiev) as a part of a vertical test stand. In this stand, a long measuring bar-waveguide or a tube were used for measuring stress in a specimen loaded in tension. The Split Hopkinson Bar (SHB) method was successfully used by A. Bragov and his co-workers for measuring forces resisting penetration of rigid strikers into soil media in reversed experiments, as well as for obtaining adiabates of low-density media [15].

Kolsky's modification of the SHB method gained more popularity both in the USSR and in Russia. S. Kokoshvili (Institute of Mechanics of Polymers, Riga) was the first researcher in the USSR who successfully used the SHB method for investigating dynamic properties of polymers and composites [16]. In the middle of the seventies of the last century, the method came to be intensively used in two Russian scientific centers – RFNC-VNIIEF, Sarov, under the leadership of Prof. S. Novikov [17], and in the Research Institute of Mechanics, Nizhny Novgorod (former Gorky) Lobachevski State University, under the leadership of Prof. A. Bragov and Prof. A. Lomunov [5],[19].

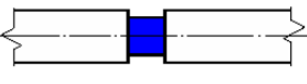
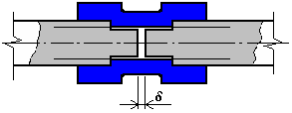
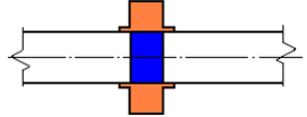
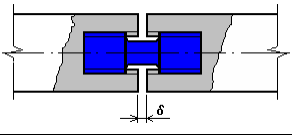
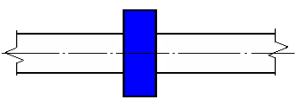
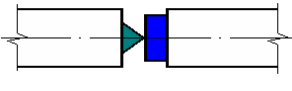
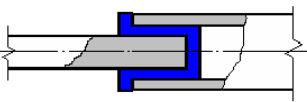
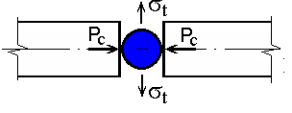
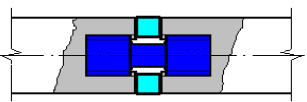
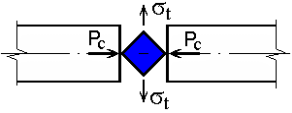
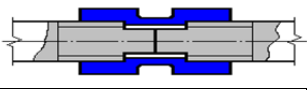
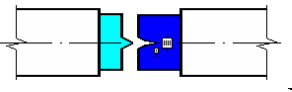
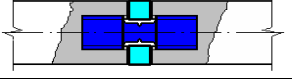
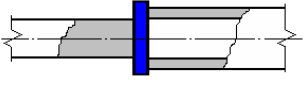
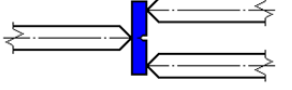
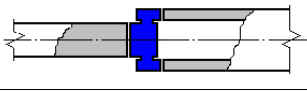
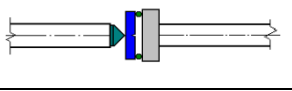
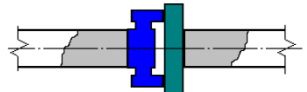
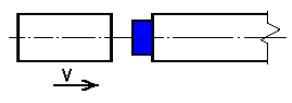
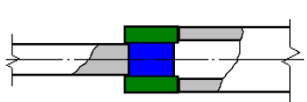
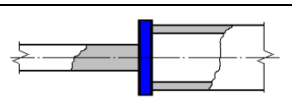
S. Novikov and co-workers used in their experiments the traditional scheme of testing in compression and a modified Lindholm scheme for testing in tension. To determine Bauschinger effect they used Ogawa's scheme [20]. Loading pulses were induced by exploding a moderate explosive charge via a damper. Much attention in works by S. Novikov was

paid to dynamic tests of radioactive materials. Experimental stands were made which could be used in the central channel of a pulsed reactor.

A. Bragov and co-workers in their dynamic tests of structural materials used Nicholas's scheme [21] for testing at tension. To test brittle materials in tension, 'Brazilian test' [22] is used. In this team, most attention was paid to developing modified versions of the SHB method, both for creating complex-history loading, including partial or total relaxation with jumps of strain rate, and new testing schemes. A more widely-known of them is a modification of the SHB method for testing weakly-bound and low-density materials in a rigid jacket. To achieve high deformation levels (up to 80%) in low-density media (soft soils, foam plastics, etc.), in this experiments it is used a SHB system where the incident bar is 3 to 4 times shorter than the transmitting one. Based on the SHB method, a methodology for determining dynamic hardness was pioneered.

Different types of tests realized in the Research Institute of Mechanics at State University of Nizhny Novgorod are shown in Tab. 1.

Tab. 1: Realized types of tests based on the SHB method.

a)	Compression (1D stress state)		l)	Bauschinger effect	
b)	Compression (1D strain state)		m)	Bauschinger effect	
c)	Compression (1D strain state)		n)	Indentation (dynamic hardness)	
d)	Tension		o)	Brazilian test (splitting)	
e)	Tension		p)	Brazilian test (splitting)	
f)	Tension		q)	Crack resistance	
g)	Shear		r)	Crack resistance	
h)	Circle shear		s)	Crack resistance	
i)	Circle shear		t)	Crack resistance	
j)	Circle shear		u)	Direct impact	
k)	Dynamic friction		v)	Plate perforation	

As in the USSR and Russia are mainly used traditional schemes of dynamic tests in tension and compression, the focus of the report is given to the author's review of the original modifications of the Kolsky method.

1.2 Using the SHB for studying shock compressibility and shear resistance of soft soils

The interest to study a behaviour of soft soil mediums in conditions of intensive short-term influences has considerably increased last years in connection with a necessity of deciding some problems: the analysis of distribution of strong seismic and explosive waves and their interactions with over-ground and underground structures, the use of energy of explosion in construction of dams, channels etc. Much works has been devoted to research of dynamic properties of soft soils (see references in [24]). However, in these investigations the range of investigated pressure ($<50\text{MPa}$) and strain rates ($<10^2\text{s}^{-1}$) are insufficiently high. The progress in development of research at large pressure and strain rates is connected with use of the modified Kolsky method. For the first time in Russia the Kolsky method for dynamic tests of soft soils in a rigid confining jacket was used by Bragov et al. [25]. In these experiments, there are 1-D strained and 3-D stressed states. The further updatings of this method were aimed at the definition a radial component of a stress tensor. Bragov et al. [26] have offered for this purpose the measurement by strain gauges of peripheral deformations of a rigid jacket.

Longitudinal stress σ_x and strain ϵ_x are obtained using the Kolsky formulae. To determine the radial stress σ_r , one can consider solving the problem of an elastic deformation of a thick-walled cylinder under internal pressure.

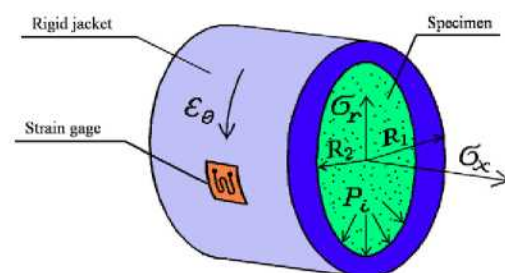


Fig. 1: Stress components and parameters in a soil specimen and in the confined jacket.

The stress involved in the deformation of a soil specimen, placed into a metal-confining jacket and loaded in a SHB system, are shown in Fig. 1.

During the jacket-confined tests, the axial stresses in the soil specimen are usually not higher than 300 MPa due to the significant difference between the impedances of the bars and specimen. These stresses must be lower than the yield strength of the jacket material. The maximum elastic radial strain of the jacket, using an analysis based on a thick-walled pipe under internal pressure loading, is greater than but of the same order as the strain seen in these experiments. The maximum circumferential strains of the jacket, as measured by the strain gauges, were not more than 0.05%; longitudinal strains in some of the specimens were as high as 10%. In such circumstances, the radial strain may be neglected in comparison to the longitudinal strain. Effectively, the strain state of the specimen may be considered one-dimensional and the stress state bi-axial. Then the main components of the stress and strain tensors will be

$$\sigma_1 = \sigma_x, \quad \sigma_2 = \sigma_3 = \sigma_r, \quad \varepsilon_1 = \varepsilon_x, \quad \varepsilon_2 = \varepsilon_3 = 0 \quad (1)$$

where σ_x and ε_x are longitudinal stresses and strains obtained using the Kolsky analysis, and σ_r the radial stresses found in the sample jacket. Inertia plays a minor role in these strain rates for these samples stresses. This effect is ignored in these experiments; however, inertia is important in the shock wave experiments.

To determine the value of radial stress σ_r , an approximation to a thick-walled cylinder was assumed, and formula (2) was used. The expression relates the stress in the jacket, σ_r to the internal pressure, P_i , causing the small elastic strain in the jacket:

$$\sigma_r = P_i = \frac{1}{2R_2^2} E(R_1^2 - R_2^2)\varepsilon_\theta, \quad (2)$$

where E is the Young modulus of the jacket material, and R_1 and R_2 are the external and internal radii of the jacket, respectively. The above expression gives the radial stress component σ_r , based on the circumferential strain (ε_θ).

Two components of the stress tensor (σ_x and σ_r) allow to determine a wide spectrum of properties of tested material: pressure P and volumetric strain θ of the specimen, tangential stress τ , the intensity of stress σ_i and strain ε_i , the factor of lateral pressure ξ and, to construct a set of needed functions: $\sigma_x \sim \varepsilon_x$, $\sigma_i \sim \varepsilon_i$, $P \sim \theta$, $\tau \sim P$, $\xi \sim P$, etc.

The maximum shear stress τ will occur at the planes inclined 45° to the longitudinal axis, and the value on these planes will be

$$\tau = (\sigma_x - \sigma_r) / 2$$

The pressure, P , in the specimen can be expressed in terms of the main stresses as

$$P = -(\sigma_x + 2\sigma_r) / 3. \quad (3)$$

The volumetric strain will take the following form:

$$\theta = \varepsilon_x. \quad (4)$$

Expressions (3) and (4), describe the uniaxial compression diagram, and allow the volumetric compressibility curve of soil to be calculated.

The stress and strain levels during the compression process are determined by

$$\sigma_i(t) = \sigma_x(t) - \sigma_r(t); \quad (5)$$

$$\varepsilon_i(t) = \frac{\varepsilon_x(t)}{(1 + \nu)} \approx \frac{2}{3} \varepsilon_x(t) \quad (6)$$

By eliminating time as a parameter, it is possible to construct the major time-invariant characteristic of soil material in its stress strain curve $\sigma_i \sim \varepsilon_i$.

The relation between axial and radial components of stress will be

$$\sigma_r(t) = \xi \sigma_x(t) = \frac{\nu}{1 - \nu} \sigma_x(t)$$

The factor of lateral pressure, linking the principal stress directions is defined as

$$\xi(t) = \frac{\sigma_r(t)}{\sigma_x(t)} \quad (7)$$

It should be noted that the term dynamic Poisson ratio as used here refers to a ratio of stresses in a dynamic, inelastic deformation process, unlike the more classical situation of a homogeneous material undergoing elastic loading. In the experiments, the longitudinal strain pulses were measured in the pressure bars and the shear strains in the jacket. A typical result is shown in Fig. 2. Computer analysis use these pulses to obtain a set of parametrical functions $t-\sigma_x-\varepsilon_x-\sigma_r-\tau-P-\xi$. After first synchronizing, the time bases of the stress pulses, effectively removing the transmission time along the bars, then eliminating time it is possible to derive a set of parameters such as: $\sigma_x-\varepsilon_x$, $\sigma_r-\varepsilon_r$, $P-\theta$ and $\tau-P$, $\xi-P$, etc.

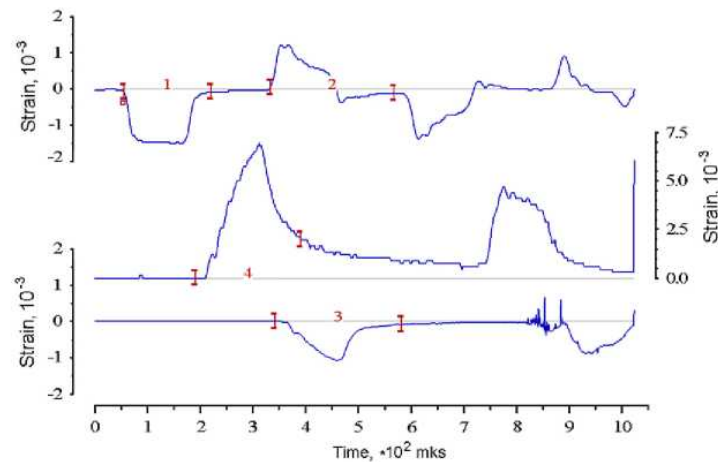


Fig. 2: Typical initial and reflected strain pulses in the pressure bars (pulses 1-3) and also in a jacket (pulse 4). The levels of the strain are small, within the elastic limits of the bars and jacket. The longitudinal strain in the much softer sand sample is considerable.

Test samples were placed in jackets and capped by circles of thin paper to prevent the sand falling out. These paper inserts had little friction with the jacket and did not influence the test results. The jackets had a wall thickness of 10 mm and a 10 mm working length. To centre the ends of the pressure bars into the sample the jackets had a thinner section outside of the working length to aid alignment. The bars were pressed into the sample to make a good contact, but no static external load was applied to the samples during the test procedure. Empirical evidence, supported by numerical simulation, has shown these sleeves do not influence the stress deformation of the jacket. The length of a sample was about equal to the working length of the jacket. During compression, the jacket had a uniform expansion along its length [27]. Depending on the loading stress investigated, the jackets were made from either an aluminum alloy or steel. For stress amplitudes up to 100 MPa, specimens used aluminum alloy jackets, for higher stresses - steel jackets. The larger deformation of the aluminum alloy, compared with steel, allows more precise measurements, at small pressures, of the strain on the external surface of the jacket.

The soft soil investigated was a quartz sand with a particle distribution centred between 150 – 212 μm within which 82% by mass of the particles lay [28]. The theoretical maximum density of the material was

2.55 g cm^{-3} and the beds used were $45 \pm 3\%$ porous. The dry sand pour density was, therefore, $\sim 1.5 \text{ g/cm}^3$.

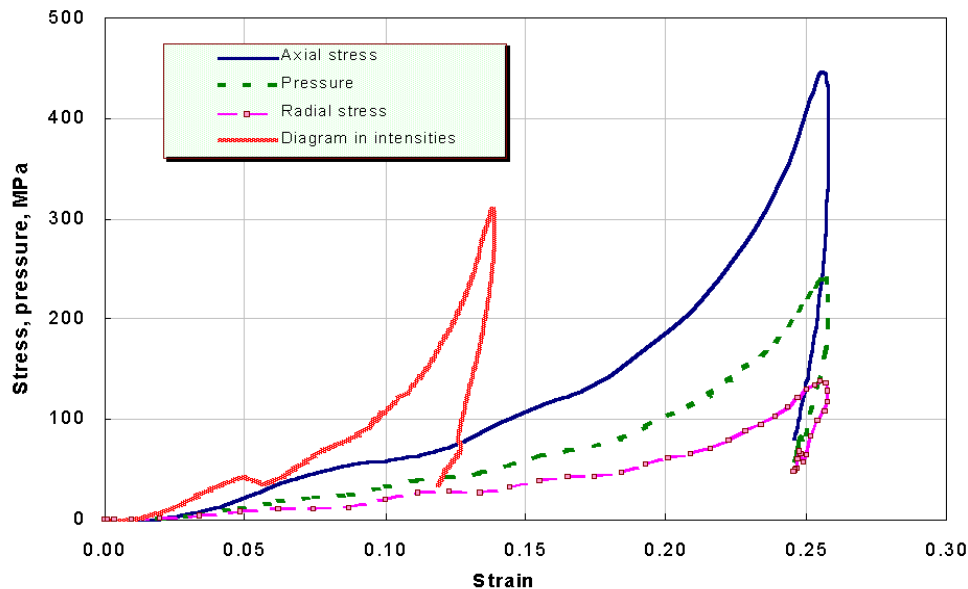


Fig. 3: Averaged curve of sand compressibility from the Kolsky system using steel jackets and steel bars, for stress loading up to 500 MPa.

As stated above, for Kolsky experiments at different load magnitudes, the pressure bars and jackets were made from an aluminum alloy or high-strength steel. The parameters of a loading pulse were varied by changing the velocity and length of the striker bar. The experiments can be divided into three groups:

- low striker velocity ($V=10-12 \text{ m/s}$)—sample stress up to 80 MPa—aluminum alloy pressure bars and jacket;
- medium striker velocity ($V=18-22 \text{ m/s}$)—sample stress up to 150 MPa—aluminum alloy pressure bars and a steel jacket and
- high striker velocity ($V=28-34 \text{ m/s}$)—sample stress up to 500 MPa—steel pressure bars and jacket.

Overall 8-10 experiments were conducted in each group. The major characteristic of soils were obtained using the analysis defined above. The results in each group were averaged. In Fig. 3, the average curves of sand compressibility, from the third group, are shown.

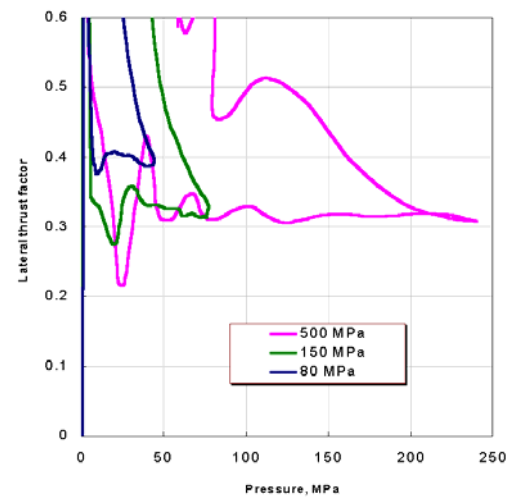
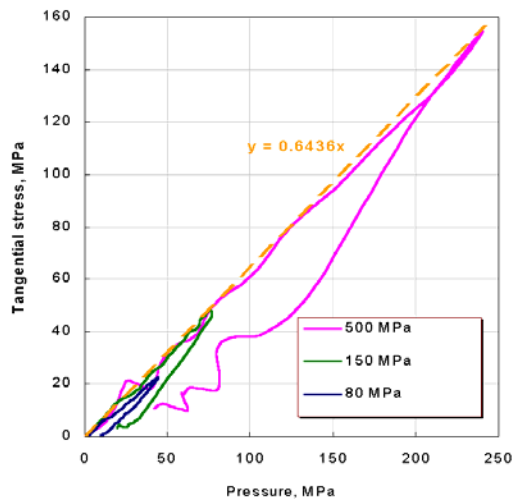


Fig. 4: Dependence of lateral stress with pressure for experiments with loading stresses of 80, 150, and 500 MPa.

Fig. 5: The characteristic of lateral thrust for experiments with loading stresses of 80, 150, and 500 MPa.

In Fig. 4, the average dependence of shear stress with pressure τ - P is given. The curve is practically linear in the loading part of the cycle and almost linear in the unloading cycle. This behaviour may be described using a Mohr-Coulomb equation: $\tau = C + \text{tg}\varphi \cdot P$, where C is the effectively the shear strength or resistance of the unloaded material, P is the applied pressure, and $\text{tg}\varphi$ gives a measure of the increase in shear resistance with applied load, φ being called the internal friction angle. It is necessary to note that the value of the specific coupling, C , is rather small, indicating a soft material, and so has a large percentage error associated with it. However, from a practical viewpoint it can be neglected. In Fig. 4 $\text{tg}\varphi = 0.64$, while the lateral thrust factor was determined to be $\xi = 0.33$ (Fig. 5).

1.3 Modification of the Kolsky method for studying properties of low-density materials under high-velocity cyclic strain

The use of the traditional Kolsky method for cyclic tests involves certain difficulties. First, correct registration of strain pulses in several loading cycles is complicated by interference of waves in pressure bars. Second, for an identical length of pressure bars, the pulse ϵ^t that passed through the specimen and was reflected from the backward face of the support

bar in the first loading cycle arrives at the specimen simultaneously with the pulse ε^r that was reflected from the specimen and arrived at it for the second time and, hence, can distort the pattern of specimen deformation. To register correctly the corresponding strain pulses and avoid distortion of the stress-strain state of the specimen, we propose to use pressure bars with the ratio of their lengths equal to the number of cycles registered [29].

Figure 6 shows the scheme of the proposed variant of the split bar and the wave $X-t$ diagram under cyclic loading of the specimen. Impactor excites an elastic pulse ε_1^i in the loading bar. The pulse propagates in the bar with a velocity C ($\tan \alpha = C$). The duration of the excited pulse t_p is determined by the impactor length L_i . Approaching specimen, part of this pulse is reflected as an extension wave ε_1^r , and the other part passes through the specimen into the support bar as a compression wave ε_1^t . The pulses are registered by the strain gauges glued onto the pressure bars at an identical distance from the specimen. If the acoustic impedances of the bar and specimen materials are significantly different, the amplitude of the reflected pulse may be rather high. The reflected pulse propagates up to the end face of the first pressure bar loaded by the impactor and is reflected from the free face (since there is no longer contact with the impactor) as a compression wave ε_2^t . The secondary wave loads the specimen, a significant part of it is reflected again, etc. Thus, the specimen is subjected to cyclic loading and unloading with a gradually decreasing amplitude. The pause between the cycles is equal to the time of the doubled run of the strain pulse over the loading bar (Fig. 6). To conduct tests with cyclic loading of specimens and registration of repeated loading cycles in one test, one has to eliminate the return of the compression wave ε_1^t transmitted through the specimen from the backward face of the support bar back to the specimen. In this case, the length of the support bar should be greater than the length of the loading bar by a factor equal to the number of cycles supposed to be registered. Taking this into account, we used a loading pressure bar of length $L_1 = 1.5$ m and a support bar of length $L_3 = 4.5$ m, which allowed us to register three loading cycles.

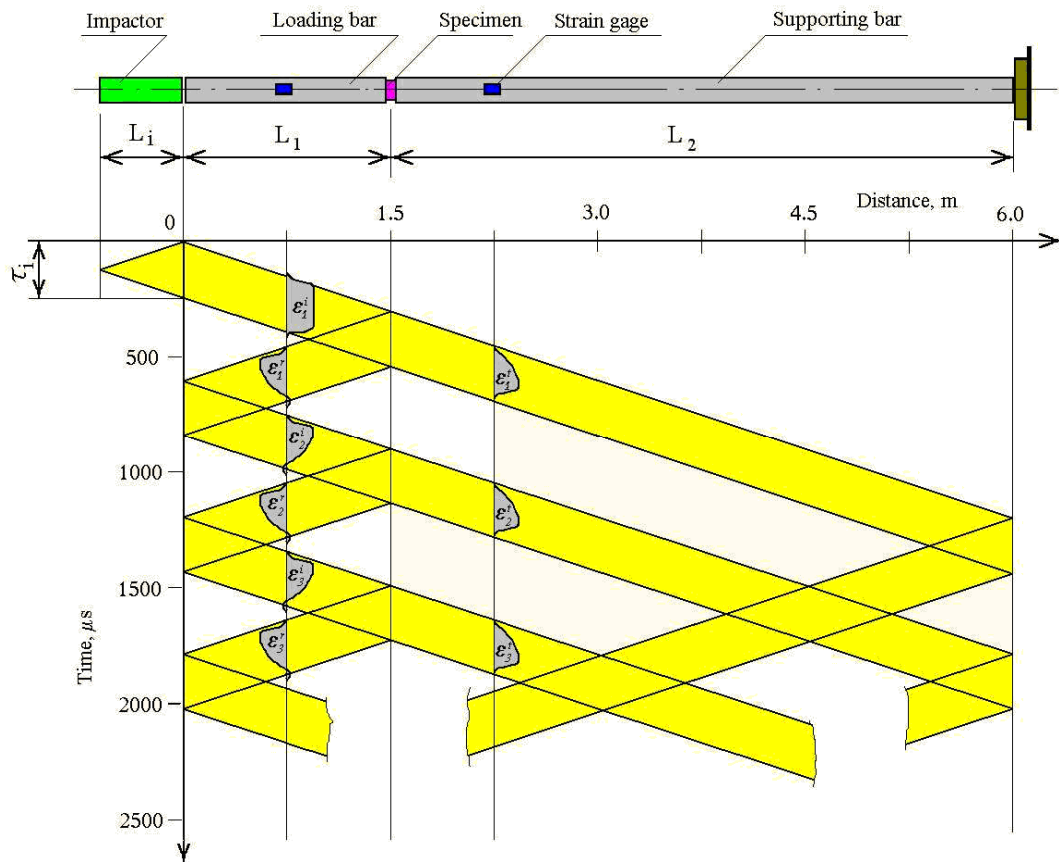


Fig. 6: X~t diagram of pulses in SHB during the registration of three cycles of loading.

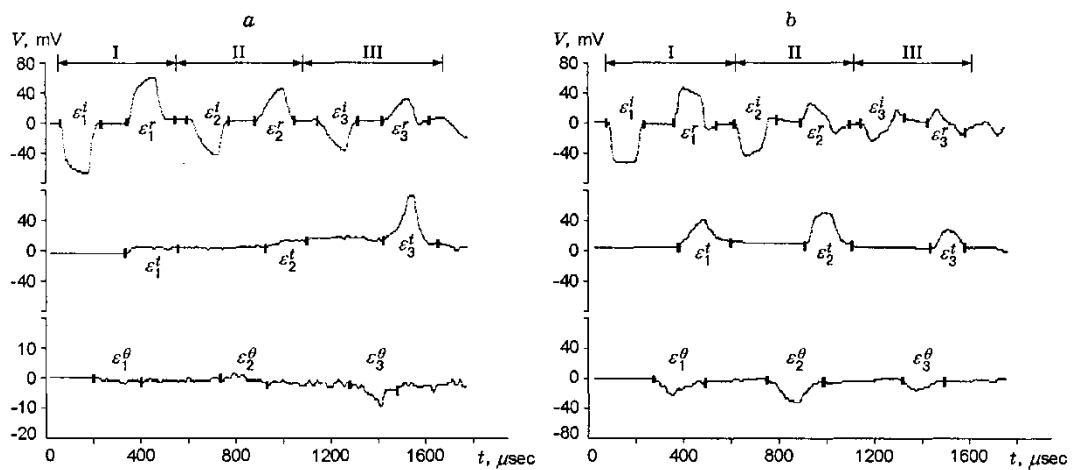


Fig. 7: The pulses in pressure bar and confining jacket during test of foam plastic of density 0.19 g/cm³ (a) and 0.67 g/cm³(b).

The oscillograms obtained in foam-plastic tests registered three beams: from the loading pressure bar, from the support pressure bar, and from the confining jacket. Figure 7 *a* and *b* show the oscillograms obtained in testing foam plastic of density $\rho=0.19$ and 0.67 g/cm^3 , respectively. The vertical strokes indicate the incident $\varepsilon_1^i, \varepsilon_2^i, \text{ and } \varepsilon_3^i$ and reflected $\varepsilon_1^r, \varepsilon_2^r, \text{ and } \varepsilon_3^r$ pulses on the first beam in the oscillograms, the pulses transmitted through the specimen on the second beam $\varepsilon_1^t, \varepsilon_2^t, \text{ and } \varepsilon_3^t$, and the pulses of circumferential deformation ($\varepsilon_1^0, \varepsilon_2^0, \text{ and } \varepsilon_3^0$) from the confining jacket on the third beam in the first, second, and third loading cycles. The ordinate axis shows the voltage registered by oscillograph channels. The duration of each cycle is marked by Roman numbers in Fig. 7. It should be taken into account that, since the signal from the support bar (pulse ε^t) is additionally amplified (because of its low value) and inverted thereby, it has the opposite polarity in the oscillogram registered. The reflected and transmitted pulses do not return to the "zero" line after the loading process is terminated, i.e., the process of unloading of the foam-plastic specimen is longer than the interval between the registration of the incident and reflected pulses because of the viscoplastic character of the deformation process. In addition, the amplitude of the reflected pulse is quite significant (up to 80% of the amplitude of the initial incident wave). As is shown above, this is caused by the significant difference in acoustic impedances of the pressure bar and the specimen.

A special feature of the behavior of foam plastic of density $\rho=0.19 \text{ g/cm}^3$ is the small amplitude of the transmitted wave (and hence, of the signal from the confining jacket) in the first and second cycles of specimen loading. Only after some compaction and choosing the gap between the side surface of the specimen and the inner surface of the jacket, the specimen starts to transmit a wave of a rather large amplitude. In this case, the signal from the jacket appears (see Fig. 7 *a*). The signal from the jacket is several times lower than the amplitude of the transmitted wave and is almost absent in the first two cycles (indiscernible at the background of noise). In the oscillogram of testing foam plastic of density $\rho=0.67 \text{ g/cm}^3$ (see Fig. 7 *b*), the amplitude of the transmitted wave already in the first cycle is sufficient to ensure registration of the signal from the confining jacket.

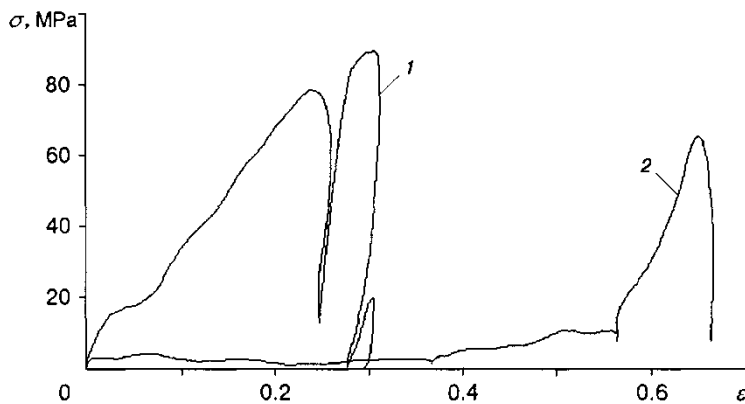


Fig. 8: Stress-strain curves for foam plastic of two densities.

Processing of initial strain pulses yields dynamic diagrams with additional loading cycles. Figure 8 shows the strain diagrams for foam-plastic specimens of densities $\rho=0.67$ (curve 1) and 0.19 g/cm^3 (curve 2) in the confining jacket for close amplitudes of the loading pulse. The mean strain rates in the first, second, and third loading cycles were, respectively, 2300 , 800 , and 300 s^{-1} for curve 1 and 2600 , 1800 , and 1000 s^{-1} for curve 2.

The proposed modification of the Kolsky method may also be used in tension tests by the Nicholas technique [21], since the reflected pulse has also a high amplitude in this case because of the significant difference in cross-sectional areas of the pressure bars and the specimen (12 : 1). Another way to obtain multicyclic loading is describe in [30]. Experimental studying of dynamic compressibility of dampers has been executed with use of the Kolsky method. For investigation of dissipative properties of materials we used some original modifications of SHPB: jacketed tests under uniaxial strain state, multicyclic loading of specimen for obtaining its mighty strain and using a polymeric transmitter bar (produced from vinylchloride) equipped with strain gauges located in immediate proximity from the sample. Last circumstance has allowed neglecting dispersion effects of impulses in a transferring is viscous-elastic bar.

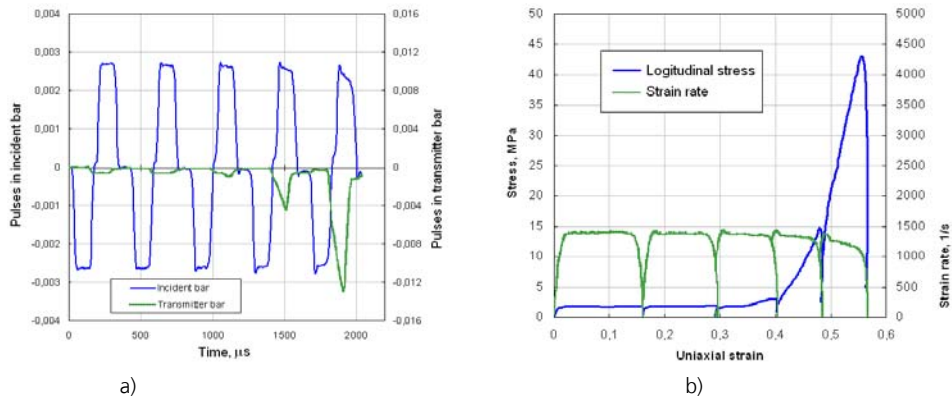


Fig. 9: Initial pulses in pressure bars (a) and resulting stress-strain curve for shamotte (b).

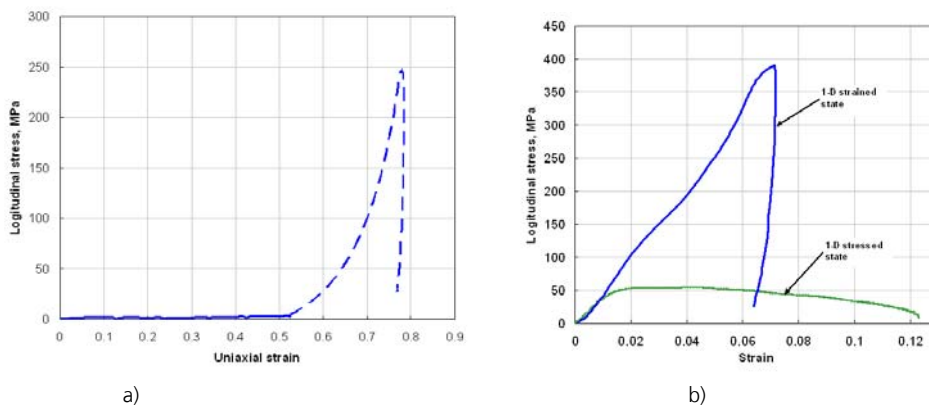


Fig. 10: Reiterated loading of the same specimen of shamotte (a) and the influence of stress-strain state for mullite (b).

During tests of high-porosity shamotte we used polymeric transmitter bar that allowed registering five cycles of load (in one experiment) and obtaining transmitted pulses of sufficient amplitudes (fig. 9). Repeated load of this specimen by greater amplitude of incident pulse allowed achieving considerable compaction of specimen and practically full closing of pores (broken line in fig. 10a). On an initial site of the diagram (up to deformation of 55 %) there occur particles reordering and removal of free poral space. These processes occur at small amplitudes of loads. After full removal of pores, a process of deformation of a continuous material begins that leads to essential growth of stress developed in the material. Diagrams of more dense refractory (mullite) are shown in fig. 10 b. This material has a strong skeleton which at once starts actively to resist to deformation.

1.4 Determining dynamic friction using a modified Kolsky method

For the adequate simulation of high-speed processes in designs subjected to dynamic influence, knowledge of both the dynamic properties of the materials and characteristics of friction between interactive surfaces is necessary. Friction and wear processes are the essential factors influencing the work of a cutting tool. Knowledge of the characteristics of friction is necessary for the development of the technological processes for high-speed machining of metals, such as rolling, deep-drawing, molding, etc. Taking this into consideration, friction is extremely important in the modeling of processes of a ballistic penetration.

For a complete characterization of friction phenomena, it is necessary to carry out numerous experiments which influence various factors that must be investigated: contact pressure, speed of relative movement and a roughness of surfaces, and temperature. In static conditions, many effective methods for defining friction characteristics are developed. As for the dynamic characteristics of friction, they are virtually not investigated due to the absence of reliable techniques for their definition.

We propose a simple and effective technique for determining the dynamic friction coefficient based on a modified Kolsky scheme using the SHPB method proposed by Lindholm [31], in which a measuring tube is employed instead of the conventional transmitting bar [32], [33]. On manufacturing of the samples, heavy-shrink fitting of a jacket on the core (figure 11) is applied and this guarantees tightness. This can be achieved by mechanical insertion or thermal fit. It is preferable to use thermal fit because the microrelief of the surfaces of interfaced elements essentially does not change.

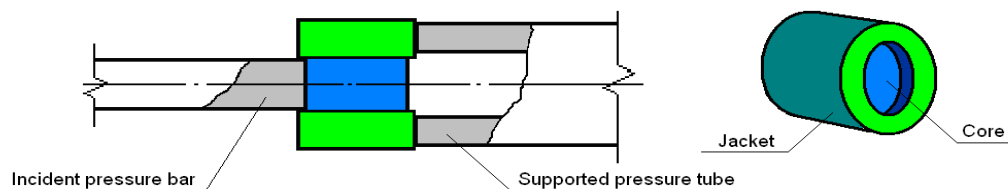


Fig. 11: Experimental scheme for investigation of dynamic friction.

Contact between the interfaced elements takes place on a cylindrical surface by diameter d and length l . The value of tightness δ (a negative

gap) is defined by accounting for the difference between the diameters of the female and male components. For heavy-shrink fitting with the guaranteed tightness on contact surfaces of the assemblage between the interfaced surfaces, a quite certain static pressure p develops, connected with tightness δ by dependence:

$$p = \frac{\delta}{\left(\frac{c_1}{E_1} + \frac{c_2}{E_2}\right) \cdot d}, \quad \text{where} \quad c_1 = 1 - \nu_1, \quad (8)$$

$$c_2 = \frac{d_2^2 + d^2}{d_2^2 - d^2} + \nu_2,$$

here E and ν - module of longitudinal elasticity and Poisson's ratio for the core (with subscript 1) and for the jacket (with subscript 2), d_2 - external diameter of a jacket.

Axial effort F is determined at a loading of the assemblage between end faces of the Hopkinson pressure bars (similar to a spew process) under the formula:

$$F(t) = EA_b \varepsilon_t(t), \quad (9)$$

where E and A_b - accordingly, is the module of elasticity and the cross-section area of the transmitter tube, $\varepsilon_t(t)$ - is the transmitted pulse.

The friction coefficient f at axial effort F and pressure p on a contact surface is determined as follows:

$$f = \frac{F}{p\pi dl}, \quad (10)$$

Experiments were performed on specimen-assemblages in which the internal core had been made from titanic alloy VT6, and external jacket had been made either from aluminium alloy AK4-1, or from titanic alloy VT6. In view of the available sizes of incident bars and transmitter tubes, the diameter of the contact surface of 14 mm was selected. Three types of the heavy-shrink fittings, differing in their tightness and therefore their contact pressure were used. The values of the elastic constants in the above specified formulae (8)-(10) for the determination of the friction coefficient are as follows:

- for titanic alloy $E_1 = 125000$ MPa, $\nu_1 = 0.34$,
- for aluminium alloy $E_2 = 72000$ MPa, $\nu_2 = 0.33$.

The importance of precise measurement of the initial diameters of the components before fitting is emphasized in order to obtain the exact value of the resulting tightness.

For each type of fitting, a series of experiments was executed in similar conditions, average curves of change of extrusion effort (figure 12) were constructed and average square-law deviations were determined at value of a relative error of 5 %.

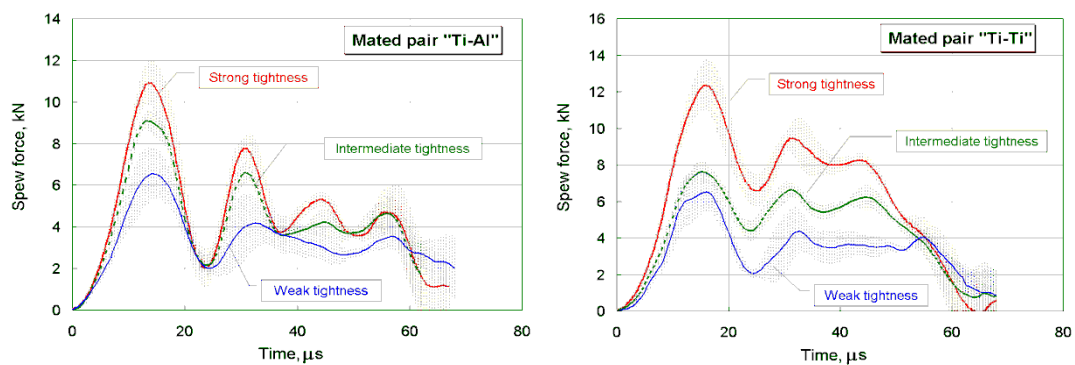


Fig. 12: Change of spew effort during extrusion of core from assemblages Ti—Al and Ti—Ti.

The vibrational character of extrusion effort changes was observed. This observation can be attributed to the spasmodic movement of the interfaced cylinders over time. It is important to note that during static extrusion, it is not possible to achieve smooth sliding of the assemblage components and movement also occurs in “jumps”. For the determination of the static friction coefficient, the first maximum on a curve of force was used; for the calculation of the coefficient of a sliding friction, the average value of effort was defined in a time interval 30-50 μs.

Based on the results obtained, the average values of dynamic coefficients of static friction and kinetic friction were determined and for pairs “Ti-Al” equal 0.45 and 0.20, and for pairs “Ti-Ti” equal 0.28 and 0.22, respectively.

1.5 Determining the dynamic hardness

Based on the Kolsky method, a novel scheme (Table 1 *n*) for determining the dynamic plasticity of materials is also proposed [5]. It differs from the conventional SHB scheme principally in that there is an accessory indenter in the form of a cone, a pyramid, or a hemisphere made of a high-strength hard material. The SHB system loading and deformation scheme in this case is practically similar to the conventional compression test scheme in the Kolsky method.

It follows from the 1-D theory of propagation of elastic waves that displacement $h(t)$ of the right-hand end of the incident bar and the indenter is described by the relation

$$h(t) = C \int_0^t [\varepsilon_i(t) - \varepsilon_r(t)] \cdot dt \quad (11)$$

Knowing the indenter geometry, relation (11) allows one to compute the indentation surface area at any time of the loading history. For a cone-like indenter with the angle at the apex of 2α , the current area $S(t)$ of the irreversible indentation will be

$$S(t) = \pi h^2(t) \frac{\operatorname{tg}^2 \alpha}{\sin \alpha} \quad (12)$$

The pulse $\varepsilon_t(t)$ in the supporting bar allows one to determine the time history of the force $F(t)$ arising when the indenter penetrates into the sample

$$F(t) = EA\varepsilon_t(t) \quad (13)$$

where E and A are elastic modulus and cross-section area of the supporting bar. Based on relations (12) and (13), one can determine the dynamic hardness, $HD(t)$, as the ratio of the effective resistance to indentation and the current indentation area:

$$HD(t) = \frac{EA\varepsilon_t(t) \sin \alpha}{\pi \left\{ \operatorname{tg} \alpha C \int_0^t [\varepsilon_i(t) - \varepsilon_r(t)] \cdot dt \right\}^2}$$

A great merit of this method is that it allows the dynamic hardness value to be computed at any stage of the indentation process.

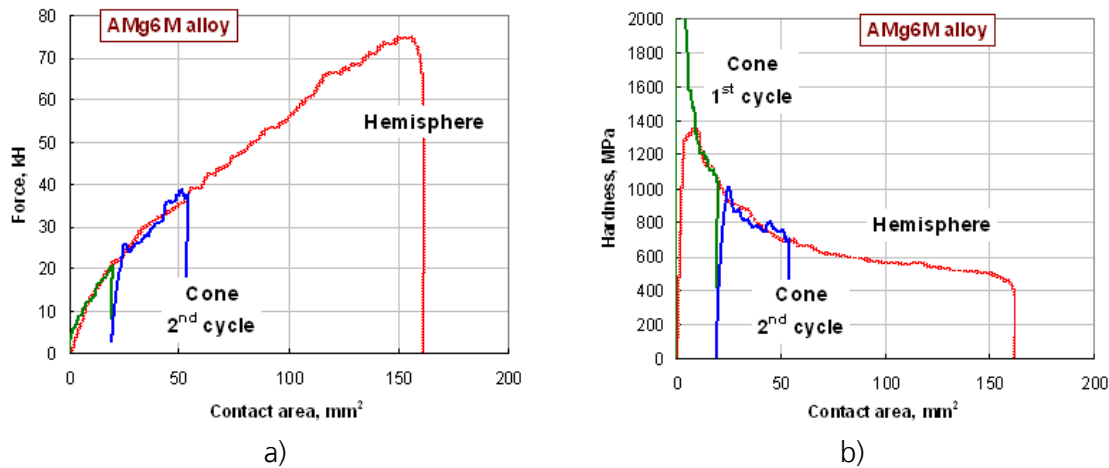


Fig. 13: Indentation of conical and hemispherical indenters.

As an example in fig.13 a represented obtained using implemented techniques dependence of force of resistance to indentation of conical and hemispherical indenters from the contact area for the AMg6M aluminum alloy at a rate of indentation ~ 20 m/s. The slope of the curve in fig. 13 a is a measured on the dynamic hardness. Fig. 13 b presented on the process of changing the dynamic hardness throughout the implementation process. References contained in the value of standard hardness for alloy AMg6M is $HB=650$ MPa, which indicates the reliability of the results. As can be clearly seen, the shape of indenters virtually no effects on the dynamic hardness.

1.6 Experimental devices for studying the strain rate history effects

Recently, great attention in dynamic plasticity has been paid to the problem of dependence of mechanical properties on the strain-rate history effects. Special attention was paid to the experiments with the incremental strain rate. To create a complex strain-rate history including partial or full loading with the subsequent after-loading of the specimen in the process of dynamic tests, it was proposed to load SHB's by specially designed projectiles [5],[34]. The projectiles are made of two or more parts of materials with different acoustic impedances.

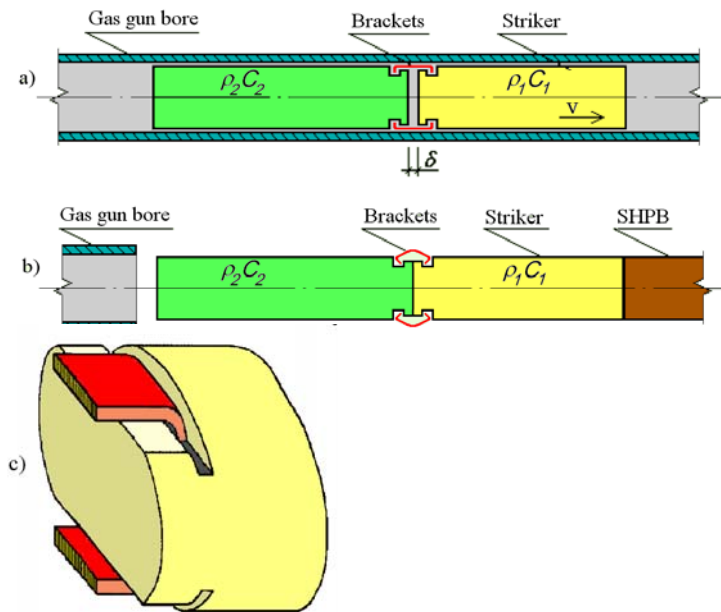


Fig. 14: Indentation of conical and hemispherical indenters.

The component bars may be arranged both with or without the gap between them (cemented together). In the former case, the projectile's bars have specially processed ends and are connected by low-strength flexible brackets (Fig. 14). On accelerating such a projectile in the bore of a gas gun, when it is subject to inertial forces, the brackets in the bore cannot bend, preventing the projectile components from approaching each other; thus, the preset gap does not change. Upon leaving the bore, the first projectile component strikes the SHB and generates in it a compressive pulse, its amplitude and duration being determined by its acoustic impedance and length, and by the projectile velocity. Meanwhile, the second projectile component continues its way due to the inertia forces and, with a certain time delay, hits the first bar, generating in it a compressive wave, its amplitude being determined by the ratio of the acoustic impedances of the projectile components. This wave passes along the first component to the incident pressure bar. Upon leaving the bore, the connecting brackets practically do not affect the pulse generation process in the SHB due to their flexibility.

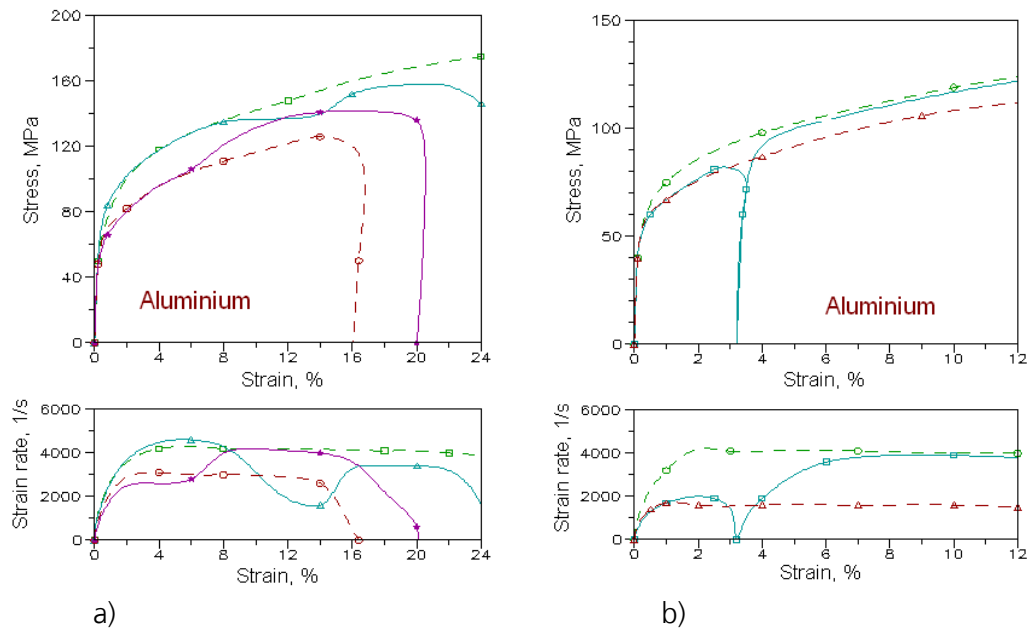


Fig. 15: Behaviour of aluminium when glued projectile (a) and projectile with a gap (b).

Using the projectiles of the second type allows one to generate in the SHB a loading pulse with a sharp increase or decrease of the amplitude, thus making it possible to carry out the tests with both the positive and negative stress-strain increments. Projectiles of the first type form in the SHB system a loading compressive pulse of a complex form consisting of two or more parts (with the same or different amplitudes) with the time intervals of several tens of microseconds between them. Such a loading mode makes it possible to perform full unloading of the specimen after it has reached some plastic deformation, with a subsequent reloading (after a controlled time interval) using a higher, a lower, or the same strain rate. Examples of using such projectiles in testing of pure aluminium are shown in Fig. 15. The deformation curves for the AD1 aluminium obtained when loading the SHB by a projectile made up of three parts cemented together (the middle part was made of aluminum alloy, and the first and the last ones of steel) are shown in Fig. 15 a. Sharp jumps from the lower strain rates to the higher ones and vice versa were accomplished in the experiments. The results are compared with the constant strain-rate curves (dotted lines in the figure). It is evident that aluminum responds quickly enough to the changes in strain rate, while being fairly sensitive to the deformation history (the curves for strain-rate jumps do not reach the ones for constant strain rates), this sensitivity increasing with the decrease of the strain rate. Fig. 15 b shows the deformation curves for aluminium

obtained using the strikers with the first component made of an aluminum alloy and the second one of steel. In one of the tests, the striker components were cemented together (the dotted curve), and in the other they were positioned with a gap (the solid curve). Analysis of the results testifies to a weak sensitivity of this material to the strain rate for its two-fold variation.

1.7 Investigation of Bauschinger effect

There are known modifications of the well-known Kolsky method, in which alternating-sign loading can be implemented under uniaxial deformation conditions at straining rates within 10^2 – 10^4 s⁻¹, thus making possible the study of the Bauschinger effect [5], [20].

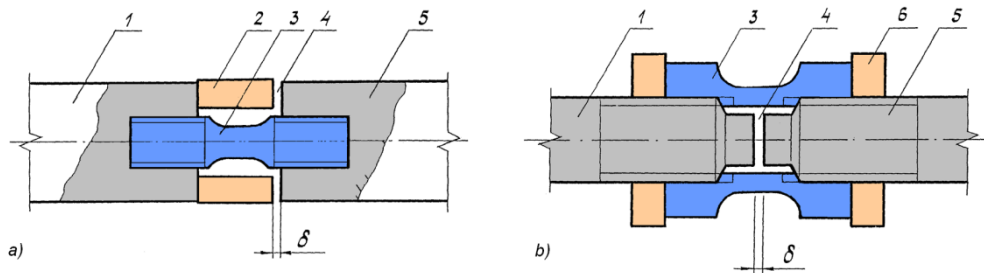


Fig. 16: Behaviour of aluminium when glued projectile (a) and projectile with a gap (b).

The present authors analyze the dynamic Bauschinger effect using a modified tensile SHB scheme. The SHB configuration versions proposed to this end are shown in Fig.16 a-b and differ from each other in a specimen type used. A tubular or a solid specimen 3 is connected to the bars 1 and 5 by a threaded connection, so that there is a small gap 4 between the bar ends allowing for an additional compressive cycle of the specimen before the tensile cycle. Until the entire gap is taken up during the first compressive loading cycle, the amplitude of the wave passing to the transmitted bar will be equal to a part of the original wave amplitude depending on the specimen material properties and the ratio of cross-section areas of the sample and the pressure bars. After deformation in the specimen had reached a certain deformation value, the bar ends will come into contact and the remaining part of the original pulse will pass entirely to the transmitted bar without any changes in the amplitude. The reached compressive strain of the specimen will remain unchanged during the effective period of the original pulse, after which relaxation of the

specimen will take place. The stress will drop to zero, the total strain will be reduced by the value of its elastic component, thus eliminating the acoustic contact between the ends of the bars. Upon reaching the free end, the compression pulse in the transmitted bar is reflected by a tensile wave. The bar ends do not prevent the specimen from free tension, the tensile pulse amplitude being adequate for plastically deforming the specimen.

However, these variants of the Kolsky method are rather difficult to implement in practice. Thus, the search for simple methods of quantitatively evaluating the dynamic Bauschinger effect is still topical. The paper describes such a relatively simple and effective method for investigation of the Bauschinger effect [35].

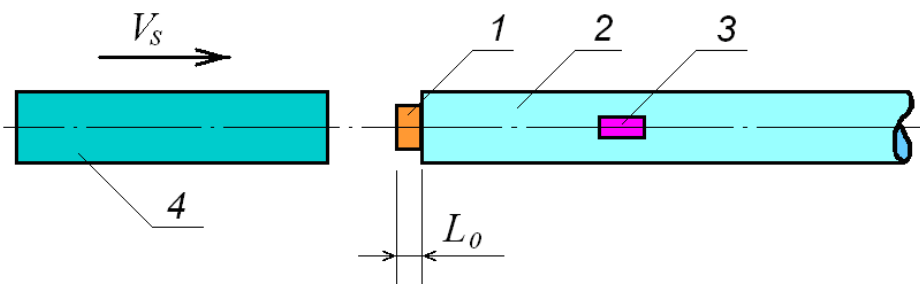


Fig. 17: Schematic diagram of the proposed method (see text for explanations).

The proposed method is based on the direct impact technique [9], which is schematically depicted in Fig. 17. According to this, sample 1 made of a material to be studied is arranged at the edge of pressure bar 2 and loaded by the impact of striker 4 accelerated in a gas gun barrel. The impact rate is adjusted so as to ensure that the sample would be deformed in a plastic domain, whereas the high-modulus (~ 2500 MPa) striker and pressure bar occur in the elastic domain.

Strain gauges 3 glued onto the pressure bar measure the compression pulse, which is generated during the impact and characterizes the main features of the high-rate straining of the sample.

Figure 18 shows the typical waveform of a compression pulse measured for a sample of D16 aluminum alloy. As can be seen, the leading front displays a region (OA) of elastic deformation, which is followed by the region (AB) of plastic flow. The unloading process starts (at point B) in a

certain period of time that can be estimated as $\tau=2l/C = 2 \times 300/5 = 120 \mu\text{s}$ (where $l = 300 \text{ mm}$ is the striker length; $C=5 \text{ mm}/\mu\text{s}$ is the sound velocity in the striker material). A distinctive feature of this process (in contrast to that observed in experiments with uniaxial stressed state) is a special two-wave configuration. First, an elastic unloading takes place (BC), which is followed by a plastic unloading wave (CD). The total duration of the unloading wave (BCD) is also equal to $\tau=2l/C$. Qualitatively similar patterns are observed in the impact tests on other materials. By measuring the stress amplitude at point A of the pulse measured in the pressure bar, one can readily determine the yield stress σ_Y^L for the given sample on loading (Fig. 18). With allowance for the known ratio of the cross-sectional areas of the pressure bar and sample (2.1 : 1), the yield stress for a sample of D16 alloy amounted to 462 MPa. This value was in agreement with the yield point of 470 MPa determined for the same alloy in independent tests using the Kolsky method. By the same token, on the passage from elastic to plastic unloading in the BCD region, it is possible to determine the yield stress for unloading as $\sigma_Y^{UL}=345 \text{ MPa}$ (by measuring the amplitude difference between points B and C and taking into account the same ratio of the cross-sectional areas). Then, the ratio of the yield stresses for the loading (σ_Y^L) and unloading (σ_Y^{UL}) can serve a

measure of the Bauschinger effect: $\delta = \frac{\sigma_Y^{UL}}{\sigma_Y^L}$.

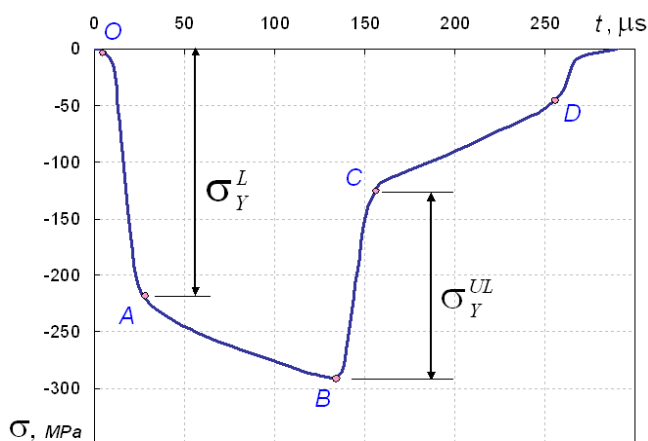


Fig. 18: Typical waveform of the measured compression pulse (see text for explanations).

The nature of this effect as manifested in the tests with uniaxial stressed state can be explained in terms of some transient processes involved in

the development and growth of uniaxial deformation in the course of loading. The results of numerical simulations [13] showed that, in the presence of friction forces at the edges of a sample, the development of the axial stress is accompanied by the appearance of radial stresses. Thus, the stress tensor has both deviator and ball components, which can account for the two-wave unloading. Since the pressure is not very large (within several hundred megapascals), its influence on the Bauschinger effect can be ignored. The magnitude of the Bauschinger effect in the D16 alloy sample plastically strained to 6% amounted to $\delta=0.75$. Thus, the proposed method allows the Bauschinger effect to be readily determined and quantitatively characterized. This provides possibility of studying the dependence of this effect on the straining rate.

1.8 Ensuring constant strain rate

It is known, that the compression tests using the SHB are not always constant strain-rate tests. Generally, a SHB is loaded by a trapezoidal compression pulse of a practically constant amplitude. During the deformation the specimen hardens and its cross-section increases. As a result, the strain rate, proportional to the pulse reflected by the specimen and determined by the difference between the incident and the transmitted pulses, tends to decrease during the experiment. To ensure a constant strain rate during the experiment it is desirable to have the loading pulse similar to the transmitted one but of a larger amplitude. To this end, it was proposed to add another SHB and an additional specimen [2] to the SHB configuration or to load the SHB by a projectile of a variable cross-section in the form of a tapered cone [39]. Practically the same results can be achieved in a simpler way, by loading the SHB through an auxiliary specimen placed at the end of the incident bar on which the projectile impacts [40]. The incident compressive pulse with an increasing amplitude formed in the SHB under such loading scheme is similar to the transmitted pulse.

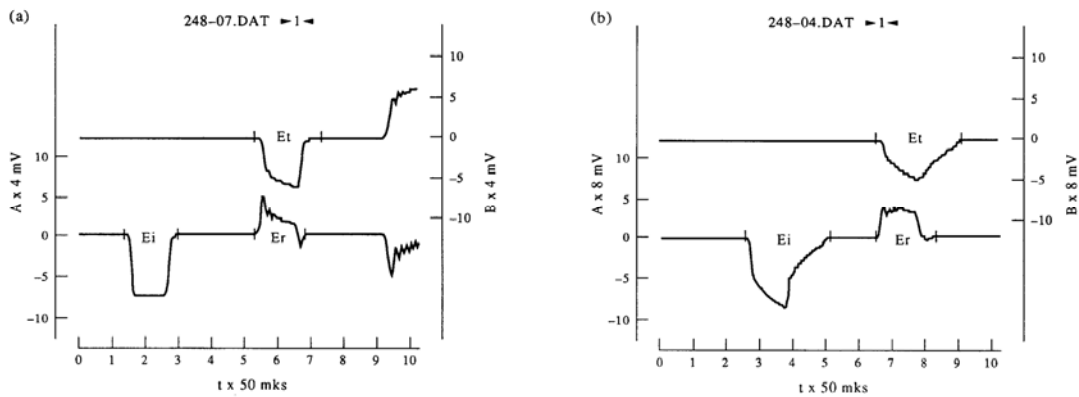


Fig. 19: Strain pulses in SHPB: traditional (a) and with pulse shaper (b).

As an example, Fig. 19 shows oscillograms of tests for the AMg6 alloy using the conventional (a) and the proposed (b) schemes. It is evident that the proposed scheme ensures a practically constant strain rate during the process of plastic deformation.

1.9 The methodology of complex experimental-numerical researches

At designing military and industrial objects, nuclear stations, large public buildings and also containners for transportation of explosive, toxic and radioactive substances the main problem is devoted to an estimation of their vulnerability in case of occurrence of emergencies: acts of terrorism, the natural and mancaused accidents, accompanied intensive dynamic influences. The use of numerical simulation in the early design stages can significantly speed up and reduce price of the developing process. However, it should be understood that the accuracy of the numerical experiment (the efficiency of its use) is largely determined by the accuracy of material models involved [30], [41].

Now it is well-known, that mechanical properties of materials change depending on speed of deformation and temperature. Taking into account an influence of these factors on mechanical characteristics of a material is very important at calculation of a stress-strained condition and strength of constructions. The major element of such calculation is the defining relationships (models) adequately describing elastic-plastic behavior of a material in a wide range of strain rates and temperatures.

There is a necessity of realization of complex experimental-numerical researches which include obtaining of a spectrum of mechanical characteristics of a material, a choice of defining relationships and their equipping by necessary parameters, and also their subsequent verification on the basis of comparison results of a set of numerical and natural verification experiments. On an example of some metals the methodology of such complex research of dynamic properties of materials is presented. For determination the dynamic stress-strain curves under compression the traditional SHPB scheme were used [1]. To determine strength and deformation failure properties of materials under tension the Nicholas' scheme was used [21].

Software package LS-DYNA is very widely using all over the world for numerical simulation. It has the big library of models (material functions) and criteria of destruction. For a few popular models of plasticity (Johnson-Cook, Zerilli-Armstrong, Cowper-Symonds etc.) necessary parameters have been defined. The problem of definition of an optimum set of parameters in this case is identical to a problem of approximation of experimental data in four-dimensional space "deformation-strain rate-temperature-yield stress". The decision of an optimizing problem was done numerically by a method of the conjugate gradients with use of mathematical packages Maple and MathCAD. Then the estimation of adequacy (verification) of the received models was carried out.

For verification of defined plasticity models, the authors used a set of original verification experiments (in natural and numerical realization) using pressure bar technique: modified Taylor test, direct impact method [9] and dynamic indentation [5] of indenters with a head-tip both in the form of a cone and a hemisphere. In modified Taylor's test, the accelerated specimen hits not on rigid semi-infinite barrier, but on the pressure bar equipped by strain gauges. In each of the specified methods for checking adequacy of parameters of models is used, except the analysis of the residual form of the specimen, a comparison of experimentally registered and numerically simulated strain pulse in a pressure bar. In modified Taylor test also high-speed film-registration of change of specimen's form during impact has been done which has allowed estimating a reliability of models more precisely. It is necessary to notice that modes (a kind of the stress-strain state, a strain-rate range) of these experiments differ from one-dimensional experiments on the Kolsky

method in which parameters of models have been obtained. Thus possibilities of models are checked at other modes of a loading.

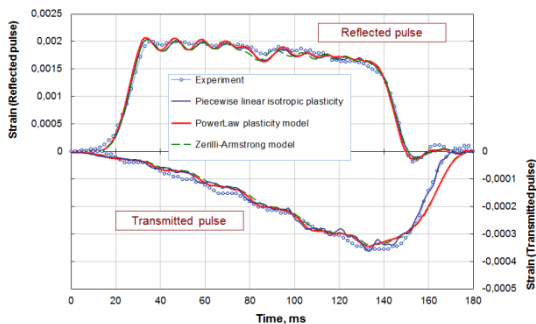


Fig. 20: Indentation of cone

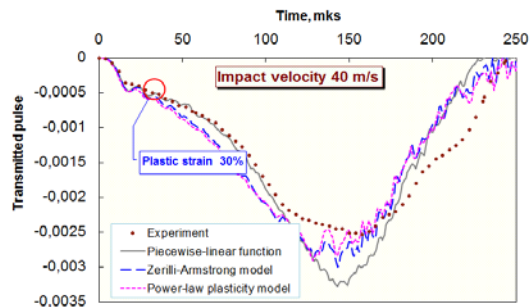


Fig. 21: Direct impact

Some results of verification for obtained models of AMg6 alloy are shown below. A comparison of natural and simulated strain pulses in pressure bar for AMg6 alloy during indentation and direct impact experiments is presented in Figs. 20-21.

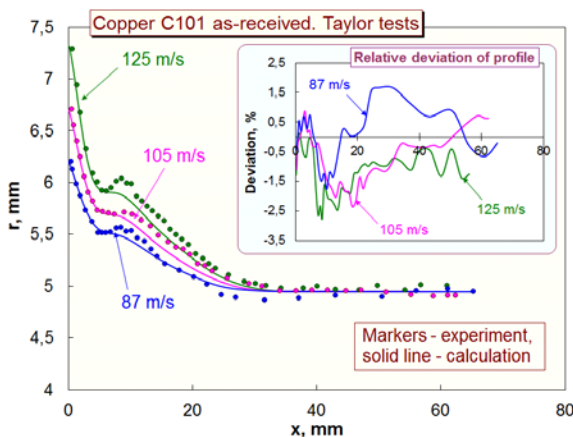


Fig. 22: Verification by modified Taylor test

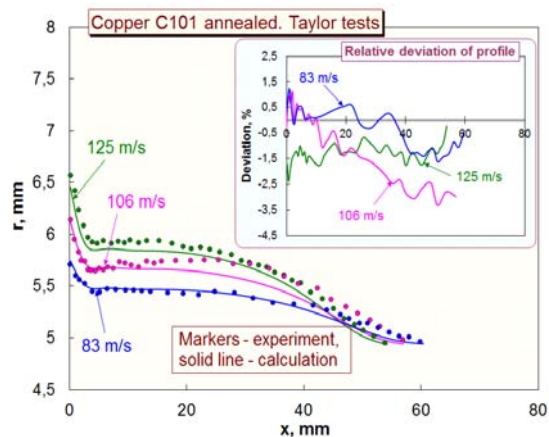


Fig. 23: Verification by modified Taylor test

In Fig. 22-23, a comparison of experimental and simulated residual profiles of C101 copper specimens both in a condition "as-received" (a) and after an annealing (b) is shown. It is well visible that after an annealing the zone of plastic deformation of the specimen is much more, though the degree of radial deformation is less. For two specified models an equally good conformity of experimental and simulated residual profiles is visible because of absence of influence of speed of deformation

on a dynamic yield point of an investigated material. It is visible that relative deviations between numerical and experimental profiles of samples after impact do not exceed 2.5 %.

1.10 Acknowledgements

The work was partially supported by grants (agreement on 27.08.2013 No 02.B.49.21.0003 between The Ministry of education and science of Russia and UNN) and with financial support from RFFI (Grants 12-08-01227 and 12-01-00805).

1.11 References:

- [14] Stepanov, G.V. Elastoplastic deformation and fracture of materials under impact loading. Kiev: Naukova Dumka, 1991. 288p. (in Russian)
- [15] Bragov, A.M., Balandin, V.V., Lomunov, A.K., Filippov, A.R.: *Determining the Impact Compressibility of Soft Soils from Inversed Test Results*. Technical Physics Letters, Vol. 32, No. 6, 2006, pp. 487-488.
- [16] Kokoshvili, S.M. Methods for dynamic testing of rigid polymeric materials. Riga: Zinatne, 1978.
- [17] Investigation of the dynamic strength of structural materials. Novikov, S.A. (ed.), Sarov, 2003. (in Russian)
- [18] Bragov, A.M., Lomunov, A.K.: *Methodological aspects of studying dynamic material properties using the Kolsky method*. Int. J. Impact Engng. 1995. Vol.16, No2, p.321-330.
- [19] Bragov, A.M., Demenko, P.V., Lomunov, A.K., Sergeichev, I.V., Kruszka, L.: *Investigation of behaviour of materials of different physical nature using the Kolsky method and its modifications*. "New Experimental Methods in Material Dynamics and Impact", Trends in Mechanics of Materials, vol.3, eds. W.K.Nowacki, J.R.Klepaczko, Warsaw, 2001, p.337-348.
- [20] Ogawa, K.: *Impact-tension compression test by using a split Hopkinson bar*. Exp. Mechanics, 1984, vol.24, N 2, p.81-85.
- [21] Nicholas T.: *Tensile testing of materials at high rates of strain*. Exp.Mech. 1981. Vol.21, N 5. P.177-195.

- [22] Rodriguez, T., Navarro, C. and Sanchez-Galvez, V.: *Splitting tests: an alternative to determine the dynamic tensile strength of ceramic materials*. Journal de Physique IV, 1994, pp.101-106.
- [23] Kolsky, H. *An investigation of the mechanical properties of material at very high rates of loading*. Proc. Phys. Soc. (London), Vol. 62B, 1949, pp.676-700.
- [24] Bragov, A.M., Demenko, P.V., Kruszka, L., Lomunov, A.K., Sergeichev, I.V.: *Investigation of dynamic compressibility and shear resistance of soft soils in a wide range of strain rate and pressure*. Fifth European Conference "Numerical Methods in Geotechnical Engineering", Mestat (ed.) 2002, Presses de l'ENPC/LCPC, Paris, p.909-917.
- [25] Bragov, A.M., Grushevsky, G.M., Lomunov, A.K.: *Use of the Kolsky Method for Confined Tests of Soft Soils*. Experimental Mechanics. 1996. Vol.36, p.237-242
- [26] Bragov, A.M., Grushevsky, G.M., Lomunov, A.K.: *Use of the Kolsky method for studying shear resistance of soils*. DYMAT Journal. 1994. Vol.1, №3. p.253-259.
- [27] Bragov, A.M., Kotov, V.L., Lomunov, A.K., Sergeichev, I.V.: *Measurement of the Dynamic Characteristics of Soft Soils using the Kolsky Method*. Journal of Applied Mechanics and Technical Physics, 2004, Vol. 45, No.4, pp.580-585.
- [28] Bragov, A.M., Lomunov, A.K., Sergeichev, I.V., Tsembelis, K., Proud, W.G.: *Determination of physicomechanical properties of soft soils from medium to high strain rates*. International Journal of Impact Engineering, Vol.35, Issue 9, September 2008, p.967-976.
- [29] Bragov, A.M., Lomunov, A.K., Sergeichev, I.V.: *Modification of the Kolsky method for studying properties of low-density materials under high-velocity cyclic strain*. Journal of Applied Mechanics and Technical Physics, 2001, Vol. 42, No.6, pp.1090-1094.
- [30] Bragov, A., Konstantinov, A., Lomunov, A., Sadyrin, A., Sergeichev, I., Kruszka, L.: *Dynamic compressibility of high-porosity dampers of thermal and shock loadings: modeling and experiment*. International Journal of Modern Physics B. 2008, Vol.22, No 9/11, pp.1183-1188.
- [31] Lindholm, U.S., Yeakley, L.M.: *High strain-rate testing: tension and compression*. Exp.Mech. 1968. Vol.8, N 1. P.1-9.

- [32] Bragov, A.M., Konstantinov, A.Yu., Lomunov, A.K.: *Determining dynamic friction using a modified Kolsky method*. Technical Physics Letters, Vol.34, No 5, 2008, pp.439-440.
- [33] Bragov, A., Konstantinov, A., Lomunov, A., Shmotin, Yu., Kruszka, L.: *Experimental definition of dynamic friction*. Journal de Physique IV. 2009, p.619-624.
- [34] Bragov, A.M., Lomunov, A.K., Medvedev, A.A.: *A modified Kolsky method for the investigation of the strain-rate history dependence of mechanical properties of materials*. Journal de Physique IV. Vol.1, 1991. P.471-475.
- [35] Bragov, A.M., Konstantinov, A.Yu. and Lomunov, A.K.: *Determining the Bauschinger effect using the direct impact technique*. Technical Physics Letters, Vol.36, No 8, 2010, pp.694-695.
- [36] Dharan, C.K.H., Hauser, F.E.: *Determination of stress-strain characteristics at very high strain rates*. Exp.Mech. 10, 370-376, 1970.
- [37] Konstantinov, A.Yu. An experimental-computational investigation of the behavior of structural materials under dynamic loading. PhD Theses, N.Novgorod, 2007.
- [38] Ellwood, S., Griffiths, L.J. and Parry, D.J.: *Material Testing at High Constant Strain Rates*. J. Phys. E: Scientific Instruments 15, 280-282, 1982.
- [39] Sato, Y. and Takeyama, H.: *The Use of the Split Hopkinson Pressure Bar to Obtain Dynamic Stress-Strain Data at Constant Strain-Rates*. Technol. Rep, Tohoku Univ., 43, 303-315, 1978.
- [40] Bragov, A.M., Lomunov, A.K.: *Specific features in deformation diagrams construction by Kolsky method*. In Prikladnye problemy prochnosti i plastichnosti. Vsesoyuz. Mezhvuz. Sb. 28, 125-137 Gorky University, 1984. (in Russian).
- [41] Bragov, A.M., Balandin, V.V., Konstantinov, A. Yu., Konstantinova, Yu.V., Lomunov, A.K., Filippov, A.R.: *Identification and Verification of Some Plasticity Models for Structural Materials by Using Pressure Bar Technique*. Journal of Ningbo University (NSEE). 25(1), 70-73, 2012.

Numerical simulation of the 45 steel deformation under Taylor impact

Chen Gang, Huang Xicheng

(Institute of systems engineering, CAEP, Sichuan, PRC, 621999)

1.1 Abstract

The Taylor impact test was originally devised as a method for estimating the dynamic strength of ductile materials at high strain rates. More recently, since it provides a range of plastic strains and strain rates, also varies of stress states are experienced, the Taylor test is often performed to verify material constitutive models by comparing numerical predictions with experimental data. When the impact velocity is sufficiently high, the specimen would generate cracks in the Taylor test. Still, only a few papers in the literature investigated fracture phenomena and mechanisms in the Taylor test. In this paper, based on the investigation of material dynamic behavior, the deformation and fracture characters of 45 steel specimens under Taylor impact were simulated using axial symmetry and three-dimensional model respectively with LS-DYNA. The final length and diameter of the specimen obtained from simulations were consistent with the experimental observations. Different dynamic fractures occurred in the Taylor tests were obtained in three-dimensional numerical simulations. The mechanisms of different failure modes were investigated with the history of the stress state triaxiality in the specimen.

Keywords: Taylor impact, Numerical simulation, 45 steel, fracture

1.2 Introduction

The Taylor test was developed by G.I. Taylor as a method of estimating the dynamic strength of ductile materials in compression. His method consists of firing a flat-nosed cylindrical projectile of the material against a massive and rigid target at normal incidence. The dynamic flow stress could be estimated by measuring the dimensions of the cylinder before and after deformation.

Taylor's original analysis was one-dimensional. But it is clear that material moves in three- dimensions during the Taylor impact test. And the strain rate during the deformation process is not constant; the strain in the deformation range varies at different place. With the development of the numerical simulation technique, nowadays it is mainly used in the validation of constitutive models ^[1-3]. And some researchers use the Taylor impact test to evaluate constitutive models and determine constants for these models ^[4].

Most of studies with the Taylor test focus on the dynamic yield stress and constitutive models of materials without considering the fracture of the rod. If the impact velocity is sufficiently high in the test, failure would occur in the material and cracks would be generated in the cylinder. But relatively few published papers deal with fracture phenomenon and fracture mechanisms in the Taylor test.

In the Taylor tests performed by Paparno with 4340 steel in different heat treatment conditions, two types of fracture behavior were observed. One type is brittle fracture with a conical fracture surface at the impact end of the projectile. The other type is the impact surface petals while the projectile remains intact ^[5]. Shear cracks were observed and found from observations of sectioned specimens to originate from shear bands by Conque in the symmetric Taylor test of tungsten alloy^[6]. A large number of void nucleation, growth and aggregation was found in the center of specimen near the of impact interface by Grady and Kipp^[7]. The similar experimental phenomena was also reported by Woodward^[8].The adiabatic shear phenomena in the Taylor impact was investigated by Stevens with axisymmetric numerical simulation ^[9]. The process of voids growth was simulated by Worswick and Pick with two-dimensional axisymmetric model too ^[10].

In fact, the fracture and fragmentation in the Taylor impact does not maintain axisymmetric characteristic, and this phenomena need to describe with the 3D model. Still, numerical prediction of crack growth and fracture in a three-dimensional body under multi-axial dynamic loading is a challenging problem. Three possible fracture modes in the Taylor impact: the confined fracture inside the cylinder, the shear cracking on the lateral surface, and the petalling, were simulated by Teng.

Based on the investigation of material dynamic behaviors, the dynamic deformation and failure of 45 steel in Taylor cylindrical impact test were investigated with the dynamic finite element simulation by using LS-DYNA.

1.3 Material behaviors and model description

Dynamic and quasi-static mechanical behaviors of 45 steel have been studied with the split Hopkinson pressure bar (SHPB) and static material test system over a wide range of strain rates and temperatures. The experimental results were given in figure 1 and figure 2.

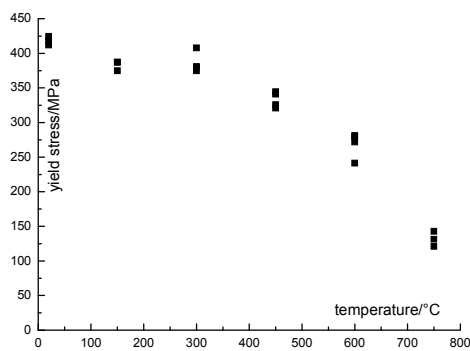


Fig. 1: Static tensile yield stress vary with temperature.

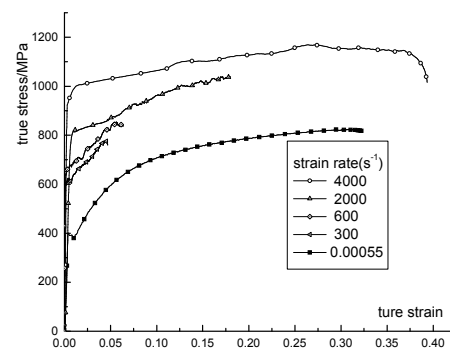


Fig. 2: Compressive stress—strain curves of 45 steel at different strain rates.

With Split Hopkinson Tension Bar tests and static material test, the effects of high strain rate, elevated temperature and stress triaxiality on the fracture behavior of 45 steel were studied. Fracture strain of 45 steel vs. stress triaxiality, temperature and strain rate of varies cases of experiments were shown in figure 3, figure 4 and figure 5, respectively. The fracture strains increase with stress triaxiality markedly, slightly decrease with temperature, and slightly increase with strain rate.

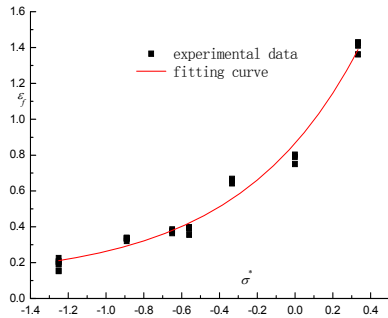


Fig.3: Failure strain of 45 steel vs. stress state.

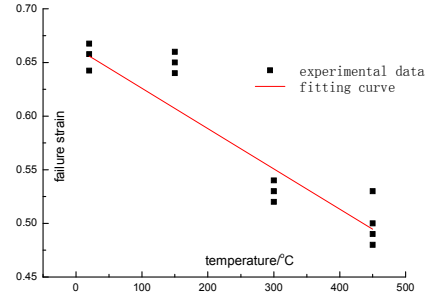


Fig. 4: Tension failure strain of 45 steel vs. temperature.

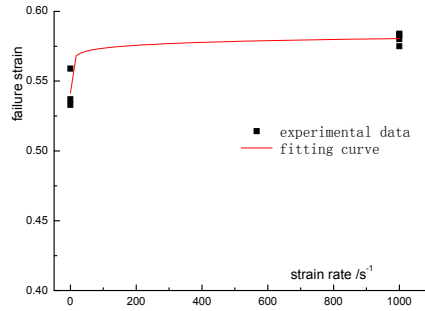


Fig.5: Failure strain of 45 steel varies with strain rate.

In the numerical simulation of dynamics, material constitutive models must be able to depict exactly material behaviors under conditions of large strain and wide range of strain rate and temperature. JC model is often applicable for the dynamic behaviors of metal from low to high strain rates, and certainly it is appropriate for the quasi-static deformation too. The plastic behavior and failure property of 45 steel material are described by Johnson-Cook(J-C) model which composed of two parts. The first part^[11] describes material plastic flow stress that varies with strain, strain rate and temperature as follows

$$\sigma_{eq} = [A + B(\bar{\epsilon}^p)^n] [1 + C \ln \dot{\epsilon}^*] [1 - (T^*)^m] \quad (1)$$

where A, B, C, n and m are material constants; $\dot{\epsilon}^* = \dot{\epsilon}^p / \dot{\epsilon}_0$ is a dimensionless strain rate, $\dot{\epsilon}_0$ is a reference strain rate; $T^* = (T - T_r) / (T_m - T_r)$ is the homologous temperature, where T is the absolute temperature, T_r is the room temperature and T_m is the melting temperature of material.

The second part^[12] describes material failure with a damage parameter D which gives as

$$D = \sum \frac{\Delta \varepsilon_p}{\varepsilon^f} \quad (2)$$

Where $\Delta \varepsilon_p$ is the increment of effective plastic strain during an integration cycle, and ε^f is the equivalent strain to failure, under the current conditions of strain, temperature, pressure and equivalent stress. Failure is allowed to occur when $D=1.0$. The general expression for the strain at fracture is given by

$$\varepsilon^f = [D_1 + D_2 \exp(D_3 \sigma^*)][1 + D_4 \ln \dot{\varepsilon}^*][1 + D_5 T^*] \quad (3)$$

Where $\sigma^* = -R^\sigma = p / \sigma_{eq}$ is the stress triaxiality ratio and p is pressure. The parameters D_1 , D_2 , D_3 , D_4 and D_5 are material constants. The failure strain and thus the accumulation of damage, is a function of mean stress, strain rate, and temperature.

Without significant heat conduction in a rare time, higher velocity impact is usually regarded as under adiabatic condition. Majority of plastic energy is converted into heat and it generates localized high temperature. The adiabatic temperature rise may be expressed as

$$\Delta T = \frac{\eta}{\rho C_p} \int_0^\varepsilon \sigma(\varepsilon_p) d\varepsilon_p \quad (4)$$

Where C_p is the specific heat and η is the fraction of plastic work converted into heat. ρ is the material density.

Based on material property experiments as shown above, with the method of least squares, the parameters used in this simulation are obtained and shown in table 1, where the reference strain rate is $1s^{-1}$.

Tab.1: Material parameters of 45 steel.

ρ (kg/m ³)	E (GPa)	μ	Cp (Wm ⁻¹ K ⁻¹)	η	Tr (K)	Tm (K)	$\dot{\epsilon}_0$ (s ⁻¹)	A (MPa)	B (MPa)
7800	200	0.3	469	1	300	1795	1	506	320
n	C	m	D1	D2	D3	D4	D5		
0.28	0.064	1.06	0.1	0.76	1.57	0.005	-0.84		

1.4 Numerical simulations on the Taylor impact deformation

The deformation response of the Taylor impact specimens under different impacting speeds were simulated with axisymmetric model using LS-DYNA. The axisymmetric model is established according to the experimental conditions, as shown in Figure 6. The mesh scale of specimen is 0.5mm × 0.5mm. The target is described with elastic material model, and the specimen material is described with the J-C model as mentioned above. The interaction of the specimen with the target was defined by the dynamic contact algorithm.

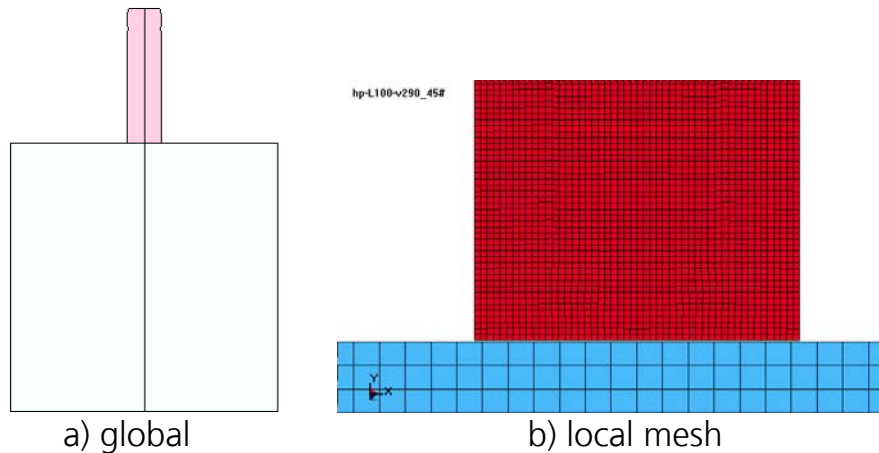


Fig. 6: Axisymmetric FEM model for Taylor impact.

The simulation results of the final deformation and the equivalent plastic strain distribution of the 45 steel Taylor impact specimens in the cases of impact velocity at 164m/s, 217m/s and 290m/s were given in figure 7. The distribution of plastic strain in the specimen is non-uniform either

radial or axial, the maximum plastic strain is located the impact section center, and the values under these three velocity are 0.64, 1.1 and 2.1, respectively. A comparison of specimen shapes between experiment and the numerical simulation is given in figure 8. The comparison of the final length and the maximum diameter of specimen are given in figure 9 too. The consistency between experimental observations and numerical simulations indicates the material parameters obtained can describe the large strain mechanical behavior of 45 steel under high speed deformation.

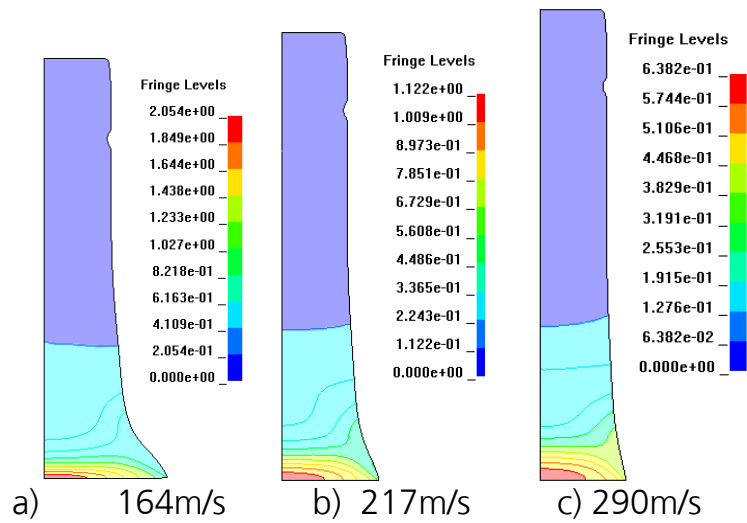
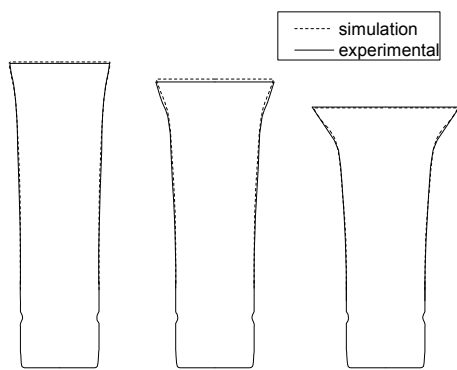


Fig. 7: The final deformation of the specimens at different impact velocities.



a) 164m/s b) 217m/s c) 290m/s

Fig. 8: Comparison of specimen final shapes between simulation and experiment.

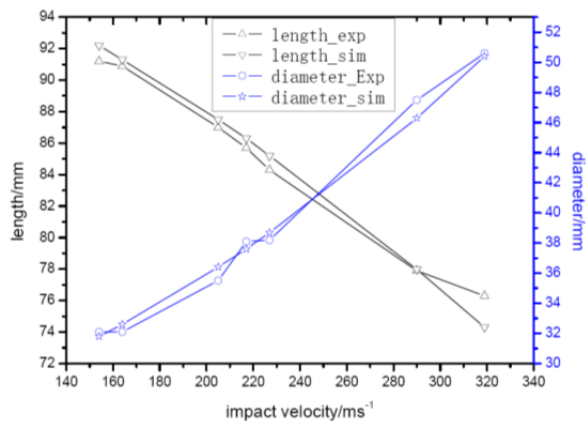


Fig. 9: Comparison of specimen final length and maximum diameter between simulation and experiment.

The loading history curves at three impact velocities from simulation were given in figure 10. All the curves have the similar characteristics. A high peak value was arose at the early stage of the impact process, and its amplitude is approximately proportional to the impact velocity; the loads then reduce to a lower level in 10 μ s and maintain at a platform, the amplitude of the plat increases with initial velocity slightly and varies at the range of 90kN to 150kN; then the impact loads decrease slowly to the end of collision after 80 μ s. The interaction duration between the specimen and target increases slightly with the impact velocity. The loading curves reflect the mechanical state of the specimen material at the process of impact as following: the material near the impact interface is almost in the state of plane strain during the initial stage, and the impact load is mainly the function of velocity; at the following stage, the loading platform reflects the stress characteristics of materials steady plastic deformation state.

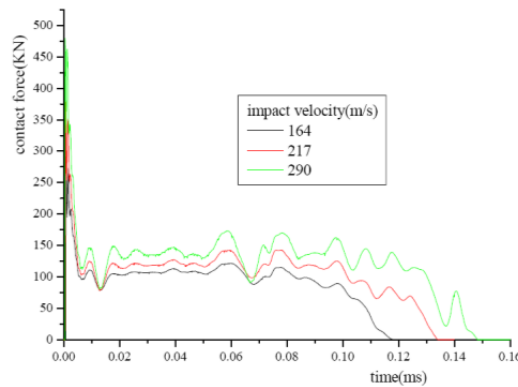


Fig. 10: The loading history curves at three impact velocities.

The specimen rigid-body velocity histories of several cases from the simulation were given in figure 5. The specimen bounced velocity is about 19m/s at the cases of impact velocity varies from 154m/s to 227m/s. While at the case of impact velocity of 319m/s, the bounced velocity is 12m/s. This is because in the condition of high speed impact, high temperature generated by large plastic deformation at the impact end of the specimen makes the material softening, which causes the bounced velocity decreases.

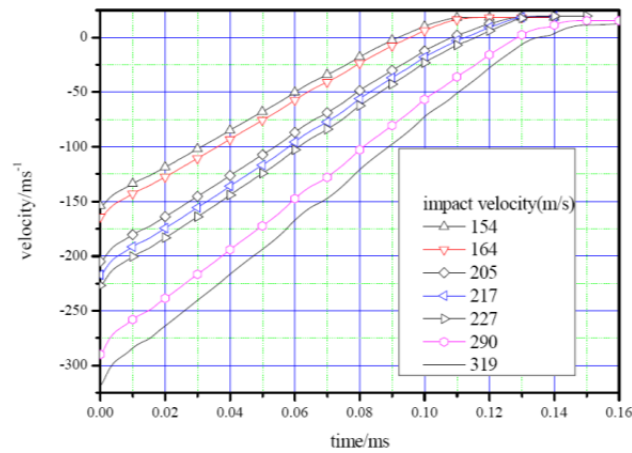


Fig. 11: Rigid-body velocity histories at several impact velocity cases.

Figure 12 and figure13 gives equivalent plastic strain histories and stress state triaxiality histories of three elements at the specimen impact end in the case of the initial impact velocity 217m/s, respectively. The three elements are located at impact end center of the specimen, edge and the middle point between the other two elements. From Figures, it can be seen that, at the initial stage of impact, all the elements are subjected to compressive loadings, and the strain of the edge element is growing faster than that of the central part; after the first stage, the strain growth at the edge becomes slow, and the strain growth at the central part maintains; finally, at the end of impact, the plastic strain at the central part is larger than that of the edge.

Figure 13 shows that, the stress state triaxiality of the element at the edge is negative in the first 5 μ s of the impact, it indicates that the stress state is compressive at that moment; after that, the triaxiality changes to be positive, it indicates that the stress state of the edge is tensile. While at the central part, the stress state triaxiality is negative at the whole impacting process; that is, the material is always subjected to compressive loading. Therefore, in consideration of the relationship of material failure strain and stress triaxiality, the material fracture may occur from the edge first even if the strain at the center part is much larger.

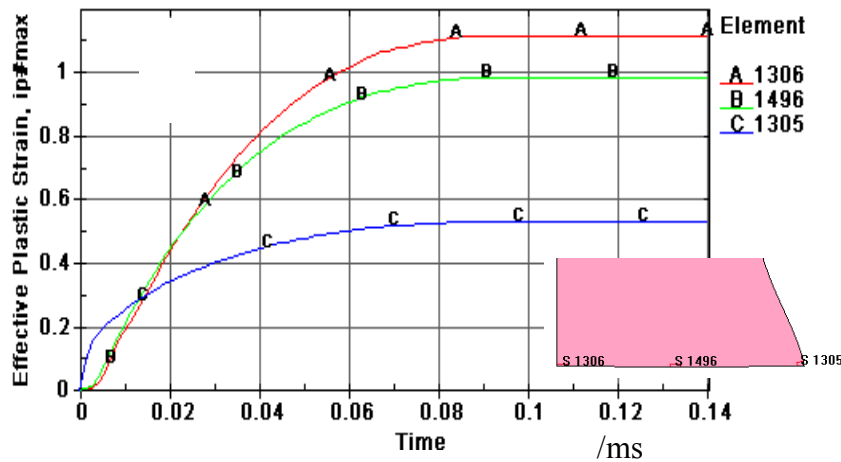


Fig. 12: Plastic strain histories of three elements at specimen impact end (217m/s).

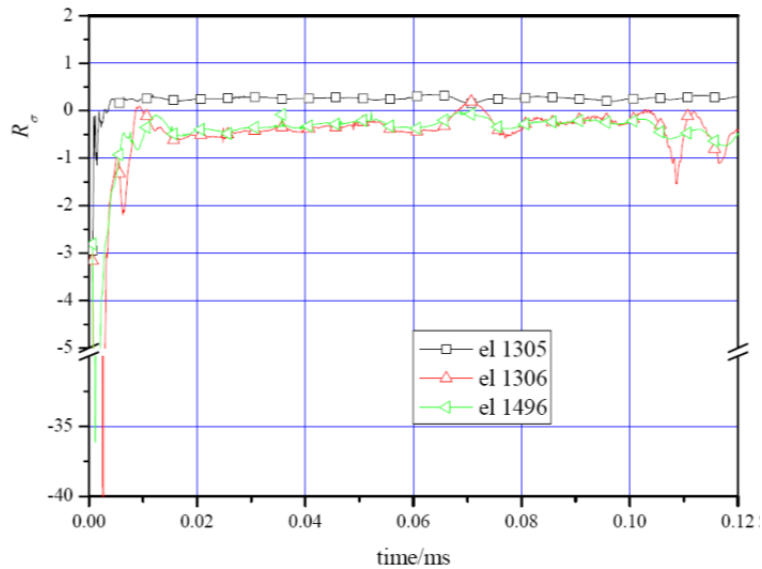


Fig. 13: Stress state triaxiality histories of three elements at specimen impact end (217m/s).

1.5 Numerical simulations on the specimen failure under Taylor impact

Although the experimental design of Taylor impact can be considered to be axisymmetric, but the failure of specimen is not symmetry. Thus simple axial-symmetric FEM modeling is unable to simulate the failure. 3D solid element was employed to model the specimen and target. The technique of element deletion is used to simulate the erosion of the specimen. When the accumulative damage of an element exceeds the critical value,

all the components of stress in the element are set to zero, the material fails, and the element is deleted in the subsequent calculation. To reduce the influence of element deletion on the structural impact, one minimizes the mesh size of the FEM, within the allowable computational time. In the simulation, the specimen element size is modeled as 0.45 mm*0.45 mm*1.25 mm, in which the longest edge is along the axial.

The specimen final deformation and damage distribution at the cases of impact velocity 217m/s, 290m/s, 319m/s and 350m/s are given in figure 14. In the case of 217m/s, the maximum damage is 0.6, and there is no failure in specimen, but the maximum damage appears at the edge of impact end; in the case of 290m/s, the edge of the impact end appears crack failure, which is consistent with the experimental observation; while the impact velocity increases to 319 m/s, the failure in the specimen is intensified, and the spiral shear failure in the specimen lateral face is observed. Various failure characteristics of Taylor impact experiments were obtained. Although there is some uncertainty, it appears that the parameters obtained can describe the fracture behavior of 45 steel under high speed deformation. When the impact velocity is further increased, at the failure appeared in the impact end, and the specimen head broken.

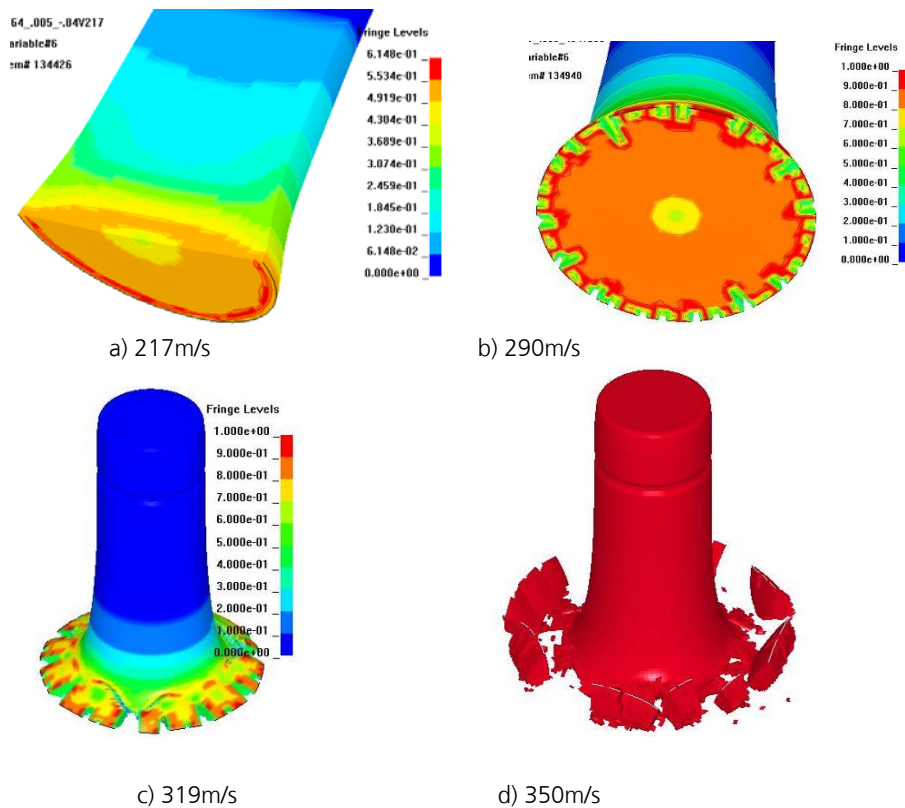


Fig. 14: The specimen deformation and damage with different impact velocities.

The deformation and failure process of 45 steel Taylor impact specimen at the case of impact velocity 310m/s is given in Figure 15. From the figure it can be seen that, at the time of 60 μ s After the impact, numerous element failure on the edge of the impact end, it began to form crack; with the specimen deformation further increases, more and more elements failure, which leads to the further development of the crack. Although initially there are a large number of cracks, but only part of the cracks grows; as the length of crack grows to a certain stage, at the time of 140 μ s, crack begins to bifurcation, and the cracks grow spirally.

The characteristics of the specimen damage and fracture can be described with stress state triaxiality histories. The failure strain of material is dominated by the stress state triaxiality, the fracture strains increase with stress triaxiality markedly. At the central part of the specimen, material always is subjected to compressive loading; and at the edge of specimen, materials is in the stress state of tensile. Thus, fail would occur at the specimen edge first.



Fig. 15: Deformation failure process of 45 steel Taylor impact specimen (310m/s).

1.6 Summary

The specimen deformation of Taylor impact with two-dimensional axisymmetric numerical simulation is consistent with experimental observation. The loading characteristics and the temperature rise were discussed among the simulation results. With analysis of stress state triaxiality histories, it is concluded that, although the strain at the center part is much larger than that at the edge, material failure may first occur from the edge.

The specimen failure under Taylor impact was simulated with 3D solid model. Various failure characteristics observed in the Taylor impact experiments were obtained.

1.7 References

- [1] Johnson GR, Cook WH. A constitutive model and data for metals subjected to large strains, high strain rates and high temperatures. 1983
- [2] Joseph C, Foster Jr, et al. The use of the Taylor test in exploring and validating the large-strain, high-strain-rate constitutive response of materials. Shock compression of condensed matter-2001, edited by Murnish MD, Thadhani NN and Horie Y, American Institute of Physics, 2002
- [3] Rohr L, Nahme H, Thoma K. A modified Taylor-test in combination with numerical simulations—a new approach for the determination of model parameters under dynamic loads. Journal De Physique IV France 2003, Vol.110, 513–518.
- [4] Johnson GR, Holmquist. Evaluation of cylinder-impact test data for constitutive model constants. J. Appl. Phys. Vol.64(1988), No.8, 15
- [5] Papirno RP, Mescall JF, Hanson AM. Beyond the Taylor test to fracture AMMRC-MS-80-4, 1980:367-385
- [6] Couque H. on the use of symmetric Taylor test to evaluate dynamic ductile compression fracture properties on metals. In: Proceedings of the 5th international conference on structures under shock and impact. 1998, Computational mechanics Inc, Billerica, MA, USA
- [7] Grady DE, Kipp ME. Fragmentation of solids under dynamic loading. In: Wierzbicki, T., Jones, N. (Eds.), Structural Failure. John Wiley & Sons, New York, 1989, pp. 1–40
- [8] Woodward RL, et al. failure mechanisms in impacting penetrators. Journal of materials science, Vol. 27, 1992
- [9] Stevens JB. Finite element analysis of adiabatic shear bands in impact and penetration problems. Master degree thesis, Virginia polytechnic institute and state university, 1996
- [10] Worswick MJ, Pick RJ. Void growth and coalescence during high-velocity impact. Mechanics of Materials 1995, Vol.19, 293–309
- [11] Johnson GR, Cook WH. A constitutive model and data for metals subjected to large strains, high strain rates and high temperatures. Proceedings of the 7th International Symposium on Ballistics[C], The Hague, Netherlands, 1983, pp. 541–547.

- [12] Johnson GR, Cook WH. Fracture characteristics of three metals subjected to various strains, strain rates, temperatures, and pressures. *Engrg. Fracture Mech.* 21 (1), 1985, 31-48

Concrete under biaxial impact loading

M. Curbach, M. Quast

Dresden University of Technology, Faculty of Civil Engineering, Institut für Massivbau,
01062 Dresden, Germany

1.1 Introduction

A large amount of our built environment is made of reinforced concrete. Among these, there are also many buildings belonging to the so-called critical infrastructure, like power plants, buildings of public water supply, government buildings, airports or hospitals. All these structures are endangered by natural and anthropogenic accidental actions. To guarantee a reliable protection of these important structures we have to know the behaviour of concrete and reinforced concrete under high dynamic loading.

At the beginning of this article, the properties of concrete under dynamic and multi-axial load will be described. Subsequently, the historical development of dynamic tension and compression tests for concrete in the HOPKINSON-pressure-bars will be presented. In this article, a novel, a biaxial Split-HOPKINSON-Pressure-Bar (SHPB) as well as the first test results regarding the multi-axial dynamic compressive strength of concrete will be shown.

1.2 Concrete properties

Concrete has been used as a building material for more than 2000 years. Its advantages are its durability and the easy production. Today's concretes have compressive strengths of 20 to 60 N/mm². Yet, high-performance concretes with considerably higher compressive strengths can also be composed. However, the tensile strength of normal concretes is only 10 % of the compressive strength. This is the reason why concrete is used in combination with reinforcement steel in most cases. Thus, the reinforcing steel transfers a significant amount of the tensile forces. Another possibility to make concrete more resistant to tensile loads is to

add steel or synthetic fibres to produce so-called fibre reinforced concrete.

Normally, concrete is made of cement, which functions as a binder, aggregate such as sand or gravel, and water. Depending on the intended application of the concrete, further chemicals can be added. Due to its components, concrete is considered as a highly inhomogeneous material at the meso-level. Thus, the cement matrix, the aggregate, the composite zone between both, and the pores have to be distinguished. Two phenomena which were usually analysed separately in the past are considered in combination in the following part. These phenomena are the change of the concrete strengths due to the loading velocity and due to multi-axial loading.

1.2.1 Concrete under impact

Similar to many other materials, the material behaviour of concrete depends on loading velocity. Due to its inhomogeneity, concrete reacts very sensitively and with different effects on its tensile and compressive strength to increasing strain rates (see fig. 3 and fig. 4).

Reasons for this increase in strength have been traced back to a number of phenomena. One first explanation was provided by KÖRMELING et al. [1] who suggested that in case of dynamic stress more aggregate particles were cut through than under static loads. GÖDDE [2] depicted this phenomenon in a numerical model for a normal concrete. He showed that a crack which starts in the concrete matrix and then hits an aggregate particle changes its direction and continues around the aggregate particle in case of slow loading velocity. Under high loading velocity, the crack does not change its direction anymore due to the inertia of the crack edges but continues through the aggregate particle.

In 1987, CURBACH [3] made an important contribution to the explanation of concrete's dynamic material behaviour: he was able to prove a number of reasons for the increase in strength (Fig.3). He showed that there is an upper limit to the velocity of the crack increase at approximately 500 m/s. This is significantly lower than the theoretical velocity of a Rayleigh wave at approximately 2300 m/s. Accordingly, the development of a crack does not occur suddenly, but the crack needs some time to cover the cross

section entirely. In this period, the concrete is still capable of sustaining load and the stress at the inside may still increase.

Because of the fast spread of the load in the concrete cross section, stress peaks at the pores' edges or at the transitions from matrix to aggregate particle cannot develop as easily. As a result, the stress distribution is evened out over the cross section. In addition CURBACH discovered a memory-effect in the concrete. This means that the strength does not only depend on the loading velocity at one specific moment but also the loading history. Thus, a concrete which has been loaded rapidly at the beginning followed by a slow load increase or even unchanging load may still achieve higher strengths than under an unchangingly slow load increase.

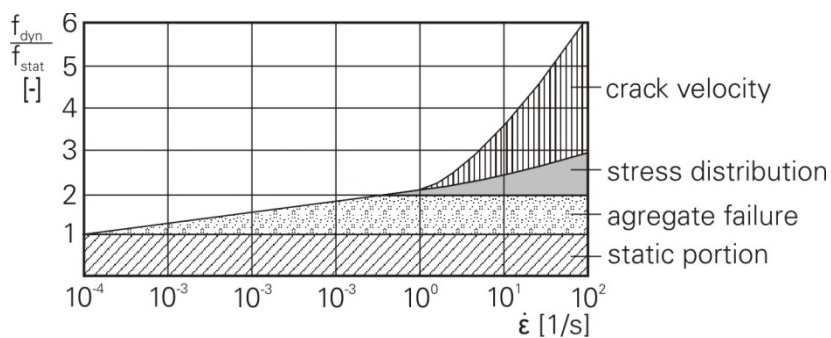


Fig. 1: Reasons for strength increase according to CURBACH [3].

The effect of free pore water in concrete is another significant factor to the strength increase due to dynamic loading. REINHARDT et al. [4] were the first to show in a series of tension tests that no increase in strength could be observed for oven-dried specimens up to a strain rate of 1.25 s^{-1} . In contrast, the samples which had been stored in a wet place tripled their strength compared to the static tests. These observations were also confirmed by ERZAR et al. [5] in spallation and direct tension tests. The basis for this phenomenon is the so-called STEFAN-effect. According to this, water between two parallel surfaces counters the movement of these surfaces with capillary action. This means that in case of the concrete, the pore water has a stabilizing effect on the pore and, thus, helps to even out the stress distribution.

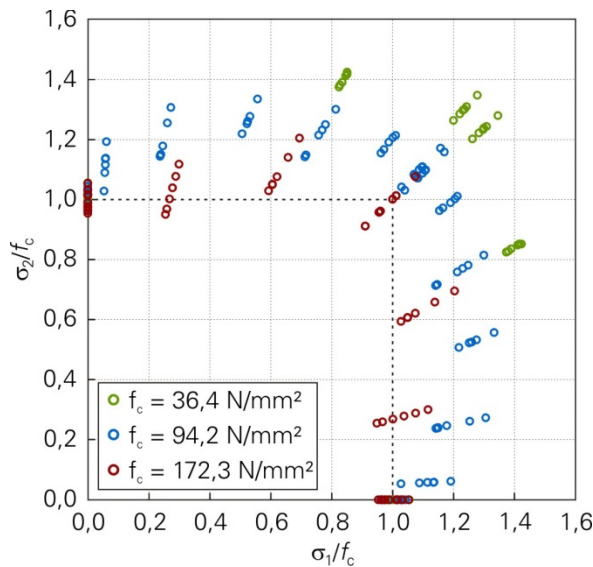


Fig. 2: Test values for biaxial compressive strength of various concretes in relation to their uniaxial compressive strength f_c according to SPECK [10].

Furthermore, REINHARDT [6] described Multiple Cracking in dynamically loaded samples in 1982 for the first time. Due to a multiple crack formation in the course of the sample's failure, more fracture energy can be absorbed under dynamic load. This is a result of the circumstance that the cracks which are not directly responsible for the failure still enlarge the fracture face.

1.2.2 Concrete under multi-axial loading

The second phenomenon which is presented here is already known, too. It is the fact that multi-axial loading has an influence on the material strength of concrete. The supporting lateral pressure resulting from biaxial compressive loading leads to an about up to 40 % higher compressive strength in the concrete (fig. 2). Numerous static tests have been conducted for these load cases. Comprehensive surveys of the different tests regarding multi-axial material behaviour of concrete can be found for example in the CEB-Bulletin 156 [7], ROGGE [8] or CURBACH et al. [9]

1.3 Hopkinson-bar experiments on concrete

Only three years after HOPKINSON [11] had presented his test setup for the examination of wave propagation, ABRAMS 1917 [12] proved that the

compressive strength of concrete increases with an increase in the loading velocity. First results of tests on concrete samples in a HOPKINSON-Bar were already published in 1923 by LANDON und QUINNEY [13]. They used a long concrete cylinder as spallation bar installed as a ballistic pendulum and applied the load by igniting gun cotton at one end through a compressive stress wave, which turned into a tensile wave at the free end and split the concrete specimen to numerous parts. However, they did not examine the changes in the concrete's tensile strength. Instead, they assumed that the concrete tensile strength remained unchanged and drew conclusions regarding the wave propagation within the bar based on the fractures of the concrete cylinder. However, another application of the HOPKINSON-Bar-technique to concrete took some more decades to come.

More intensive research into the behaviour of concrete in connection with velocity began in the 1960s and 70s [14, 15, 16, 17]. At this time, a drop weight, a pendulum or pneumatic or hydraulic installations were usually applied as load equipment.

1.3.1 Hopkinson-bar tension tests on concrete

The HOPKINSON-Technology [11] was used in particular to examine the dynamic properties of metals as well as brittle materials such as ceramics and rocks. Only in 1966, GOLDSMITH et al. [18] were the first to publish results concerning the material properties of concrete and cement mortar under exposure to shock loads. These had been determined with the help of the HOPKINSON-technique. To this end, a long thin concrete cylinder ($\varnothing \frac{3}{4}$ in. x 24 in.) was hung up as a ballistic pendulum and directly shot at with a steel cylinder ($\varnothing \frac{1}{2}$ in.). Two different impact velocities were chosen: 3300 in./s and 1650 in./s (84 m/s und 42 m /s). The main aim of this test was to investigate the applicability of this test setup to determine the material properties of concrete. Strains were measured at the surface of the samples in five different measuring points along the bar's length with the help of strain gauges. The results showed that while the impulse did not disperse to a significant degree down the length of the bar, its amplitude decreased. However, it has to be taken into account that the respective position of each strain gauge on the inhomogeneous material and the measuring grid length had a definitive influence on the measurements. This is due to the circumstance that a strain gauge which has been applied close to an air pore or an aggregate particle, leads to a

wrong measurement result. The strain gauges on the more homogeneous mortar samples produced much more balanced results. This shows that the applied measuring arrangement were not suitable for an inhomogeneous material such as concrete. Apart from this, the YOUNG's Modulus for the concrete was determined under high loading velocities which showed that it increased to a significant degree compared to the static YOUNG's modulus. The concrete's tensile strength could not be determined since the applied impulse was not big enough to destroy the concrete under this one-time loading. Just a slightly increased number of micro-cracks could be observed after the loading had been applied.

Approximately at the same time, similar tests were conducted at the Ohio River Division Laboratories of the US Army by MELLINGER, BIRKIMER und LINDEMANN [19], [20]. Basically the same test setup as the one used by GOLDSMITH et al. served to examine the dynamic tensile strength of various concretes under impact. The cylindrical specimen had a cross section of 2 in. and a length of 10.25 in. They were dynamically and statically tested at an age of 7 to 10 days. At a strain rate of 23 s^{-1} , the tensile strength was determined to have increased by a Dynamic Increase Factor $\text{DIF} > 5.1$ in the case of plane concrete (without fibres), a DIF of 3.8–5.0 for concrete with nylon fibres and a DIF of 4.9 for steel fibre reinforced concrete. The test results were validated by determining the strain in the specimen in two independent ways: In one case, the strain of the transmitted pressure wave and the reflected tension wave was measured directly on the sample's surface. In the second case, a disc was loosely attached to the free end of the sample. This disc is removed from the sample by the impact loading. The measured particle velocity of the disc then serves to calculate the strain in the sample. Both measurement methods were considered feasible for the dynamic examination of rock and concrete.

In about 1980, the first Split-HOPKINSON-Tension-Bar (SHTB) for testing concretes under dynamic tension loading was developed in the Stevin Laboratories at TU Delft. In the following years, numerous series of tests were conducted in this test setup and the results were published by KÖRMELING et al. [1]. The setup consists of a vertical Split-HOPKINSON-Bar whose lower transmission bar is the incident bar. The concrete specimen is fixed between the incident bar (lower bar) and the transmission bar (upper bar). The pulse is induced by a drop weight which slides down the incident bar and hits a collar attached to the end of the bar. In doing so,

a tensile wave is induced into the incident bar. Through variation of drop weight and drop height, different load pulses can be created. Thus, strain rates between $0.05\text{--}25\text{ s}^{-1}$ can be attained. The induced tensile wave is propagated toward the specimen. There it is partly reflected and partly transmitted into the transmission bar. In the course of this, the specimen is torn apart.

In 1980, initially pure tension tests were conducted on approximately 150 short notched concrete cylinders ($\text{Ø } 74\text{ mm} \times 100\text{ mm}$) of different concrete qualities [1]. These resulted in a logarithmic correlation between dynamic and static strength which depended on concrete quality, temperature and moisture. Later, the test setup was modified so that further influences such as repeated dynamic loading could be taken into consideration. To this end, 89 tests were carried out under repeated tensile shock loads [21]. For this purpose, a pneumatic lifting system was added to the test setup. This system can lift and drop the drop weight from a defined height up to 16 times per minute. The drop weight was installed in such a way that the maximum induced stress was lower than the expected dynamic tensile strength. The loading was repeated until the test sample failed and the number of loadings was counted. Later, the influence of low temperatures on the dynamic tensile strength of concrete was tested [22]. To this end, tests were conducted at 20°C and -170°C and the results were compared. The samples were cooled in a freezer which operated on liquid nitrogen. However, the low temperatures had only very limited influence on the dynamic tensile strength. With the aim to also test the influence of lateral pressure, a cross beam with a hydraulic press was added level with the test sample. The hydraulic press served to apply a compression force of up to 400 kN through force transmission brushes to prismatic samples ($50 \times 50 \times 100\text{ mm}$) [23]. The results resembled the failure curve for the static case. However, the factor was increased by two due to the shock loads.

Ross et al. [24] carried out a number of different test programmes in a SHPB. Amongst others, direct tension tests were conducted. To this end, the enlarged end of the SHPB's transmission bar was impacted with a hollow striker. This induced a tensile wave in the incident bar. Subsequently, the wave ran through the sample and destroyed it. Additionally, splitting tensile tests (Brazilian-Disc-Tests) were carried out on flat concrete cylinders ($\text{Ø } 51\text{ mm}$, height: 21 or 51 mm) which were

installed in a right angle to the bar axis. Thus, a compression wave was selectively applied at the edge of the sample. As a result, tensile stress developed vertically to the pressure load which then brought about splitting tensile failure. A comparison of the results showed that splitting tensile tests led to similar increases in strength as direct tensile tests. The different lengths of the splitting tensile specimen showed that the specimen's size has a decisive influence on the results as was also the case for static tests. In the same year, TEDESCO et al. [25] published a numerical validation of the dynamic splitting tensile tests in the SHPB.

In 1993, BACHMANN [26] presented various tensile test results from concrete in a modified Split-HOPKINSON-Bar. In this setup, the front part of the incident bar is pre-stressed and separated from the remainder of the incident bar by rigid clamping. By suddenly releasing the clamping, a rapidly increasing tensile wave is created. Thus, the sample is directly subjected to tension. BACHMANN dynamically applied pressure to the samples up to various load levels and then kept the load at a certain level. By these means, he was able to prove the load history's influence on the dynamic concrete tensile strength.

In 1994, ALBERTINI and MONTAGNANI [27] presented a HOPKINSON-Bar-Bundle. With the aim of testing bigger concrete objects such as cubes with an edge length of 20 cm, incident and transmission bars with cross sections of 20 x 20 cm were installed in an existing test setup with pre-stressing technology. In the direction of the sample, the transmission bars' cross sections were separated into 25 single prisms and each prism was equipped with a strain gauge. Thus, the stress distribution within the bars, and accordingly also in the sample, could be recorded in the course of time and in different places of the cross section.

Already in 1995, a HOPKINSON-Bar was constructed in the Laboratory of Physics and Mechanics of Materials (Metz) which would make it possible to conduct dynamic tension tests on brittle materials based on the principle of spallation. First valid results for concrete with strain rates between 20 and 120 s⁻¹ were published by KLEPACZKO und BRARA [29]. In addition, they presented an exhaustive and feasible analysis of the recorded data including the correction of the geometrical dispersion.

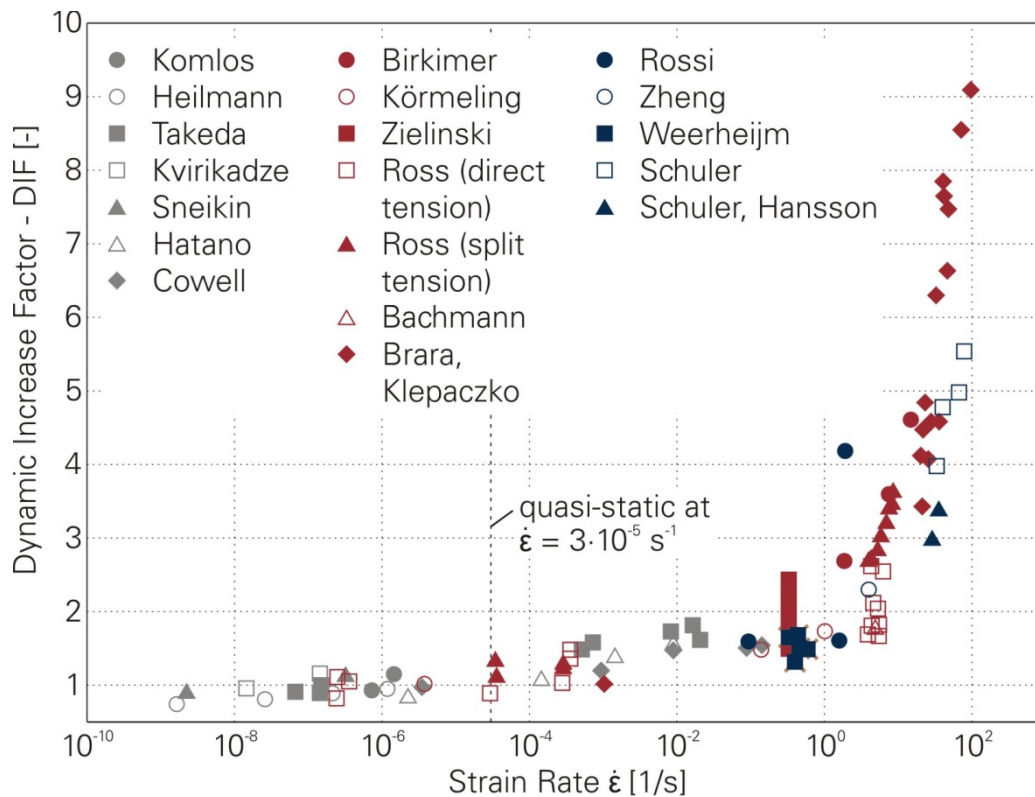


Fig. 3: Increase of concrete's tensile strength according to Bischoff [28].

A number of further tests regarding the dynamic tensile strength of various concretes has been carried out in recent years. Examples are ROSSI et al. [30], ZHENG [31], WEERHEIJM [32], und SCHULER [33]. Fig. 3 offers an overview of test results for the dynamic tensile strength of various concretes from the last 100 years. The most important milestones in the dynamic testing of concrete based on the HOPKINSON-technique have been highlighted in red. Blue marks further results for concretes in HOPKINSON-Bars and the grey symbols stand for early results which were produced in other test setups.

1.3.2 Hopkinson-bar compression tests on concrete

In the 1970s, concrete under dynamic loading was tested in Sweden various times to examine pile foundations. The required pressure loads were applied through, amongst other things, detonations, drop weights or pendulums. In 1977, BHARGAVA and RHENSTRÖM [34] published an article in which they presented for the first time a modified version of a

SHPB for compression tests on concrete in connection with some results. The test setup consisted of three vertical aluminium bars of 2 m length and a cross section of 100 mm which have been positioned on top of each other. These are an incident bar and a transmission bar. The sample is positioned between these two bars. In addition there is a momentum bar, which serves to absorb the pulse propagated through the transmission bar. The test setup is fixed in a steel frame which is 18 m high. This is necessary to provide a fall height between 1 and 10 m for a falling aluminium cylinder of 250 mm above the incident bar. Four types of concrete in the shape of cylinders (\varnothing 100 mm x 200 mm) were tested. Strength increases between 1.46 and 1.67 were determined. However, the loading velocity has not been mentioned. Based on the given load data, a strain rate of approximately 20 s^{-1} can be estimated. Further results from the same test setup were published in 1979 by FAGERLUND und LARSSON [35]. The tested specimens were in the shape of cylinders. They were 100 mm long and had a cross section of 100 mm. They were tested at a dynamic strain rate of 30 s^{-1} compared to a static strain rate of $5 \cdot 10^{-5} \text{ s}^{-1}$. The result was a strength increase by a factor of 1.42 for a concrete with a static compressive strength of 46 N/mm^2 .

In 1984, TANG et al. [36] presented tests on mortar samples in a small SHPB with a cross section of only 19 mm at the University of Florida. The results showed a linear relation between the concrete's strength and the strain rate up to 800 s^{-1} . With the aim to test samples with bigger aggregates, a new SHPB with a bar cross section of 76 mm was developed in 1984. In 1985, MALVERN et al. [37] reported the first results from the new SHPB. They achieved DIFs of 1.74 to 2.20 in a strain rate range of 60 to 110 s^{-1} .

Later, the SHPB at the University of Florida was used for the first dynamic compression tests on confined concrete. To this end, the sample was fitted into an empty steel or aluminium cylinder with a wall thickness of approximately 30 mm. This confinement hindered the sample's lateral pressure and, thus, leads to a multi-axial stress condition in the concrete. In 1990, GONG and MALVERN [38] published the results from this test configuration. The tests were conducted on normal concrete with a compressive strength of 31 N/mm^2 . In the case of uniaxial loading without confinement, the concrete displayed a dynamic compressive strength between 87 and 120 n/mm^2 depending on impact velocity. With confinement, the samples did not fail under dynamic loading. As a result,

the remaining load-bearing capacity after the impact was determined as a criterion for comparability. After the samples had been loaded with lower impact velocities of about 7.5 m/s, the remaining load-bearing capacity, 36.5 N/mm², was slightly higher than the static compressive strength. The authors traced this back to the compression of the sample. Subsequently, the remaining load-bearing capacity clearly decreased with increasing impact velocity. This loss of strength was explained with an increased degree of damage because of higher impact energy.

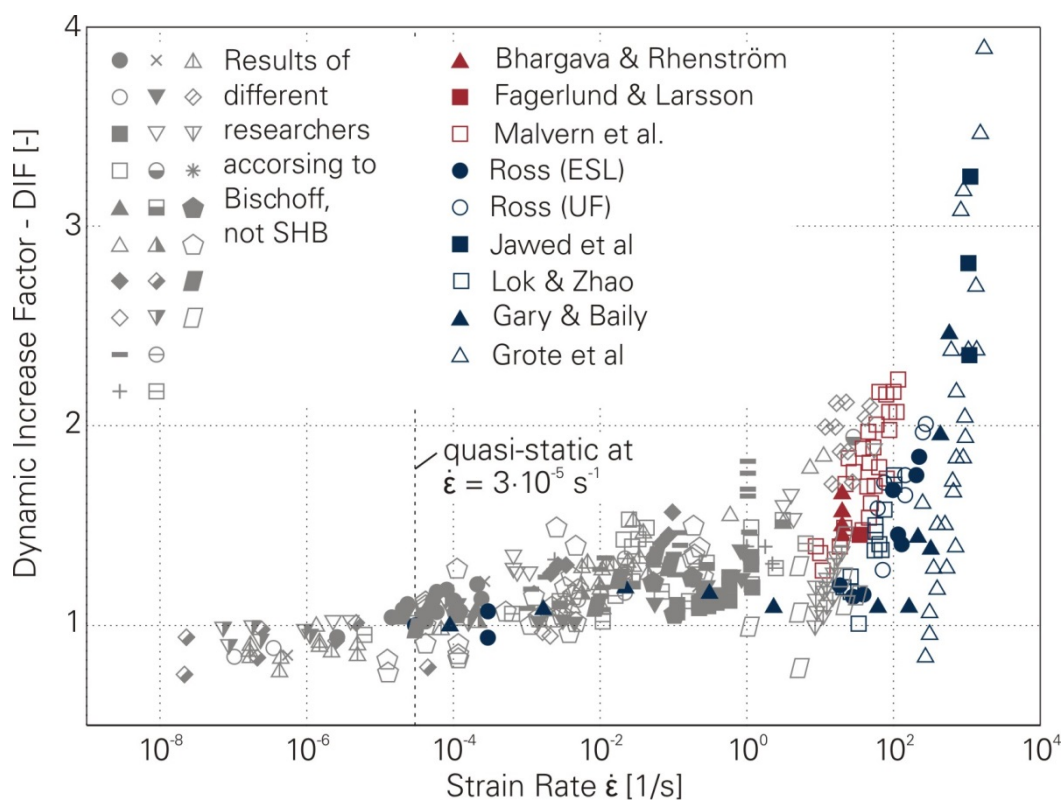


Fig. 4: Increase of the compressive strength of concrete according to Bischoff [28].

In the following years, numerous other tests were conducted in HOPKINSON-Bars regarding the dynamic compressive strength of various concretes with and without confinement. Some studies of note are GROTE et al. [39], LOK and ZHAO [40] and GARY and BAILY [41]. Figure 4 gives an overview of the results of the dynamic concrete compressive strength. The colours have been chosen according to the colours in Figure 3. Apart from this, the HOPKINSON-Bar-technique was also used for bond tests between concrete and reinforcing steel. However, these tests will not be considered in this paper.

1.4 The biaxial split-Hopkinson-bar

After two effects which lead to an increase in concrete strength have been explained in chapter 2, the question whether and how these two phenomena may interfere with each other in case of multi-axial dynamic loading remain to be answered. With the aim of researching the behaviour of concrete under such loads, a biaxial SHPB was developed at the Institute of Concrete Structures at TU Dresden (Fig. 5). This test setup makes it possible to put weight on concrete samples with a strain rate of 30–200 s⁻¹ from two sides at the same time.

1.4.1 The test setup

The basic structure of the test setup are two, orthogonally arranged SHPBs which meet in the middle. In this place, a sample is installed between each incident und transmission bar. In addition, some special requirements have to be met for tests on concrete samples in contrast to tests on homogeneous materials. First of all, the SHPB's transmission bars have to have a relatively wide cross section. Since concrete is a very heterogeneous material, the sample's cross section has to be at least three times as wide as the maximum aggregate size [42]. Accordingly, from the maximum aggregate size of 16 mm ensues a minimum size of 48 mm for the sample. The width chosen for the cross section is 50 mm. In addition, the bar's length has to be at least 20 times as long as the bar's cross section is wide to minimize disturbances to the longitudinal wave propagation [43]. In this specific case, a bar length of 3.00 m was chosen. This corresponds to the relation $l_{\text{bar}}/d_{\text{bar}} = 60$. Third, the best possible wave transition between the transmission bars and the sample has to be guaranteed. That is why the impedance of the bar's material has to be as similar as possible to the concrete's impedance. A comparison of the mechanical impedances of concrete ($I_{\text{concrete}} \approx 7.7 \dots 10.4 \text{ MNs/m}^3$), steel ($I_{\text{steel}} \approx 40.5 \text{ MNs/m}^3$), which is usually used for transmission bars, and aluminium ($I_{\text{aluminium}} \approx 13.7 \text{ MNs/m}^3$) shows clearly that the impedance of aluminium is much lower than the impedance of steel and, accordingly, much closer to the properties of concrete. To guarantee the highest possible resilience, aluminium EN AW 7075 was chosen.



Fig. 5: Biaxial SHPB at TU Dresden.

The striker bars are bronze cylinders ($\varnothing 49.5$ mm) of different lengths. The striker bars are accelerated to the required velocity with the help of two gas pressure guns (one per load direction). The air pressure is measured in the storage tank of the gas gun and serves as a control parameter to control the desired terminal velocity of the striker bar. Apart from this, a photoelectric sensor is installed at the end of the barrel. It serves to trigger the beginning of the measurements as well as to determine the actual velocity of the striker bar at the moment before it hits the incident bar. Figure 5 shows the entire test setup in OTTO-MOHR-Laboratory at TU Dresden.

The release of both gas guns and their synchronisation is controlled by PC, microcontroller and solenoid valve. In spite of this exact control, there is still a variation of almost one millisecond in the time lag between the two directions. Accordingly, just 2 % of the conducted tests are within the time lag of less than $20 \mu\text{s}$ which is the objective to be met so that a dynamic biaxial stress state can develop in the sample. However, tests with a greater time lag between both directions can also be evaluated. This topic will be dealt with in chapter 5. An optimization of the test setup is constantly worked at.

1.4.2 The specimen

As already mentioned, the samples have to have a minimum size of 48 mm. The samples used in uniaxial tests are in the shape of cylinders

(Ø 50 mm x 80 mm). For biaxial test, i. e. when the samples shall be loaded from two directions the concrete specimens have to have the shape of cubes. Since the bars must not collide, the sample has to jut out over the bars' width. The incident bar has to be able to move freely for at least one entire wave pulse. In the course of this, the bars' end moves by 2-3 mm toward the test sample. An overhang of 5 mm was chosen on all sides so that there is sufficient reserve. Consequently, the concrete cube has an edge length of 60 mm. Further movement of the incident bars is prevented by special clamps, which are screwed onto the bars.

This naturally raises the question of the influence of the sample's geometry – cube versus cylinder – and the stress distribution at the edges of the sample which are not directly loaded by the bars. To this end, uniaxial test series with cylinder and cube shaped concrete samples were conducted. These showed that the respective time curves of the pressure pulse measured in the transmission bar were very similar in shape for both sample geometries. However, they differ in their amount. Due to its wider cross section, the same maximum stress lead to a greater force transmission in the cube. Furthermore, the stress ratio in the transmission bar clearly deviated from the relation of the samples' cross sections. This leads to the assumption that the stress did not evenly distribute over the entire cross section of the cube. With the aim to confirm this assumption, another test series with aluminium samples with different geometries was conducted. In this context, the strain on the surface of the samples was also measured. The evaluation of these tests yielded the result that the ratio of the maximum strain inside the cube to the strain measured in the transmission bar is 0.6825. This is more or less the same result as in the test on concrete samples. Based on this knowledge about the ratio, the maximum strain in the cube samples can also be exactly determined now.

1.5 Experimental results

All in all, 194 tests on concrete samples of the strength class C40/50 ($f_{c,stat} = 40.9 \text{ N/mm}^2$) were conducted in the biaxial SHPB. All tests were carried out with a bronze striker bar of 120 mm length and an impact velocity of 22 m/s. This results in a pressure pulse with an amplitude of 200 N/mm^2 , a rise time of 25-30 μs and a pulse length of approximately 200 μs . As a basis for comparison, cylindrical samples were tested in a uniaxial SHPB with various strain rates. After the test setup had been

installed, a calibration phase of more than 1000 tests followed to synchronize both load directions of the test setup. Only then did the tests on concrete specimen start.

Based on the first evaluation, the tests could be divided into three groups. (1) Due to the rise time of 25-30 μs , the waves from both load directions have to hit the sample within approximately 20 μs . The two wave rises superimpose in the sample and lead to an increased strain rate in both directions. Accordingly, a biaxial dynamic load situation can be assumed for tests with a maximum time lag of 20 μs . (2): In case of a time lag of more than 20 and less than 400 μs , a measurable strain was still transmitted into the transmission bar from the direction which introduced the load later. (3): in case of time differences of more than 400 μs , the strain introduced from the second direction can be neglected since the test sample has already been more or less destroyed uniaxially.

Based on the crack pattern, these effects could be confirmed with a high speed camera (Fig.6). In tests with greater time lags, the cracks develop successively and parallel to the load axes so that they eventually form a checkerboard pattern. In case of biaxial tests, diagonal cracks develop from the middle of one pressure area to the respective neighbouring pressure areas in the shape of rhombi.

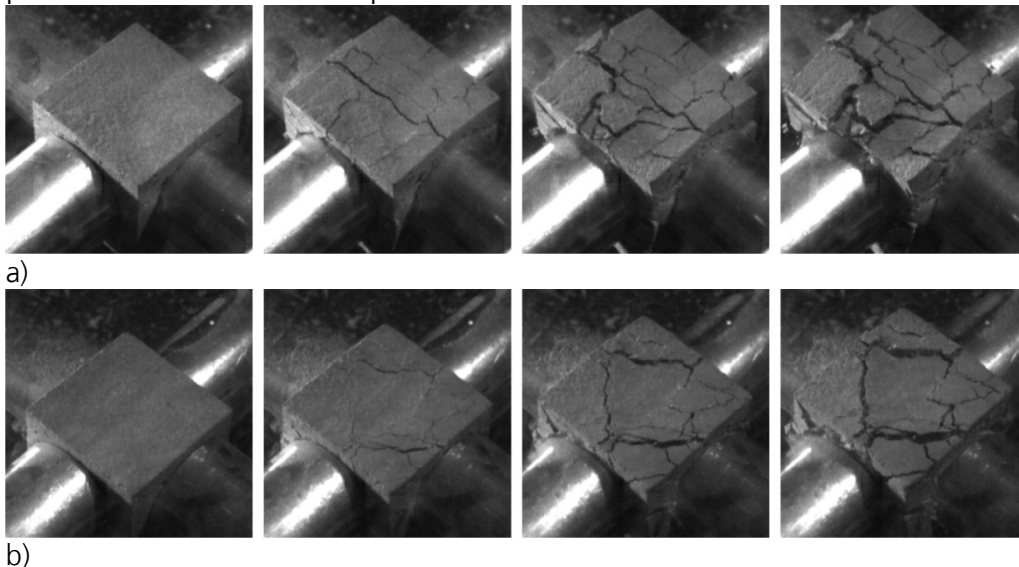


Fig. 6: Crack pattern of test sample after a) a test with delay and b) a biaxial test.

Fig.7 shows which strengths have been achieved in the axis which was loaded first depending on the strain rate. These have been categorized

according to the time lag between both load directions. Each average value has been depicted as a square.

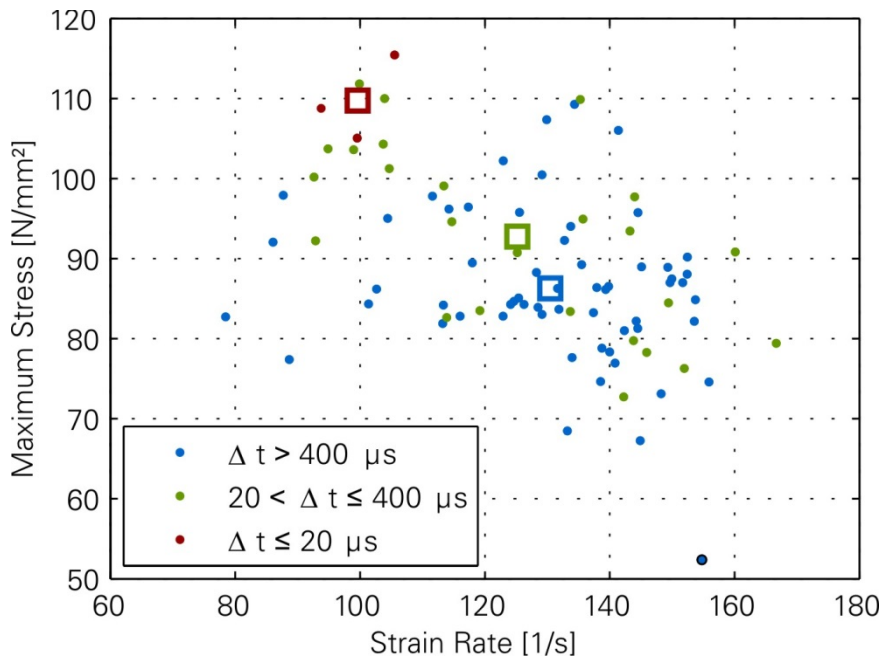


Fig. 7: Dynamic concrete strength depending on the strain rate.

The average values for strength and strain rate have been listed in Tab.1. A clear influence of the biaxial tests on the strength can be seen. It is about 20-30 % higher than for tests with a greater time lag. However, the influence of the average time lag of 20 to 400 μs compared to tests with a greater time lag is insignificant. Even if the average values differ by 4 N/mm^2 , the scatter areas (Fig. 7) of both test categories are very similar.

Tab. 1: Average values of the dynamic concrete strengths depending on the time difference between both directions.

Δt [μs]	$\dot{\epsilon}$ [1/s]	$f_{c,dyn}$ [N/mm^2]
< 20	99,6	109,8
20–400	125,2	91,7
>400	132,1	87,5

Another analysis showed that the strain ratio between axis 1 (the axis where the load pulse hits earlier) and axis 2 (the axis where the load pulse hits later) lies between 1:1 and 1:0.7. In this case, the biaxial dynamic strength is clearly higher than in uniaxial dynamic tests. The tests with a time lag of 20-50 μs resulted in similar stress ratios as the biaxial tests. However, the strengths were lower and much closer to uniaxial dynamic strengths. All other tests whose load time lag was higher than 50 μs have a stress ratio of 1:0 to 1:0.25. Fig. 8 shows the concrete strengths for uniaxial dynamic concrete compressive strength. The points marked in the diagram indicate the maximum equivalent stress from both axes ($\sigma_{\text{equivalent}} = (\sigma_1^2 + \sigma_2^2)^{0,5}$), this is the greatest distance to the origin. These results suggest that the strength increasing effects of the dynamic loading and the multi-axial pressure loads superimpose each other at least in part and lead to a still greater biaxial dynamic concrete compressive strength.

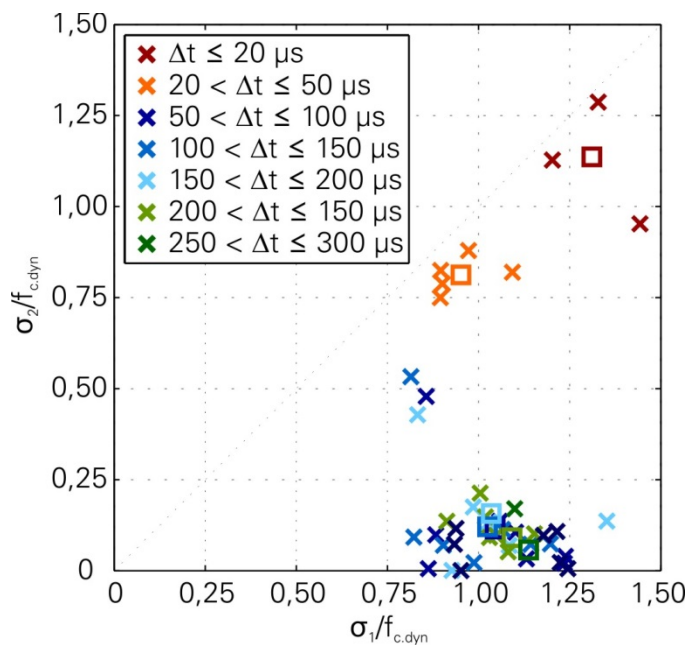


Fig. 8: Biaxial strength values in relation to the uniaxial dynamic strength.

Fig. 9 shows the time curves of the equivalent stress ($\sigma_{\text{equivalent}}$) in the test sample for tests with varying time lags between the two loading directions. Based on these, a direct superimposition of both load pulses and, accordingly, a clearly increased equivalent stress at the beginning of the load transmission (Fig. 9a) can be seen for biaxial tests. In the case of the tests with a time difference of 20 to 50 μs , the later stress peak only superimposes the descending part of the first load pulse's curve. This

results in a slightly higher equivalent stress directly after the first load pulse (Fig. 9b). In all other tests – i.e. in tests with a time lag of more than $50 \mu\text{s}$ –, the load pulse from the earlier axis propagates through the test sample first with an average maximum strain of 90 N/mm^2 . This test result is qualitatively and quantitatively the same as the results from uniaxial tests with the same strain rate (Fig.9c-f). This means that the test sample is already damaged to the point of failure by the first pulse. Due to the limited crack velocity and the material's inertia, the test sample has not been entirely fragmented and, as a result, can still absorb some delayed load in the second load direction.

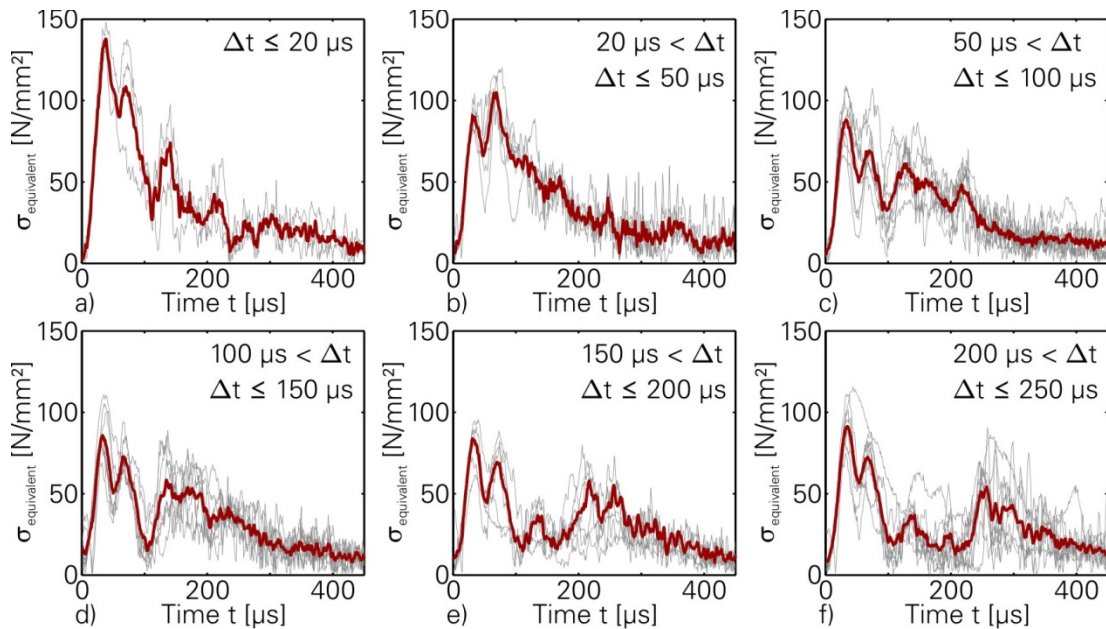


Fig. 9: Curve of the equivalent stress ($\sigma_{\text{equivalent}}$) in the test sample, depending on the time difference to the second load pulse.

This means that the concrete still has some lateral strength for a short time after the dynamic load bearing capacity has been exceeded once. This is reflected in the second, lower peak of the equivalent stress. This peak is increasingly late and decreases with an increasing time lag between the load pulses. This shows that in the course of time, the sample is increasingly fragmented by the damage in the first direction and, thus, can absorb increasingly less stress in the second direction. Accordingly, the lateral strength decreases with time after the first damage has occurred. For the chosen sample size of 60 mm , a lateral strength can be observed up to $400 \mu\text{s}$ after the first damage occurred.

However, this phenomenon cannot necessarily be transferred to other test sample geometries or even entire components. Such a conclusion requires further extensive research.

1.6 Conclusions

In this paper, a new SHPB setup was described and first tests on concrete of the strength class C40/50 were presented. The test results show a clear increase of the biaxial dynamic strength compared to the uniaxial dynamic case. This allows the conclusion that the effects of multi-axial loading and dynamic loading in the concrete superimpose each other at least in part. Furthermore, the course of the equivalent stress shows that the concrete sample displays a recordable lateral strength even up to 400 μs after the first damage. Thus, a phenomenon which has not been described so far and which cannot be recorded with the usual multi-axial tests with static lateral pressure or confinement orthogonal to the dynamic load direction could be observed.

In future tests the behaviour of other types of concrete will be determined and compared with each other. In addition, static biaxial tests and dynamic tests with static lateral strength will be conducted.

1.7 Acknowledgements

The presented project was funded by the German Federal Ministry of Economic Affairs and Energy (BMWi, project no. 1501377A) on basis of a decision by the German Bundestag.

1.8 References

- [7] Körmeling, H. A., Zielinski, A. J., Reinhardt, H. W.: Experiments on Concrete under Single and Repeated Uniaxial Tensile Loading. Delft University of Technology, Stevin Report No. 5-80-3, 1980.
- [8] Gödde, P.: Rechnerische Untersuchungen zur Betonzugfestigkeit unter hoher Belastungsgeschwindigkeit. Universität Dortmund, Diss. 1986.

- [9] Curbach, M.: Festigkeitssteigerung von Beton bei hohen Belastungsgeschwindigkeiten. Universität Fridericiana zu Karlsruhe, Diss. 1987.
- [10] Reinhardt, H. W., Rossi, P., van Mier, J. M. G.: *Joint Investigation of Concrete at High Rates of Loading*. Materials and Structures, 23, 213-216, 1990.
- [11] Erzar, B., Forquin, P., Pontiroli, C., Buzaud, E.: *Influence of Aggregate Size and Free Water on the Dynamic Behaviour of Concrete Subjected to Impact Loading*. EPJ Web of Conferences, 6(39007), 1-8, 2010.
- [12] Reinhardt, H. W.: Concrete under Impact Loading, Tensile Strength and Bond. Heron 27, 1982.
- [13] CEB Bulletin 156: Concrete under Multiaxial States of Stress: Constitutive Equations for Practical Design. June, 1983.
- [14] Rogge, A.: Materialverhalten von Beton unter mehrachsiger Beanspruchung. Technische Universität München, Diss. 2001.
- [15] Curbach, M., Hampel, T., Scheerer, S., Speck, K.: Experimentelle Analyse des Tragverhaltens von Hochleistungsbeton unter mehraxialer Beanspruchung. Beuth-Verlag, Berlin, 2011.
- [16] Speck, K.: Beton unter mehraxialer Beanspruchung. Technische Universität Dresden, Diss. 2008.
- [17] Hopkinson, B.: A Method of Measuring the Pressure Produced in the Detonation of High Explosives or by the Impact of Bullets. Philosophical Transactions of the Royal Society Mathematical, Physical & Engineering Sciences, 213, 437-456, 1914.
- [18] Abrams, D. A.: *Effect of Rate of Application of Load on the Compressive Strength of Concrete*. American Society for Testing and Materials: Proceedings of the 20th Annual Meeting, 17, 364-377, 1917.
- [19] Landon, J. W., Quinney, H.: *Experiments with the Hopkinson Pressure Bar*. Proceedings of the Royal Society of London. Series A, Containing Papers of a Mathematical and Physical Character, 103, 622-643, 1923.
- [20] Hatano, T., Tsutsumi, H.: *Dynamical Compression Deformation and Failure of Concrete under Earthquake Load*. Proceedings of the Second World Conference on Earthquake Engineering, 1963-1978, 1960.
- [21] Takeda, J., Tachikawa, H.: *The Mechanical Properties of Several Kinds of Concrete at Compressive, Tensile, and Flexural Tests in*

- High Rates of Loading*. Transactions of the Architectural Institute of Japan, 77, 1-6, 1962.
- [22] Cowell, W. L.: Dynamic Properties of Plain Portland Cement Concrete. U. S. Naval Civil Engineering Laboratory, Port Hueneme, California, Technical Report No. R 447, 1966.
- [23] Komlos, K.: *Investigation of Rheological Properties of Concrete in Uniaxial Tension*. Materialprüfung, 12, 300-304, 1970.
- [24] Goldsmith, W., Polivka, M., Yang, T.: Dynamic Behavior of Concrete, Experimental Mechanics, 6(2), 65-79, 1966.
- [25] Mellinger, F. M., Birkimer, D. L.: Measurement of Stress and Strain on Cylindrical Test Specimens of Rocks and Concrete under Impact Loading. U.S. Army Corps of Engineers, Ohio River Division Laboratories, 1966.
- [26] Birkimer, D. L., Lindemann, R.: *Dynamic Tensile Strength of Concrete Materials*. American Concrete Institute Journal, 68, 47-49, 1971.
- [27] Zielinski, A. J., Reinhard, H. W., Körmeling, H. A.: *Experiments on Concrete under Repeated Uniaxial Impact Tensile Loading*. Materials and Structures, 14(81), 163-169, 1981.
- [28] Körmeling, H. A.: Impact Tensile Strength of Steel Fibre Concrete. Delft University of Technology, Stevin Report No. 5-84-8, 1984.
- [29] Zielinski, A. J.: Concrete under Biaxial Loading: Static Compression-Impact Tension. Delft University of Technology, Stevin Report No. 5-85-1, 1985.
- [30] Ross, A., Thompson, P. Y., Tedesco, J. W.: *Split-Hopkinson Pressure-Bar Tests on Concrete and Mortar in Tension and Compression*. ACI Materials Journal, 86(5), 475-481, 1989.
- [31] Tedesco, J., Ross, C. A., Brunai, R. M.: *Numerical Analysis of Dynamic Split Cylinder Tests*. Computers & Structures, 32, 609-624, 1989.
- [32] Bachmann, H.: Die Massenträgheit in einem Pseudo-Stoffgesetz für Beton bei schneller Zugbeanspruchung. Universität Fridericiana zu Karlsruhe (TH), Diss., 1993.
- [33] Albertini, C., Montagnani, M.: *Study of the True Tensile Stress-Strain Diagram of Plain Concrete with Real Size Aggregate; Need for and Design of a Large Hopkinson Bar Bundle*. Journal de Physique IV, 4(C8), 113-118, 1994.
- [34] Bischoff, P. H.: Compressive Response of Concrete to Hard Impact. University of London Imperial College, Diss. 1988.

- [35] Klepaczko, J. R., Brara, A.: *An Experimental Method for Dynamic Tensile Testing of Concrete by Spalling*. International Journal of Impact Engineering, 25, 387-409, 2001.
- [36] Rossi, P., van Mier, J. G. M., Boulay, C., le Maou, F.: *The Dynamic Behaviour of Concrete: Influence of Free Water*. Materials and Structures, 25, 509-514, 1992.
- [37] Zheng, S., Beton bei variierender Dehngeschwindigkeit untersucht mit einer neuen modifizierten Split-Hopkinson-Bar-Technik. Universität Fridericiana zu Karlsruhe (TH), Diss. 1996.
- [38] Weerheijm, J.: Concrete under Impact Tensile Loading and Lateral Compression. Delft University of Technology, Diss. 1992.
- [39] Schuler, H., Experimentelle und numerische Untersuchungen zur Schädigung von stoßbeanspruchtem Beton. Fraunhofer-Institut für Kurzzeitdynamik, Ernst-Mach-Institut EMI, Freiburg, Diss. 2004.
- [40] Bhargava, J., Rehnström, A.: *Dynamic Strength of Polymer Modified and Fiber-Reinforced Concretes*. Cement and Concrete Research, 7, 199-208, 1977.
- [41] Fagerlund, G., Larsson, B.: Betongs slaghallfasthet (Impact Strength of Concrete). Cement-och Betong Institutet (CBI) Stockholm, FO 4:79, 1979.
- [42] Tang, T., Malvern, L. E., Jenkins, D. A.: *Dynamic Compressive Testing of Concrete and Mortar*. Engineering Mechanics in Civil Engineering, Borese, A.P., Chong, K. P. (eds), New York, 1984.
- [43] Malvern, L. E., Jenkins, D. A., Tang, T., Ross, C. A.: *Dynamic Compressive Strength of Cementitious Materials*. Proceedings of 2nd Symposium on the Interaction of Non-Nuclear Munitions with Structures, 1994-199, Florida, 1985.
- [44] Gong, J. C., Malvern, L. E.: *Passively Confined Tests of Axial Dynamic Compressive Strength of Concrete*. Experimental Mechanics, 30, 55-59, 1990.
- [45] Grote, D. L., Park, S. W., Zhou, M.: *Dynamic Behavior of Concrete at High Strain Rates and Pressures: I. Experimental Characterization*. International Journal of Impact Engineering, 25(9), 869-886, 2001.
- [46] Lok, T. S., Zhao, P. J.: *Impact Response of Steel Fiber-Reinforced Concrete Using a Split Hopkinson Pressure Bar*. Journal of Materials in Civil Engineering, 16, 54-59, 2004.

- [47] Gary, G., Bailly, P.: *Behaviour of Quasi-Brittle Material at High Strain Rate. Experiment and Modelling*. European Journal of Mechanics - A/Solids, 17, 403-420, 1998.
- [48] DIN 1048-2: Prüfverfahren für Beton - Teil 2: Festbeton in Bauwerken und Bauteilen. Juni, 1991.
- [49] Kolsky, H.: *An Investigation of the Mechanical Properties of Materials at Very High Rates of Loading*. Proceedings of the Physical Society. Section B, 62, 676-700, 1949.

The joint time-frequency analysis of wave propagation in SHPB by means of wavelet transform

Roman Gieleta

Department of Mechanics and Applied Computer Science
Faculty of Mechanical Engineering
Military University of Technology
2 Gen. Sylwester Kaliski Str., 00-908 Warsaw, Poland
E-mail: rgieleta@wat.edu.pl

1.1 Introduction

The split Hopkinson pressure bar technique is widely used in material dynamic testing and allows dynamic loading of a specimen sandwiched between incident and transmitter bars. In this technique it is considered that there is no wave dispersion, as a result, the normal forces at both specimen ends can be derived from the incident, reflected and transmitted waves. However, in real bar materials such as metals and, in particular, polymers the wave dispersion effect is caused by the spread of phase velocities over the signal spectrum.

In the conventional SHPB apparatus, data processing is carried out with a few idealized assumptions that bars are linearly elastic (constant distribution of the stresses over the cross section of the bar) and that a 1D elastic wave theory is valid and can be used for data processing. However, the actual stress waves in bars are still two dimensional due to free movement in the radial direction (Poisson's effects).

The problem of wave dispersion in SHPB bars is still extensively discussed in science literature. The first investigators were Pochhammer (1876) and Chree (1889). They independently solved the equation of motion for a sinusoidal wave propagating in an infinitely long cylinder. Their solution reveals an important fact for data processing that the propagation velocity of a stress wave decreases with decreasing wavelength (high-frequency stress wave travels slower than a wave which has a lower frequency). Different models of the stress wave propagation in elastic and

viscoelastic bars were developed and employed for dispersion and attenuation correction in SHPB data processing. However, it is out of scope of the paper to describe and evaluate all those methods, therefore, the Reader is encouraged to study references [1-30].

The main aim of the paper is to draw the Reader attention to the wavelet transform as to a very efficient tool in the wave propagation analysis.

1.2 Why wavelet transform?

Wavelet transform signal analysis uses wavelike functions known as *wavelets* [31]. Wavelets are used to transform the signal under investigation (from the incident or transmitted bar) into another representation which presents the signal in a more useful 3D (time-frequency distribution of the magnitude) transform form. The wavelet transform using the Gabor wavelet (as an example) effectively decomposes transient signal from strain gauges. For this transform, arrival times of waves are indicated by the peaks of the time-frequency distribution and allows the dispersion relation of the group velocity to be identified for a wide range of frequencies.

1.3 The fundamentals of the wavelet transform

The wavelet transform of signal $x(t)$ is defined as [31-37]:

$$WT(a, b) = w(a) \int_{-\infty}^{\infty} x(t) \psi^* \left(\frac{t - b}{a} \right) dt$$

where:

$WT(a, b)$ - transformation coefficient for scale "a" and translation "b",

a - scale parameter (dilation),

b - translation value,

w(a) - weighting function,

x(t) - analyzed signal,

(t) - elementary wavelet function (mother wavelet),

$\psi^*(t)$ - complex conjugate of function (t),

t - time.

Each transformation coefficient $WT(a, b)$ is normalized by weighting function $w(a)$, which provides the condition, that internal energy of each wavelet function $\psi_{a,b}(t)$ is independent of the scale parameter "a".

Wavelet transform can be considered as a linear transformation which decomposes given signal $x(t)$ into elementary functions $\psi_{a,b}(t)$, by scaling (dilation) and translation, whereas dilation "a" is responsible for frequency-segmentation and translation "b" is related to time-decomposition.

In order to be classified as a wavelet, function (t) must satisfy the following criteria:

1. A wavelet function $\psi(t)$ must have finite energy:

$$E = \int_{-\infty}^{\infty} |\psi(t)|^2 dt < \infty$$

2. The wavelet function $\psi(t)$ must have a zero mean (no zero frequency component):

$$C_g = \int_0^{\infty} \frac{|\hat{\psi}(f)|^2}{f} df < \infty$$

where:

C_g - admissibility constant,

$\hat{\psi}(f)$ - the Fourier transform of $\psi(t)$.

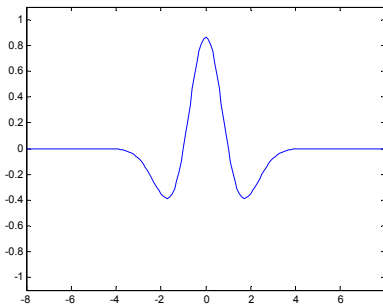
3. The Fourier transform of (t) must be real as well as vanish for negative frequencies.

The cases of well-known wavelets commonly used in practise are presented in Tab. 1 and Fig. 1.

Tab. 1: Wavelet functions and definitions.

Wavelet function	Definition
Mexican hat	$\psi(t) = \frac{2}{\sqrt[4]{\pi}\sqrt{3}}(1 - t^2)e^{-\frac{t^2}{2}}$
Morlet (complex)	$\psi(t) = Ce^{-i\omega_0 t} \left(e^{-\frac{t^2}{2}} - \sqrt{2}e^{-\frac{\omega_0^2}{4}}e^{-t^2} \right)$
Haar	$\psi(t) = \begin{cases} 1 & 0 \leq t < \frac{1}{2} \\ -1 & \frac{1}{2} \leq t < 1 \\ 0 & \text{otherwise} \end{cases}$
Daubechies (Daub4)	Scaling coefficients for Daub4 0.48296291 0.83651630 0.22414386 -0.12940952 Wavelet coefficients for Daub4 -0.12940952 -0.22414386 0.83651630 -0.48296291

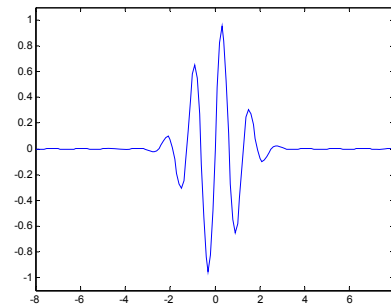
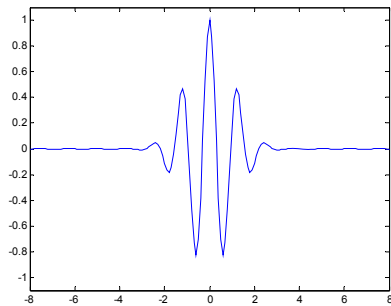
a) Mexican hat



b) Morlet

real part

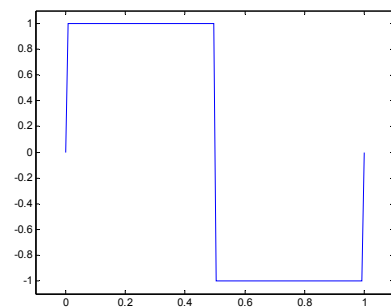
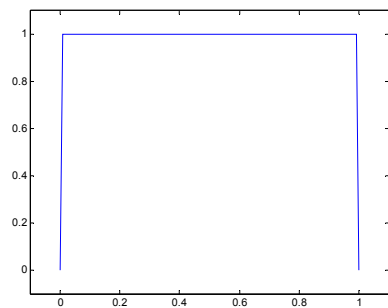
imaginary part



c) Haar

scaling function

wavelet function



d) Daub4

scaling function

wavelet function

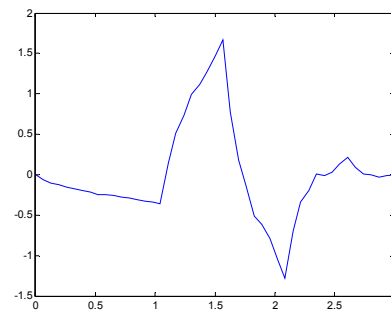
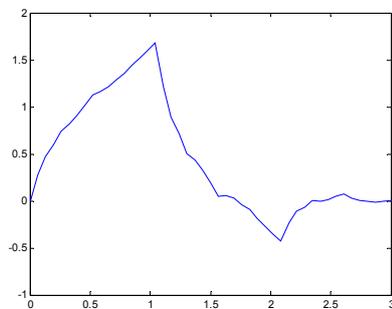


Fig. 1: Examples of wavelets, a) Mexican hat, b) Morlet (complex), c) Haar, d) Daubechies (Daub4).

1.4 Wavelet transform versus Fourier transform

A wavelet transform demonstrates a significant advantage over the other transforms commonly used in engineering applications. A very popular and widely used Fourier transform, contrary to wavelet transforms, does not provide local information about analyzed signal $x(t)$ owing to the infinite character of the trigonometric functions which are utilized in this transform. This is crucial for non-stationary (transient) signals analyzed in Split Hopkinson Pressure Bar apparatus.

As an example of how the wavelet transform works, let us consider the signals defined by taking 4096 samples of the following functions:

a) sum of three sinusoids:

$$x_1(t) = 7.5 \sin(2\pi 5t) + 2.5 \sin(2\pi 12t) + 0.8 \sin(2\pi 20t)$$

b) three sinusoids arranged in serial:

$$x_2(t) = 7.5 \sin(2\pi 5t) (t < 0.8) + 2.5 \sin(2\pi 12t) (t \geq 0.8 \ \& \ t < 1.6) \\ + 0.8 \sin(2\pi 20t) (t \geq 1.6)$$

These signals as well as their Fourier and wavelet transforms are plotted in Fig. 2. Taking into account the results of the numerical tests, it is easy to draw conclusion that Fourier transform demonstrates some important disadvantages. Spectrograms Figure 2b) and 2e) include information on frequencies in signals but it is impossible to recognize their interrelations. However, they also reveal Fourier transform errors connected with different lengths of particular sinusoids.

On the other hand, the results obtained from the wavelet transform (Mexican hat) called scalograms, Figure 2c) and 2f) are much easier to interpret and emphasize some of the features contained in the signal as well.

An advantage of the wavelet transform is a possibility to determine its coefficients $WT(a, b)$ for each value of the scale parameter "a" (frequency), which means that for a given scale value, the elementary wavelet function $\psi_{a,b}(t)$ is translated in the whole domain interval of the analyzed signal and reveals its local features.

Another general characteristic of the wavelet transforms is that the calculation of the coefficients from the signal can be carried out efficiently, most of them require the same number of operations as in the case of the fast Fourier transform [32].

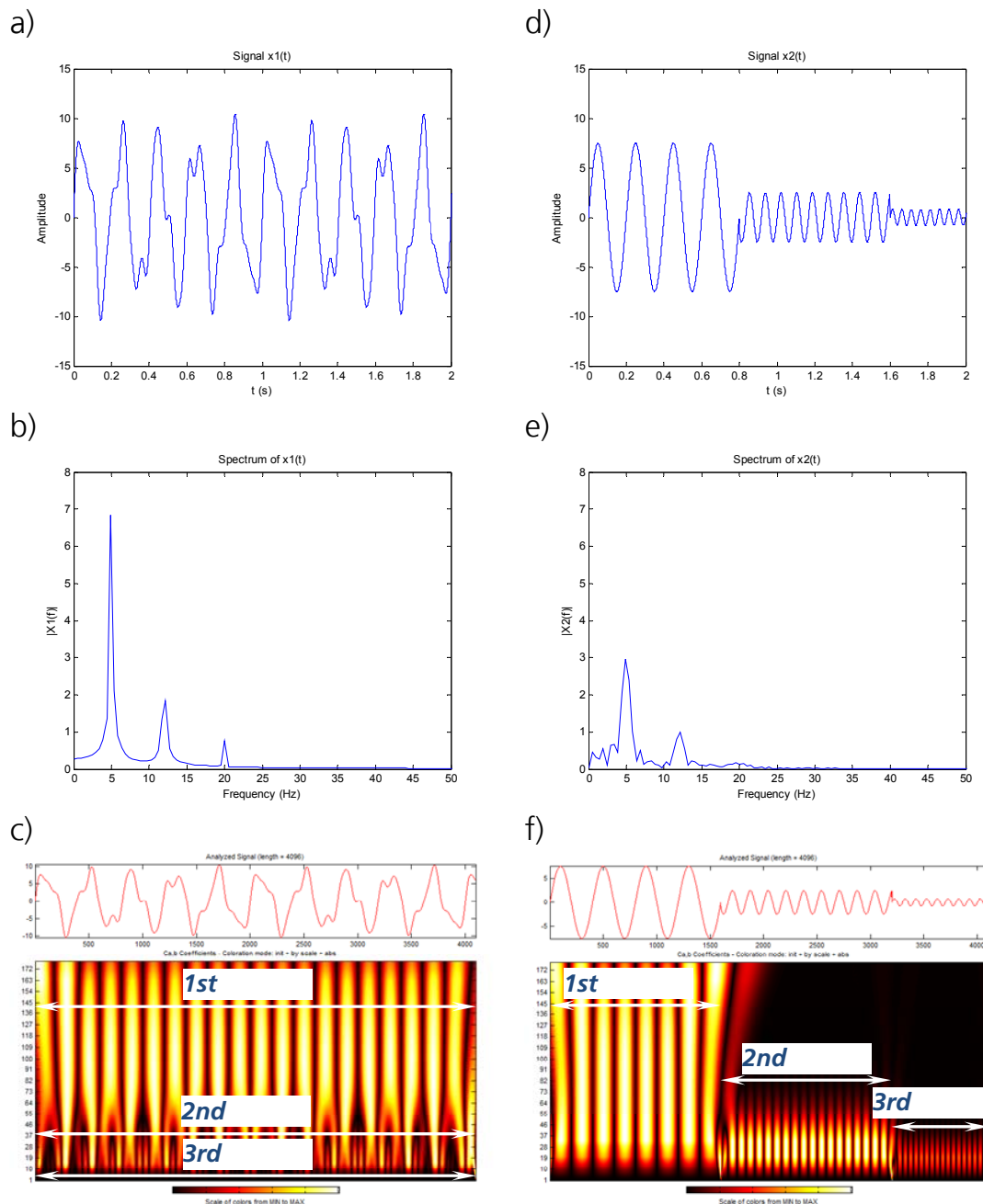


Fig. 2: Test signals and their Fourier and wavelet transforms.

1.5 Experimental setup and tests

Experimental measurements of waves were performed on the conventional SHPB apparatus (Fig. 3) designed and assembled by the Author. The apparatus consists of a gas gun, incident and transmission bars, (made of different materials, both 2000 mm long), an energy absorption element, a data acquisition system and a control system. The striker (made of different materials) is launched using highly compressed gas and impacts the incident bar. This generates an elastic or viscoelastic wave which travels through the incident bar. Waves in the incident bar are sensed by EA-06-060LZ-120 strain gauge which is placed in the middle of the bar.

In order to measure pressure bar signals, a strain gauge connected in a quarter bridge configuration is used. The signal from the strain gauge (from the Wheatstone bridge) was conditioned with a transient amplifier LTT 500 (LTT Labortechnik Tasler GmbH, Germany) and recorded with a computer and high-speed A/D computer board NI USB-6366 (National Instruments, USA). The main components of the SHPB apparatus are presented in Fig. 3. In the described apparatus, the amplifier and the A/D computer board with 1MHz frequency response what allows for accurately recording the transient signals from the strain gauge. In the set-up, the signals are recorded digitally with a 0.5 μ s sampling step.



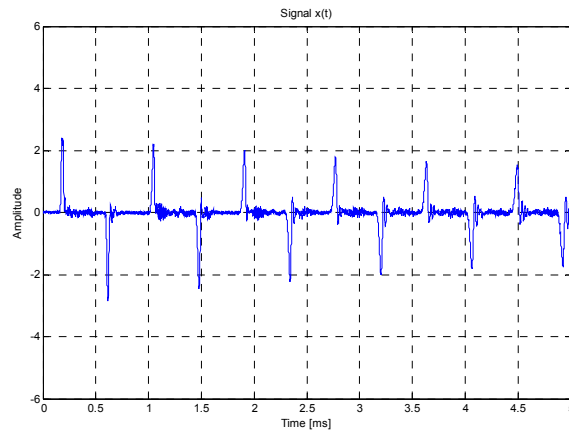
Fig. 3: Split Hopkinson Pressure Bar apparatus with data acquisition and control systems.

For the purpose of the paper, the experimental measurements of the impulses were carried out. As a result, signals from the strain gauges placed on the incident bar were obtained (Fig. 4). In order to investigate elastic and viscoelastic waves, bars made of maraging steel V720, polymethacrylate (PMMA) and polycarbonate (PC) were taken into

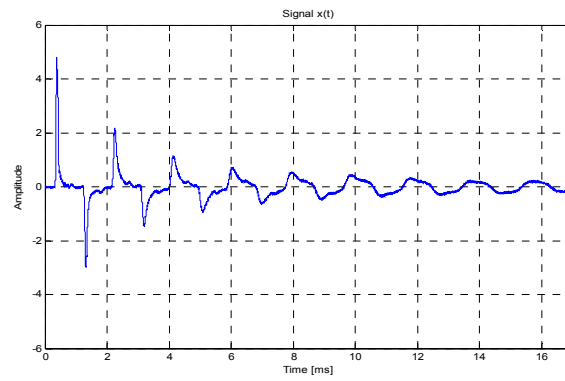
consideration. The strikers were made of the same material as bars and were 50 mm long.

The recorded signals unveil a different level of attenuation and dispersion for tested materials. It can be clearly observed that, from measurement point of view, the bar made of PMMA is not the best choice owing to relatively high attenuation.

a)



b)



c)

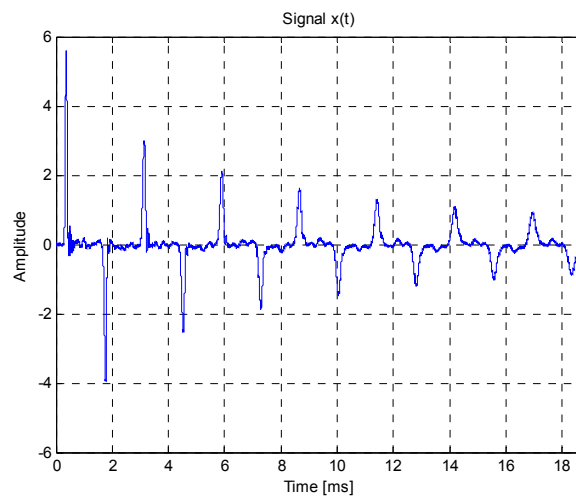


Fig. 4: Signals obtained from experimental tests a) maraging steel, b) polymethacrylate (PMMA), c) polycarbonate PC.

1.6 Wave dispersion in elastic and viscoelastic bars

In order to obtain a quantitative measure of dispersion and attenuation in the bars, the wavelet transform was used. The analyses of signals were carried out only for two impulses to shorten the calculation time and Mexican hat was implemented as a wavelet function. The representative plot of time-frequency analysis (TFA) with a wavelet transform for PMMA bar is shown in Fig. 5. The plot confirms that wavelet transform coefficients make it possible to analyse the signal simultaneously in a time and frequency domain. Impulses contained in the signals are easily recognizable as separate areas with colours directly proportional to the amplitude of each frequency. It can be easily observed that the magnitude of each frequency is decreasing significantly during propagation. It can be also noticed that some of the frequencies are disappearing after a few reflections.

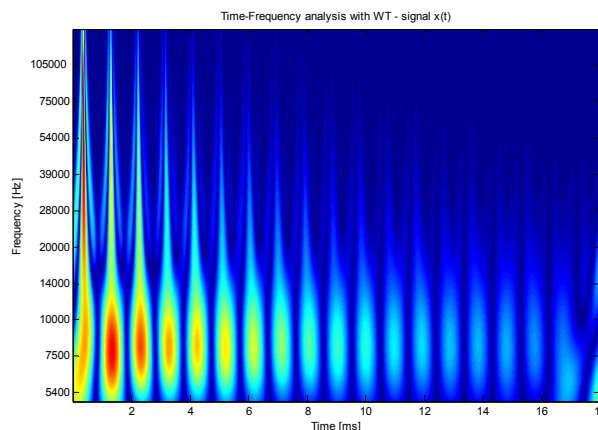


Fig. 5: Wavelet transform coefficients for PMMA (signal Fig. 4b).

Wavelet transform coefficients calculated for each material were processed to obtain local maxima lines (ridges) which are directly connected with peaks of each frequency contained in the analysed signal. Group velocity for each frequency was calculated from the formulae:

$$C_g(f) = \frac{\Delta L}{\tau_g(f) - t_0}$$

where:

$C_g(f)$ – the group velocity of the wave at frequency f ,

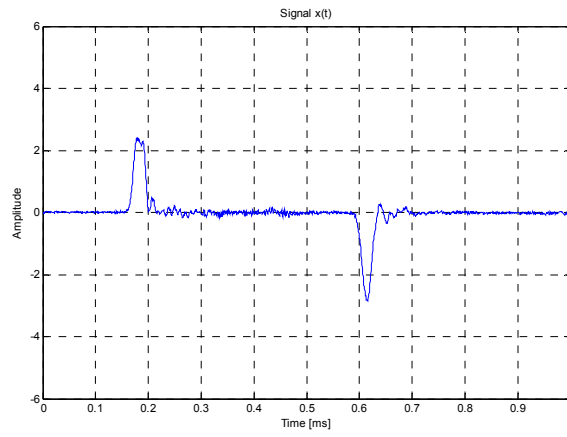
ΔL – distance (2000 mm),

$\tau_g(f)$ – the group delay of the wave at frequency f ,

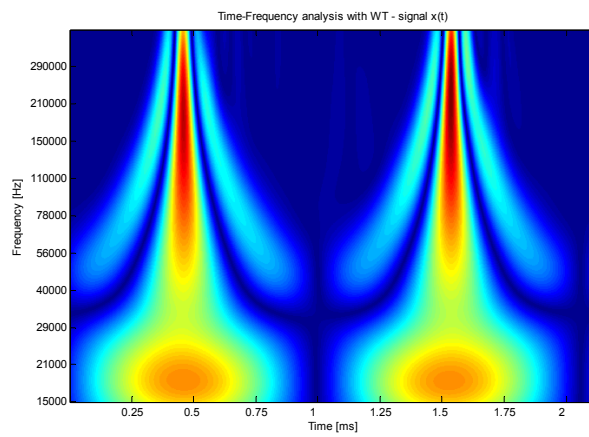
t_0 – time (arbitrarily fixed – first impulse).

The results of calculations and WT coefficients processing are presented in Figs. 6 to 8. Group velocity dispersion curves for three bar materials are shown in Fig. 9.

a)



b)



c)

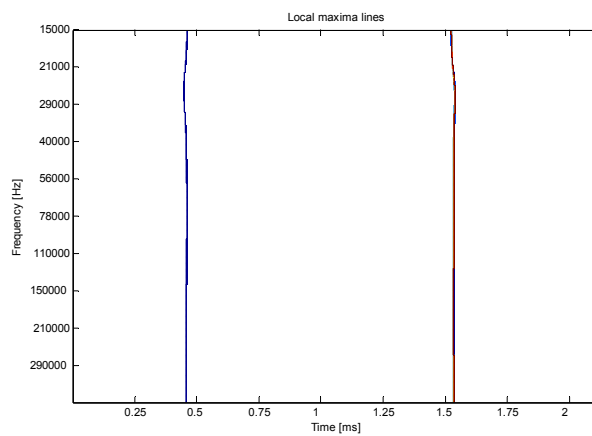


Fig. 6: Processing of recorded signal for maraging steel a) signal, b) WT coefficients, c) local maxima lines.

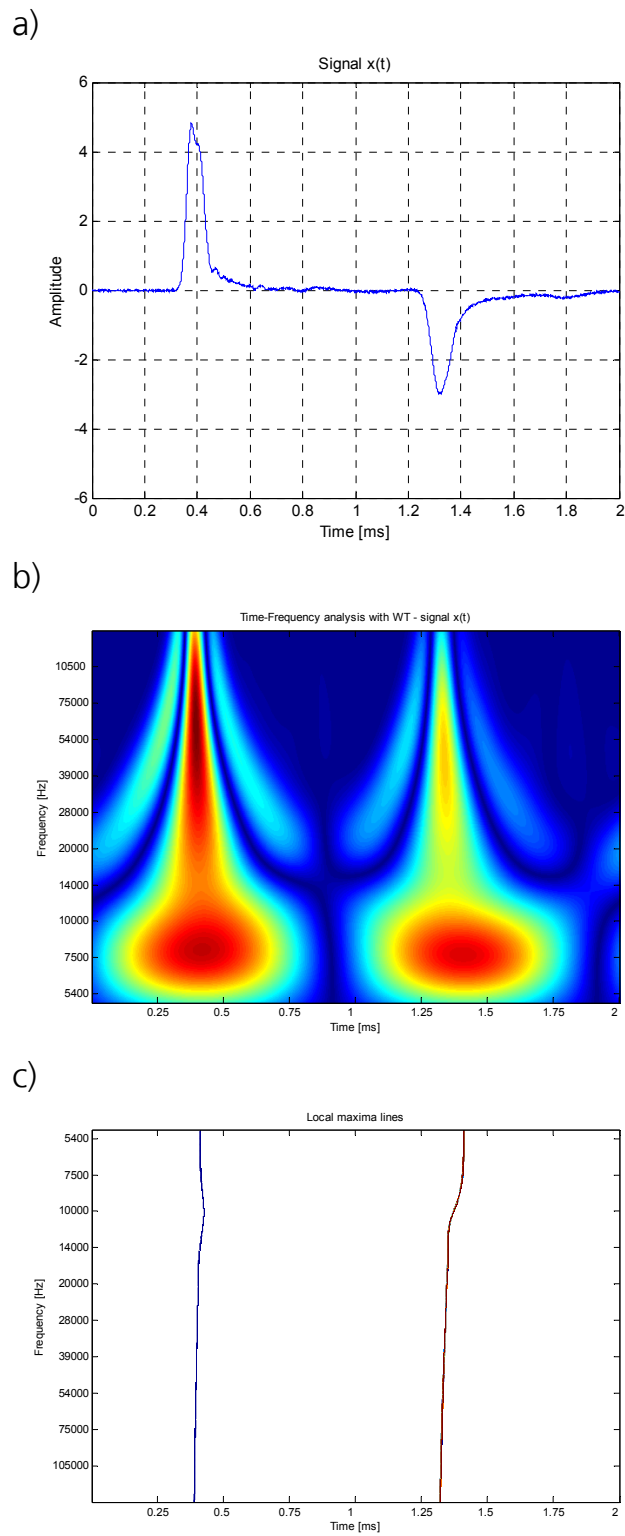


Fig. 7: Processing of recorded signal for PMMA a) signal, b) WT coefficients, c) local maxima lines.

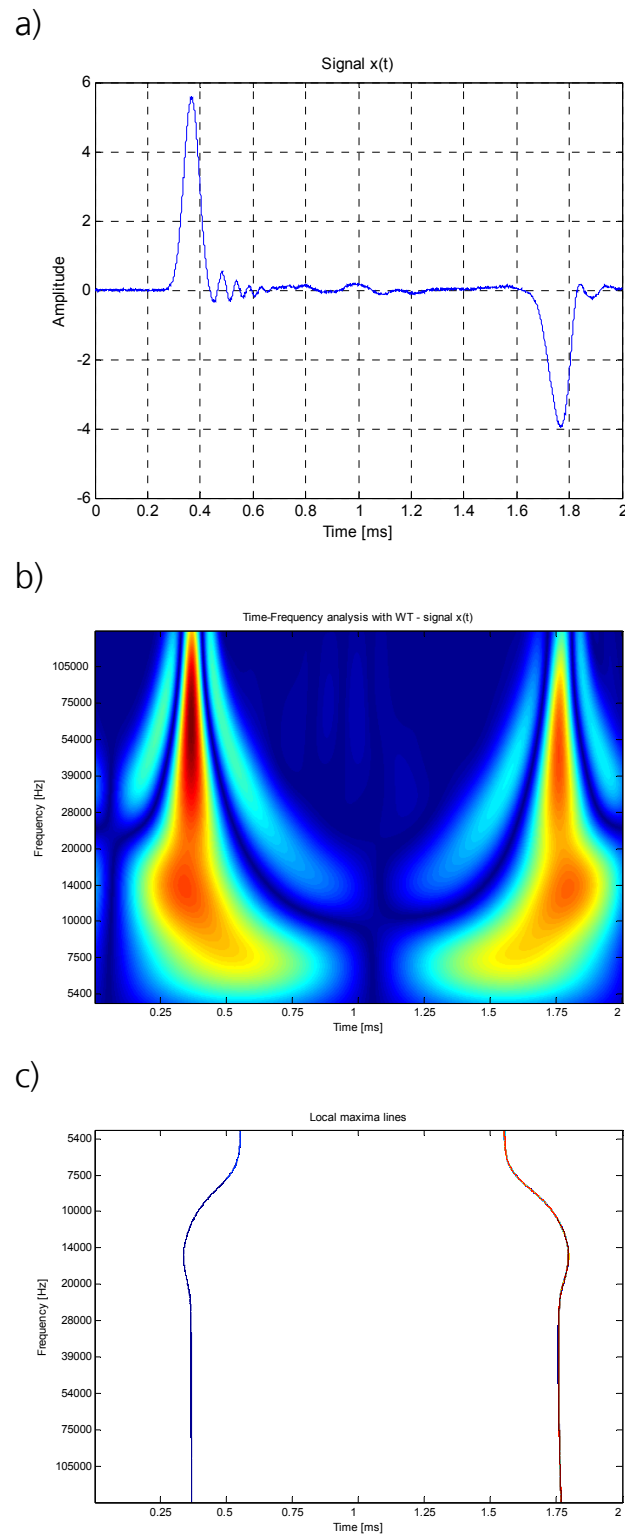
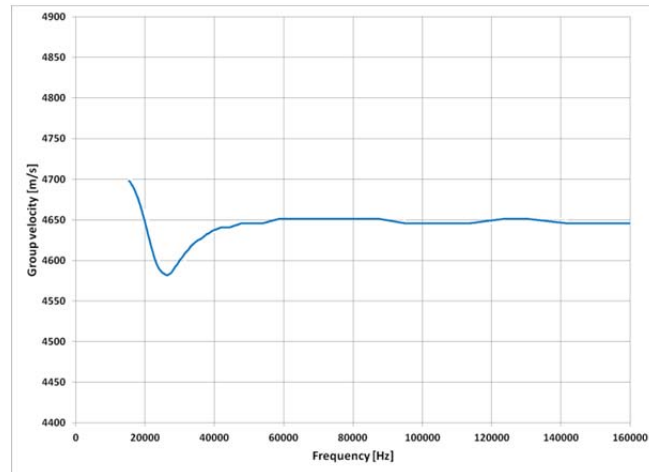
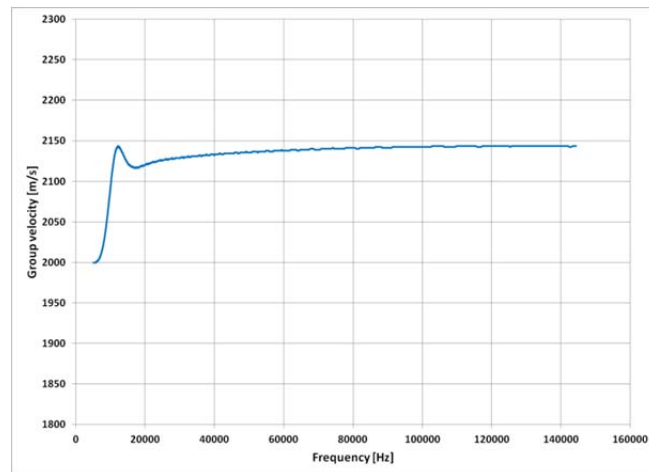


Fig. 8: Processing of recorded signal for polycarbonate (PC). a) signal, b) WT coefficients, c) local maxima lines.

a)



b)



c)

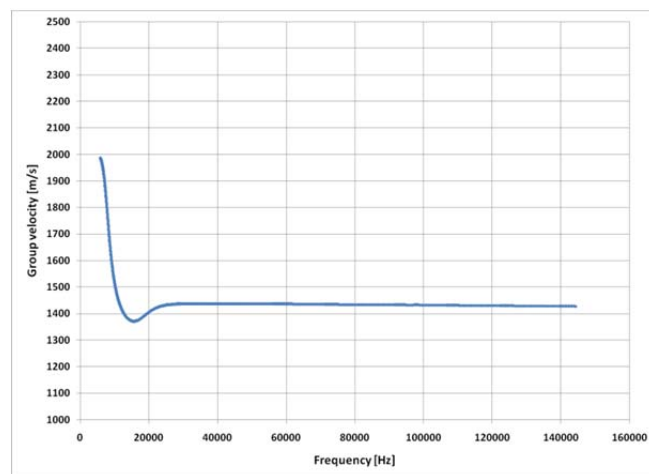


Fig. 9: Dispersion curves a) maraging steel, b) polymethacrylate (PMMA), c) polycarbonate (PC).

1.7 Next steps

Positive results of the investigations concerning the joint time-frequency analysis of waves in solids, in particular bars, allow further discussion of that matter and encourage to implement this efficient tool in a SHPB data processing. Therefore, a new two points algorithm based on both forward and inverse wavelet transforms is proposed. The algorithm takes into consideration all the steps of data processing. However, presently, the details of this process are not possible to be presented owing to the fact that the method is still being developed.

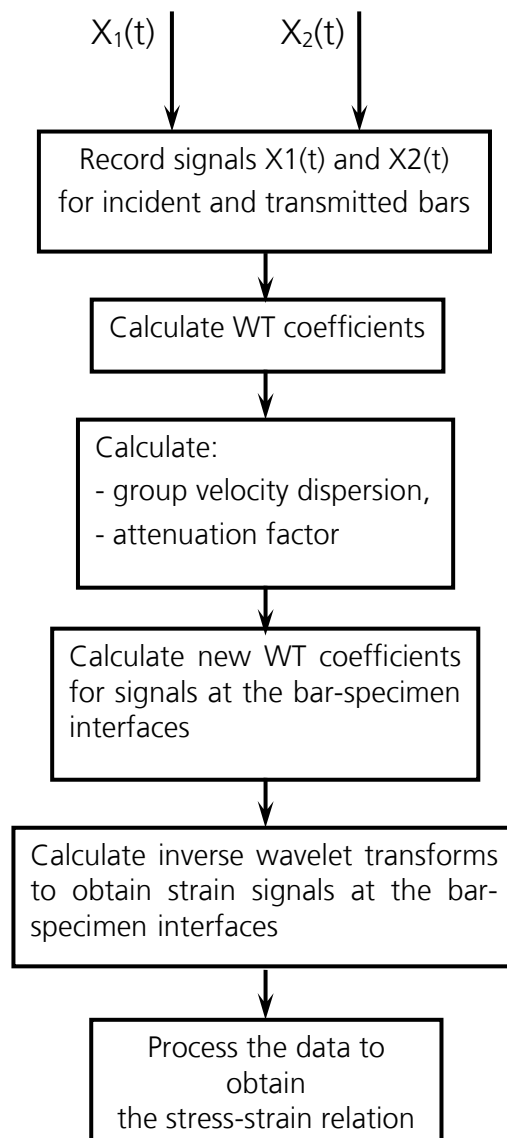


Fig. 10: Algorithm for SHPB data processing based on wavelet transform.

1.8 Conclusions

A new method based on a wavelet transform aimed at estimating the wave dispersion in SHPB elastic and viscoelastic bars has been presented. The method takes an advantage of analysis in a time-frequency domain and WT coefficients as a representation of the propagating wave in the bar, which allows for efficient estimation of wave dispersion as well as attenuation. Taking into account the fact that the calculations of WT

coefficients require comparable time to other methods, in particular FFT transform, it is possible to bring the described method into effect in SHPB community.

1.9 Acknowledgement

The author wish to thank Anna Kossowska for improving the quality of the-English language of the paper.

1.10 References

- [1] Chree, C.: The Equations of an Isotropic Elastic Solid in Polar and Cylindrical Co-ordinates, their Solution and Application. Cambridge, 1889,
- [2] Bancroft, D.: The Velocity of Longitudinal Waves in Cylindrical Bars. *Physical Review*, Vol. 59, 1941.
- [3] Love, A., E., H.: A Treatise on the Mathematical Theory of Elasticity. Fourth Edition, Dover Publications, New York, 1944.
- [4] Davies, R., M.: A Critical Study of the Hopkinson Pressure Bar. *Phil. Trans. R. Soc. London, A* 240, pp. 375-457, 1948.
- [5] Kolsky, H.: *Stress Waves in Solids*. Dover Publications, New York, 1963.
- [6] Graff, K., F.: *Wave Motion in Elastic Solids*. Dover Publications, New York, 1975.
- [7] Yew, C., H., Chen, C., S.: Study of Linear Wave Motions Using FFT and its Potential Application to Non-Destructive Testing. *Int. J. Engng. Sci.*, Vol. 18, pp. 1027-1036, 1980.
- [8] Follansbee, P., S., Frantz C.: Wave Propagation in the Split Hopkinson Pressure Bar. *Journal of Engineering Materials and Technology*, Vol. 105/61, 1983.
- [9] Lifshitz, J., M., Leber, H.: Data Processing in the Split Hopkinson Pressure Bar Tests. *International Journal of Impact Engineering* Vol. 15, No. 6, pp. 723-733, 1994.
- [10] Zhao, H., Gary, G.: A Three Dimensional Analytical Solution of the Longitudinal Wave Propagation in an Infinite Linear Viscoelastic Cylindrical Bar. Application to Experimental

- Techniques. *J. Mech. Phys. Solids*, Vol. 43, No. 8, pp. 1335-1348, 1995.
- [11] Doyle, J., F.: *Wave Propagation in Structures. Spectral Analysis Using Fast Discrete Fourier Transforms. Second Edition.* Springer-Verlag, New York, 1997.
- [12] Zhao, H., Gary, G., Klepaczko, J., R.: On The Use of a Viscoelastic Split Hopkinson Pressure Bar. *International Journal of Impact Engineering*, Vol. 19, No. 4, pp. 319-330, 1997.
- [13] Zhao, H., Gary, G.: A new Method for the Separation of Waves. Application to the SHPB Technique for Unlimited Duration of Measurement. *J. Mech. Phys. Solids*, Vol. 45, No. 7, pp. 1185-1202, 1997.
- [14] Cheng, Z., Q., Crandall, J., R., Pilkey, W., D.: Wave Dispersion and Attenuation in Viscoelastic Split Hopkinson Pressure Bar. *Shock and Vibration*, 5 pp. 307-315, 1998.
- [15] Kaiser, M., A.: *Advancements in the Split Hopkinson Bar Test. Thesis of Master of Science in Mechanical Engineering,* Blacksburg, Virginia, 1998.
- [16] Bacon, C.: Separation of Waves Propagating in an Elastic or Viscoelastic Hopkinson Pressure Bar with Three-dimensional Effects. *International Journal of Impact Engineering*, 22, pp. 55-69, 1999.
- [17] Bacon, C., Brun, A.: Methodology for a Hopkinson Test with a Non-uniform Viscoelastic Bar. *International Journal of Impact Engineering*, 24, pp. 219-230, 2000.
- [18] Li, X., B., Lok, T., S., Zhao, J., Zhao, P., J.: Oscillation Elimination in the Hopkinson Bar Apparatus and Resultant Complete Dynamic Stress-Strain Curves for Rocks. *International Journal of Rock Mechanics & Mining Sciences*, 37, pp. 1055-1060, 2000.
- [19] Tyas. A., Watson, A., J.: An investigation of Frequency Domain Dispersion Correction of Pressure Bar Signals. *International Journal of Impact Engineering*, 25, pp. 87-101, 2001.
- [20] Bussac, M., N., Collet, P., Gary, G., Othman, R.: An Optimisation Method for Separating and Rebuilding One-Dimensional Dispersive Waves From Multi-Point Measurements. Application to Elastic or Viscoelastic Bars. *Journal of the Mechanics and Physics of Solids*, 50, pp. 321 - 349, 2002.
- [21] Benatar, A., Rittel, D., Yarin, A., L.: Theoretical and experimental analysis of longitudinal wave propagation in

- cylindrical viscoelastic rods. *Journal of the Mechanics and Physics of Solids*, 51, pp. 1413 - 1431, 2003.
- [22] Casem, D., T., Fournay, W., Chang, P.: Wave Separation in Viscoelastic Pressure Bars Using Single Point Measurements of Strain and Velocity. *Polymer Testing*, 22, pp. 155-164, 2003.
- [23] Marais, S., T., Tait, R., B., Cloete, T., J., Nurick G., N.: Material Testing at High Strain Rate Using the Split Hopkinson Pressure Bar. *Latin American Journal of Solids and Structures*, 1, pp. 319-339, 2004.
- [24] Liu, Q., Subhash, G.: Characterization of Viscoelastic Properties of Polymer Bar Using Iterative Deconvolution in the Time Domain. *Mechanics of Materials*, 38, pp. 1105-1117, 2006.
- [25] Hagedorn, P., DasGupta, A.: *Vibrations and Waves in Continuous Mechanical Systems*. Wiley, England, 2007.
- [26] Aleyaasin, M., Harrigan, J., J.: Wave Dispersion and Attenuation in Viscoelastic Polymeric Bars: Analysing the Effect of Lateral Inertia. *International Journal of Mechanical Sciences*, 52, pp. 754-757, 2010.
- [27] Gabriel, D., Plešek, J., Kolman, R., Valeš, F.: Dispersion of Elastic Waves in the Contact-Impact Problem of a Long Cylinder. *Journal of Computational and Applied Mathematics*, 234, pp. 1930_1936, 2010.
- [28] Ahonsi, B., Harrigan, J., J., Aleyaasin, M.: On the Propagation Coefficient of Longitudinal Stress Waves in Viscoelastic Bars. *International Journal of Impact Engineering*, 45, pp. 39-51, 2012.
- [29] Currya, R., Cloete, T., Govender, R.: Implementation of Viscoelastic Hopkinson Bars. *EPJ Web of Conferences* 26, 01044, 2012.
- [30] Chen, W., Song, B.: *Split Hopkinson (Kolsky) Bar. Design, Testing and Applications*. Springer, New York, 2011.
- [31] Addison, P.: *The Illustrated Wavelet Transform Handbook*. Taylor & Francis, New York, 2002.
- [32] Burrus, C., S., Gopinath, R., A., Guo, H.: *Introduction to Wavelets and Wavelet Transforms. A Primer*. Prentice Hall, New Jersey, 1998.
- [33] Daubechies, I.: *Ten Lectures on Wavelets*. Society for Industrial and Applied Mathematics, Philadelphia, Pennsylvania, 1992.
- [34] Mallat, S.: *A Wavelet Tour of Signal Processing. The Sparse Way*. Third Edition. Academic Press, 2009.

- [35] Walker, J., S.: A Primer on Wavelets and Their Scientific Applications. Second Edition. Chapman & Hall/CRC, Taylor & Francis Group, 2008.
- [36] Qian, S., Chen, D.: Joint Time-Frequency Analysis. Methods and Applications. Prentice Hall PTR, New Jersey, 1996.
- [37] Gopalakrishnan, S., Mitra, M.: Wavelet Methods for Dynamical Problems. CRC Press Taylor & Francis Group, 2010.

Mechanical Characterization and Modelling of Reactive Polymeric Materials with the SHPB

N. Heider ¹, H. Aurich ², A. Steinbrenner ¹, M. Salk ²

¹ Ernst-Mach-Institut, Eckerstr. 4, 79104 Freiburg, Germany
Phone: +49 (0)761/2714-336, Fax: +49 (0)76121714-316, email:

heider@emi.fhg.de

² Ernst-Mach-Institut, Am Christianswuh 2, 79400 Kandern, Germany

1.1 Introduction

The application of modern high explosives HE must take into account more and more the analysis of safety aspects. This includes especially possible reaction and initiation mechanisms of the materials. An important point in this context is the characterization of the dynamical mechanical behaviour of the HE that precedes the reactive processes.

Plastic bonded high explosives PBX are heterogeneous materials with a composition of explosive grains with high strength and stiffness and a soft binder material with viscoelastic behaviour. The material response depends strongly on the polymeric binder and its viscoelastic properties with typical relaxation processes after application of stresses onto the material. In ref. [1] and [2] a material model for PBX was presented which includes a viscoelastic as well as a damage description, which is based on the statistical crack mechanics SCRAM model (cf. [3] and [4]). The damage part of the model was originally developed for the description of damage processes in brittle materials like ceramics (cf. [5]). This type of model can be used to describe the mechanical behaviour in the highly dynamical loading regime and extended to the description of initiation processes in HE due to shock waves (cf. [6] and [7]).

We propose in this paper an approach which allows a separated determination of the material properties. To achieve this we use the Split Hopkinson Pressure Bar SHPB technique for loading HE material samples in different strain rate regimes. For smaller strain rates we observe mainly a viscoelastic behaviour of the test sample. For higher strain rates viscoelasticity and additional damage determine the material behaviour.

The analysis of these experiments allows a separation of the viscoelastic and damage behaviour and gives a possibility for the determination of the corresponding material parameters.

The time scale of interest is in the range of 0.1 up to 1 millisecond and cannot be covered with classical experimental and mathematical methods used for the analysis of polymeric or explosive materials (cf. [8] and [9]). It is therefore necessary to use adequate experimental characterisation techniques for this loading regime. The SHPB technique is ideally suited for this purpose and allows material testing up to strain rates of 2000 1/s. In the literature this technique has already been used for the characterization of soft materials and explosives (cf. [8], [9] and [10]). Special care must be given to the selection of the bars in connection with the testing of soft materials. For sufficient high strain signals in the bars the impedance match condition between the bars and the test sample must be taken into account [11]. We therefore chose PMMA bars for testing of soft polymeric materials. The SHPB technique gives detailed information about the strain rates in the material and the corresponding stress states that are created in the test sample. For unconfined SHPB experiments the deformation in the sample is characterized by a uniaxial stress state and a multi-dimensional strain state.

1.2 Split Hopkinson Pressure Bar SHPB

1.2.1 Fundamental principles and signal analysis

The Split Hopkinson Pressure Bar (e.g. [12]) can be used to determine the dynamic material parameters of reactive materials. A sketch of the used setup is shown in Fig. 1. The test sample is positioned between the two bars of the system. A striker is accelerated by a gas gun and its impact on the incident bar generates a pressure pulse that runs through the bar with the characteristic speed of sound of the bar material. The speed of the striker shortly before impacting the incident bar is determined by a light barrier system. The induced pulse is then partly transmitted through the sample in the transmission bar and partly reflected back in the incident bar as a tension pulse.



Fig. 1: Principal setup of the SHPB facility.

The incident pulse (ε_i) and the reflected pulse (ε_r) are detected by strain gauges in the middle of the incident bar. The transmitted pulse (ε_t) is detected by strain gauges in the transmission bar. An example of a measured signal is shown in Fig. 2 a). The pulses are then time shifted to the edges of the sample Fig. 2 b) [13]. This method has to include damping and dispersion effects on the wave propagation in the bars.

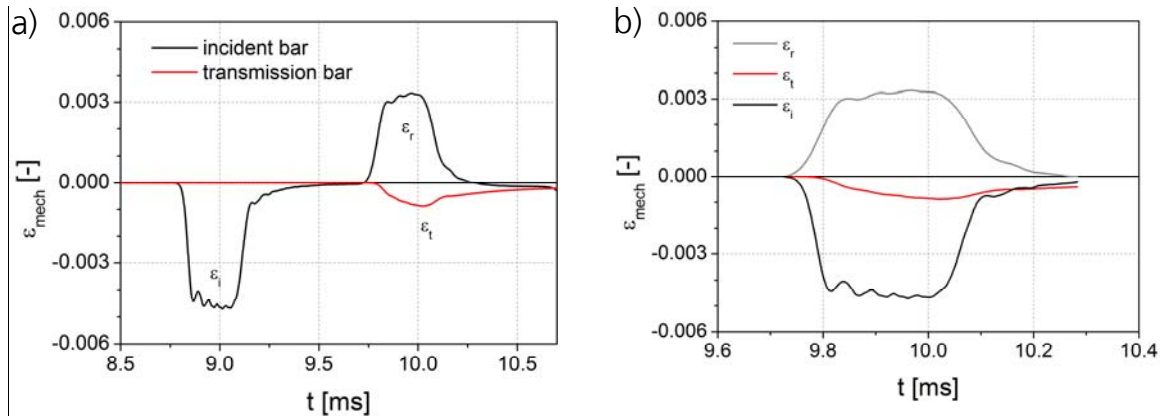


Fig. 2: a) Strain measurement in the incident bar (black) and the transmission bar (red). b) shifted signals.

The strain rate in the test sample is calculated from

$$\dot{\varepsilon}_S = -\frac{c_b}{L} (\varepsilon_r + \varepsilon_t - \varepsilon_i)$$

with c_b the speed of sound in the bar material and L the length of the sample. Integration of the strain rate over time gives the strain

$$\varepsilon_S = \int_0^t \dot{\varepsilon}_S dt = -\frac{c_0}{L} \int_0^t (\varepsilon_r + \varepsilon_t - \varepsilon_i) dt$$

The stress is calculated from the transmitted signal only

$$\sigma_a = kE_b \frac{A_b}{A_s} \varepsilon_t$$

and then multiplied by a correcting factor k , considering the damping of the waves in the bars. E_b is the Young's modulus of the bar material and A_b and A_s are the cross section of the bar and the sample, respectively.

1.2.2 SHPB facility with PMMA bars

A SHPB with PMMA (polymethyl methacrylate) bars is used to characterize the mechanical behaviour of PBX. An image of the system at EMI Kandern is shown in Fig. 3 a). The bars have a diameter of 40 mm with a mechanical impedance that is similar to the investigated reactive polymeric material. The use of bar materials with low impedance to test foam- or rubber-like samples has been investigated in the literature, e. g. [11, 14].

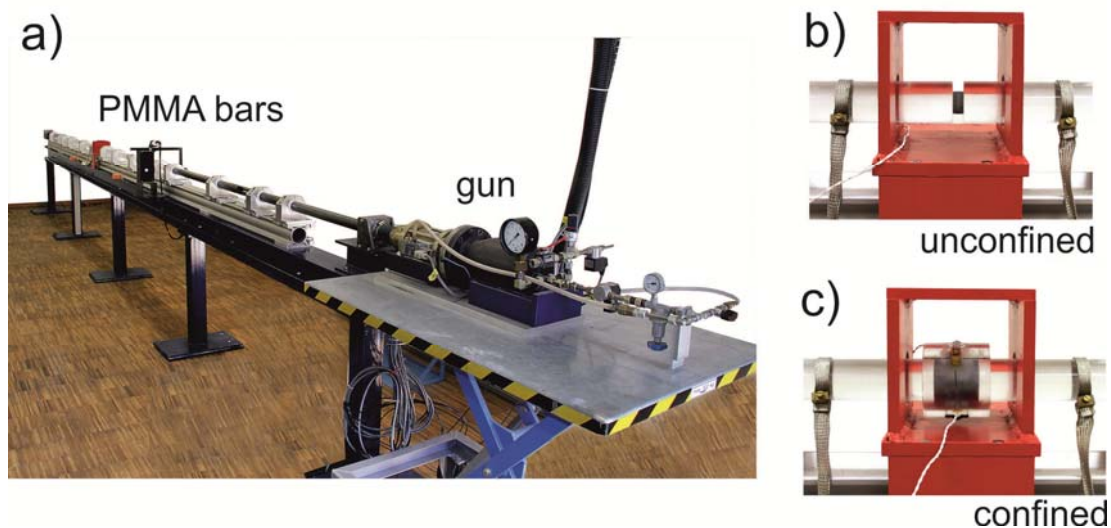


Fig. 3: a) SHPB facility with PMMA bars. b) Unconfined test setup. c) Confined test setup.

Fig. 3 b) shows an image of a sample positioned between the incident bar and the transmission bar. The investigated samples have a diameter $D = 20 \text{ mm}$ and a length $L = 10 \text{ mm}$. This ratio $L/D = \frac{1}{2}$ has been

chosen to minimize longitudinal and radial inertia effects in the sample [15].

With this SHPB facility striker velocities between $v_p = 5$ m/s and 20 m/s can be realized, leading to maximum strains in the samples in the range

$$500 \text{ s}^{-1} \leq \dot{\varepsilon}_{s,max} = \frac{v_p}{L} \leq 2000 \text{ s}^{-1}.$$

Additionally to these experiments with unconfined samples it is also possible to load samples in a PMMA confinement. An image of the configuration for confined experiments is shown in Fig. 3 c).

1.2.3 SHPB facility with aluminum bars

With the help of confined test samples significantly higher stresses can be achieved in the analysed material. Typical pressures in the PBX samples during tests with unconfined SHPB PMMA bars are only in the range of 10 to 20 MPa. To load material samples with higher pressures a modified SHPB facility with aluminum bars has to be used. This SHPB has a bar diameter of 40 mm. An image of the test setup with the aluminum bars is shown in Fig. 4 a). The aluminum confinement used for the experiments can be seen in Fig. 4 b). The corresponding sample length is 20 mm with a sample diameter of 40 mm. Because of the higher impedance of the aluminum bars compared to the PMMA, pressures achieved in the samples are higher by a factor 5.7. Fig. 5 shows the typical strain measurements in the SHPB bars and the aluminium confinement for KS-32.

As in the unconfined case the measurement of the strain pulses in the incident bar and the transmission bar are used for the determination of the axial stress σ_a in the test sample. The confined case allows the additional measurement of the radial stress that is built up in the material. Precondition for this method is that the deformation in the confining material is purely elastic. Under this assumption the measurement of the circumferential strain ε_θ in the confinement can be used to calculate the radial stress σ_r in the test sample. Strain gauges on the surface of the confinement are used for the determination of the elastic strain ε_θ . The radial stress in the test sample can be calculated from

$$\sigma_r = \frac{1}{2R_2^2} E_c (R_1^2 - R_2^2) \epsilon_\theta$$

with R_1 and R_2 being the outer and inner diameter of the confinement and E_c the Young's modulus of the confinement material. The pressure in the sample is then given by

$$p = \frac{1}{3} (\sigma_a + 2\sigma_r).$$

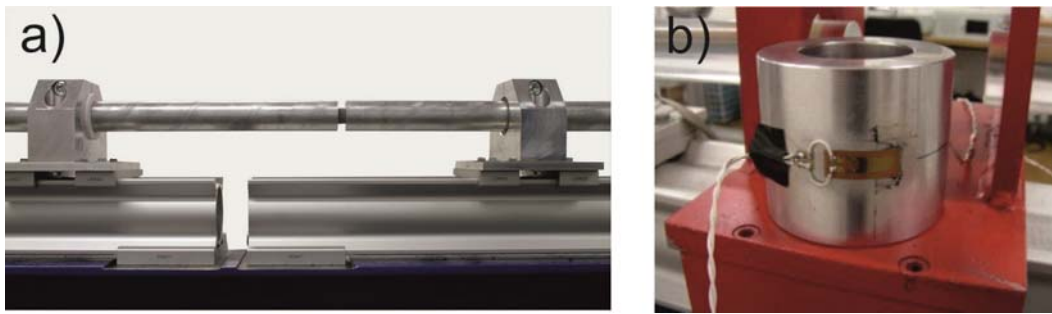


Fig. 4: a) SHPB facility with aluminum bars. b) Aluminum confinement.

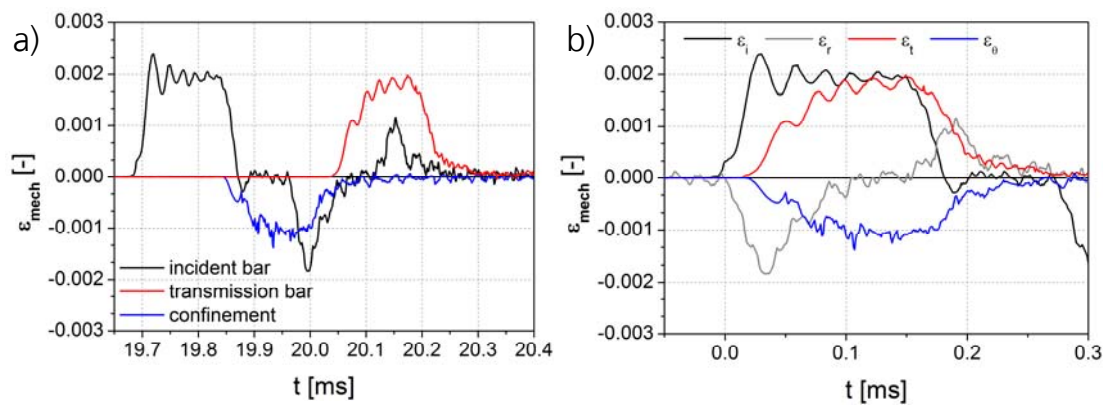


Fig. 5: a) Strain measurement with the confined SHPB facility (additional radial strain measurement in the confinement). b) Time-shifted signals.

1.3 Material behaviour – viscoelasticity and damage

The material behaviour of plastic bonded high explosive is determined by the interaction of the stiff solid grains with the viscoelastic binder. An appropriate material model must therefore include viscoelasticity and damage. The material model approach presented in the following is based on the SCRAM model (cf. [1] - [5]). The rheological description of the viscoelastic part uses a series of parallel Maxwell elements (Fig. 6 a). One element is only built up of a spring and represents the long-time stiffness behaviour of the material. All other elements consist of a spring and a damper which model the characteristic short time behaviour and the relaxation of stresses with time. The relaxation times of each Maxwell element depend on the shear modulus and the viscosity of the element.

A statistical crack model is used for the description of damage (cf. [5]). The pristine material is characterized by an exponential distribution of crack radii with arbitrary orientation in space (Fig. 6 b). By an averaging and integration process over these orientations an average crack radius can be determined. The dynamics of this average crack radius is calculated from the mechanical stresses in the material and the actual crack radius in relation to the original value is a measure for the observed damage.

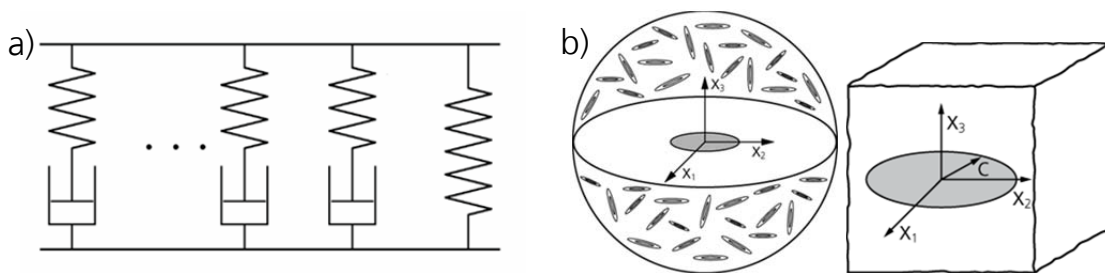


Fig. 6: a) Viscoelastic material model with Maxwell elements. b) Damage material model based on crack dynamics.

In the following, a short summary of the mathematical model is given. Starting point are the stress- and strain tensors σ_{ij} and ε_{ij} ($i,j=1,2,3$) of the continuum mechanical description of the material. Separation of the pressure σ and the mean strain ε leads to the deviatoric parts s_{ij} and e_{ij} of the stress- and strain tensors:

stress deviator
$$s_{ij} = \sigma_{ij} - \sigma \cdot \delta_{ij}$$

strain deviator $e_{ij} = \varepsilon_{ij} - \varepsilon \cdot \delta_{ij}$

with $\sigma = \frac{1}{3} \cdot \sigma_{ii}$ and $\varepsilon = \frac{1}{3} \cdot \varepsilon_{ii}$.

The material model is thus separated into the equation of state eos (pressure-density-relation $\sigma(\varepsilon)$) and the deviatoric description for which the viscoelastic-damage approach is used. The determination of the eos requires the direct measurement of the compression behaviour. For very high pressures servo-dynamic press facilities are necessary. For low and medium pressures confined tests with aluminium SHPB can be used. Different functional expressions can be chosen to describe the experimentally determined pressure-density relation. The selected eos relation $\sigma(\varepsilon)$ has a strong influence on the following determination of the deviatoric part of the stress tensor.

The differential equation for the deviatoric stress as a function of the deviatoric deformation rate for a model with N Maxwell elements is given in the following (the physical parameters are defined in Table 3):

$$\dot{s}_{ij} = \Psi \dot{e}_{ij} - \Theta (s_{ij} + \lambda_{ij}), \quad \Psi = \frac{2 \cdot G}{1 + \left(\frac{c}{a}\right)^3}, \quad \Theta = \frac{3 \left(\frac{c}{a}\right)^2 \frac{\dot{c}}{a}}{1 + \left(\frac{c}{a}\right)^3}, \quad \lambda_{i,j} = \frac{\sum_{n=1}^N \frac{s_{ij}^{(n)}}{\tau^{(n)}}}{3 \cdot \left(\frac{c}{a}\right)^2 \frac{\dot{c}}{a}},$$

and the corresponding differential equation for the deviatoric stress components in the Maxwell element with number n :

$$\dot{s}_{ij}^{(n)} = 2 \cdot G^{(n)} \cdot \dot{e}_{ij} - \frac{s_{ij}^{(n)}}{\tau^{(n)}} - \frac{G^{(n)}}{G} \left(3 \cdot \left(\frac{c}{a}\right)^2 \cdot \frac{\dot{c}}{a} \cdot s_{ij} + \left(\frac{c}{a}\right)^3 \cdot \dot{s}_{ij} \right), \quad (1)$$

$$G = \sum_{n=1}^N G^{(n)}$$

An important physical variable is the crack growth velocity \dot{c} , which determines the crack propagation due to the mechanical stresses in the material. The actual crack radius $c(t)$ in relation to the original distance a between the cracks can be regarded as measure for the damage.

The crack velocity \dot{c} depends on the stress concentration factor K_I and can be defined in different ways, e.g. point wise definition or analytical

expressions especially used in fracture mechanics. In the present work the following approach is used:

$$\dot{c}(K_I) = c_{\max} \left(1 - e^{-\left(\frac{K_I}{K_0}\right)^m} \right), \quad K_I = \begin{cases} \left(\frac{3\pi c}{2} s_{ij} s_{ij} \right)^{\frac{1}{2}}, & \sigma < 0 \\ \left(\frac{3\pi c}{2} \sigma_{ij} \sigma_{ij} \right)^{\frac{1}{2}}, & \sigma \geq 0 \end{cases} \quad (2)$$

with the three additional material parameters fracture toughness K_0 , maximum crack velocity c_{\max} and damage exponent m .

Table 3 summarizes the complete data set of physical parameters that define the presented deviatoric part of the material model. To complete the material description the above listed parameters for the viscoelastic behavior and the damage development have to be determined from experiments. In the following sections appropriate experimental tests with the corresponding procedure for the determination of the material parameters are presented.

Table 3: Physical parameters of the material model.

Poisson number	ν
Viscoelastic parameters	
Shear Modulus of Maxwell element n	$G^{(n)}$
Relaxation Time of Maxwell element n	$\tau^{(n)}$
Damage parameters	
Initial crack radius	$c_0 = c(0)$
Crack distance (flaw size)	a
Max. crack velocity	c_{\max}
Fracture Toughness	K_0
Damage Exponent	m

1.4 Material characterization of KS-32

The plastic bonded high explosive KS-32 was chosen as an example of the presented systematic method for material characterization. KS-32 is a heterogeneous material with a composition of explosive hexogen grains (85% mass fraction) and the polymeric binder (15 % mass fraction).

1.4.1 Characterization of the mechanical behaviour

Three unconfined experiments with the PMMA SHPB and one test with the confined aluminium SHPB at different strain rates have been performed (see Table 4). In the different columns the number of the experiment, the striker velocity, the strain rate, the maximum strain and the maximum stress are noted.

Table 4: Experiments with SHPB.

Experiment	Bar material	v_{striker} [m/s]	$d\varepsilon/dt$ [1/s]	σ_{max} [MPa]	ε_{max}
Exp. 1 (unconfined)	PMMA	5.7	539	8.9	0.15
Exp. 2 (unconfined)	PMMA	9.1	781	13.4	0.21
Exp. 3 (unconfined)	PMMA	17.2	1353	19.4	0.38
Exp. 4 (confined)	Al	20.6	990	140	0.045

The results of the unconfined experiments are shown in Fig. 7. In the first graph, Fig. 7 a), the strain rates are plotted over the time. The strain rates increase within 0.05 ms to their maximum values, are constant for approx. 0.3 ms and decrease to zero again. A plot of the strain rates over the technical strains can be seen in Fig. 7 b).

The axial stresses in the samples for the different strain rates over time are shown in Fig. 7 c). The maximum strain measured for the highest strain

rate of 1353 1/s is approx. 20 MPa. In Fig. 7 d) the axial stress is plotted over the technical strain.

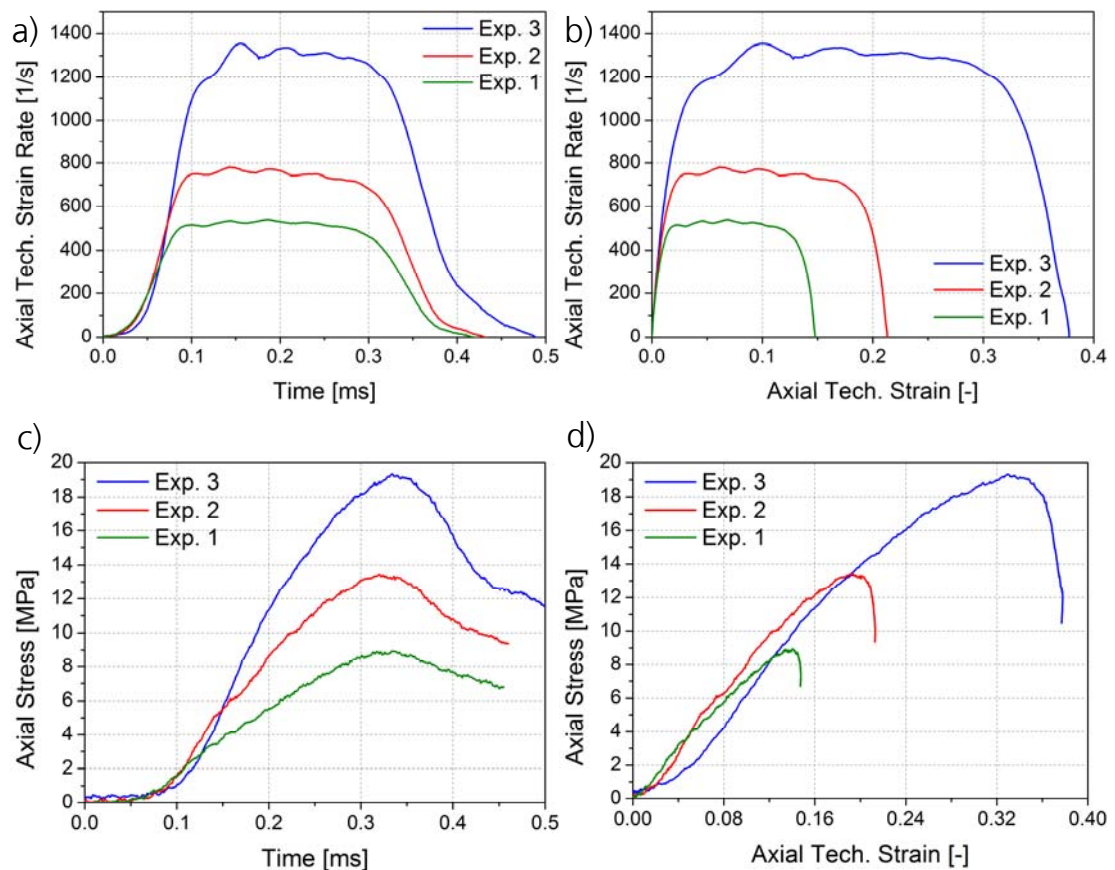


Fig. 7: Results for samples loaded in SHPB experiments with different loading conditions. a) and b) Strain rate as a function of time and strain, respectively. c) and d) Axial stress as a function of time and strain, respectively.

A high speed video camera was used to capture the compression process during the pressure pulse load. A sequence of images of the first loading pulse is shown in Fig. 8. The strain rate in this experiment was 1353 1/s. The time interval between the individual images is 66.7 μ s.

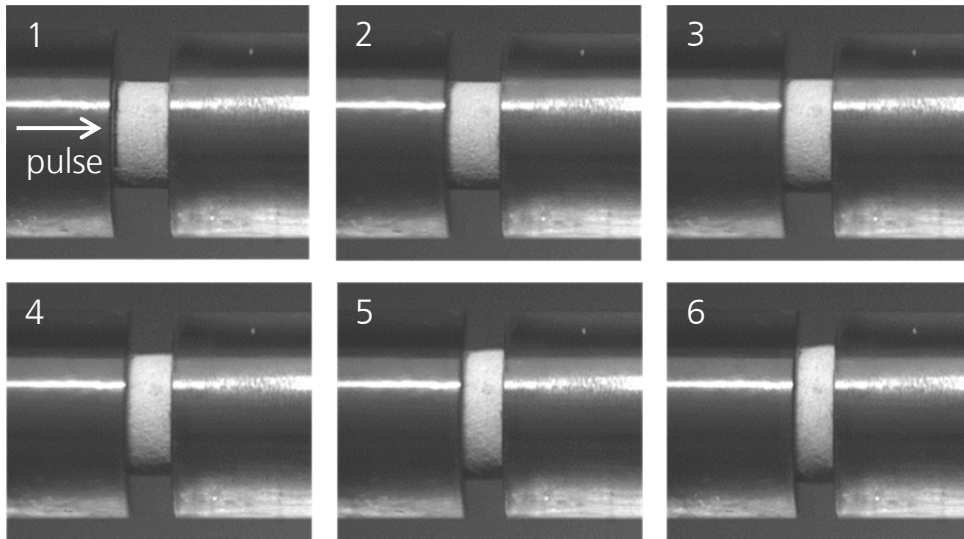


Fig. 8: Image sequence of the high-speed video during experiment Exp. 3.

In addition, tests with confined samples and aluminium bars were conducted. This type of test allows the measurement of the complete stress tensor and thus the determination of the equation of state eos. The strain rate, the axial and radial stress in the sample and the calculated pressure-strain relation are shown in Fig. 9. Pressures up to 1000 bars can be achieved with confined test configurations.

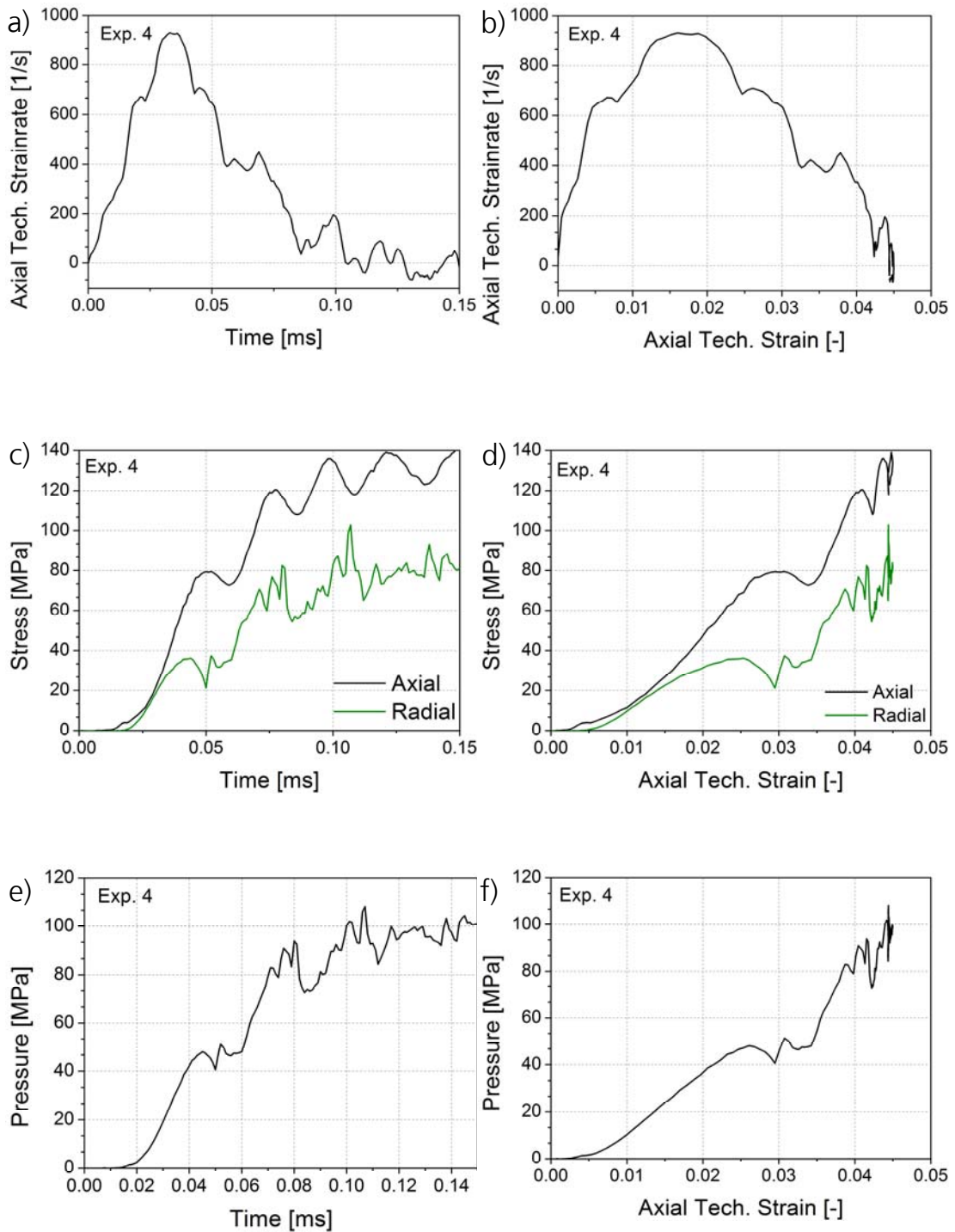


Fig. 9: Strain rate, axial stress, radial stress and pressure in the confined SHPB experiment.

1.4.2 Thermal loading of SHPB samples

To analyse the increase of the sample temperature during the deformation process a high speed thermo camera was used. A sequence of images of an experiment with a strain rate of 1550 1/s is shown in Fig. 10. The time interval between the images is 1.1 ms. The images show therefore the sample after several compressive pulses. The highest temperature $T_{\max}=26.3^{\circ}\text{C}$ was detected at the interface between the sample and pressure bars. It is due to friction effects at this interface. The measured temperature increase is 4.3°C above room temperature. This shows that temperature effects must not be taken into account in the modelling process in a first step. The material model presented in the preceding chapter is implicitly based on an isothermal approach that is justified with the experimentally observed thermal behaviour during the SHPB test.

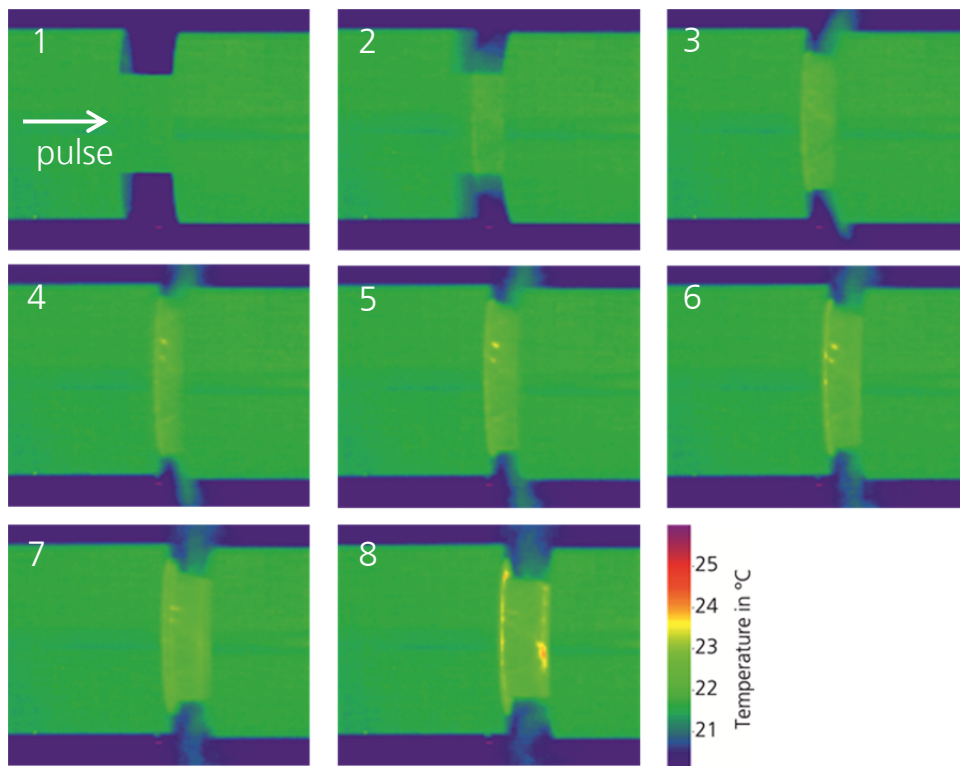


Fig. 10: Image sequence of the high-speed thermo camera.

1.4.3 Damage analysis with computer tomography

For the detection of damage in the loaded samples, computer tomography (CT) is used. CT allows a contact-free and non-destructive examination of the samples. The depth and orientation of the cross section can be chosen freely.

Fig. 11 shows a CT with a comparison of a pristine HE sample (on top) with a multiply loaded sample (below). The heterogeneous structure can be clearly seen with the lighter RDX grains embedded into the darker polymeric binder matrix. The loaded sample shows typical damage effects like broken grains, cracks in the binder material and debonding at the grain-binder interface.

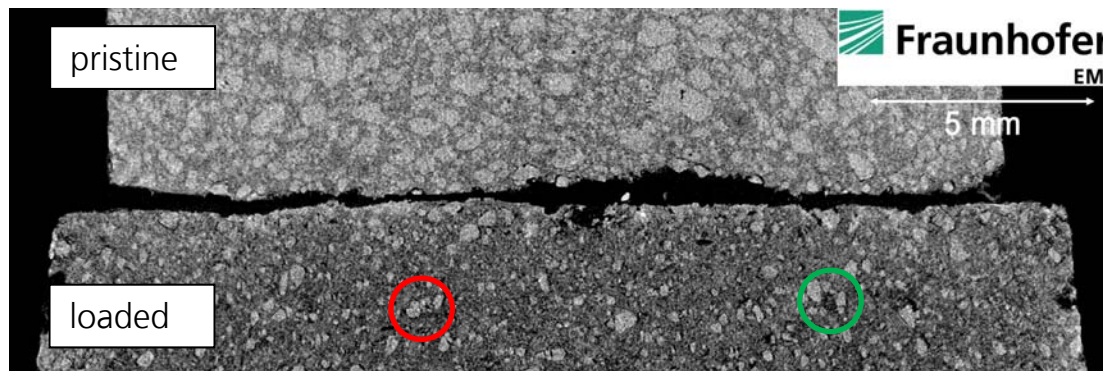


Fig. 11: Computer tomography of pristine and loaded HE samples. The loaded sample shows typical damage: Broken grains (red), cracks in binder and debonding (green).

1.5 Determination of material parameters

In the preceding chapter, the experimental results from the unconfined PMMA and confined aluminium SHPB were presented. These data form the basis for the determination of the material parameters for the high explosive KS-32. The presented material model combines in a complex way the equation of state, viscoelasticity and the damage description. It is therefore necessary to define an approach that allows the separation of these effects and thus the determination of the corresponding material parameters. In a first step the eos has to be independently determined. It was shown how confined SHPB experiments can be used for this purpose with pressures up to 1000 bar achievable. For even higher pressures other

test method as servo-hydraulic machines must be used. This procedure assumes that viscoelasticity and strain rate effects are of minor importance for the eos. The eos for KS-32 that is used in this paper for the separation of the stress tensor in the spherical and deviatoric part is shown in Fig. 12.

The selected approach for the determination of the deviatoric part of the model is based on the fact that in the tests 1 and 2 with lower strain rates the HE sample shows only minor damage formation. Only for test 3 with the high strain rate (1500 1/s) significant damage in the sample was observed. Therefore we chose the following approach for the determination of the material parameters:

- in a first step, test 1 and 2 with smaller strain rates were used for the determination of the purely viscoelastic part of the material model.
- in a second step, test 3 (high strain rate 1500 1/s) was used for determination of the damage part of the model.

A software tool was developed for this purpose that coupled the experimental strain rate and stress data from the unconfined SHPB tests with the presented material model. In an iterative way the material parameters were adjusted to the experimental data. The data set that shows the best agreement with the experimental data finally defines the material model parameters. The evaluation requires the separately measured Poisson number and equation of state of KS-32 (cf. [1] and [2]). The material data set for KS-32 determined in this way is shown in Table 5.

A comparison of the SHPB tests with the model equations is shown in Fig. 13 – Fig. 15 for the 3 SHPB experiments with different strain rates. Each figure compares the experimental stresses with the corresponding stresses from the model. The calculated stresses are shown for 2 cases. Case 1 is for the complete model including viscoelasticity and damage. Case 2 neglects damage and is the purely viscoelastic part of the model. As expected for the two low strain rates the stress-strain-curve can be reproduced with a purely viscoelastic description. For the strain rate 1500 1/s strong effects from damage are observed. Using a purely viscoelastic description leads to maximum stresses that are more than 50 % higher than the observed experimental values (nearly 30 MPa compared to the

experimental value of 18 MPa). Considering damage processes reduces the maximum stress to a value of around 18 MPa which is seen the experiment. The corresponding crack growth rate is presented in Fig. 16. It can be regarded as a measure for the damage that occurs in the HE sample due to dynamical loading.

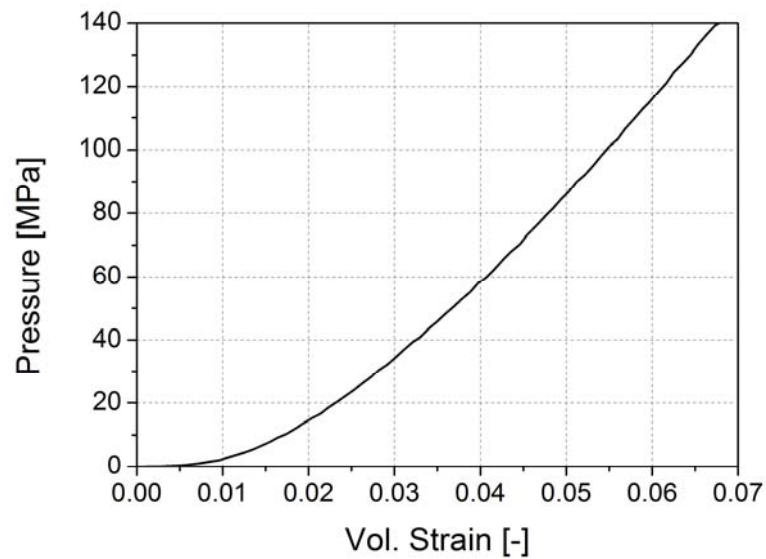


Fig. 12: Equation of state eos for KS-32.

Table 5: Material parameter data set for KS-32

Poisson Number		0.474
Viscoelastic Parameters		
Relaxation Time 1	[ms]	∞
Shear Modulus 1	[MPa]	10
Relaxation Time 2	[ms]	0.17
Shear Modulus 2	[MPa]	47
Damage Parameters		
Initial Crack Radius	[mm]	0.017
Flaw Size	[mm]	0.2
Max. Crack Velocity	[m/s]	2.0
Fracture Toughness	[MPa $\sqrt{\text{mm}}$]	20
Damage Exponent	[-]	2

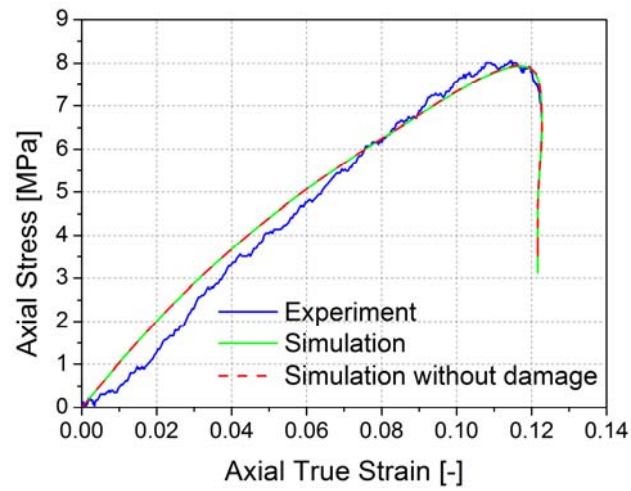


Fig. 13: Comparison of the stresses from the SHPB with the material model (strain rate 400 1/s).

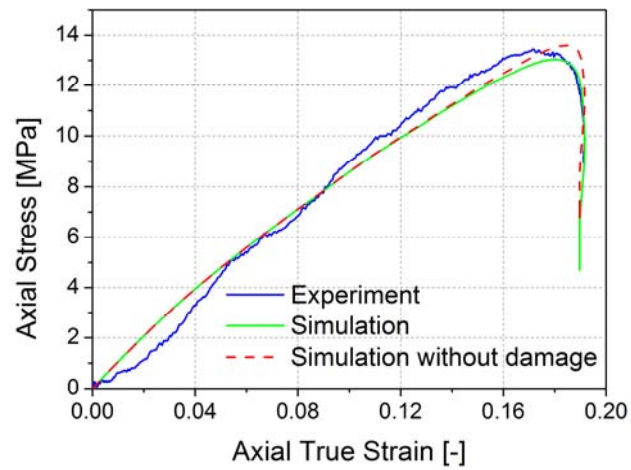


Fig. 14: Comparison of the stresses from the SHPB with the material model (strain rate 800 1/s).

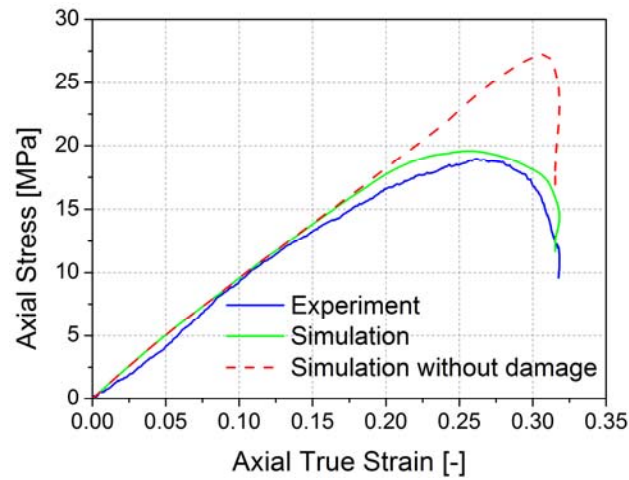


Fig. 15: Comparison of the stresses from the SHPB with the material model (strain rate 1500 1/s).

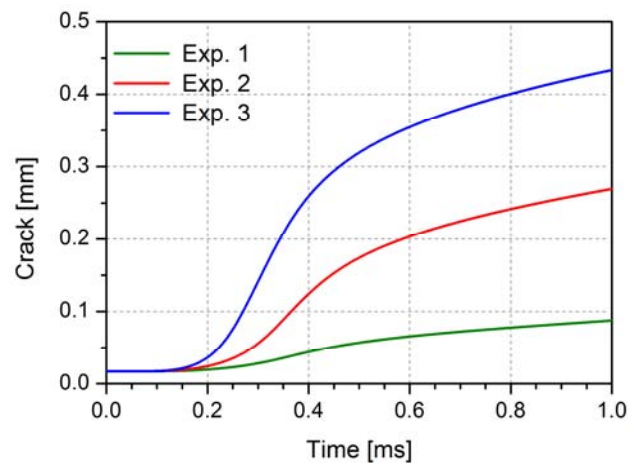


Fig. 16: Mean crack radius as a function of time (can be regarded as a qualitative damage parameter).

1.6 Summary

The application of the SHPB technique for the characterization of the material behaviour of soft materials was demonstrated. Two different test set ups were used with unconfined and confined material samples. The facility with unconfined samples used PMMA bars for a sufficient impedance match with the analysed material to ensure sufficient high strain signals in the loaded PMMA bars. For the determination of the equation of state a confined test set up was used which allowed the

generation of pressures of more than 1000 bar in the test sample. The analysed material was the insensitive high explosive KS-32. The SHPB allowed the analysis of the material under highly dynamic conditions with strain rates up to 1500 /s. A procedure was presented that allowed the separation of viscoelastic and damage processes in the material. The complete material parameter set was derived and the resulting stress-strain relations were validated with the experimental SHPB data.

1.7 References

- [1] N. Heider, A. Steinbrenner, H. Aurich und M. Salk, Characterization of the viscoelastic highly dynamic behaviour of PBX KS32, 45th International Annual Conference ICT Karlsruhe, 2014.
- [2] N. Heider, A. Steinbrenner, P. Weidemaier, H. Aurich und M. Salk, Modelling of the mechanical behaviour of PBX KS32, 44th International Annual Conference ICT Karlsruhe, 2013.
- [3] J. Bennett and et al., "A Constitutive Model for the Non-Shock Ignition and Mechanical Response of High Explosives," J. Mech. Phys. Solids, vol. 12, pp. 2303-2322, 1998.
- [4] R. Hackett and J. Bennett, "An Implicit Finite Element Material Model for Energetic Particulate Composite Materials," Int. J. Numer. Meth. Engng., vol. 49, pp. 1191-1209, 2000.
- [5] F. L. Addessio and J. N. Johnson, "A Constitutive Model for the Dynamic Response of Brittle Materials," J. Appl. Phys., vol. 67, no. 7, 1990.
- [6] J. K. Dienes and J. D. Kershner, "Multiple Shock Initiation Via Statistical Crack Mechanics," Proc. 11th Symposium Detonics, 1998.
- [7] J. K. Dienes und et al., „Impact Initiation of Explosives and Propellants via Statistical Crack Mechanics," J. Mech. Physics of Solids, 54, 2006.
- [8] G. T. Gray und et al., „High and Low Strain Rate Compression Properties of Several Energetic Material Composites as a Function of Strain Rate and Temperature," Proc. 11th Symposium Detonics, 1998.
- [9] J. Corley and et al., "A Combined Experimental/Computational Approach for Assessing the High Strain Rate Response of High

- Explosive Simulants and Other Viscoelastic Particulate Composite Materials," AIP Conf. Proc., pp. 705-708, 2002.
- [10] A. M. Bragov und et al., „Determination of physicomechanical properties of soft soils from medium to high strain rates," International Journal of Impact Engineering, pp. 967-976, 2008.
- [11] B. Song und W. Chen, „Split Hopkinson pressure bar techniques for characterizing soft," LAJSS, 2, pp. 113-152, 2005.
- [12] W. Chen und B. Song, Split Hopkinson (Kolsky) Bar, New York: Springer, 2011.
- [13] D. Mohr, G. Gary und B. Lundberg, „Evaluation of stress–strain curve estimates in dynamic experiments," Int. J. Imp. Eng., 37, pp. 161-169, 2010.

An automatic SHPB pulses delimitation method with a novel optimization

Gueraiche Larbi^{1,2}, Tarfaoui Mostapha², Osmani Hocine¹ and Aboulghit El Malki Alaoui²

¹ Laboratoire des Matériaux Non Métalliques, UFAS Sétif 19000, Algérie

² Laboratoire Brestois de Mécanique et des Systèmes (LBMS), ENSTA Bretagne, 2 Rue François Verny, 29806 Brest Cedex 9, France

1.1 Abstract

Data processing in split Hopkinson pressure bar technique is known to be sensitive to limits and durations of the three pulses. The dynamic stress-strain curves were found to be affected by dispersion and shifting of elastic strain pulses travelling in elastic bars. The dispersion is corrected by phase adjustment of each component in frequency domain using FFT analysis. Many studies suggest analysing the three pulses in three identical windows that propagate along the time axis with a reference velocity $c_0 = \sqrt{E/\rho}$. Before doing that, several methods have been used to determine starting times of pulses, including visual inspection, calculating the travel times based on the distance between the bar strain gage and the specimen–bar interface, matching the shapes of simulated waves of fictitious specimen with the real pulses, iterative shifting processes and a fitted linear regression line to the leading edge of the strain pulse. However, these methods are subjective or rather complex in their application and for some of them non-start and non-return linearly to zero of some shaped pulses making them a source of error. So, we developed a more consistent delimitation method that will be presented in this paper. Starting from the maximum and minimum of the reflected pulse and minimums of incident and transmitted pulses, the starting points and end points of pulses are determined using recursive and progressive iterations respectively. A slope is used to interpolate the interception point with time axis at the end of each iteration. The reflected pulse starting time is optimized by travelling the wave twice the length between gage's middle and interface incident bar/specimen. The developed iterative method is validated by typical experimental results

presented for $[0^\circ]_{40}$ Glass /EPOLAM2020 composite tested in plane at strain rate of 508 s^{-1} .

Keywords: Split Hopkinson pressure bar, High strain rate, data acquisition, data post processing, time starting points, FFT, dispersion, glass/epoxy.

1.2 Introduction

Split Hopkinson Pressure Bar (SHPB) systems are commonly used to investigate the mechanical behaviour of materials at high strain rates ranging from 10^2 to 10^4 s^{-1} . This experimental technique is based on the early work of Hopkinson [1], who recorded a pressure-pulse profile using one slender bar. This technique is widely adopted since the critical study of Davies [2]. The actual configuration using a specimen sandwiched between two bars is due to Kolsky [3]. A comprehensive review of developments in SHPB testing has been reported by several authors [4-6]. The accuracy of SHPB measurements are mainly related to the accuracy of forces and velocities at specimen faces. These global quantities are obtained from the recorded wave signals without consideration of the specimen [7]. Lifshitz and Leber [8] suggested analysing the three pulses in three identical windows that propagate along the time axis with a reference velocity c_0 . The starting points of the measured strain pulses have to be determined precisely before computing stress, strain and strain rate in the specimen as a function of time. Several methods have been used to do this, including visual inspection, calculating the travel times based on the distance between the bar strain gage and the specimen-bar interface, matching the shapes of simulated waves of fictitious specimen with the real pulses [9], iterative shifting processes [10]. Previous methods are subjective or rather complex in their application. Vuoristo et al [11] used a procedure based on fitting a linear regression line to the baseline and to the leading edge of each strain pulse then taking the intersection of the two fitted lines as the starting point of the pulse. Pulses are corrected for dispersion before calculating stress, strain and strain rate in the specimen.

We present in this paper a new iterative method more easy for delimiting pulses without neglecting the beginning and the end of shaped signals as in case of using rounded tip strikers.

1.3 Split Hopkinson pressure bar test set

The split Hopkinson pressure bar is a technique widely used to evaluate material behaviour at high strain rates ranging from 10^2 to 10^4 s^{-1} . It consists essentially from a striker bar (0.4m), an input bar (1.9850 m) of and an output bar (1.8450 m) as illustrated on Fig.1. A cubic Glass/Epoxy specimen is sandwiched between the input and output bars. A striker is lunched with an initial impact pressure provided by the air gun. The two bars and the striker are made from maraging steel and have 20mm in diameter. A stress wave generated by impact of a striker on the free end of an incident bar, propagates through them until reaching the interface between the incident bar and the specimen (IB-S), where it divides into two parts: a reflected part that goes back through the incident bar, and a transmitted part that goes through the specimen to the transmitted bar. The stress waves are recorded by a pair of two half bridges that compensate the bending effect of the bars.

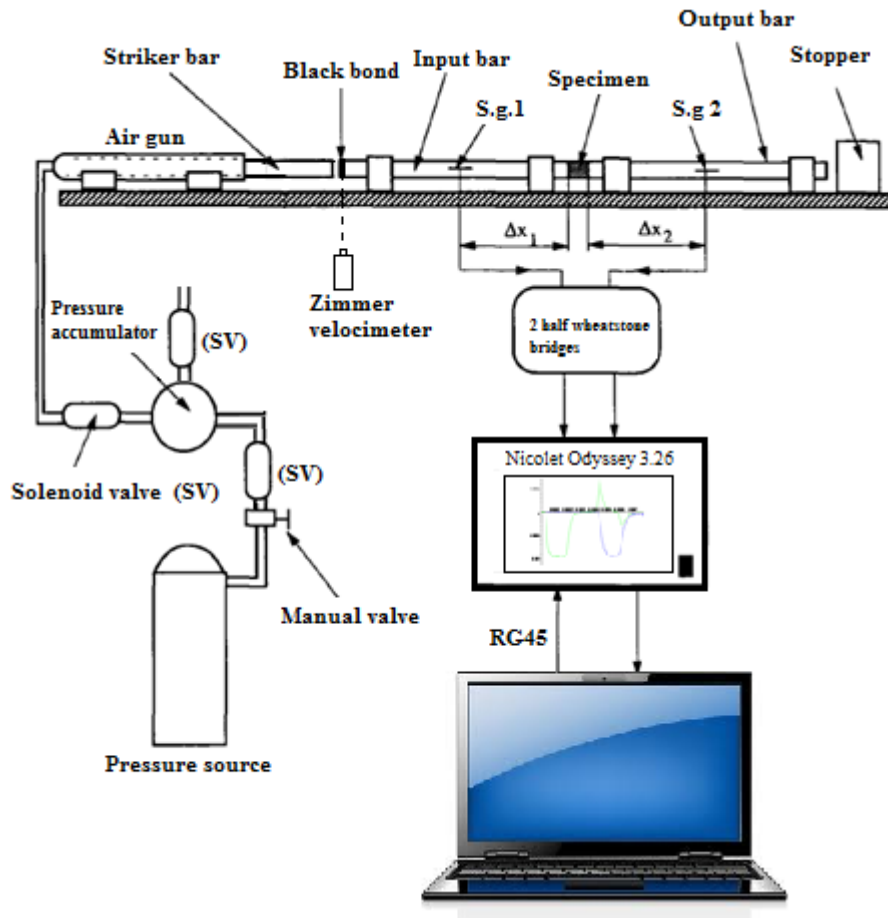


Fig. 17: Schematic diagram of LBMS Split Hopkinson pressure bar (MC/TCM).

Knowing the striker's length L , the sound velocity of the bars c_b and their density ρ_b , the duration and the amplitude of the incident stress wave generated by impact of a striker fired at a velocity V_s can be estimated respectively as follows:

$$\tau = \frac{2L}{c_b} \quad (1)$$

$$\sigma_i = -\frac{1}{2}\rho_b c_b V_s \quad (2)$$

1.4 Assumptions for a valid SHPB test

Analytical expressions for determining material properties under high strain rate loading have been developed [4, 5, 7, 12, 13]. Original high strain rate analysis by Kolsky [3] was based on the following basic assumptions:

1. Maintaining the striker, the incident and the transmitted bars under linear elastic state is satisfied by using high strength steel such as maraging steel, which has yield strength σ_y of 2300 MPa for MC/TCM bars. Also, for a bar velocity c_0 , we can maintain the stress in the bars under σ_y by controlling the velocity of the striker ($V_s < 2\sigma_y/c_0$).
2. Stress wave propagation can be described by 1D wave propagation theory. It is necessary to look the exact solution for wave propagations to ensure whether this assumption is valid [13]. For this assumption to hold well, the elastic bars should have a slenderness ratio (L_b/d_b) of at least ~ 20 (Weinong chen, Bo Song; Safa K, Gary G), where L_b and d_b are the length and the diameter of the elastic bars. In the current study, an L_b/d_b of more than 90 is used. Despite this the assumption of no dispersion effects is not valid for a finite diameter bar but it needs to be corrected as it will be discussed later in this paper.
3. The incident bar-specimen and specimen-transmitted bar interfaces remains plane at all time. This assumption is true in case when the specimen diameter is equal to that of the bars, and in the case of acoustically soft specimens, as compared to the bar material. Acoustically soft specimen means having a low acoustic impedance ($Z = \rho_s \cdot c_0$) where ρ_s is the specimen density. In our case glass/epoxy composite has low acoustic impedance compared to maraging steel. A method for punching correction is proposed by Safa et al [14] for hard specimens.
4. Inertia effects and friction effects in specimen are negligible. Gray III [5] suggested that the radial and longitudinal inertia and friction effects can be lessened by minimizing the areal mismatch between the bar and the specimen ($d_s \approx 0.8d_b$); and choosing

$0.5 < L_S/d_S < 1.0$. For non-circular specimens, Srinivasan et al [15] proposed a slenderness ratio valid for any cross-section. This ratio providing interfacial friction properly reduced is given as $1.4 < L_S/\sqrt{J/A_S} < 2.8$, where J is the inertia moment and A_S is the specimen section.

5. Stress equilibrium throughout the specimen and constancy of strain rate [5]. The assumption of specimen stress equilibrium during testing has been discussed by researchers previously [4, 5, 16-18]. Equilibrium and axial uniformity of stress in a Kolsky bar specimen is assessed by comparing the stresses using 1-wave and 2-wave analyses [5] or forces applied on interfaces incident bar-specimen and specimen-transmitter bar. The stress equilibrium is achieved after an initial "Ringing-up" period corresponding to a couple of stress wave reverberations (3-4, exactly π) (Davies EDH and Hunter SC). However if the specimen experience damage initiation and evolution, stress wave attenuation would take place within the specimen during testing and the assumption of stress equilibrium would not be valid [12]. Uniform strain rate throughout the experiment could be achieved using the pulse shaper technique [6,20-22].
6. The specimen is not compressible. As reviewed by Gary III [5], the importance of this requirement to all types of Hopkinson bar testing using the detailed one-dimensional wave assumptions is that true stress in a sample in the Hopkinson bar cannot be extracted for materials whose volumes are not conserved. The instantaneous sample area used later in equation (16) is deduced from the reflected strain signal in the incident bar assuming that the constancy of volume assumption is valid in the sample (i.e., there is a fixed relationship between sample cross-sectional area and its length).

1.5 Data acquisition

The transient strain histories are recorded from strain gages mounted on the incident and the transmitted bars. Two gages EA-06-125AC-350 are mounted diametrically opposite to each other on each bar to cancel any

bending strains. To avoid wave overlapping (Weinong chen, Bo Song), locations of strain gages measured relatively to interfaces bar/specimen are chosen at least twice the length of the striker. The strain gage voltages can then be converted into strain using Eq. (3), and thus the incident ε_i , reflected ε_r , and transmitted ε_t strains are obtained.

$$\varepsilon = \frac{2. \Delta Em}{k. (U_0 - 2\Delta Em)} = \frac{1}{\frac{k. U_0}{2\Delta Em} - k} \quad (3)$$

where: ε , ΔEm , k and U_0 are respectively the strain, the bridge output voltage, the gage factor ($k = k_{inc} = K_{trans} = 2.105$) and the bridge supply voltage.

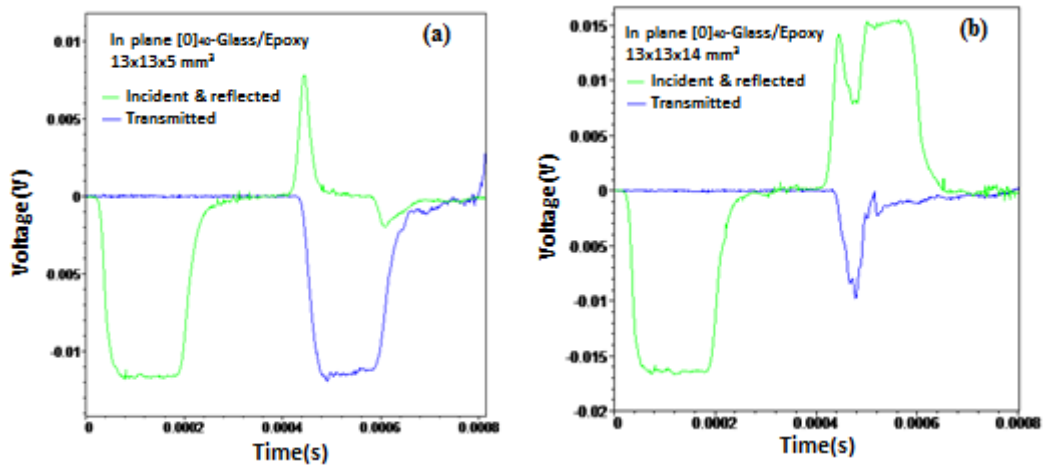


Fig. 18: Typical signals for LBMS compression split Hopkinson bar tests. (a) in case of non-damaged and (b) for a damaged $[0^\circ]_{40}$ glass / epoxy specimens.

Gages histories are recorded using Nicolet Odyssey 3.26 high speed data acquisition system at a sampling rate of 1 MHz. Typical signals are given both for non-damaged specimen (Fig. 18 (a)) and for a damaged $[0^\circ]_{40}$ glass/epoxy specimen as shown in Fig. 18 (b). The reflected signal for none damaged specimen consists of a positive pulse followed by a negative part however the damaged one presents only a positive part with two peaks.

1.6 Basic SHPB governing equations

The determination of the stress-strain behavior of a material being tested in a Hopkinson bar, whether it is loaded in compression as in figure 1 or in a tensile or torsion bar configuration, is based on the same principles of one-dimensional elastic-wave propagation within the pressure loading bars as previously reviewed [5].

The subscripts 1 and 2 are used in this description to denote the incident and transmitted bar ends of the specimen, respectively. The strains in the bars are then designated as ϵ_i, ϵ_r and ϵ_t (incident, reflected, and transmitted strains, respectively) and the displacements of the ends of the specimen as u_1 and u_2 at the incident bar-specimen and specimen-transmitted bar interfaces as given schematically in the enlarged view of the test specimen in Fig. 19.

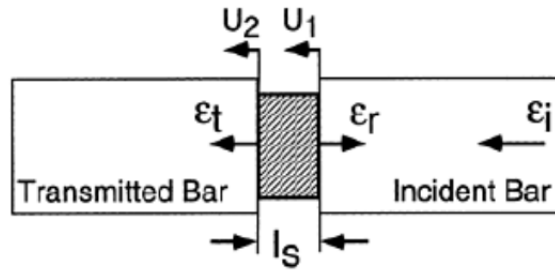


Fig. 19: Expanded view of incident bar/specimen/transmitted bar region.

From elementary wave theory, it is known that the solution to the wave equation:

$$\frac{\partial^2 u}{\partial x^2} = \frac{1}{c_b^2} \frac{\partial^2 u}{\partial t^2} \quad (4)$$

can be written as:

$$u = f(x - c_b t) + g(x + c_b t) = u_i + u_r \quad (5)$$

For the incident bar, where f and g are functions describing the incident and reflected wave shapes, and c_b is the longitudinal wave speed in the pressure bars.

By definition, the 1-D strain is given by:

$$\varepsilon = \partial u / \partial x \quad (6)$$

Therefore, differentiating equation (5) with respect to x , the strain in the incident rod is given by:

$$\varepsilon(t) = f' + g' = \varepsilon_i(t) + \varepsilon_r(t) \quad (7)$$

Differentiating equation (5) with respect to time and using equation (7) gives for the incident bar:

$$\dot{u}_1(t) = c_b(-f' + g') = c_b(-\varepsilon_i(t) + \varepsilon_r(t)) \quad (8)$$

The time derivative of the displacement in the transmitted bar, $u = h(x - c_b t)$, yields:

$$\dot{u}_2(t) = -c_b \varepsilon_t(t) \quad (9)$$

Equations (8) and (9) are true everywhere, including at the ends of the pressure bars. The strain rate in the test specimen is:

$$\dot{\varepsilon}(t) = \frac{\dot{u}_1(t) - \dot{u}_2(t)}{L_S} \quad (10)$$

where L_S is the instantaneous length of the specimen, and $\dot{u}_1(t)$ and $\dot{u}_2(t)$ are respectively the velocities at the incident bar-specimen and specimen-transmitted bar interfaces calculated using gages records propagated to interfaces. During traveling to interfaces, dispersion is corrected by propagating harmonics at their own phases and after that velocities are reconstructed using FFT.

The strain rate $\dot{\varepsilon}(t)$ is calculated by:

$$\dot{\varepsilon}(t) = \frac{c_b}{L_s} (-\varepsilon_i(t) + \varepsilon_r(t) + \varepsilon_t(t)) \quad (11)$$

The forces applied on bars interfaces are:

$$F_1(t) = AE(\varepsilon_i(t) + \varepsilon_r(t)) \quad (12)$$

$$F_2(t) = AE\varepsilon_t(t) \quad (13)$$

where A is the cross-sectional area of the pressure bar, and E is the Young's elastic modulus of the bars (normally equal, given that identical material is used for both the incident and transmitted pressure bars).

After an initial "ringing-up" period of π reverberations in the specimen, it is assumed that the specimen is in force equilibrium and deforming uniformly. If these assumptions are valid, a simplification can be made by equating the forces on each side of the specimen (i.e., $F_1(t) = F_2(t)$). Comparing equations (12) and (13), therefore, means that:

$$\varepsilon_t(t) = \varepsilon_i(t) + \varepsilon_r(t) \quad (14)$$

Substituting this criterion into equation (11) yields:

$$\dot{\varepsilon}(t) = -\frac{2c_b\varepsilon_r(t)}{L_s} \quad (15)$$

Based on 1-wave analysis, the engineering stress can be written as:

$$\sigma(t) = \frac{AE\varepsilon_t(t)}{A_s} \quad (16)$$

where A_s is the instantaneous cross-sectional area of the sample.

For 2-wave analysis, the engineering stress can be given as:

$$\sigma(t) = \frac{AE(\varepsilon_i(t) + \varepsilon_r(t))}{A_s} \quad (17)$$

For the 3-wave analysis, the specimen stress is then simply the average of the two forces divided by the combined interface areas:

$$\sigma(t) = \frac{F_1(t) + F_2(t)}{2A_s} \quad (18)$$

Substituting equations (12) and (13) into equation (18) then gives:

$$\sigma(t) = \frac{EA}{2A_s} (\varepsilon_i(t) + \varepsilon_r(t) + \varepsilon_t(t)) \quad (19)$$

According to [21], true stress–strain can be obtained from the engineering stress–strain by following formulations:

$$\sigma_t(t) = (1 - \varepsilon(t))\sigma(t) \quad (20)$$

$$\varepsilon_t(t) = -\ln(1 - \varepsilon(t))$$

where $\sigma_t(t)$, $\varepsilon_t(t)$ represent true stress and true strain, respectively, $\varepsilon(t)$ and $\sigma(t)$ represent engineering stress and strain, respectively.

1.7 Data processing

1.7.1 Starting and end times of pulses

To shift strain histories recorded at gages locations to specimen faces; we developed algorithms for delimiting the three pulses. The algorithm checking incident pulse starting and end times is illustrated on the flow chart of Fig. 20. After retrieving the index of the minimum incident strain ($i_{\varepsilon_{MIN}}$), recursive iteration is carried out to seek the incident pulse starting time d_i at intersection with time axis.

The expression of d_i given in equation (21) allows even to calculate the incident starting time if strain vanishes or to interpolate them using a slope between the two last values just before and after intersection as follows:

$$d_i = t(i - 1) + \frac{\varepsilon(i - 1) \cdot (t(i) - t(i - 1))}{\varepsilon(i - 1) - \varepsilon(i)} \quad (21)$$

For the end time f_i , a progressive iteration is performed starting from the minimum strain value until intercepting time axis. Then, f_i is interpolated using an upslope between the two last values just before and after intersection as it is given by the following equation:

$$f_i = t(i) - \frac{\varepsilon(i) \cdot (t(i + 1) - t(i))}{\varepsilon(i + 1) - \varepsilon(i)} \quad (22)$$

For the reflected pulse, it is a little more complex since its shape changes depending on damage or none damage of the specimen as shown in Fig. 18. To check the reflected pulse starting time d_r , the algorithm starts from the maximum reflected strain index ($i_{\varepsilon_{RMAX}}$) as can be observed in Fig. 21. After that, recursive iteration is performed to seek the reflected pulse starting time d_r at interception with time axis. If there is no time for which strain is null, d_r will be interpolated using a downslope between the two values just before and after intercepting time axis as follows:

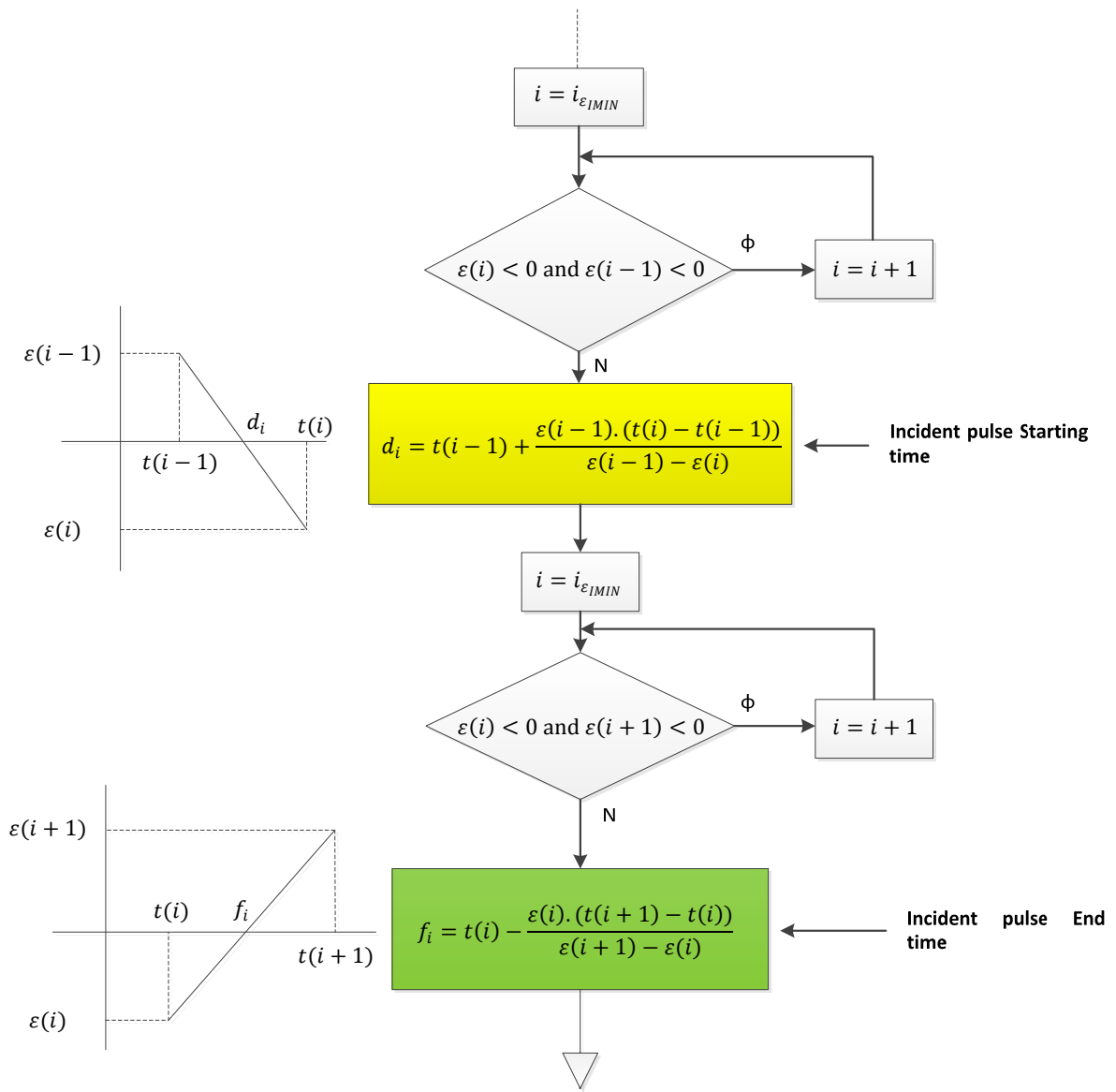


Fig. 20: Flow chart for incident pulse starting and end times detection.

$$d_r = t(i) - \frac{\epsilon(i) \cdot (t(i) - t(i-1))}{\epsilon(i) - \epsilon(i-1)} \quad (23)$$

Also, the reflected starting time may be predicted by traveling the starting of incident pulse twice the distance between the incident strain gage and the specimen/bar interface as follows:

$$d'_r = d_i + \frac{2 \cdot \Delta x_1}{c_0} \quad (24)$$

In case where the checked starting time d_r and the predicted one d'_r don't stick together, a correction of c_0 is recommended using equation (25).

$$k_{c_0} = \frac{2 * \Delta x_1}{c_0(d_r - d_i)} \quad (25)$$

where $c_0 = \sqrt{E/\rho}$ with E is the Young's elastic modulus of the bars and ρ is there density.

Since in case of none damage, the reflected pulse presents in addition to the positive part a negative part at the end. So to check the reflected pulse end time, the algorithm verifies if the minimum reflected strain is positive (Fig. 21); in that case, f_r will be $t(N_{inc})$ with N_{inc} is the number of operands retained between cursors for the incident strain bridge record while exporting data from Nicolet Odyssey high speed data acquisition system . Otherwise, as presented in Fig. 22 for a negative minimum reflected strain, a progressive iteration will be performed starting from the index of this later ($i_{\varepsilon_{RMIN}}$) until matching the time axis in a similar logic as for the end of the incident pulse and hence f_r may be interpolated as follows:

$$f_r = t(i) - \frac{\varepsilon(i) \cdot (t(i+1) - t(i))}{\varepsilon(i+1) - \varepsilon(i)} \quad (26)$$

The algorithm also checks f_r if there is a value for which the reflected strain vanishes. However the last time $t(N_{inc})$ is taken as the reflected end time if the curve doesn't across time axis.

As presented in Fig.7, the transmitted pulse algorithm for determining the starting and end times is in general similar to the incident one. The transmitted starting time d_t may be interpolated using the ensuing equation:

$$d_t = t_t(i-1) - \frac{\varepsilon_t(i-1) \cdot (t_t(i) - t_t(i-1))}{\varepsilon_t(i-1) - \varepsilon_t(i)} \quad (27)$$

In case of interception with time axis, the transmitted end time can be interpolated by:

$$f_t = t_t(i) - \frac{\varepsilon_t(i) \cdot (t_t(i+1) - t_t(i))}{\varepsilon_t(i+1) - \varepsilon_t(i)} \quad (28)$$

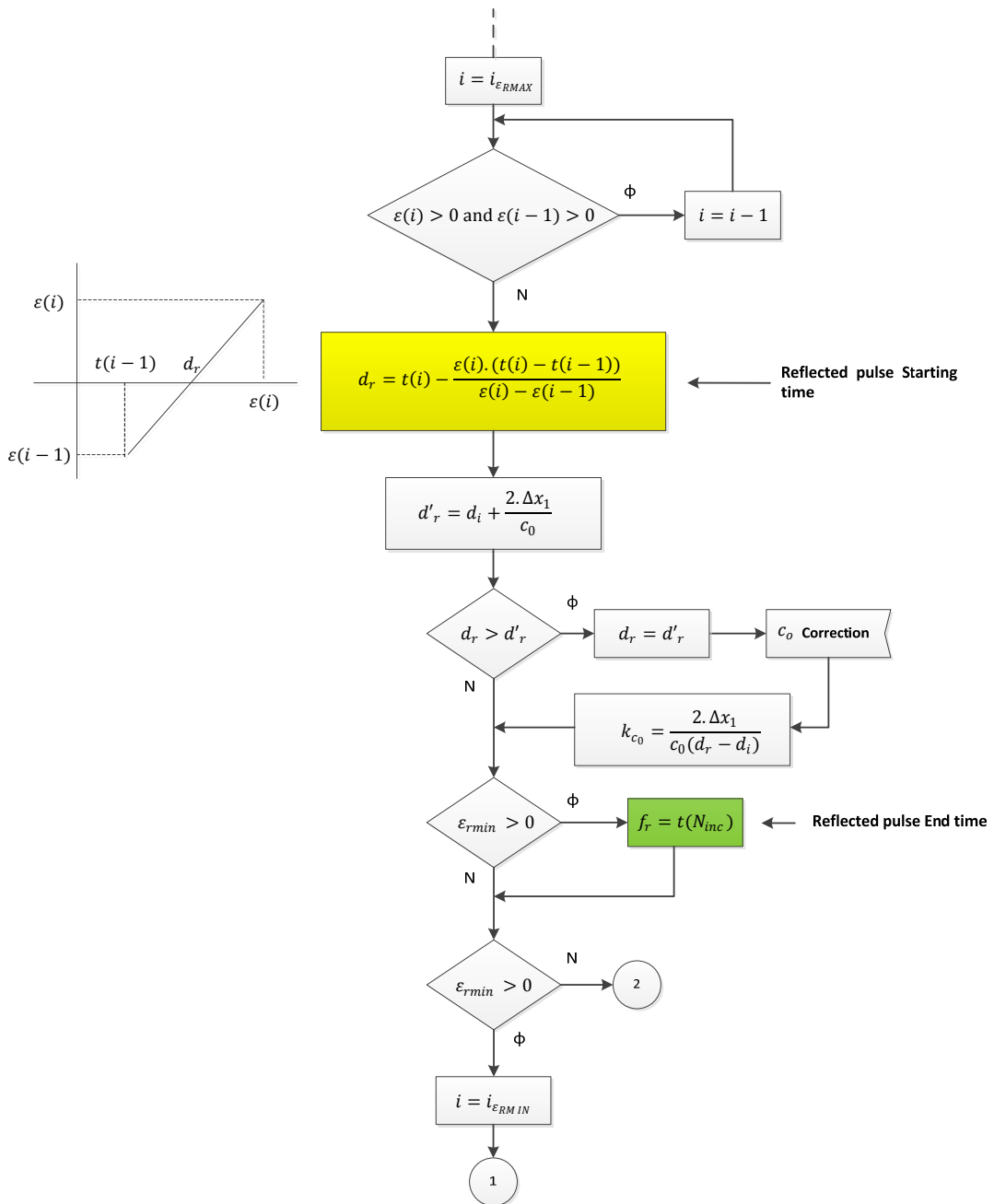


Fig. 21: Flow chart for reflected pulse starting and end times detection (Part 1).

The algorithm is also able to check f_t if there is a value for which transmitted strain vanishes. However the last time $t(N_{trans})$ is taken as the transmitted end time if the curve doesn't cross time axis. N_{trans} here is the number of operands retained for the transmitted strain bridge record.

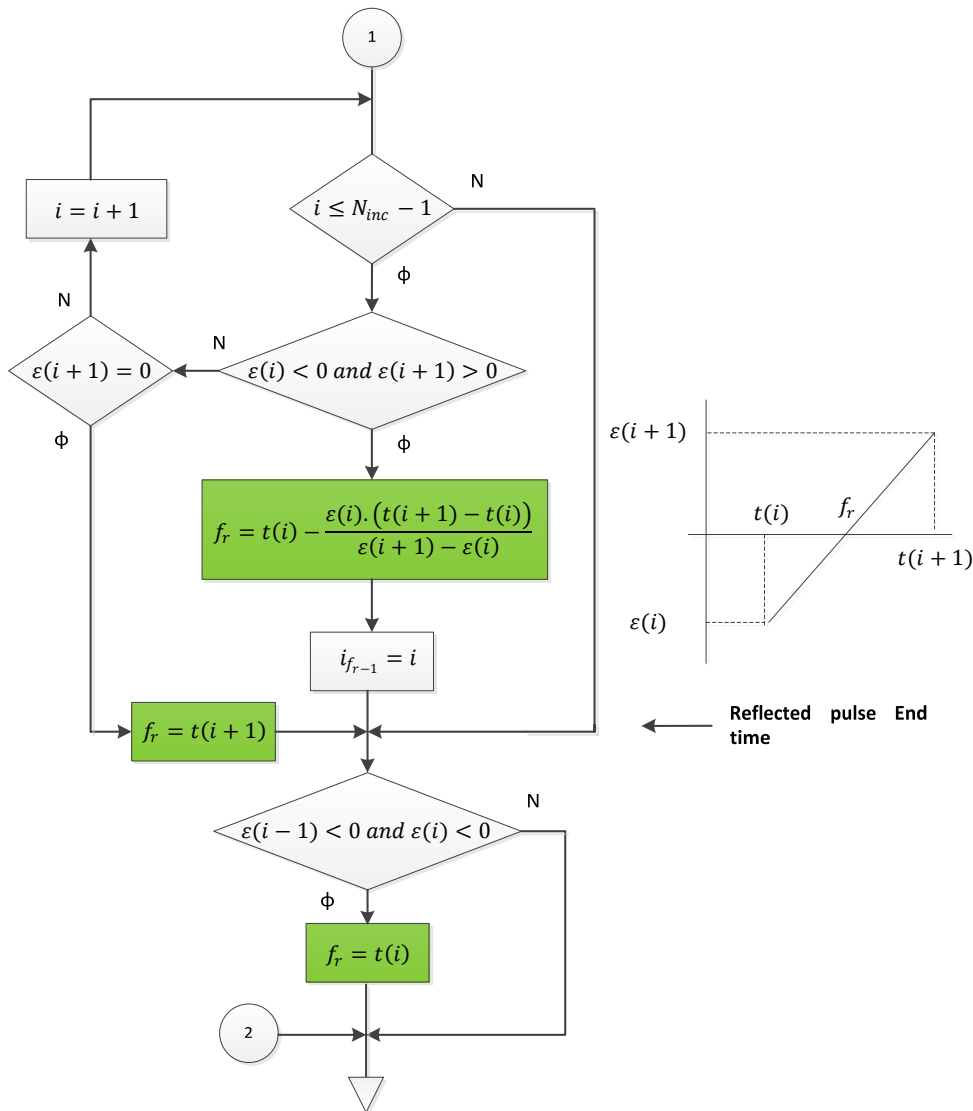


Fig. 22: Flow chart for reflected pulse end time detection (Part 2).

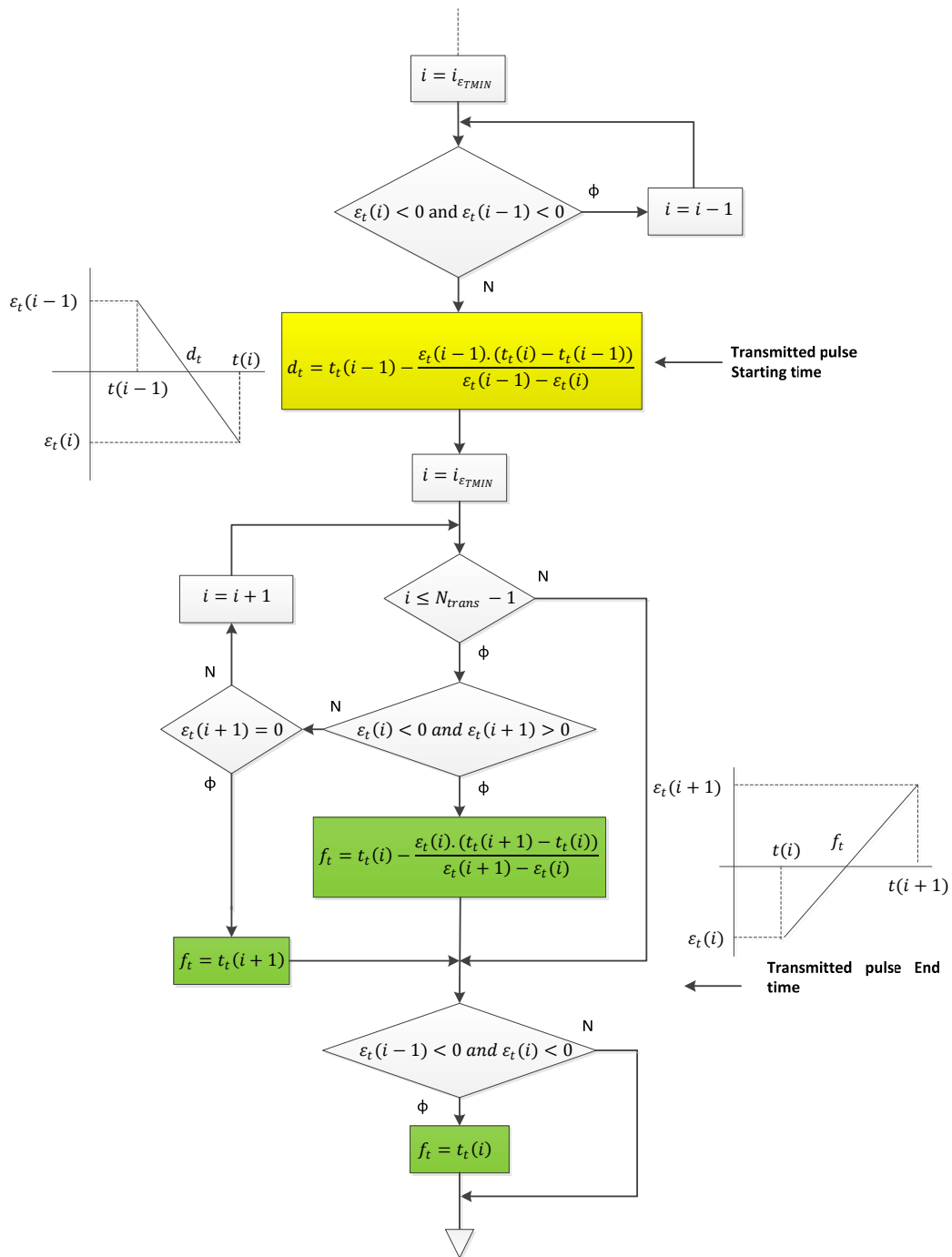


Fig. 23: Flow chart for transmitted pulse starting and end times detection.

1.7.2 Dispersion correction

To correct dispersion, phase velocities for discrete Fourier frequencies are calculated using of the Pochhammer-Chree frequency equation. The delimited strain gage pulses are traveled and reconstructed from their measurement locations to the specimen faces using Fourier transform and dispersion equation. The method described by Li and Lambros [23] is followed; which is a revisiting of the methods described by Follansbee and Frantz [24] and Gong et al [25].

The Fourier series expansion of $\epsilon(t)$ can be expressed in a discrete form as:

$$\epsilon(n\Delta t) = \frac{A_0}{2} + \sum_{k=1,2,..}^K [A_k \cos(k\omega_0 n\Delta t) + B_k \sin(k\omega_0 n\Delta t)] \quad (29)$$

where Δt is the time interval of sampling. $n = 0,1,2,3, \dots, N-1$; with N being the number discretized time points. $k = 1,2,3, \dots, K$; with the maximum K is limited by the number of sampled time points as $K = N/2$ (with $\omega_K = K\omega_0$ corresponding to the Nyquist frequency). The fundamental frequency is defined as $\omega_0 = 2\pi/T = 2\pi/(N\Delta t)$. Also the Fourier coefficients can be calculated by:

$$A_0 = \frac{2}{T} \int_0^T \epsilon(t) \cdot dt = \frac{2}{T} \cdot \sum_{n=1,2,..}^K \epsilon(n\Delta t) \cdot \Delta t \quad (30)$$

$$A_k = \frac{2}{T} \int_0^T \epsilon(t) \cos(k\omega_0 t) dt = \frac{2}{T} \sum_{n=1,2,..}^K \epsilon(n\Delta t) \cdot \cos(k\omega_0 n\Delta t) \Delta t \quad (31)$$

$$B_k = \frac{2}{T} \int_0^T \epsilon(t) \sin(k\omega_0 t) dt = \frac{2}{T} \sum_{n=1,2,..}^K \epsilon(n\Delta t) \cdot \sin(k\omega_0 n\Delta t) \Delta t \quad (32)$$

To perform a discretization correction in the discretized time domain we need to shift the phase of each sine and cosine term in equation (29) by an amount related to the propagation velocity of their particular frequency.

We call ϕ_{dk} the phase change after the particular frequency component travels a distance Δx . It can be expressed as:

$$\phi_{dk} = k\omega_0 \frac{\Delta x}{c_k} \quad (33)$$

where c_k is the value of phase velocity corresponding to the harmonic $k\omega_0$ and is obtained from Pochhammer-Chree solution. Δx is positive for forward dispersion correction and negative for backward correction. Reconstruction of the strain pulse after having traveled a distance Δx is obtained by summation of all frequencies up to $k\omega_0$ as follows:

$$\varepsilon(n\Delta t) = \frac{A_0}{2} + \sum_{k=1,2,\dots}^K [A_k \cos(k\omega_0 n\Delta t) + B_k \sin(k\omega_0 n\Delta t)] \quad (34)$$

So reconstructions of the Incident pulse, reflected and transmitted strain pulses are respectively performed as follows:

$$\varepsilon_i(n\Delta t) = \frac{A_0}{2} + \sum_{k=1,2,\dots}^K [A_k \cos\left(k\omega_0 n\Delta t + \frac{\Delta x}{c_k}\right) + B_k \sin\left(k\omega_0 n\Delta t + \frac{\Delta x}{c_k}\right)] \quad (35)$$

$$\varepsilon_r(n\Delta t) = \frac{A_0}{2} + \sum_{k=1,2,\dots}^K [A_k \cos\left(k\omega_0 n\Delta t - \frac{\Delta x}{c_k}\right) + B_k \sin\left(k\omega_0 n\Delta t - \frac{\Delta x}{c_k}\right)] \quad (36)$$

$$\varepsilon_t(n\Delta t) = \frac{A_0}{2} + \sum_{k=1,2,\dots}^K [A_k \cos\left(k\omega_0 n\Delta t - \frac{\Delta x}{c_k}\right) + B_k \sin\left(k\omega_0 n\Delta t - \frac{\Delta x}{c_k}\right)] \quad (37)$$

1.8 Experimental results

The material of study consists of EPOLAM 2020 resin reinforced with 2400 Tex E-glass unidirectional fibers. The resin is an EPOLAM prepolymer mixed with EPOLAM 2020 hardener and 2020 accelerator. The reinforcement consists of a plain weave fabric with 90% warp yarns and 10% weft yarns. Specimens with 40 cross plies $[0^\circ]$ were cut from a Panel

made by infusion process. The useful shape of specimens is illustrated in Fig. 24.

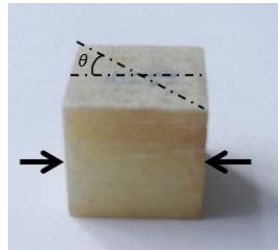


Fig. 24: $[0^\circ]_{40}$ Glass / EPOLAM composite $13 \times 13 \times 13 \text{ mm}^3$.

In this section, we show typical results for the specimen illustrated in Fig. 24 tested with a striker of 0.4m launched under 1.3 bars (9.4 m/s). The raw strain signals are shown in Fig. 25 (a). The pulses separated using the developed method and shifted to the start of the incident pulse with dispersion correction are presented in Fig. 25(b).

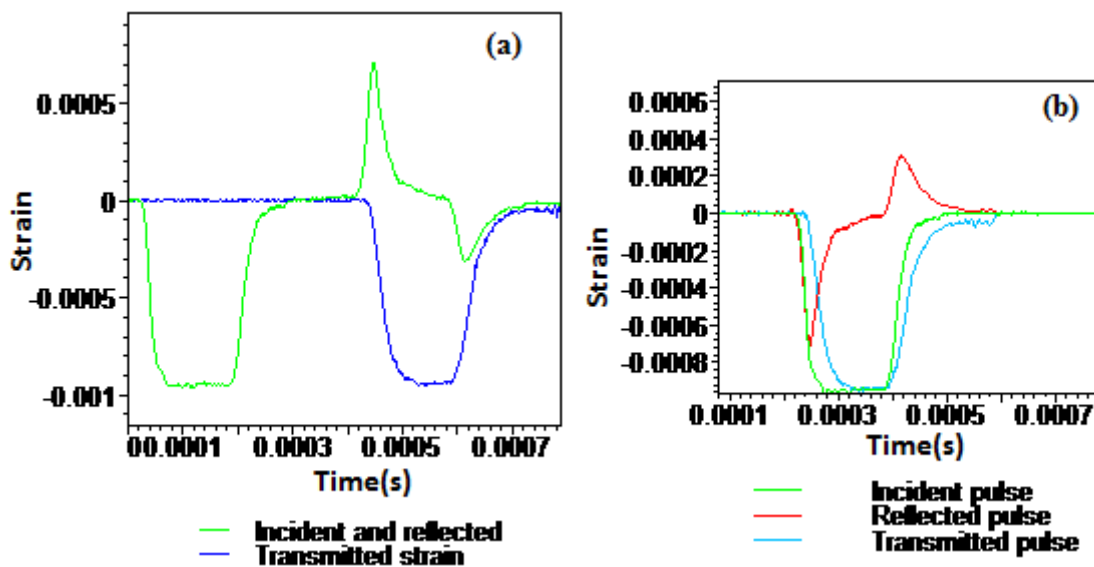


Fig. 25: Typical signal separated using the developed method. (a) represents raw strain signals and (b) shows the three pulses separated using the developed method and shifted to the incident start time.

As presented in Fig. 26, efforts applied on the faces of the specimen shows in general a good equilibrium during the overall test apart the

aliasing observed when forces attain 50KN and also in the end stage of the test ($t > 0.25\text{ms}$).

Stress-strain curve presented in Fig. 27 shows an increase in term of compressive strength with increasing strain till 330MPa for a strain of 1.7% and after bars scattering the stress decrease with keeping the same tendency as for the first rising part. The curve exhibits a plastic deformation of 0.25% in the end. The $[0^\circ]_{40}$ Glass / EPOLAM2020 specimen tested in plane at a strain rate of 508s^{-1} is not damaged.

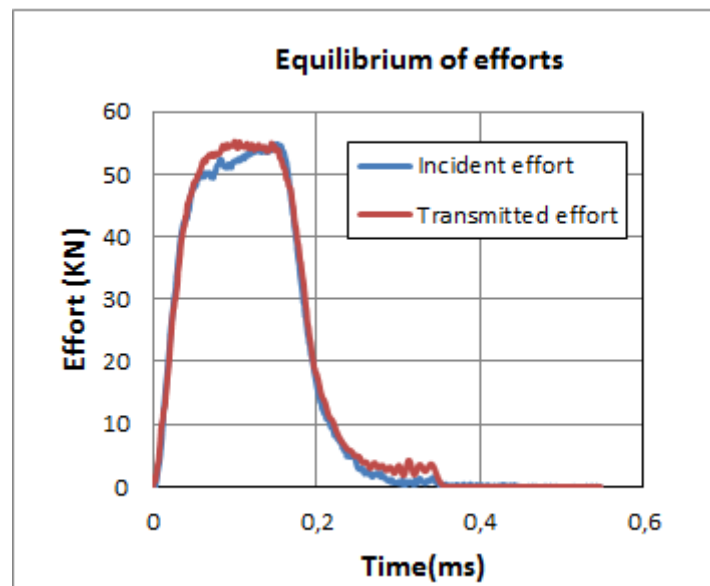


Fig. 26: Equilibrium of efforts during SHPB test.

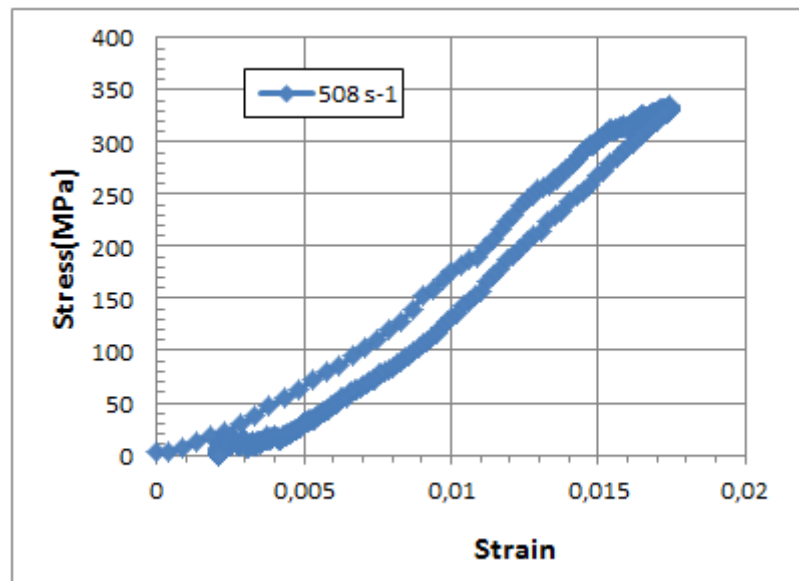


Fig. 27: Stress-strain curve for $[0^\circ]_{40}$ specimen of E-glass/EPOLAM 2020 loaded in plane at a strain rate of 508 s^{-1} .

1.9 Conclusions

A practical way of performing successful SHPB tests is presented in this paper including assumptions of validity, data acquisition, basic governing equations, data processing and typical experimental results. We presented a new consistent and easy method of delimiting pulses. Starting from the maximum and minimum of the reflected pulse and minimums of incident and transmitted pulses, the starting points and end points of pulses are determined using recursive and progressive iterations respectively. A slope is used to interpolate the interception point with time axis at the end of each iteration. For the incident bar, the reflected pulse starting time is also optimized by travelling the wave twice the length between gage's middle and interface incident bar/specimen. The pulses are shifted to the incident starting time after delimitation and dispersion correction.

Typical experimental results presented for $[0^\circ]_{40}$ Glass / EPOLAM2020 composite tested in plane at strain rate of 508 s^{-1} validate our developed delimitation method. Strain signals are well shifted to the incident starting time using the developed iterative method. The derived forces from delimited strains have given representative curves that prove stress

equilibrium during test. Also, a representative stress-strain curve is obtained. The developed iterative method is tested elsewhere with large number of specimens and proved its consistence and reliability with real time gain in data processing.

1.10 References

- [1] Hopkinson B, "A method of measuring the pressure in the deformation of high explosives by the impact of bullets," *Phil Trans Roy Soc*, vol. A213, p. 437–52, 1913.
- [2] Davies RM, "A critical study of the Hopkinson pressure bar," *Philos. Trans. R. Soc. London, Ser. A*, vol. 240, no. 821, p. 375–457, 1948.
- [3] Kolsky H, "An Investigation of the Mechanical Properties of Materials at very High Rates of Loading," *Proc. Phys. Soc. B*, vol. 62, p. 676–700, 1949.
- [4] Gama, Bazle A, Lopatnikov, Sergey L, Gillespi, John W, "Hopkinson bar experimental technique: A critical review," *Appl Mech Rev*, vol. 57, no. 4, pp. 223-250, July 2004.
- [5] Gray III GT, "Classic Split-Hopkinson Pressure Bar Testing," *ASM handbook 8:mechanical testing and evaluation*, pp. p.462-76, 2000.
- [6] Weinong chen, Bo Song, *Split Hopkinson (Kolsky) bar.Design, testing and applications.Mechanical Engineering Series*, Springer, 2011, p. 388.
- [7] Dirk Mohr, Gérard Gary, Bengt Lundberg, "Evaluation of stress-strain curve estimates in dynamic experiments," *International journal of impact engineering*, vol. 37, pp. 161-169, 2010.
- [8] Lifshitz JM and Leber H, "Data processing in the split Hopkinson," *Int. J. Impact Eng*, vol. 15, no. 6, p. 723–733, 1994.
- [9] Han Zhao, Gérard Gary, "On the use of SHPB techniques to determine the dynamic behavior of materials in the range of small strains," *International Journal of Solids and Structures*, vol. 33, no. 23, pp. 3363-3375, 1996.
- [10] Li Z and Lambros J, "Determination of the dynamic response of brittle composites by the use of split Hopkinson pressure bar," *Compos.Sci. Technol*, vol. 59, p. 1097–1107, 1999.

-
- [11] Vuoristo T, Kuokkala V-T, "Creep, recovery and high strain rate response of soft roll cover materials," *Mechanics of Materials*, vol. 34, p. 493–504, 2002.
- [12] Naik NK, Kedar S Pandya, Jayaram R Pothnis, Tamrat Abishu Gelu, "Revisiting Kolsky bar data evaluation method," *Composite Structures*, vol. 111, p. 446–452, 2014.
- [13] Hosur MV, Alexander J, Vaidya UK, Jeelani S, "High strain rate response of carbon/epoxy laminate composites," *Composite structures*, vol. 52, pp. 405-417, 2001.
- [14] Safa K, Gary G, "Displacement correction for punching at a dynamically loaded bar end," *Int.J.Impact Eng*, vol. 37, pp. 371-384, 2010.
- [15] Srinivasan Arjun Tekalura, Oishik Sena, "Effect of Specimen Size in the Kolsky Bar," *Procedia Engineering*, vol. 10, p. 2663–2671, 2011.
- [16] Jue Zhua, Shisheng Hu,Lili Wang, "An analysis of stress uniformity for concrete-like specimens during SHPB tests," *International Journal of Impact Engineering*, vol. 36, p. 61–72, 2009.
- [17] Yang LM, Shim VPW, "An analysis of stress uniformity in split Hopkinson bar test specimens," *International Journal of Impact Engineering*, vol. 31, p. 129–150, 2005.
- [18] Zilong Zhou, XibingLi n, AihuaLiu,YangZou, "Stress uniformity of split Hopkinson pressure bar under half-sine wave loads," *International Journal of Rock Mechanics & Mining Sciences*, vol. 48, p. 697–701, 2011.
- [19] Davies EDH and Hunter SC, "The dynamic compression test of solids by the method of the split Hopkinson pressure bar(SHPB)," *J.Mech. Phys. Solids*, vol. 11, p. 155–179, 1963.
- [20] Naghdabadia R , Ashrafia MJ,Arghavanic J, "Experimental and numerical investigation of pulse-shaped split Hopkinson pressure bar test," *Materials Science and Engineering A* , vol. 539, p. 285–293, 2012.
- [21] Xiangyang Haoa et al., "Dynamic mechanical properties of whisker/PA66 composites at high strain rates," *Polymer*, vol. 46, p. 3528–3534, 2005.
- [22] Ramirez H, Rubio-Gonzalez C, "Finite-element simulation of wave propagation and dispersion in Hopkinson bar test," *Materials and Design*, vol. 27, p. 36–44, 2006.

- [23] Zhouhua Li, John Lambros, "Determination of the dynamic response of brittle composites by the use of the split Hopkinson pressure bar," *Composites Science and Technology*, vol. 59, pp. 1097-1107, 1999.
- [24] Follansbee PS and Frantz C, "Wave propagation in the split Hopkinson pressure bar," *ASME J. Eng. Mater. Technol*, vol. 105, p. 61–66, 1983.
- [25] Gong JC, Malvern LE, and Jenkins DA, "Dispersion investigation in the split Hopkinson pressure bar," *ASME J. Eng. Mater. Technol*, vol. 112, p. 309–314, 1990.

Initial Development of Microdamage in a Zr-BMG under Plate Impact Loading

Zhong Ling¹, Xin Huang² and Lanhong Dai¹

¹LNM, Institute of Mechanics, Chinese Academy of Sciences
Beijing 100190, P.R. China

²Institute of Structural Mechanics, China Academy of Engineering Physics
Mianyang 621900, Sichuan, P.R. China

1.1 Abstract

Plate-impact experiments, using specially designed flyers, are conducted to impact on Zr-based bulk metallic glasses (Zr-BMGs) samples. The experiments focus on the initial development of microdamages under uniaxial strain conditions within very short stress duration, allowing recovery of the samples to examine the induced microdamages. Under impact, the resulted tensile pulses propagate through the Zr-BMG samples and eventually incur microdamages. Carefully polished cross-section surfaces of the recovered samples are then examined. Observations show flaws of $10^{1-2}\mu\text{m}$, perpendicular to tensile pulse propagating direction, distributed on the cross-section surfaces in a narrow zone located around where maximum tensile stress is. Particularly with varied stress durations, the scale and number of the induced flaws vary. Furthermore, microdamage evolution of spallation is observed inferring fracture modes evolution from nano-scale ductile failure to micro-scale brittle fracture. The results also show success of the plate-impact experiments in generating stress-duration dependent microdamages under the well-characterized loading conditions.

1.2 Introduction

Spallation is a typical catastrophic failure occurred in solids under impulsive loading. In crystalline materials, it is recognized to result from nucleation, growth and coalescence of microcracks or microvoids [1]. In bulk metallic glasses (BMGs), the spallation mechanism is far from understood due to the unique amorphous structures and lack of long-range order in the materials [2,3]. Therefore, during the last decade, the

spallation behavior of BMGs has been received great attentions [4-10]. Notable works include to use plate- impact techniques to study macro-responses under impulsive loading, the dependence of BMGs' spallation strength on strain rates, micro-compounds [4-5], Hugoniot elastic limit and dynamic yield strength [5,6]. In particular, it is found that spallation microdamage occurred in Zr-BMGs seems to be very sensitive to stress amplitudes. With stress amplitudes varying from 3-4GPa to 6GPa, spallation fractography presents dimple structures [9,10] or vein (spark-like) patterns [6,7], corresponding to microvoids and microcracks, respectively. Under higher stress amplitude (impact speed $\sim 500\text{m/s}$), zigzag cracks appeared [5]. Clearly, as a dynamic response of BMGs' microstructure, spallation results from the evolution of microdamages caused by stress waves with certain amplitude applied for a period of duration. To gain insights into the patterns of spallation fractography, it is important to further study the behavior of the evolution of microdamages, especially the stress-duration-dependent microdamage of BMGs [1].

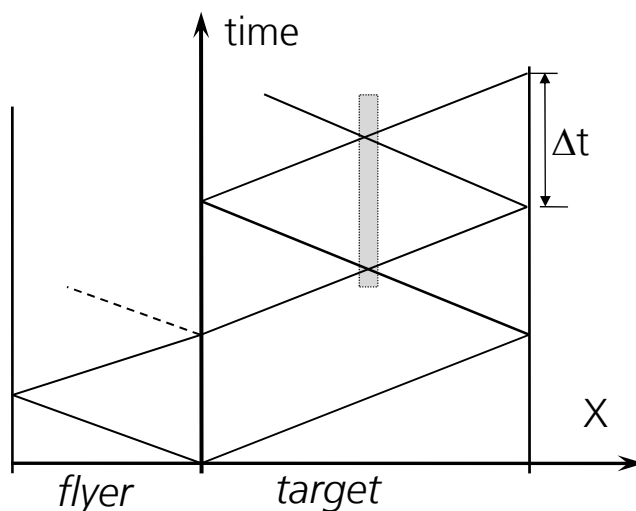


Fig. 1: Lagrangian X-t diagrams for traditional plate impact experiments, where the shadow is location of maximum tensile stress and Δt is its duration.

Plate-impact technique is an effective method to produce tensile pulses and capture the evolution of microdamages in laboratories. By varying target(sample) and flyer thicknesses and impact velocity, one can examine the behaviors of samples subjected to varied amplitudes and duration of tensile pulses [1]. Figure 1 presents a Lagrangian X-t diagram for the flyer and target in plate-impact experiments. When a flyer (thin plate) is

accelerated and strikes a target (flat plate specimen), elastic compressive waves run forward in the target and backward in the flyer. They reflect as unloading or rarefaction waves at the flyer and target free surfaces. Each rarefaction wave reduces the compressive stress to zero behind it. The two rarefaction waves intersect at a place in the target. The shadowed region in the figure indicates where the two tensile stress waves intersect, in which tensile stress's amplitude reaches the maximum and Δt is the maximum tensile stress duration (see Fig.1). Supposing both flyer and target is of the same impedance, the location of the maximum tensile stress depends on flyer's thickness the thinner the flyer, the closer the maximum tensile stress region (the shadowed area in the figure) toward the target's free edge or rear surface [1].

The plate-impact technique was developed and applied to examine changes of defects or microdamage configurations under known short stress pulses in metals, ceramic as well as many crystalline materials [11-15]. More recently, multi-stress pulse technique is also applied to a Zr-BMG for examination of the spallation microdamage evolution in the material[9,10]. Fractography of spallation surface presents microdamage in the material with microvoids $\sim 10^3\text{nm}$, whose nucleating size is deduced to be around 10^0nm [9] and growing size 10^{1-2}nm , when microvoid's coalescence is ignored. Noticing that the whole spallation takes about 300ns in the plate-impact experiment, the duration of microvoids nucleation is inferred to be 100ns, while the time for the growth of microvoids is at most 100ns or so. Therefore, to effectively capture the evolution of BMGs' spallation microdamage by the plate-impact technique, one has to carefully control the duration of stress within 10^2ns with a given stress amplitude.

As discussed, short stress duration around 10^2ns is commonly obtained by making flyer's thickness thin enough through plate-impact experiments. However, extreme care must be taken. As we know, microdamage or microvoids in spallation always appear within the region where the tensile stress reaches its maximum. In the case of a thin flyer, the possible microdamage region may be very close to target's free edge (see Fig.1), which clearly is not good for metallographic examinations of the region with microdamage [1,14,15]. Moreover, reducing flyer's thickness would weak flyer's stiffness, leading to unsuccessful plate-impact experiments. In this investigation, a plate impact method is developed to obtain BMGs' spallation microdamage evolution behavior within 10^2ns under a given

stress amplitude. BMGs' samples are subjected to a stress wave of varied durations (100-300ns) and recovered afterwards for metallographic examination of the damages induced by known stress pulses. Our study focuses on stress duration dependent microdamages of BMGs' spallation behavior.

1.3 Experimental procedure

1.3.1 Developed short stress duration technique

To obtain very short stress duration in plate-impact experiments, Clifton et al employed a longitudinal-momentum trap and a specially designed flyer plate shape to minimize effects of reflected waves to the target (sample) [12-13]. Specifically, the tensile pulses with durations of 5-60ns were obtained, controlled by a gap between the target and the trap[13]. Worthy to notice, in their impact tests, a single flyer was still employed. Inspired by previous studies of [13] and tailoring to the characteristics of microstructure and spallation microdamages of the BMGs, a set of double-flyers with a given gap is proposed here instead of the single flyer commonly used in plate-impact tests. Figure 2 exhibits a Lagrangian X-t diagram for stress waves' propagating through the double flyers and target of the developed plate-impact experiments. As shown in the figure, an impactor assembly consists of two flyers, a front and a back, of the same impedance with a pre-set gap between them.

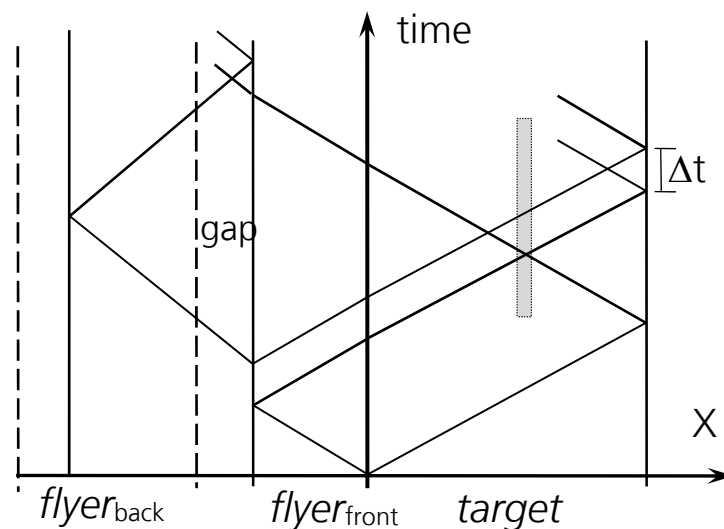


Fig. 2: Lagrangian X-t diagram for current plate-impact experiments, where Δt is maximum tensile stress duration.

When the front flyer impacts the target, a compressive pulse is generated, propagating through the interior of the flyer and the target, and then reflecting as rarefaction waves at the free surfaces. In the target, two rarefaction waves, transferred from the flyer and reflected from the target's rear surface, would meet at a position, indicated by the shadows in the figure, and produce a maximum tensile stress. The back flyer runs after the front once the tensile pulse reflects from the front flyer's rear surface. Another compressive pulse generated in the front flyer when the two flyers strike, propagates into the target. Afterwards this compressive pulse in the target meets the tensile pulse reflected from the target's rear surface. Consequently, the duration of the maximum tensile stress, in the target, is equal to the time required to close the gap, Δt . Particularly, the target's thickness and diameter are designed with a proper ratio to avoid rare waves from lateral boundaries of the target.

1.3.2 Plate-impact experiments

The material used in the experiments is a Zr-based amorphous alloy with the nominal composition $\text{Zr}_{41.2}\text{Ti}_{13.8}\text{Cu}_{12.5}\text{Ni}_{10}\text{Be}_{22.5}$ (Vit 1). Conventional x-ray diffraction verified that all the samples were fully amorphous before the spallation experiments. Flyers' material is brass, whose impedance approximates to Vit 1's. Table 1 presents physical properties of the materials used in the experiments, where ρ is the density, E the elastic modulus, ν the Poisson ratio and c_L the longitudinal wave speed.

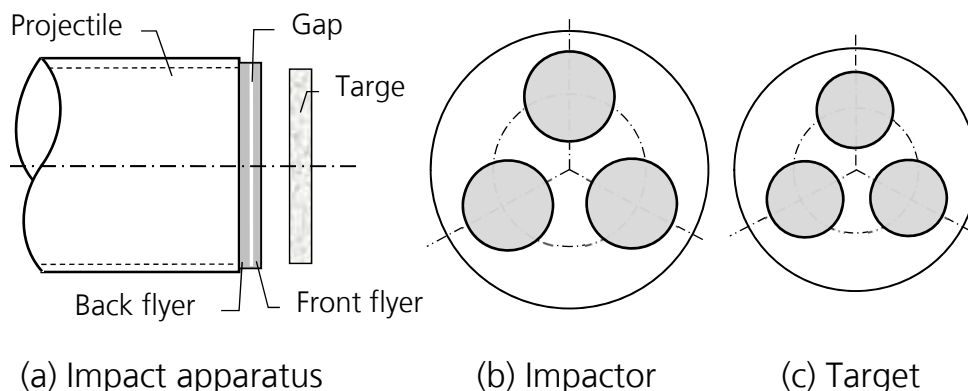


Fig. 3: A schematic of the special designed plate-impact apparatus (a) Plate-impact apparatus; (b) Impactor and (c) Target.

Table 1: Materials and their physical parameters in the spall tests.

Materials	ρ [kg/m ³]	E [GPa]	ν	c_L [m/s]
Vit 1	6000	98.6	0.354	5182
Brass	8400	90	0.31	3740

The plate-impact experiments were performed with a 101 mm single-stage light gas gun. To study the initial development of microdamage evolution in Zr-BMG, the developed short-stress pulse technique was applied. In our plate-impact experiments, instead of using a single flyer, double-flyers are employed. Figure 3 gives a schematic of the specially designed apparatus, where three BMG samples are impacted by the three sets of double-flyers with gaps in varied size, so that different stages of microdamage, under the same stress amplitude, could be "frozen in" the BMG samples. The experimental implementation is similar to that of [9]. It is noticed that in each plate all surfaces of flyers and targets were kept flat and parallel with cares. Meanwhile, to minimize the influence of projectile's rotation, i.e. always less than 1°[9], the flyers' diameter was designed to be 25mm, to be larger than 20mm of the targets' diameter. Therefore each flyer could cover, in case of the maximal rotation angle, the corresponding sample during the impact. More details of the experimental implements can be found in [9]. After the impact experiments were performed the samples of Zr-BMG were recovered and sectioned to observe the induced microdamages. Each of the tested samples was cut along its diameter. After refined polishing with cares, a scratch-free cross-section of samples was obtained by etching with a solution of HNO₃ and CH₃OH (1:3), temperature below 0 °C and voltage~10 Volt [17].

Table 2: Experimental data for the plate-impact experiments.

Sample	V [m/s]	δ [μm]	Δt [ns]	d_f [mm]	d_b [mm]	d_t [μm]	L_s/d_t
1-1	200	25	125	0.777	1.888	2505	0.42
1-2	200	50	250	0.837	1.764	2573	0.44
1-3	200	75	375	0.811	1.833	2585	0.43

As their etching priority microdamages or shear bands could be caught with high resolution SEM [17]. Table 2 lists experimental parameters of spallation microdamage evolution tests, where V is impact velocity, σ stress amplitude, δ thickness of the gap, Δt maximum tensile stress duration, d_f , d_b and d_t is the thickness of the front flyer, back flyer and target, respectively. The last term is the ratio of the designed spalling position to targets' thickness. L_s is the designed distance from position of σ_{\max} to the rear surface of a target.

1.4 Experimental results

1.4.1 Micro-observations to BMG samples

Figure 4 displays observations of parts of cross-section of microdamaged samples under varied stress durations and impact velocity of 200m/s. The arrow shows the impact direction. Fig.4d schematically shows a cross-section of a sample, where the red square indicates the region shown in Figs. 4a, 4b and 4c. As exhibited in the figure, the cross-section of each sample was etched as scratch-free, but the strip-like concave regions were verified as microdamage regions. Under the same stress amplitude of 3.2GPa, the number of such microdamage regions observed in the samples changes with varying stress durations. With almost the same magnifications and under the same stress amplitude, no microdamage region can be seen on the cross-section of the sample with a stress duration of 125 ns (Fig.4a).

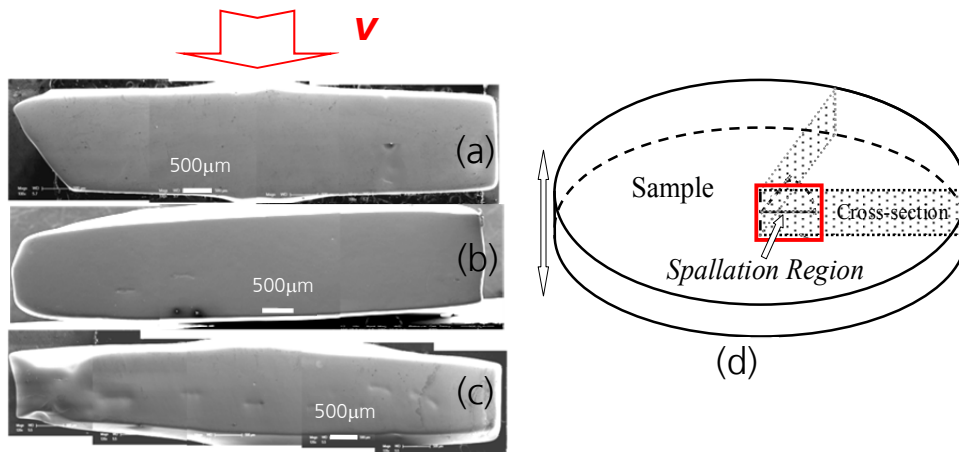


Fig. 4: Close-up observations of micro-damaged samples under different stress durations, $V=200\text{m/s}$ ($\sigma=3.2\text{GPa}$), (a) $\Delta t=125\text{ns}$; (b) $\Delta t=250\text{ns}$; (c) $\Delta t=375\text{ns}$; (d) A schematic of a cross-section of a sample, where microdamage zones showed in (a), (b) and (c) are indicated as the squared.

When the stress duration is increased to 250ns, a few strip-like microdamage regions appear at the centre part of the sample's cross-section (Fig. 4b). However, while stress duration increases to 375ns, more such microdamage regions are observed distributed over the majority of the cross-section (Fig. 4c). As displayed in the figure, such strip-like microdamage regions are always $10^2\mu\text{m}$ in length and parallel to each other. The strip regions seem to be scattering only in zones slightly closer to the samples' rear edges or the rear surfaces, approaching the designed positions of the maximum tensile stress. Each strip-like microdamage region is almost perpendicular to the impact direction. The above observation suggests that, such strip-liked microdamage regions are microscopic flaws of $10^2\mu\text{m}$ resulted in the BMG samples' spalling under plate impacting.

Details of these strip-liked microdamage regions or micro-flaws are examined with high magnifications. The micro-flaws in length of $10^2\mu\text{m}$ are found to consist of several shorter flaws in length of $10^1\mu\text{m}$. Figure 5 displays typical micrographs of the flaws. Figure 5a shows a partial cross-section for a sample, $\sigma=3.2\text{GPa}$, $\Delta t=250\text{ns}$. It is observed that in region-A, there is a strip-like damage region in length of $10^2\mu\text{m}$.

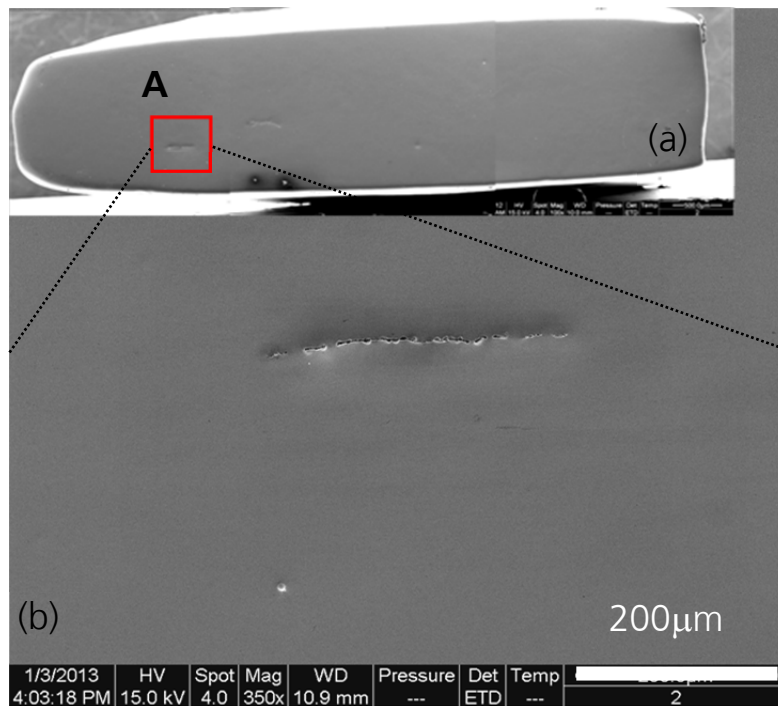


Fig. 5: Close-up observations to a sample ($\sigma=3.2\text{GPa}$, $\Delta t=250\text{ns}$): (a) A part cross-section of the sample; (b) An enlarged image of region-A in the cross-section.

Figure 5b is an enlarged image of region-A. Obviously, the strip-like microdamage region, with length about $\sim 300\mu\text{m}$, appeared to be a microscopic flaw shown in Fig.5a, indeed consists of several disconnected short micro-flaws or microvoids in lengths of $10\text{-}30\mu\text{m}$ (Fig.5b). Such shorter micro-flaws are distributed along a strip, almost parallel to the rear edge of the sample and thus are perpendicular to the impact direction. These flaws are typical mode-I cracks in microscopic levels. Moreover with much higher magnifications, micrographs of these shorter micro-flaws of $10^1\mu\text{m}$ exhibit dimples with 10^{1-2}nm in size, without any tortuous, distributed over the flaws' visible surfaces [16].

1.4.2 Analysis and discussion

As shown in figures 4 and 5, the strip-like flaws of $10^2\mu\text{m}$ on the cross-sections of the Zr-BMG samples, parallel to each other and perpendicular to the impact direction, represent characteristics of mode-I cracks in microscopic levels. The number of flaws also increases with an increasing tensile pulse duration. It is straightforward to understand that the flaws are induced by tensile pulse and grow with the pulse duration. Noticing the flaws' locations in the samples and samples' uniaxial strain

environments, one can identify that these flaws are spallation microdamages, resulting from plate impact loading. This therefore deduces that the current experiments employed with double-flyers are successfully performed. In addition, the morphology of these flaws, similar to mode-I cracks and not reported in previous studies for BMGs [6-8,17-20], is of spallation striation, which can be further explained from microdamage evolution in the material.

The micrograph of $10^{1-2}\mu\text{m}$ micro-flaws under high magnifications reveals some useful information about microdamage evolution in the material. In our BMG samples, dimples of size 10^{1-2}nm , without any tortuous, appeared in the flaws visible surfaces [16] infer dimple rupture in nano-scale, corresponding to ductile failure in nano-scale [17]. Whereas the flaws of $10^1\mu\text{m}$ and several $10^2\mu\text{m}$ cracks shown in Figs. 4b, 4c or 5a, refer brittle fracture in microscopic levels. Except for the flaws orientation, such ductile-brittle microscopic mode of fracture in spallation of metallic glasses seems to be like what was observed in previous studies for BMGs [17]. We know, due to its unique amorphous structure and lack of a long-range order in the atomic structure [2,3], BMGs failure exhibits unusual fracture behaviors. BMGs' fracture and failure under uniaxial tensile stress or plane stress, whether quasi-static or dynamic, do occur along directions with an angle to the tensile axis or along a slip band (or shear band) that has an angle to the tension axis [17,18,20]. The fracture topography is found to be of typical veins pattern formed with ridges and flat, smooth surface in the BMG samples. The vein-like pattern was suggested to be formed first by nucleation of cores due to tensile stresses then by the beginning of crack/voids propagation under shear stresses[17,18]. As illustrated by Spaepen and Turnbull [19], such fracture pattern in the BMGs is considered to be the result of the breaking of a fluid layer between two solid surfaces. Under uniaxial tensile loading, slip bands or shear bands are easy to be driven along the maximum shear stress direction[17,18,20]. Within these narrow bands, density of free volumes, intrinsic defects in BMGs[21], increases to form a fluid layer and eventually the fluid layer breaks and leaves vein patterns. Worthy to notice here, Spaepen and Turnbull [19] stressed that the increased free volume is created by the hydrostatic tension existent at the head of a growing band in the BMGs.

However, micrographs of current study show that there is no slip or shear band with any angle to the impact direction in the microdamaged Zr-

BMG samples, even with higher magnifications. This is quite different from what has been reported in previous studies. As we know, nucleated microdamage can grow in varied modes determined by the matrix material properties and the stress and strain environments [17]. Clearly, the stress environment of spallation of solids in laboratories is uniaxial strain corresponding to 3-D stress and an instantaneous pulse with a high stress amplitude. Such stress-strain environment provides hydro-tension and high strain rates in Zr-BMG samples, under which the density of free volumes in BMGs prefers to increase [19,22]. Thus, in the case of BMG's spallation especially under high strain rates of impact, the density of free volume in a Zr-BMG sample becomes much higher, driving a fluid layer to easily form. The fluid layer is of course located to where the maximum tensile stress, and is perpendicular to the impact direction. Free volumes in high density would coalesce to form voids in nano-scales in the fluid layer [9]. These nano-voids would then grow to become micro-voids under hydro-tensile stress with increasing tensile stress duration. Eventually micro-flaws or cracks would form (Fig. 5b) and link together, leading to the fluid layer finally breaking. The fluid layer breaking leaves traces of dimples in various sizes on flaws' visible surfaces[16] or the flaws in various sizes on the cross-sections. Especially, once the fluid layer forms and microdamages nucleate in the Zr-BMG samples, stresses in the areas nearby or around the layer are to be relaxing, so that there would be no more new energy to drive slips or shear bands forming. That is why no obvious traces of shear bands but strip-like microdamages are observed in the cross-sections of the Zr-BMG samples.

1.5 Conclusions

A plate-impact technique is developed to capture the initial microdamage of spallation occurred in Zr-BMG samples. Conclusions are as follows:

- 1) In the current plate-impact technique, two flyers are applied instead of a single flyer commonly used in plate-impact experiments. Especially, short stress durations of 10^2 ns are controlled by a given gap between the two flyers. The spallation location in the targets can be designed by this technique;
- 2) On the cross-section of the samples, strip-like microdamages, parallel to each other and perpendicular to the impact direction, are appeared

around the designed spallation location. Micro-observations show that the microdamages are those of spallation;

3) With an increasing stress duration, the scale, number and form of the microdamage are changed even if under the same stress amplitude. Microdamage patterns varying with stress durations illustrate that spallation microdamage evolution in the Zr-BMG infers to the fracture modes transferring from nano-scale ductile failure to micro-scale brittle fracture.

1.6 Acknowledgements

This work is financial supported from the NSFC (Grants Nos.: 11272328 and 10872206) and the National Natural Science Foundation of China-NSAF. Grant No: 10976100. Z Ling is grateful to Prof. LT Shen and Ms. YL Deng for their advisable suggestions on the impact experiments of this work.

1.7 References

- [50] Curran, D.R., Seaman, L., Shockey, D.A.: *Dynamic failure of solids*, Phys. Report, 147, 253-388, 1987.
- [51] Inoue, A., Kato, A., Zhang, T., Kim, S.G. and Masumoto, T.: *Mg-Cu-Y amorphous alloys with high strengths produced by a metallic mold casting method*, Mater. Trans. JIM, 32, 609, 1991.
- [52] Peker, A. and Johnson, W.L.: *A highly processible metallic glass $Zr_{41.2}Ti_{13.8}Cu_{12.5}Ni_{10.0}Be_{22.5}$* , Appl. Phys. Lett. 63, 2342, 1993.
- [53] Eliaz, N., Moshe, E., Eliezer, S., Eliezer, D.: *Hydrogen effects on the spall strength and fracture characteristics of amorphous Fe-Si-B alloy at very high strain rates*, Metall. Mater. Trans. A, 31(4), 1085-1093, 2000.
- [54] Zhuang, S.M., Lu, J., and Ravichandran, G.: *Shock wave response of a zirconium-based bulk metallic glass and its composite*, Appl. Phys. Lett., 80(24), 4522-4524, 2002

- [55] Turneaure, S.J., Dwivedi, S.K. and Gupta, Y.M.: *Shock-wave induced tension and spall in a zirconium-based bulk amorphous alloy*, J. Appl. Phys., 101(4), 043514, 2007.
- [56] Escobedo, J.P. and Gupta, Y.M.: *Dynamic tensile response of Zr-based bulk amorphous alloys: Fracture morphologies and mechanisms*, J. Appl. Phys. 107 (12), 123502, 2010.
- [57] Martin, M., Kecskes, L. and Thadhania, N.N.: *Dynamic compression of a zirconium-based bulk metallic glass confined by a stainless steel sleeve*, Scripta Mater. 59, 688–691, 2008.
- [58] Huang, X., Ling, Z., Zhang, H.S., Ma, J., Dai, L.H., *How does spallation microdamage nucleate in bulk amorphous alloys under shock loading?* J. Appl. Phys. 110(10), 103519, 2011.
- [59] Ling, Z., Huang, X., Shen, L.T. and Dai, L.H.: *Spallation behavior of a Zr-metallic glass*, Proceedings of DYMAT2012, EPJ Web of Conferences 26, 02003, 2012.
- [60] Flinn, J. E., Duvall, G. E., Fowles, G. R. and Tinder, R. F.: *Initiation of dislocation multiplication in lithium fluoride monocrystals under impact loading*, Journal of Applied Physics 46, 3752-3759, 1975.
- [61] Kumar, P. and Clifton, R. J.: *Dislocation motion and generation in LiF single crystals subjected to plate impact*, J. Appl. Phys. 50(7), 4747-4762, 1979.
- [62] Clifton, R.J., Raiser, G., Ortiz, M. and Espinosa, H.: *A soft recovery experiment for ceramics*, in Shock Compression of Condensed Matter-1989, S.C. Schmidt, J.N. Johnson, and L.W. Davison, Editors., Elsevier Science: New York., 437-440, 1990.
- [63] Bai, Y. L., Ling, Z., Luo, L. M. and Ke, F. J.: *Initial development of microdamage under impact loading*, J. Appl. Mech.-Tran. ASME, 59 (3), 622-627, 1992.
- [64] Ling, Z. and Shen, L. T.: *Microcracks propagation in metal matrix composites under impact loading*, J. Phys. IV 134, 957-964, 2006.
- [65] Huang, X.: Doctoral dissertation, University of CAS, 2013.
- [66] Pampillo, C.A.: *Flow and fracture in amorphous alloys*, J. of Mat.Sci. 10, 1194-1227, 1975.
- [67] Zhang, Z.F., Eckert, J., Schultz, L.: *Difference in compressive and tensile fracture mechanisms of $Zr_{59}Cu_{20}Al_{10}Ni_8Ti_3$ bulk metallic glass*, Acta Mater. 51, 1167-1179, 2003.
- [68] Spaepen, E. and Turnbull, D.: *A mechanism for the flow and fracture of metallic glasses*, Scripta Met. 8,563-568, 1974.

- [69] Spaepen, F.: *A microscopic mechanism for steady state inhomogeneous flow in metallic glasses*, Acta Metallurgica, 25(4), 407-415, 1977.
- [70] Turnbull, D. and Cohen, M.H.: *Free-volume model of the amorphous phase: glass transition*, J. Phys. Chem. Solids, 34,120-125, 1961.
- [71] Flores, K.M., Dauskardt, R.H.: *Mean stress effects on flow localization and failure in a bulk metallic glass*, Acta Mater., 49, 2527-2537, 2001.

Dynamic Tensile Properties of Bioplastic Polymer Blends and Fracture Surface

Masahiro Nishida

1.1 Introduction

Biodegradable plastics (plastics that can decompose in the natural environment) and bioplastics (plant-derived or renewable plastics) are being investigated extensively, and new biodegradable plastics and bioplastics continue to be developed. Such plastics are already used in many industrial products, such as the interior parts of cars, components of computer and cell phone cases, and packing peanuts (foam peanuts). However, such applications are currently limited to machine parts that are not subjected to high loads. Many studies have been conducted to develop various industrial products that can be manufactured using biodegradable plastics and bioplastics.

In most cases, the impact properties of plastics including biodegradable plastics and bioplastics have been determined based on the experimental results of Izod/Charpy impact strength tests and Dynatup impact tests. However, the basic mechanical properties of such plastics, including their strain rate sensitivity to yield stress, elongation at break, and fracture morphology, remain unknown. The author's group has been studying the mechanical properties of bioplastics and their composite materials with respect to dynamic compression/tension using compression and tensile split Hopkinson bar methods and universal testing machines. I would like to introduce two of our experimental results.

1.2 Experimental setup

At high strain rates, the dynamic properties of the specimens were examined using the tensile split Hopkinson bar test, as shown in Fig. 1. The diameters and lengths of input and output bars were 12 mm and 2000 mm respectively. Strain gages were applied to both sides of the input and output bars at distances of 1750 mm and 350 mm from the specimen, respectively. The stresses and strains of the specimens [1, 2]

were calculated from the strains of the bars measured by strain gages, based on the following equations:

$$\sigma(t) = \frac{AE}{A_s} \varepsilon_T(t) \quad (1)$$

$$\varepsilon(t) = \frac{2c_3}{L} \int_0^t [\varepsilon_I(t) - \varepsilon_T(t)] dt \quad (2)$$

where ε_I and ε_T are the axial strains in the input bar induced by the incident wave, and the axial strain in the output bar induced by the transmitted wave, respectively. E and c_3 are the Young's modulus and the elastic wave velocity of the input and output bars, respectively. L is the specimen's thickness. A and A_s are the cross-sectional areas of the input/output bars and the specimens. The input and output bars were made of stainless steel (SUS304), and their material constants used in the calculations are listed in Table 1. We preserved the specimens in a desiccator at a humidity of 30–40% until just before use in order to avoid the effects of moisture absorption on the specimens. During the experiments, our laboratory was maintained at a temperature of 25 ± 2 °C and a humidity of 19-54%. Plate-type specimens were employed for the dynamic tensile tests, as shown in Fig. 2. The specimens were connected with the input and output bars using support jigs, fixing pins of 3 mm in diameter, and glue.

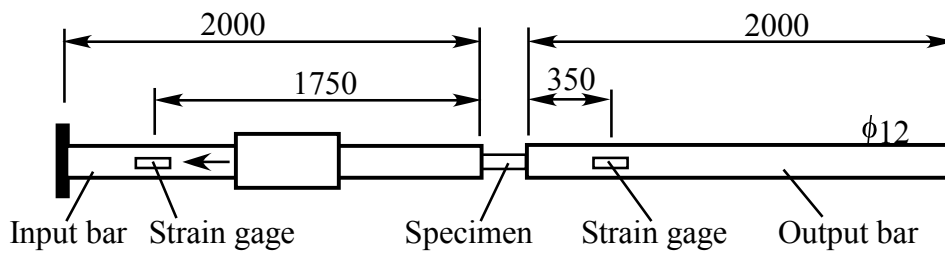


Fig. 1: Experimental setup for tensile Hopkinson bar (Kolsky bar) method.

Tab. 1: Material constants of input and output bars used in calculations.

Density [kg/m ³]	Elastic wave velocity in bar, c_3 [m/s]	Young's modulus E [GPa]
8.0×10^3	4970	200

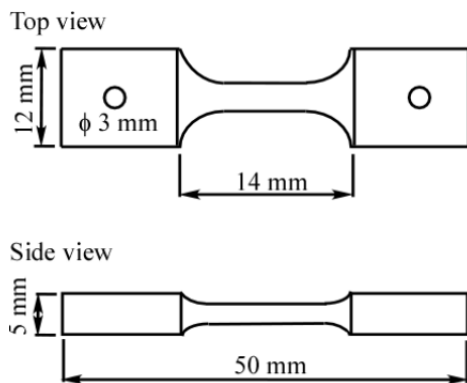


Fig. 2: Dynamic tensile test specimen.

1.3 Experimental results

1.3.1 PLA/PBAT polymer blends

Fukuda [3] showed that the Izod impact strength of PLA/PBAT polymer alloys is large when 2,5-Dimethyl 2,5-di(tert-butylperoxy) hexane (NOF Corporation, PERHEXA 25B) was added as a crosslinking agent for grafting PLA and PBAT. In particular, when the mixing ratio of PLA/PBAT/crosslinking agent was 60/40/1, the Izod impact strength was 60 kJ/m^2 , which was comparable to that of polycarbonate (PC) [4]. We measured the stress-strain curves of the polymer alloys using a universal testing machine to determine the main reason for the increase in Izod impact strength [5-6].

1.3.1.1 Materials

Polymer blends of PLA and PBAT were prepared using PLA from Toyota Motor Co. (Eco-plastic S-17) and PBAT from BASF (Ecoflex). The mixing ratios (mass fraction) of PLA and PBAT were 80/20, 70/30, 60/40. The crosslinking agent, 2,5-Dimethyl 2,5-di(tert-butylperoxy) hexane was added at a weight ratio of one. The polymer alloys were prepared using a twin-screw extruder (Technovel Co.) at 180°C . The screw speed was 300 rpm, and the pellet feed rate was 100 g/min. After melt mixing, the strands prepared by the twin-screw extruder were cooled by water, pelletized, and then dried. Then, plates were made using a hot press at 190°C and 5 MPa for 30 min. The tensile test specimens had a gage

length region of approximately 2 mm × 2 mm and a gage length of 4 mm.

1.3.1.2 Dynamic Tensile Properties

Fig. 3 shows the stress-strain curves of specimens. In the case of PLA/PBAT=80/20, the crosslinking agent addition only slightly increased the elongation at break. When the mixing ratio of PBAT was minor, the effect of the crosslinking agent addition was small. In the case of PLA/PBAT=60/40, the crosslinking agent addition clearly increased the elongation at break. The crosslinking agent addition did not affect the flow stress and/or yield stress or Young's modulus.

1.3.1.3 Fracture Surface

Fig. 4 shows that, in the case of PLA/PBAT=60/40, there are many spherical or hemi-spherical holes and clusters of holes (0.1 to 0.3 mm in diameter) in the fracture surface of the specimens. Fig. 5 shows images of the fracture surfaces using SEM. Regardless of the crosslinking agent used, the stretching of the matrix was observed from the photographs of the fracture surfaces of all specimens.

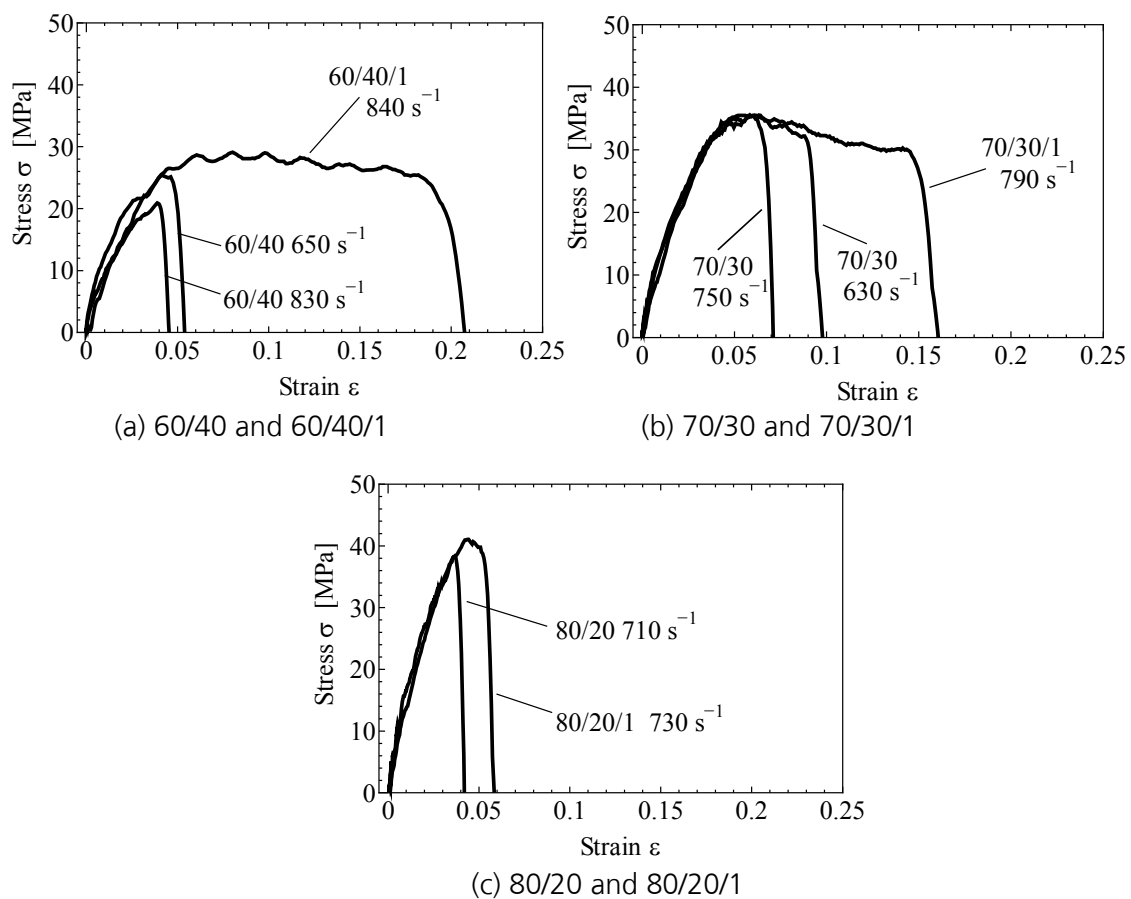


Fig. 3: Effect of crosslinking agent.



Fig. 4: Enlarged images of 60/40.

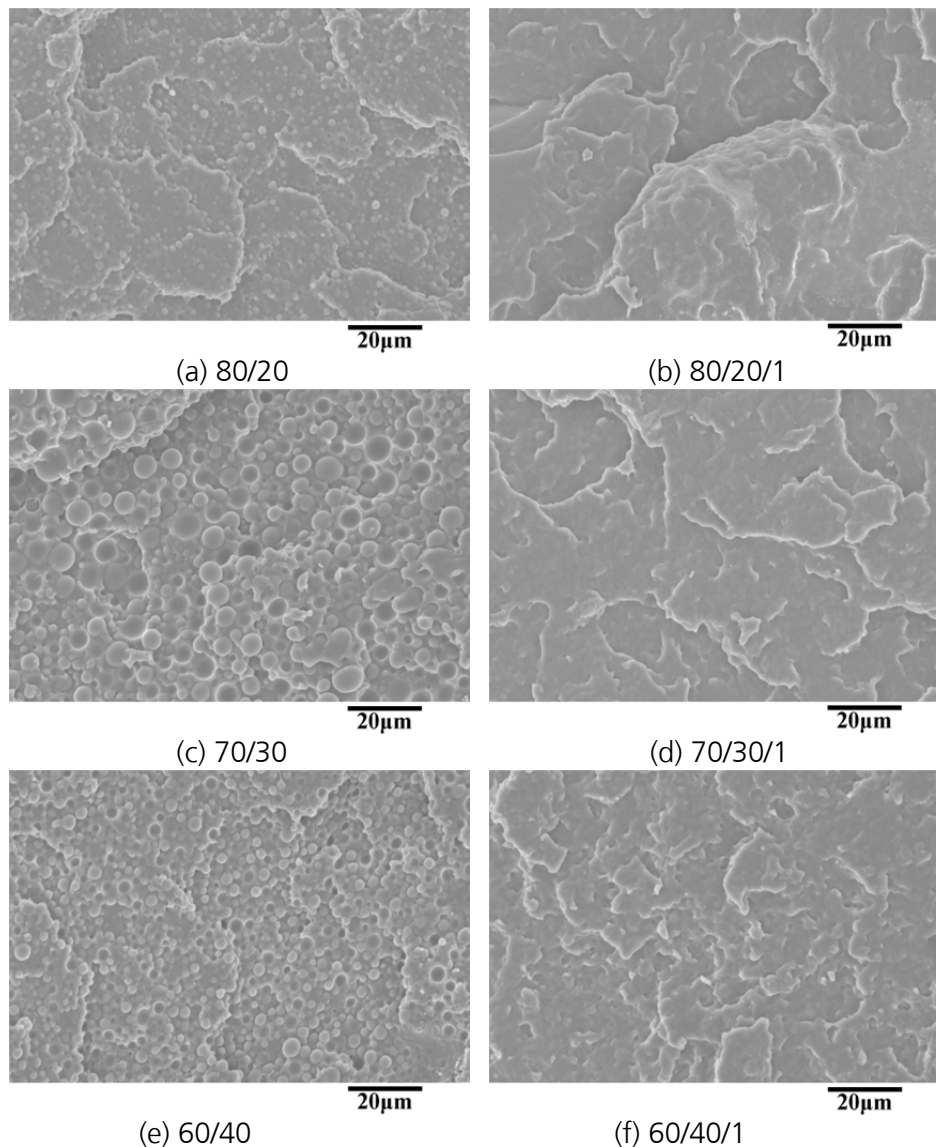


Fig. 5: Effect of crosslinking agent on fracture surface (SEM photographs)

1.3.2 PA11/nanoparticle composite materials blends

Polyamide 11 (PA11) is a bioplastic [7]. It is produced from castor seeds (renewable resources). Castor seeds are inedible. Bioplastics derived from inedible resources are important because of future food security issues and starvation issues. In order to use PA11-based industrial products more widely, mechanical properties have to be improved by polymer blends, polymer alloys, and the addition of particulate fillers or fibers. Several attempts have been made to improve the mechanical properties of PA11 [8-10]. In order to increase the Young's modulus, in this study,

silica nanoparticles were added to PA11. We examined the effects of silica nanoparticle addition on the stress-strain curves of polymer composites at high strain rates. We used silica particles with surface treatments and untreated silica particles.

1.3.2.1 Materials

We used polyamide 11 (Arkema; Rilsan PA11, BMN O TLD). The silica nanoparticles that were used as filler (Admatechs Co., Admafine, SO-C2) were spherical and their average diameter was 0.5 μm . In order to improve the interface between the matrix and fillers, we used silica nanoparticles with surface treatments, aminosilane treatments (SC2500-SXJ), and epoxy silane treatments (SC2500-SEJ). The mixing ratio of PA11 to nanoparticles was 90/10 by weight. The polymer composites were prepared by using a twin-screw extruder (Technovel Co.) at 210°C. The screw speed was 300 rpm, and the pellet feed rate was 100 g/min. After melt mixing, the strands prepared by the twin-screw extruder were cooled by water, pelletized, and then dried. Then, plates were prepared by using a hot press at 210°C and 5 MPa for 30 min.

1.3.2.2 Dynamic Tensile Properties

Fig. 6 shows nominal stress-strain curves of the dynamic tensile tests at a strain rate of 600 s^{-1} . The dynamic Young's moduli (initial slopes of stress-strain curves) were increased by adding silica nanoparticles. The surface treatment did not affect the dynamic Young's modulus. The specimen with nanoparticles of aminosilane treatments did not break at a strain of 0.17, which is the maximum tension for the tensile split Hopkinson bar method as well as the neat PA11. The specimen with nanoparticles of epoxy silane treatments broke at a strain of 0.04, which was in an elastic region. The yield stresses of neat PA11, specimens with SO-C2 (untreated) particles, and nanoparticles of aminosilane treatment were almost the same. The maximum stress of the specimens with nanoparticles of epoxy silane treatments was small because these specimens broke before showing yield stress.

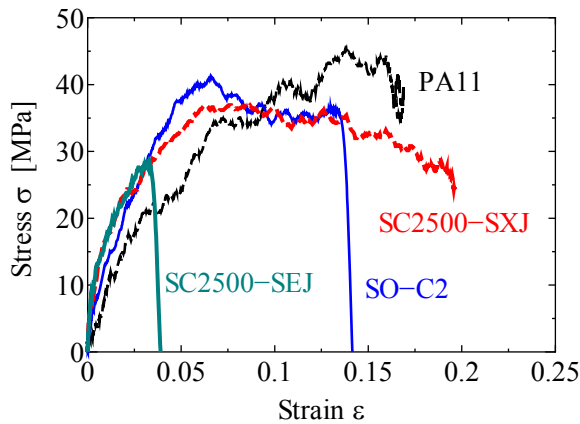


Fig. 6: Effect of nanoparticle addition (strain rate 600 s^{-1}).

1.3.2.3 Fracture Surface

Fig.7 shows photographs of the fracture surface captured by a scanning electron microscope. In the case of specimens without treatment and with epoxy silane treatment, the fracture surfaces were flat. In the case of specimens with amino silane treatment, the fracture surface did not exhibit material stretching, but holes were observed.

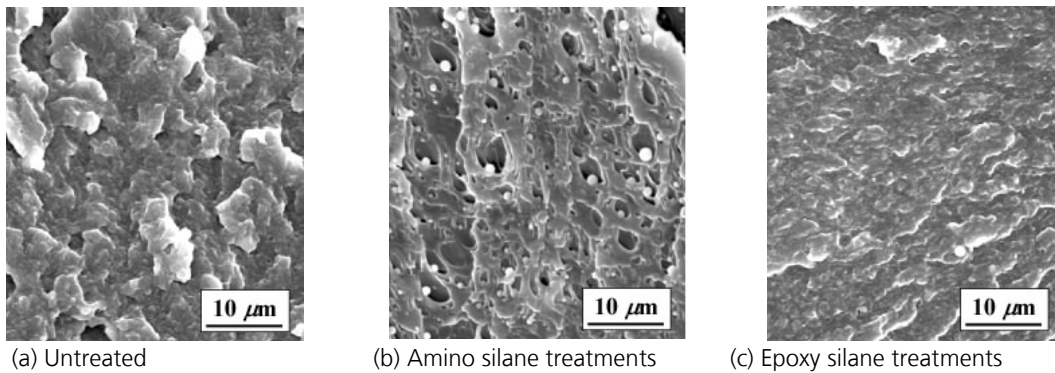


Fig. 7: Effect of silica nanoparticle addition on fracture surface (SEM photographs).

1.4 Conclusions

The stress-strain curves of bioplastics and their composite materials using split Hopkinson bar methods could explain their dynamic properties, including the results of Izod impact strength. In the future, we will examine the mechanical properties of bioplastics and their composite materials with respect to dynamic compression/tension, using

compression and tensile split Hopkinson bar methods to create new bioplastics-based composite materials with higher impact strength.

1.5 References

- [72] Gray, G.T. III: *Classic split Hopkinson pressure bar testing*, ASM Handbook Vol. 8, Mechanical Testing and Evaluation, ASM, 462-476, 2000.
- [73] Chen, W., Song, B.: *Split Hopkinson (Kolsky) Bar: Design, Testing and Applications*, Springer, 2010.
- [74] Fukuda, N.: Patent 2008-239645 in Japan, 2008.
- [75] Nishida, M., Ichihara, H., Fukuda, N.: *Evaluation of dynamic compressive properties of PLA/PBAT polymer alloys using split Hopkinson pressure bar method*, Eng. Trans., 59(1), 23-30, 2011.
- [76] Nishida, M., Ichihara, H., Watanabe, H., Fukuda, N., Ito, H.: *Effect of dialkyl peroxide blending on tensile properties of PLA/PBAT polymer alloys*, Eng. Trans., 60(2), 171-184, 2012.
- [77] Nishida, M., Ichihara, H., Watanabe, H., Fukuda, N., Ito, H.: *Improvement of dynamic properties of PLLA/PBAT polymer alloys using dialkyl peroxide*, Dynamic Behavior of Materials, Volume 1. Springer, New York, 329-335, 2013.
- [78] Arkema, manufacturer report.
- [79] Shimizu, H., Li, Y., Kaito, A., Sano, H.: *Formation of nanostructured PVDF/PA11 blends using high-shear processing*, Macromolecules, 38(19), 7880-7883, 2005.
- [80] Stoclet, G., Seguela, R., Lefebvre, J.-M.: *Morphology, thermal behavior and mechanical properties of binary blends of compatible biosourced polymers: Polylactide/polyamide11*, Polymer, 52, 1417-1425, 2011.
- [81] Capsal, J.-F., Pousserot, C., Dantras, E., Dandurand, J., Lacabanne, C., *Dynamic mechanical behaviour of polyamide 11/Barium titanate ferroelectric composites*, Polymer, Vol. 51, pp. 5207-5211, 2010.
- [82] Nishida, M., Natsume, R., Fukuda, N., Ito, H.: *Effects of spherical nanoparticle addition on dynamic properties of polyamide 11*, Dynamic Behavior of Materials, Volume 1. Springer, New York, 2014. (in press)

Comparative study of damage kinetics and energy absorption of 2D and 3D glass/vinylester composite materials under dynamic compression

M. Tarfaoui^{1, a}, C. Bouery^{1, b}

¹ENSTA-Bretagne, 2 rue François Verny, 29806 Brest Cedex - France

^a mostapha.tarfaoui@ensta-bretagne.fr

1.1 Abstract

In-plane impact behaviours of two and three dimensional orthogonal woven E-glass composites were tested on a Split Hopkinson Pressure Bar along in-plane configurations. For the 3D woven composite, two different configurations were studied: compression responses along the stitched direction (SD), and orthogonal to the stitched direction (OSD). Dynamic response, energy dissipation and failure mode were discussed. It was found that the effect of the z-yarns along the 3rd direction exhibit an increase in strength.

Keywords: Composites; Damage tolerance; Dynamic fracture; Strain rate effects.

1.2 Introduction

Composite materials are increasingly being used as a substitute for metallic materials in many technological application like aeronautics, aerospace, marine, armour, auto- motive and civil engineering applications [1-3]. Many of these applications, the structure are subjected to high impact loading. The mechanical behaviour of composites being dependent on loading rate [3-11], knowledge of constitutive models is of interest of scientists and designer. Delamination of 2D composites is known to be one of the most critical problems for designing composite structure, especially when impact loading is present. 3D composites were introduced in order to enhance the delamination resistance, by introducing z-yarns (or binder yarns) that weave multiple laminas [12]. During the weaving process, the resulting created spaces, due to

wrapping of lamina tows, are filled with matrix material which in turn causes low fibre volume fraction thus degradation of in-plane material properties [13].

Several tests were conducted on 3D reinforced composites. Tensile tests at low strain rates revealed crack initiation, associated with the resin rich areas near the z-yarns [14-15]. Whereas compressive tests showed a significant increase in the mode I, and moderate increase in mode II fracture toughness [16-18]. Transverse impact tests shows that the damage is independent on the loading rate, and it was noted that through-the-thickness reinforcement prevented delamination [19]. High velocity ballistic impact tests showed that z-yarns weaving did not prevent delamination at rates higher than the ballistic limit but it has reduced the damage during the dynamic loadings [2, 17]. In this manuscript a comparative study of mechanical behaviour and damage kinetics induced for 2D and 3D glass fibre vinylester woven composite under dynamic compression process is presented.

1.3 Experimental study

1.3.1 Composite specimen

The 2-D and 3-D woven composite (2DWC & 3DWC) shown in figure 1 respectively, were manufactured with the same vinylester matrix DION 9102 and E-glass fibres, and have the characteristics listed respectively in table (1) and (2). The vinylester resin can be used as an alternative to polyester and epoxy materials in matrix or composite materials, where its characteristics, strengths, and bulk cost intermediate between polyester and epoxy. Vinylester has lower resin viscosity (approx 200 cps) than polyester (approx 500 cps) and epoxy (approx 900 cps), and has good characteristics in a corrosive medium and under high temperature, therefore it is well adapted for naval application [20, 21].

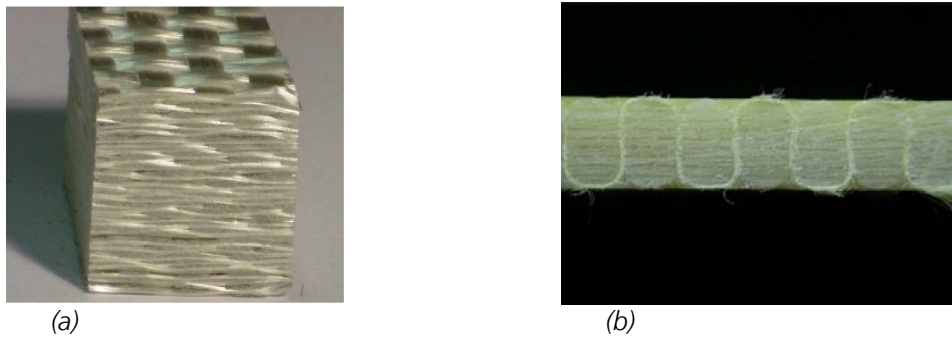


Fig. 1: (a) 2D and (b) 3D stitched orthogonal woven composite.

Tab. 1: Characteristics of the 2D and 3D stitched composite specimen.

Characteristic	Symbol	2D Value	3D Value
Longitudinal & transverse Young modulus (MPa)	$E_{11} = E_{22}$	23711	24878
Through-the-thickness Young modulus (MPa)	E_{33}	9000	9000
Shear modulus in plane 12 (MPa)	G_{12}	4498	4083
Shear modulus in plane 13 & 23 (MPa)	$G_{13} = G_{23}$	2977	3146
Poisson coefficient	ν_{12}	0.151	0.129
Poisson coefficient	$\nu_{13} = \nu_{23}$	0.20	0.20
Tensile strength (MPa)	$X_t = Y_t$	372	371
Compressive strength (MPa)	$X_c = Y_c$	355	372
Shear strength along 12 plane (MPa)	S_{12}	73	68
Shear strength along 13 & 23 plane (MPa)	$S_{13} = S_{23}$	104	102

The E-glass woven fibre of 500 g/m² are known of having high strength/mass ratio and a low cost compared to other reinforcements, therefore they are commonly used for naval applications [21, 3]. The reinforcement consists of a plain weave fabric with 50% warp yarns and 50% weft yarns. The composite used in this study has a thickness of 12 mm.

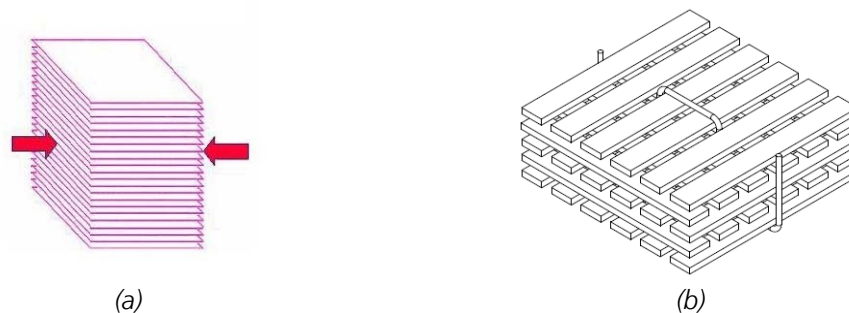


Fig. 2: Schematic of (a) in-plane (IP) tests and (b) the 3D woven composite.

Several tests were done along the in-plane configuration, figure 2a. For in-plane test, the 3D composite is performed along two different planes: compression along the stitched direction (3DWC-SD) and orthogonal to the stitched direction (3DWC-OSD). Note that only one binder yarn is stitched in the middle of the specimen, figure 2b.

1.3.2 Split Hopkinson pressure bar testing

The split Hopkinson pressure bar (SHPB) test is a technique of characterization that is based on the material response to 1-D wave propagation for high strain rate from 100 to 5000 s^{-1} [22].

In these dynamic compression tests, a cubic sample of size 12 mm \times 12 mm cut from the composite tile is placed between the two bars, of same diameter 20 mm. The striker, incident and transmitted bar has a length of 0.8 m, 3 m and 2 m, respectively. These bars are correctly aligned and are able to slide freely on the base. The composite is not attached to the bar in order to prevent perturbations of measurements due to additional interfaces [23]. The striker is lunched with different impact pressures and the specimens were subjected to different strain rate. The resulting signals were recorded by a digital oscilloscope. As figure 3 shows, for each test a minimum of three tests were achieved for each impact pressure in order to verify the test reproducibility.

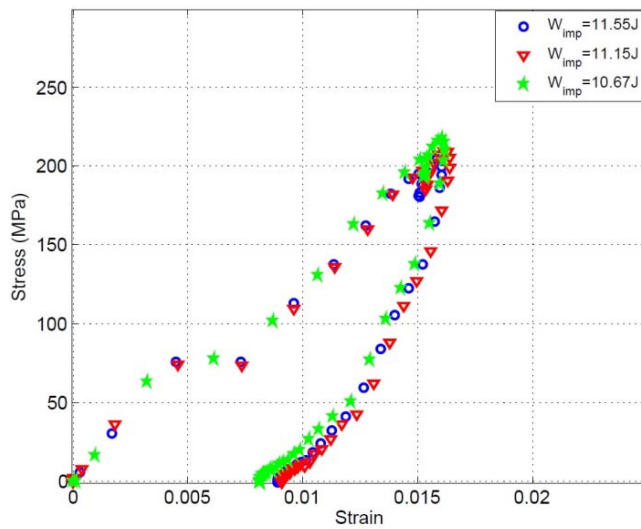


Fig. 3: Test reproducibility for the composite specimen.

1.4 Results and discussions for in-plane tests

1.4.1 Dynamic response

Figure 4 shows load-displacement curves when the material is subjected to three different impact energies. For each case, the load increases significantly at initial loading stages until it reaches a maximum value, then decreases gradually. The maximum load increases with increasing impact energy. These figures show that the specimen fails drastically for the 2D and 3DWC-OSD for high impact energy (>100 J), whereas 3DWC-SD composite did not fail for the same level of impact energy. The load-displacement response shows a rate dependent behaviour of the material at these rates.

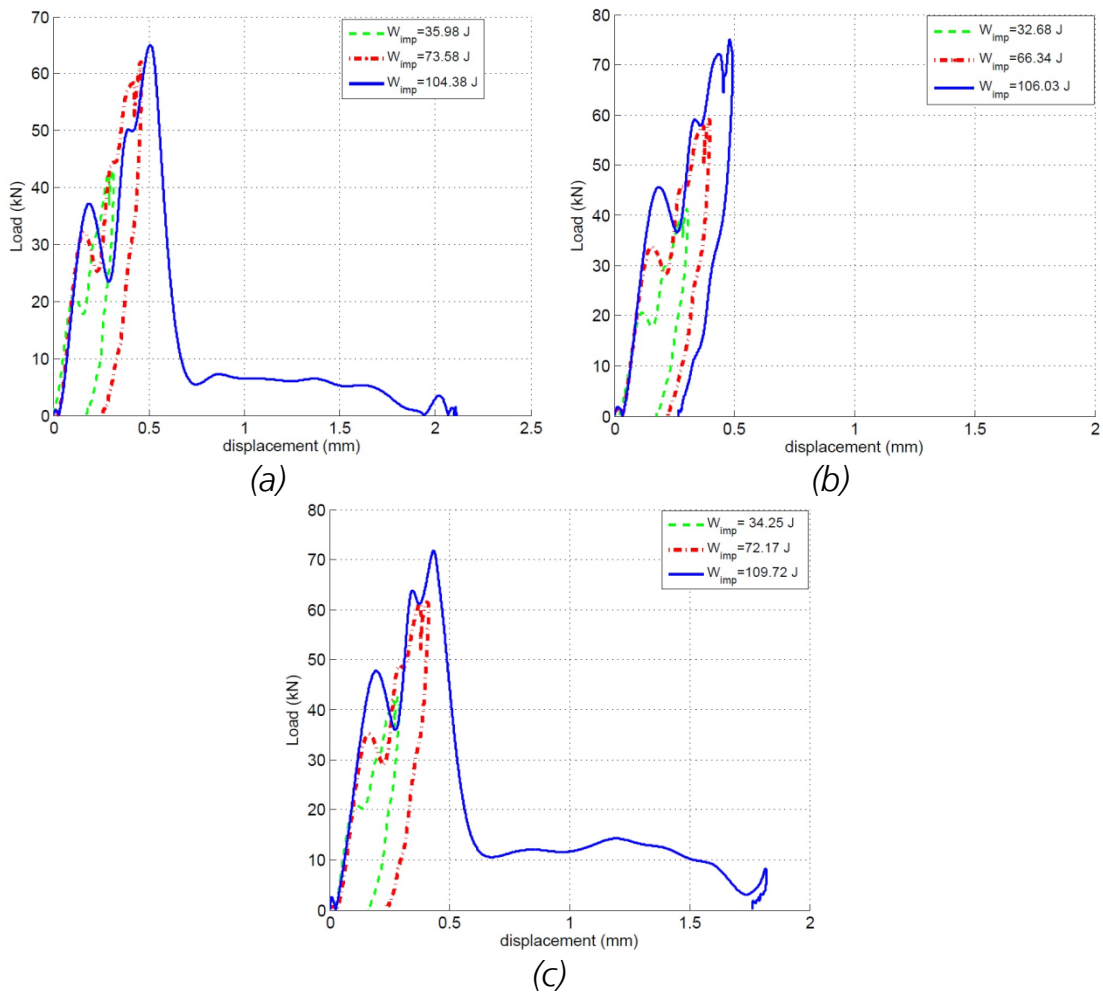


Fig. 4: Load-displacement history for in-plane test: (a) 2D woven composite (b) 3DWC-SD (c) 3DWC-OSD.

Figure 5 shows an increase of strength with increasing impact energy for different specimens. For low impact energy the strength is nearly identical for different composite, whereas for higher impact energy the 3DWC-SD shows higher resistance to damage when compared to the two others.

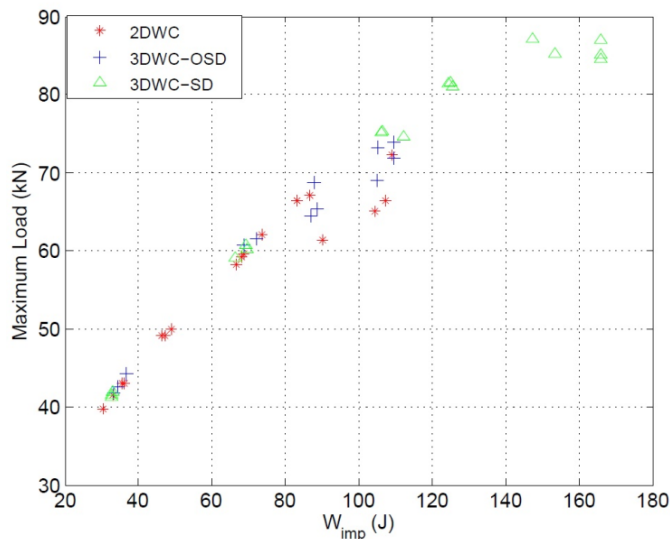


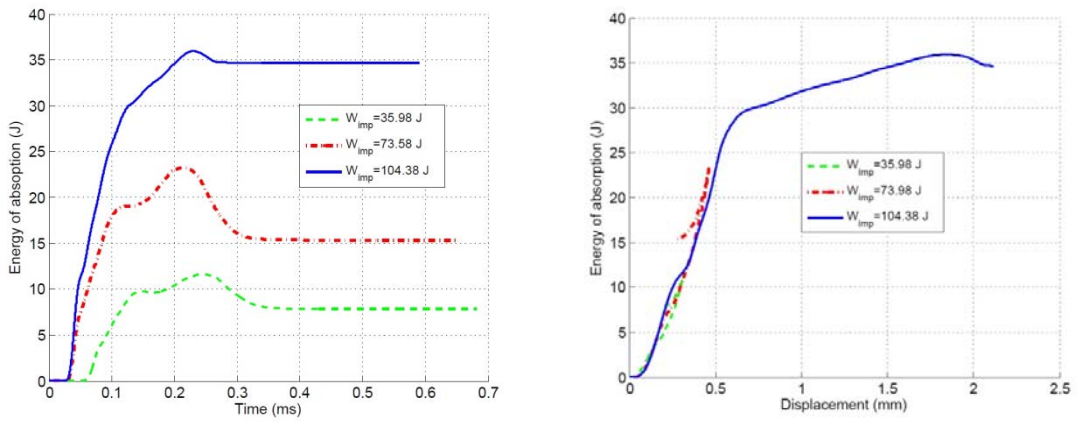
Fig. 5: Strength vs. impact energy for in-plane test.

1.4.2 Energy dissipation

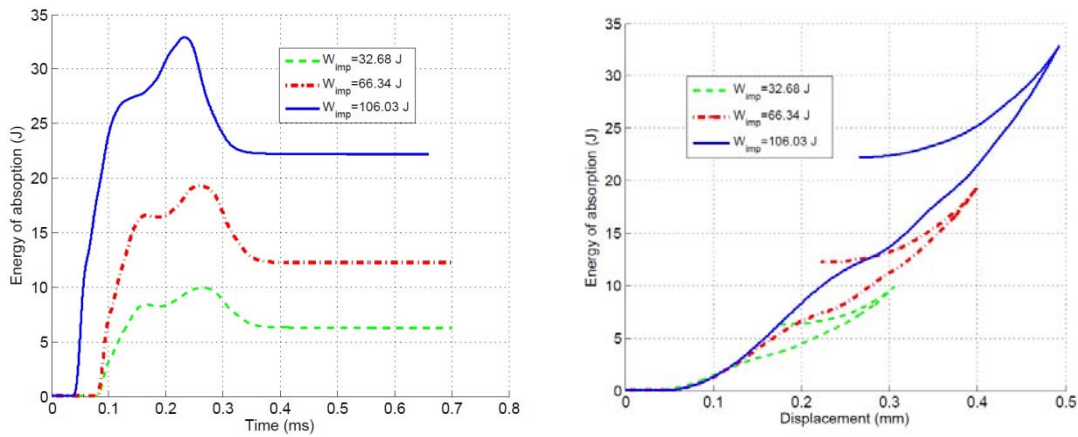
The energy of absorption can be determined by evaluating the area beneath the loading and unloading curves, figure 4. This energy is decomposed into an elastic part and an inelastic part that is unrecoverable. The inelastic part is expended on inducing damage in different forms including matrix cracking, fibre breakage, fibre/matrix debonding or delamination. The energy absorption plots tend toward a constant value, after the first cycle (incident-reflected-transmitted signal). This value represents the energy dissipated permanently through damage in the specimen [30].

Figure 6 shows the energy of absorption of the three type of composites architecture at different impact energies. The fluctuations in the profiles represent the storage and release of strain energy during the experiment. We can see clearly that at low impact energies, a significant portion of the input energy W_{elas} is stored during loading and released during unloading. When impact energy is increased, most the energy is dissipated through damage and only a small part is stored and released as strain energy.

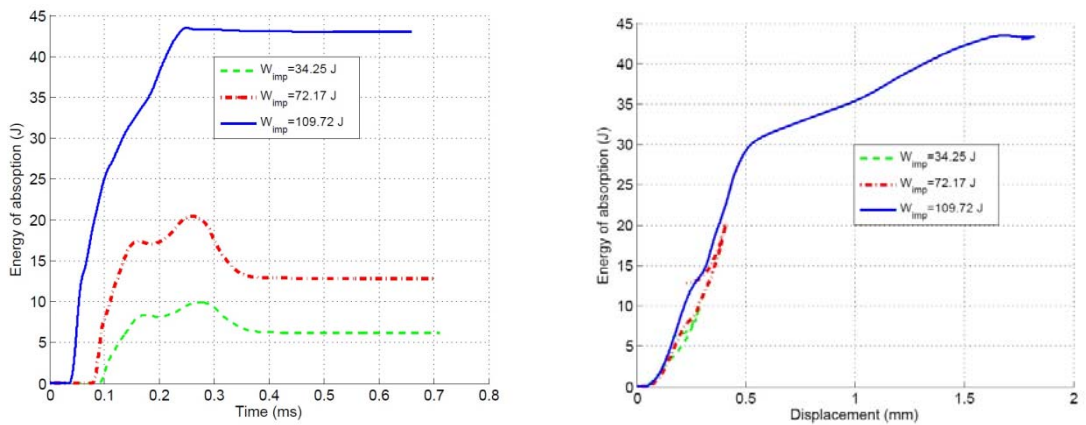
Comparative study of damage kinetics and energy absorption of 2D and 3D glass/vinylester composite materials under dynamic compression



(a) 2DWC



(b) 3DWC-SD



(c) 3DWC-OSD

Fig. 6: Energy of absorption for in-plane test.

The left part of figure 6 shows the energy of absorption of different composites at different impact energies. We can see clearly the increase of W_{ab} when the displacement u is increased and the release of W_{elas}

during rebounding. This latter (W_{elas}) makes up most of W_{ab} at lower impact energy, whereas W_{diss} takes higher fraction of W_{ab} when energy impact increases. Note that the release of W_{elas} is not seen in plot when macroscopic damage is present in the specimen. It can also be noticed that the loading parts of the curves at different impact energies are consistent and overlap with each other. On the other hand, there is a slight increase in the slope with increasing impact energy suggesting that the response is slightly rate-dependent. Note that the 3DWC-SD tend to absorb less energy for approximately the same impact energy resulting in a less induced damage.

1.4.3 Failure modes

Figures 7, 8 and 9 show the failure mode of the different composite specimens at different impact energies. As the impact energy increases, the energy absorption increases resulting a larger damage area. For in-plane test, the 3DWC-SD failed for higher impact energy, in comparison with the two other cases: 2D and 3DWC-OSD.

The 2D woven composite failed catastrophically. Damage initiation consisted of a shear band forming a 'V' shape and appearance of delamination on its tip. As damage mechanism progresses, it manifests in terms of matrix/fibre failure, fibre pullout and fibre bundle failure. For the same impact energy, the 3DWC-OSD failed less severely, and damage consisted mostly of shear banding forming a 'V' shape along the diagonal. As damage propagates, delamination is manifested, but often prevented from propagating due to the binder yarn (z-yarn) reinforcement.

The 3DWC-SD showed higher resistance to damage (>150 J) in comparison with the 2D and 3D-OSD (100 J), and the failure mode contains a shear band forming along the diagonal, and follows many of the different warp and weft tows in the specimen. It has also been noticed that often individual tows (weft and warp tows) remain intact except where they have sheared across.

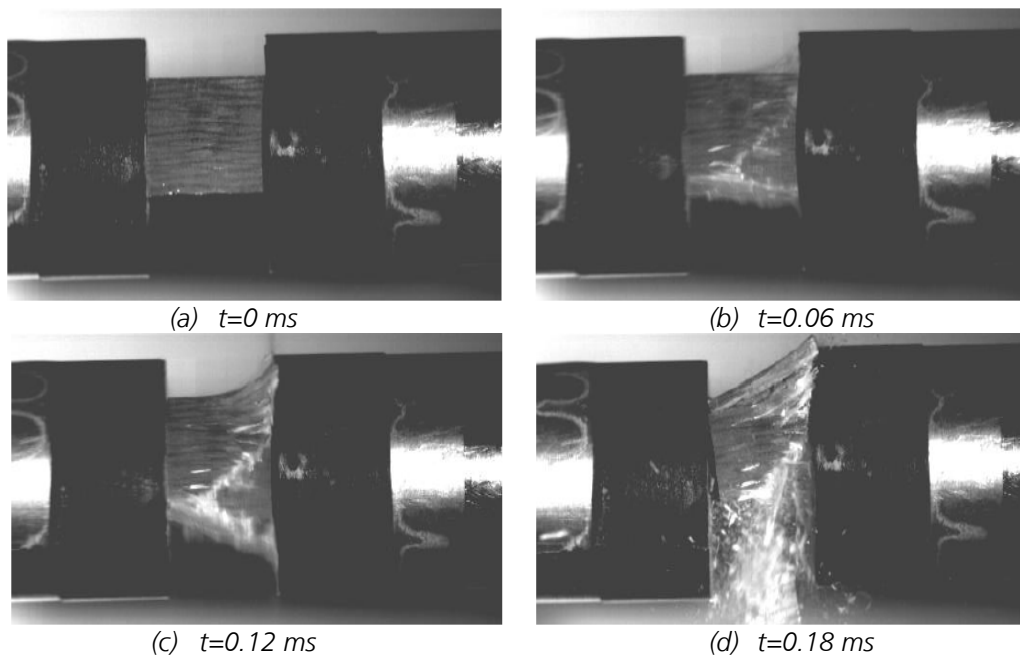


Fig. 7: In-plane failure mode for the 2D woven composite at impact energy of 104 J.

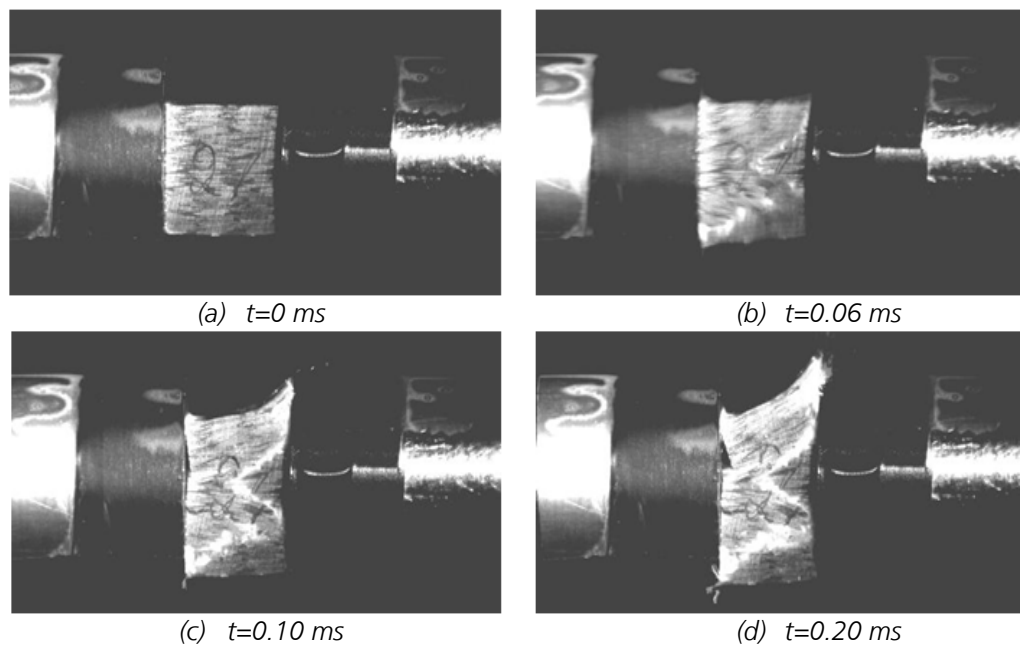


Fig. 8: In-plane failure mode for 3DWC-OSD, at impact energy of 109 J.

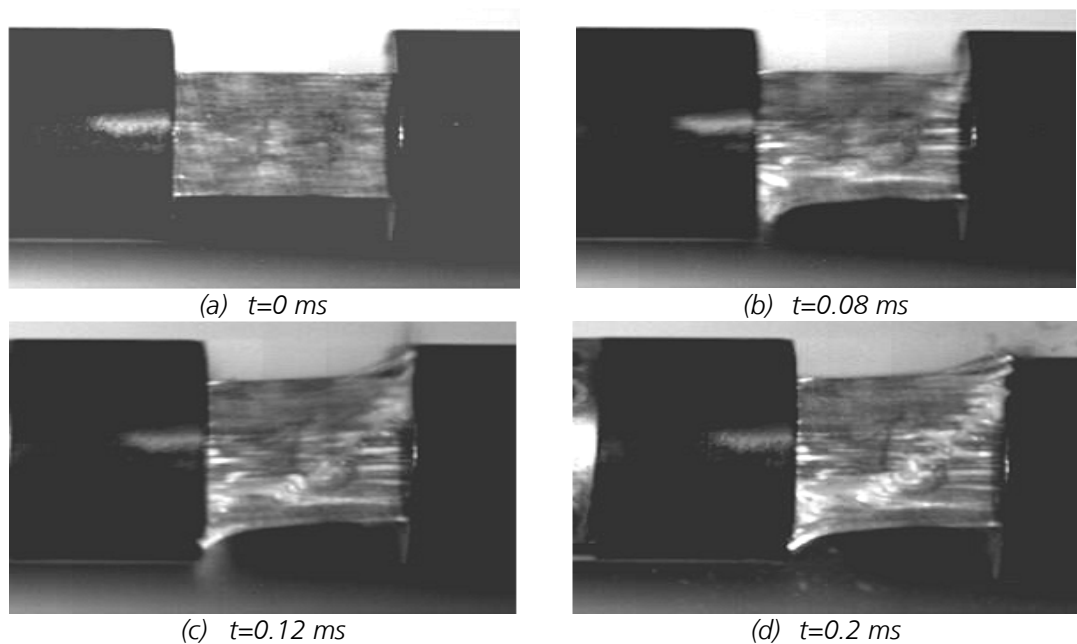


Fig. 9: In-plane failure mode for 3DWC-SD, at impact energy of 165 J.

1.5 Conclusion

A SHPB was used to conduct high rate compression tests for 2D and 3D woven composite. These tests showed the capacity of the 3DWC to prevent delamination because of 3-direction yarn in the specimen. Mechanical behaviour and damage mode were presented for both composite along different configurations. Two different configurations were studied for the 3D composite when loaded along the plane: a compression test along the stitched direction (3DWC-SD) and orthogonal to the direction where the z-yarn is stitched (3DWC-OSD). In these tests, material strength increases with increasing impact energy. Morphologies of the damaged composite specimens show the different failure modes for 2D and 3D composites along different configurations. The failure load and energy of absorption of composites increase as the impact energy increases. Failure mode for the 2D composite consists of delamination, whereas for 3D composites it consists of shear banding for in-plane test.

1.6 Acknowledgements

The authors of this paper gratefully acknowledge the financial support of the DGA, France.

1.7 References

- [83] Lal Ninan, J. Tsai, C.T. Sun. "Use of split Hopkinson pressure bar for testing off-axis composites". *International Journal of Impact Engineering*, 25:291-313, 2001.
- [84] T.R. Walter, G. Subhash, B.V. Sankar and C.F. Yen. "Damage modes in 3D glass fibre epoxy woven composites under high rate of impact loading". *Composites: Part B*, 40:584-589, 2009.
- [85] M. Tarfaoui, S. Choukri and A. Neme. "Effect of fibre orientation on mechanical properties of the laminated polymer composites subjected to out-of-plane high strain rate compressive loadings". *Composite Science and Technology*, Volume 68, Issue 2, 477-485, 2008.
- [86] P. Kumar and B.D. Agrawal. "Dynamic compressive behaviour of unidirectional GFRP for various fibre orientations". *Mater Letter*, 4(2):111-6, 1986.
- [87] A. El-Habak. "Mechanical behaviour of woven glass fibre-reinforced composites under impact compressional load". *Composites* 1991; 22(2):129-34.
- [88] W. Goldsmith, C.K.H. Dharan and H. Chang. "Quasi-static and ballistic perforation of carbon fibre laminates". *International Journal of Solids and Structures*, 32(1):89-103, 1995.
- [89] J. Tsai and C.T. Sun. "Dynamic compressive strengths of polymeric composites". *International Journal of Solids and Structures*, 41(11-12):3211-3224, 2004.
- [90] J. Tsai and C.T. Sun. "Strain rate effect on in-plane shear strength of unidirectional polymeric composites". *Composites Science and Technology*, 65(13):1941-1947, 2005.
- [91] J. W. Gillespie, BA Gama, C.E. Cichanowski and J.R. Xiao. "Interlaminar shear strength of plain weave S2-glass/SC79 Composites subjected to out-of-plane high strain rate

- compressive loadings". *Composites Science and Technology*, 65(13):1941-1947, 2005.
- [92] M. Tarfaoui. "Experimental Investigation of Dynamic Compression and Damage Kinetics of Glass/Epoxy Laminated Composites under High Strain Rate Compression". Book: *Advances in Composite Materials*. Chapter 16 pp 359-382, 2011.
- [93] R. Sierakowski, J. Neville, C. Ross and E. Jones. "Dynamic compressive strength and failure of steel reinforced epoxy composites". *Journal of Composite Materials*, 5:362-77, 1971.
- [94] SK. Sharma, BV. Sankar. "Effects of through-the-thickness stitching on impact and interlaminar fracture properties of textile graphite/epoxy laminates". NASA contractor report 195042; 1995.
- [95] RL. Karkkainen and BV. Sankar. "A direct micromechanics method for analysis of failure initiation of plan weaves textile composites". *Composites Science and Technology*, 66:137-50, 2006.
- [96] PJ. Callus, AP Mouritz, MK. Bannister and KH. Leong. "Tensile properties and failure mechanisms of 3D woven GRP composites". *Composites Part A: Applied Science and Manufacturing*, 30:1277-87, 1999.
- [97] P. Tan, L. Tong, GP Steven and T. Ishikawa. "Behavior of 3D orthogonal woven CFRP composites. Part I. Experimental investigation". *Compos Part A: Applied Science and Manufacturing*, 31:259-71, 2000.
- [98] AP. Mouritz. "Review of z-pinned composite laminates". *Composites Part A. Applied Science and Manufacturing*, 38:2383-97, 2007.
- [99] AP. Mouritz. "Ballistic impact and explosive blast resistance of stitched composites". *Composites Part B: Engineering*, 32:431-9, 2001.
- [100] T. Rys, BV. Sankar and PG. Ifju. "Investigation of fracture toughness of laminated stitched composites subjected to mixed mode loading". *Journal of Reinforced Plastics and Composites*, 2009.
- [101] Y. Luo, L. Lv, B. Sun, Y Qiu and B. Gu. "Transverse impact behaviour and energy absorption of three-dimensional orthogonal hybrid woven composites". *Composite Structures* 81:202-9, 2007.

- [102] L. Hamitouche. PhD Thesis: "Endommagement et rupture des assemblages en T de structures composites pour des applications navales ». Université de Bretagne Occidentale, 2008.
- [103] M. Tarfaoui, A. Neme and S. Choukri. "Damage kinetics of glass/epoxy composite materials under dynamic compression". Journal of Composite Materials 43: 1137-1154, 2009.
- [104] H. Kolsky. "An Investigation of the Mechanical Properties of Materials at Very High Rates of Loading". Proceedings of the Physical Society, 62B:676-700.
- [105] D. Bancroft. "The velocity of Longitudinal Waves in Cylindrical Bars". Physical Review, 59:588-593.
- [106] E. Davies and S. Hunter. "The dynamic compression testing of solids by the method of the split Hopkinson pressure bar". Journal of the Mechanics and Physics of Solids, 11:155-79, 1963.
- [107] P. Follansbee and C. Frantz. "Wave propagation in the split Hopkinson pressure bar". Journal of Engineering Materials and Technology, 105:61-6, 1983.
- [108] P. Follansbee. "The Hopkinson bar, Section: high strain rate testing". Metal handbook, 9th ed., vol.8, Mechanical testing. Cleveland, OH: American Society for Metals. p. 198-203, 1985.
- [109] S.W.Park, M. Whou and D.R. Veazie. "Time-Resolved Impact Response and Damage of Fiber-Reinforced Composite Laminates". Journal of Composite Materials, Vol 34, No10, 2000.

Experimental and numerical investigation of glass/epoxy composite materials under in-plane dynamic compression

M. Tarfaoui^{1, a}

¹ENSTA-Bretagne, 2 rue François Verny, 29806 Brest Cedex - France

^a mostapha.tarfaoui@ensta-bretagne.fr

1.1 Abstract

Recently applications have exposed polymer matrix composite materials to very high strain rate loading conditions, requiring an ability to understand and predict the material behaviour under these extreme conditions. Many composite aircraft structures such as fuselage and wing skins, engine nacelles, and fan blades are situated such that impacts at high strain rates are a realistic threat. To investigate this threat, high velocity impact experiments and subsequent numerical analyses were performed to study the compressive loading at high strain rates on composite materials. The compressive material properties are determined by testing the laminate systems with different orientations from low to high strain rates. Samples of cubic geometry are tested in in-plane direction for seven fibre orientations, 0° , $\pm 20^\circ$, $\pm 30^\circ$, $\pm 45^\circ$, $\pm 60^\circ$, $\pm 70^\circ$ and 90° . The tests show a strong material sensitivity to dynamic loading and fibre direction. After carrying out the dynamic tests, the aim of the second part of this study is their modelling by using finite element method. The FEA results of the dynamic tests resulting in no damage appeared satisfactory. The FEA gives results which are in coherence with the experimental values. The improved understanding of these phenomena and the development of predictive tools is part of an ongoing effort to improve the long-term integrity of composite structures under dynamic loads.

Keywords: Composites; Dynamic compression; Damage; Dynamic fracture; Strain rate effects; experimental approach, finite element modelling.

1.2 Introduction

The composite materials with organic matrix found important applications in the shipbuilding industries. New applications of the composites are identified, including their current and potential use in superstructures, platforms and some large military equipment, such as destroyers and aircraft carriers. The mechanical characteristics of these materials are well known for static loading; however, with the strain rate they are likely to evolve [1-4].

The study of the composite materials behaviour at high strain rates is still relatively new and reliable data on strain rate effects is very scarce. Even though the problem of obtaining reliable data is accentuated by difficulties encountered in design and conducting impact tests on composites [5], the qualitative relationship between the dynamic constitutive response and the dynamic damage evolution for composites at high strain rates is still far from being fully understood. Significant efforts have been made to examine the high strain rate behaviour of more brittle materials such as composites and ceramics using the split Hopkinson bar to measure dynamic response of materials under varying loading conditions [6-7]. Ochola et al. [8] studied the strain rate sensitivity of both carbon fibre reinforced polymer (CFRP) and glass fibre reinforced polymer (GFRP). The results show that the dynamic material strength for GFRP increases with increasing strain rates and the failure strain for both CFRP and GFRP is seen to decrease with increasing strain rates. Vinson and Woldensenbet's [9] results show that the ultimate stress increases with increasing strain rate. Most recently, the study conducted by Hosur et al. [10] presents the effect of in-plane off-axis testing of an 8-harness satin weave carbon fabric/SC15 composite specimen. The specimens were tested in the in-plane direction of 0°, 15°, 30°, 45°, 60°, 75°, and 90° in a range of strain rates from 1092 to 2425 s⁻¹. From this study it was noted that the high strain rate-tested specimens showed a considerable increase in the stress to failure and stiffness of the composite compared with the quasistatic loaded specimens. Depending on the fibre orientation of the specimens, the ultimate strength and strain varied considerably and exhibited a nonlinear stress-strain response that increased with angles up to 45°. Gary and Zhao [11] employed the use of low impedance materials such as nylon, for the incident and output bars of the split Hopkinson bar, to test the strain rate behaviour of glass epoxy composite panels. The failure strength of the glass epoxy panel tested by Gary and Zhao is

reported to be strain rate sensitive. Fibre orientation effects on high strain rate properties were considered recently for a carbon epoxy system. Many different models [12-13] have been developed to predict failure stress and modes in composites subjected to quasi-static loading. However, few criteria have been developed and experimentally validated for high strain rate loading.

In this study, specimens of glass/epoxy composite were subjected to dynamic compression loading. Dynamic tests were conducted on the split-Hopkinson pressure bar (SHPB). Samples were tested in-plane (IP) direction. The fibre orientations of the samples were 0° , $\pm 20^\circ$, $\pm 30^\circ$, $\pm 45^\circ$, $\pm 60^\circ$, $\pm 70^\circ$ and 90° . Stress-strain curves at increasing strain rates were obtained for different cases. The second part of this study deals with the modelling of the dynamic tests by using finite element method. The models are used for validating material characteristics and predicting their elastic behaviour.

1.3 Materials

The material used in this study consists of 2400 Tex E-glass fibres impregnated with an epoxy matrix. The resin is an EPOLAM pre-polymer, EPOLAM 2020 hardener and 2020 accelerator from Axson. Glass fibres are commonly used for naval applications because of their high strength/mass ratio and their low cost compared to other reinforcements. The reinforcement consists of a plain weave fabric with 90% warp yarns and 10% weft yarns. Panels are made by an infusion process and seven orientations are studied: 0° , $\pm 20^\circ$, $\pm 30^\circ$, $\pm 45^\circ$, $\pm 60^\circ$, $\pm 70^\circ$ and 90° . The square panels, 500×500 mm, were cut into cubic samples of the geometry dimensions as shown in Table 1.

Tab. 1: Geometry and fibre mass fraction of the samples, standard deviation in brackets.

Panel	Thickness, (mm)	Surface (mm ²)	Void fraction (%)	Stacking sequence	Fibre volume fraction (%)
A	13.00 (0.1)	13×13 (0.2)	2.26	[0] ₄₀	53.5 (0.5)
B	12.52 (0.3)	13×13 (0.2)	2.00	[±20] ₂₀	54.0 (0.5)
C	13.00 (0.1)	13×13 (0.2)	1.78	[±30] ₂₀	55.0 (0.5)
D	12.78 (0.2)	13×13 (0.2)	1.69	[±45] ₂₀	54.3 (0.5)

1.4 Dynamic compression loading

The split Hopkinson bar test is the most commonly used method for determining material properties at high strain rates, Figure 1. This technique of characterization, based on the response of material to wave propagation for high strain rate from 100s^{-1} to 5000s^{-1} , was improved by Kolsky [14].

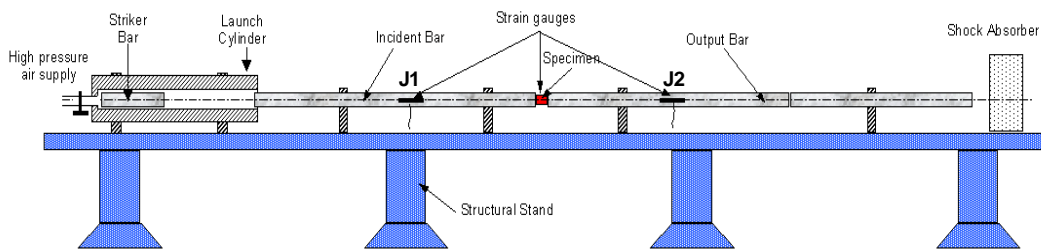


Fig. 1: Typical compressive split Hopkinson bar apparatus.

1.4.1 Data processing procedure

The dynamic compression test conducted in this study consists in placing a cubic sample (13mm in length) between two bars with a high elastic limit, called input bar and output bar. The bar diameter was 20mm. The striker bar was 0.8m long, while the incident bar length was 3m and the transmission bar 2m. These bars are correctly aligned and are able to slide freely on their support. The composite specimen is not attached to the

bar in order to prevent the perturbations of measurements due to additional interfaces [15]. The experimental set-up consists of (1) a stress generating system which is comprised of a split Hopkinson bar and the striker, (2) a specimen, (3) a stress measuring system made up of sensors (typically, resistance strain gauges), and (4) a data acquisition and analysis system. The signals are treated with Maple Software using Fast Fourier Transformation to obtain the evolution of the dynamic parameters: stress vs. strain, strain rate vs. time, incident and transmitted load and velocity at the interfaces input bar/sample and output bar/sample vs. time.

The specimens $[0]_{40}$, $[\pm 20]_{20}$, $[\pm 30]_{20}$, $[\pm 45]_{20}$, $[\pm 60]_{20}$, $[\pm 70]_{20}$ and $[90]_{40}$ were subjected to the in-plane loading with nine different impact pressures of the striker bar on the input bar: 0.5, 0.6, 0.7, 0.8, 0.9, 1.0, 1.2, 1.4 and 1.6bar.

1.4.2 Strain rate dependencies of dynamic mechanical properties

Before launching the experimental study for a dynamic case, it is necessary to ensure that the tests can be reproduced. With this objective in mind, for each fibre orientation, a minimum of three tests were carried out at the same impact pressure in order to analyze the tests reproducibility. As figure 2 shows, it is noted that the tests are repeatable and a fact that was checked for each test.

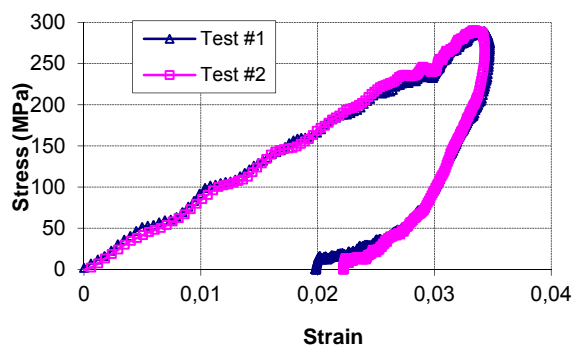


Fig. 2: Test reproducibility for IP tests, $[0]_{40}$ – $P = 0.5$ bar.

Tab. 1: Critical impact pressure for appearance of second peak.

IP Tests	0°	±20°	±30°	±45°	±60°	±70°	90°
P _c (bar)	1.2-1.4	0.9	0.8-0.9	0.8	0.7-0.8	0.7	0.6

The strain rate evolution is sensitive to the entry pressure P in the chamber of compressed air (impact pressure of the striker on the input bar), the loading direction and the sample lay-up (angle θ). The fibre orientation has an effect on the strain rate evolution. Figure 3 gives the evolution of the strain rate vs. time of $[0]_{40}$, $[\pm 20]_{20}$, $[\pm 30]_{20}$, $[\pm 45]_{20}$, $[\pm 60]_{20}$, $[\pm 70]_{20}$ and $[90]_{40}$ for 9 impact pressures. The presence of a second peak is the principal characteristic of these curves, which characterizes the onset of macroscopic damage, which is detailed in [14]. The critical pressure P_c responsible for the appearance of a second peak is shown in table 2. The appearance of a second peak is around 1.4bar for $[0]_{40}$ and between 0.6-0.9bar for the other orientations. The dynamic behaviour for IP tests is dominated by compressive properties of the polymeric matrix and the damage kinetics is affected by fibre orientation. Figure 3 shows the dynamic behaviour of the laminates for the 9-impact pressure. One can note that $[\pm 20]_{20}$ - $[\pm 30]_{20}$ and $[\pm 60]_{20}$ - $[\pm 70]_{20}$ have similar tendencies. For the $[90]_{40}$ laminate, a brittle behaviour is noted, which is controlled by matrix failure. According to the various orientations, the nonlinear part of the $\sigma = f(\varepsilon)$ curves is different and corresponds to different damaging modes.

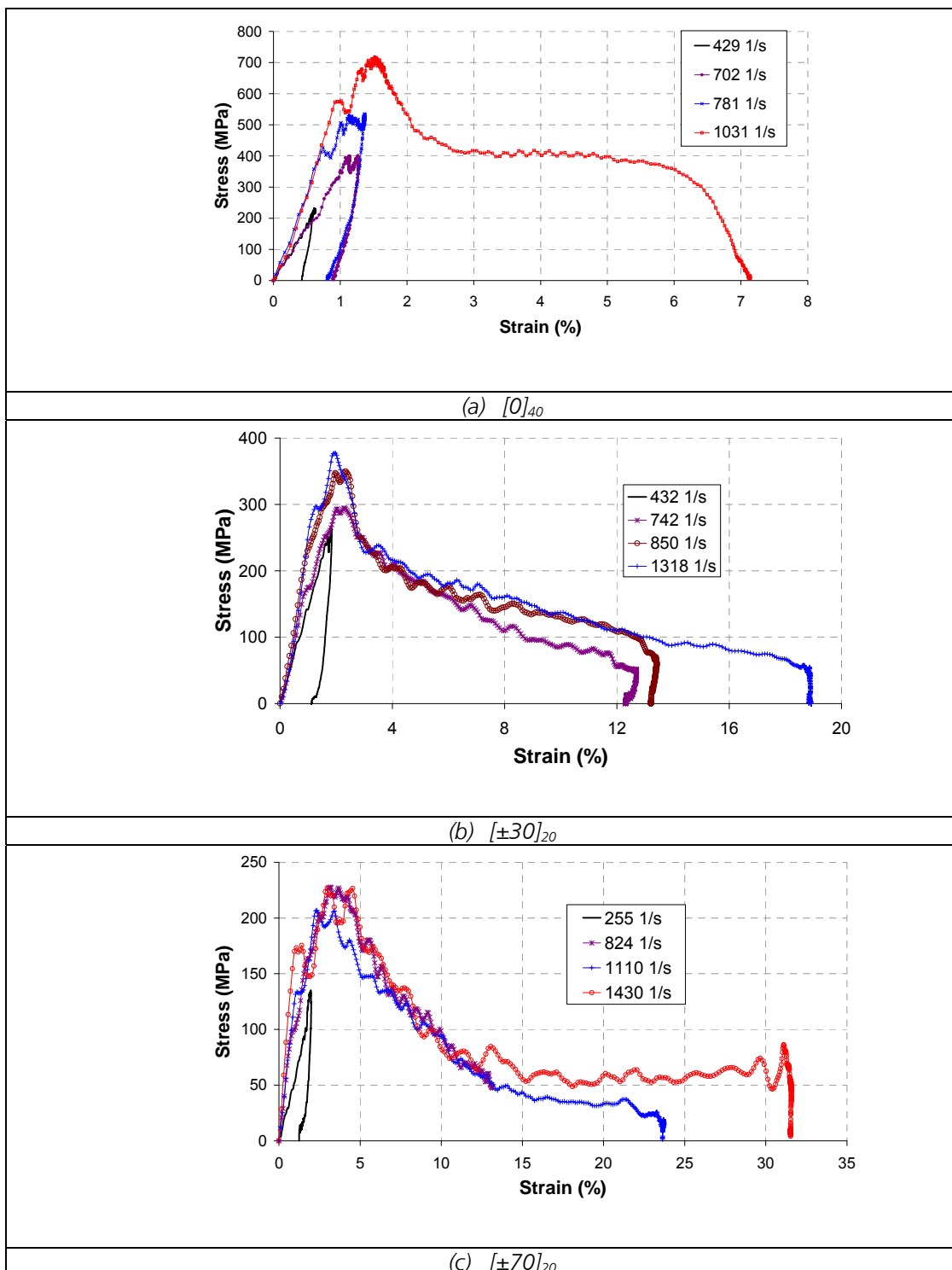


Fig. 3: Stress-strain curve evolution versus strain rate.

1.5 Finite element analysis

After a detailed experimental study of the static and dynamic behaviour of glass epoxy composite which is widely used in the naval and aeronautic field for strain rates up to 2000 s⁻¹ [25-26], in this section the numerical modelling of non-damage tests and his satisfaction in comparison with experimental results are presented.

The experimental dynamic tests on the glass/epoxy composite specimens were simulated using Abaqus Explicit 6.11 [17]. Hexahedral solid elements with reduced integration C3D8R, in impact cases available in the library were used. Based on microscopic observations, the composite specimen was modeled as solid laminated elements with transversely isotropic plies. The bars (input, output bars and impactor), of great stiffness (quenched steel) compared to the composite specimen, was modeled as deformable body and the surfaces in contact with the specimen were taken as the "master surface". Modeling as deformable body requires a 3D elements which generates a very important computing time. The potential contact area of the specimen was taken as a "slave surface" so the individual nodes of the composite were constrained not to penetrate the surfaces of the bars. The relative motions of the contact surfaces were modeled as "small sliding", which assumes that contact surfaces do not move very much relative to each other. The contact algorithm used is based on the penalty method. Meshes consist of isometric elements. For these two types of elements, five integration points are considered in the thickness of each layer. The integration method uses the Simpson rule. The selected elements have linear interpolation. They give better results for modeling contact and impact with the possibility of severe distortions of the elements.

1.5.1 Dynamic compression without damage

The dynamic compression tests with SPHB were presented. In this section, one will examine the prediction of the dynamic response without damage. Our choice is focused on a model with solid elements. The projectile and the bars are modelled as deformable bodies. The studied samples are thick. Furthermore, they are modelled also by solid elements, Figure 4.

Note that the mesh used is as follows:

- 1 mm meshes size of the sample.
- 13 mm mesh size of the striker.
- Mesh of the cross-section of the bars: 8 elements for the diameter and 24 of the perimeter.
- mesh lengths:
 - Parts 1 and 4: coarse mesh of 13mm.
 - Parts 2 and 3: biased mesh (refined in the direction of the sample: 150 elements with a ratio of 5).

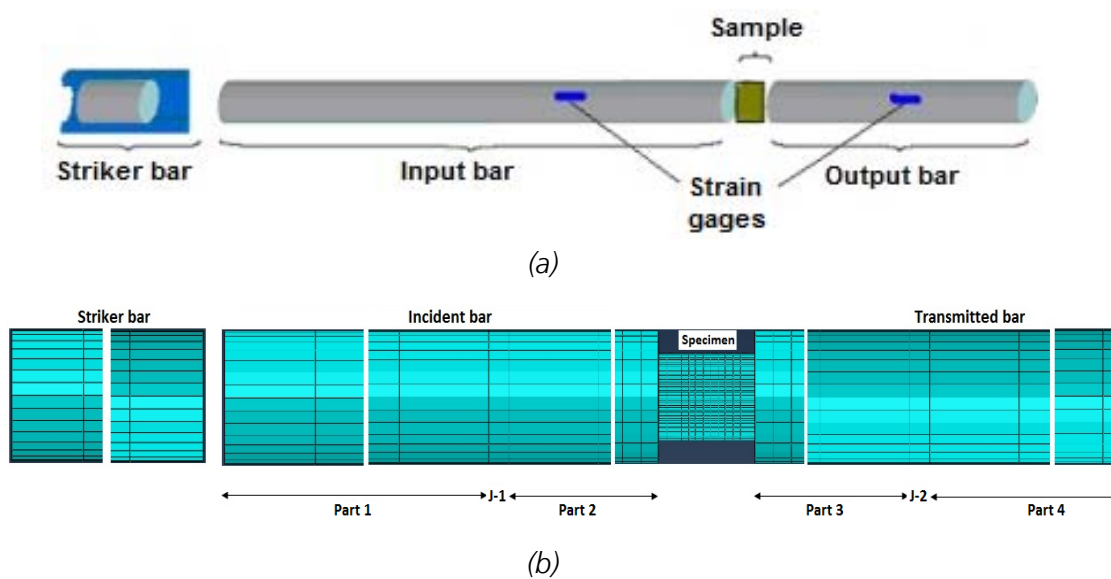


Fig. 4: Full model (FM) with striker bar.

The different physical quantities analyzed and compared with experimental results are :

- F_i and F_t : loads applied to the sample, interfaces Input bar / sample / Output bar,
- V_i and V_t : the incident and transmitted velocity,
- Strain of the bar at the location of the two gauges: incident (J_1) and transmitted (J_2).

1.5.2 Results and discussion

Figures 5-6 provide a comparison between the experimental results and those given by the full model with impactor (MC+I). One sees that there is effectively a good correlation in the majority of the curves between the

full model and experimental results for different orientations from 0 ° to 90 °. If one conducts a detailed analysis of the numerical results, we can note the following points:

- For the strain of incident and reflected compression wave measured by the gauge J_1 , the numerical model gives a good estimate of the experimental results. Small gaps that may exist between the results of numerical model (MC + I) and those of the experimental data can be linked to inputs of FE model i.e. the velocity of the impactor. The latter is estimated from the average value given by the gauge incident signal.
- The correlation of the transmitted strain reveals a good agreement. It may be noted, however, that the absence of the damper bar in the global model causes multiple reflections where the presence of a tensile wave of the same amplitude.
- For the incident velocity, one has acceptable correlation in the first part of the curve, but the second part has divergence. Indeed, as the numerical velocity is taken at the incident surface of the bar in contact with the sample, one has multiple reflections of the wave which generate overlapping velocities of opposite signs.
- The transmitted numerical velocity gives a good approximation with the experimental results.
- The evolution of the incident and transmitted loads, given at 2 interfaces of the bars in contact with the sample are well simulated. We have the same level of the maximum load and the same rise and fall of the load. At the experimental results we find a slight difference between the incident and transmitted load which may be related to the experimental conditions: the geometry of the samples is not perfectly cubic, the parallelism of the facets in contact with the bars...

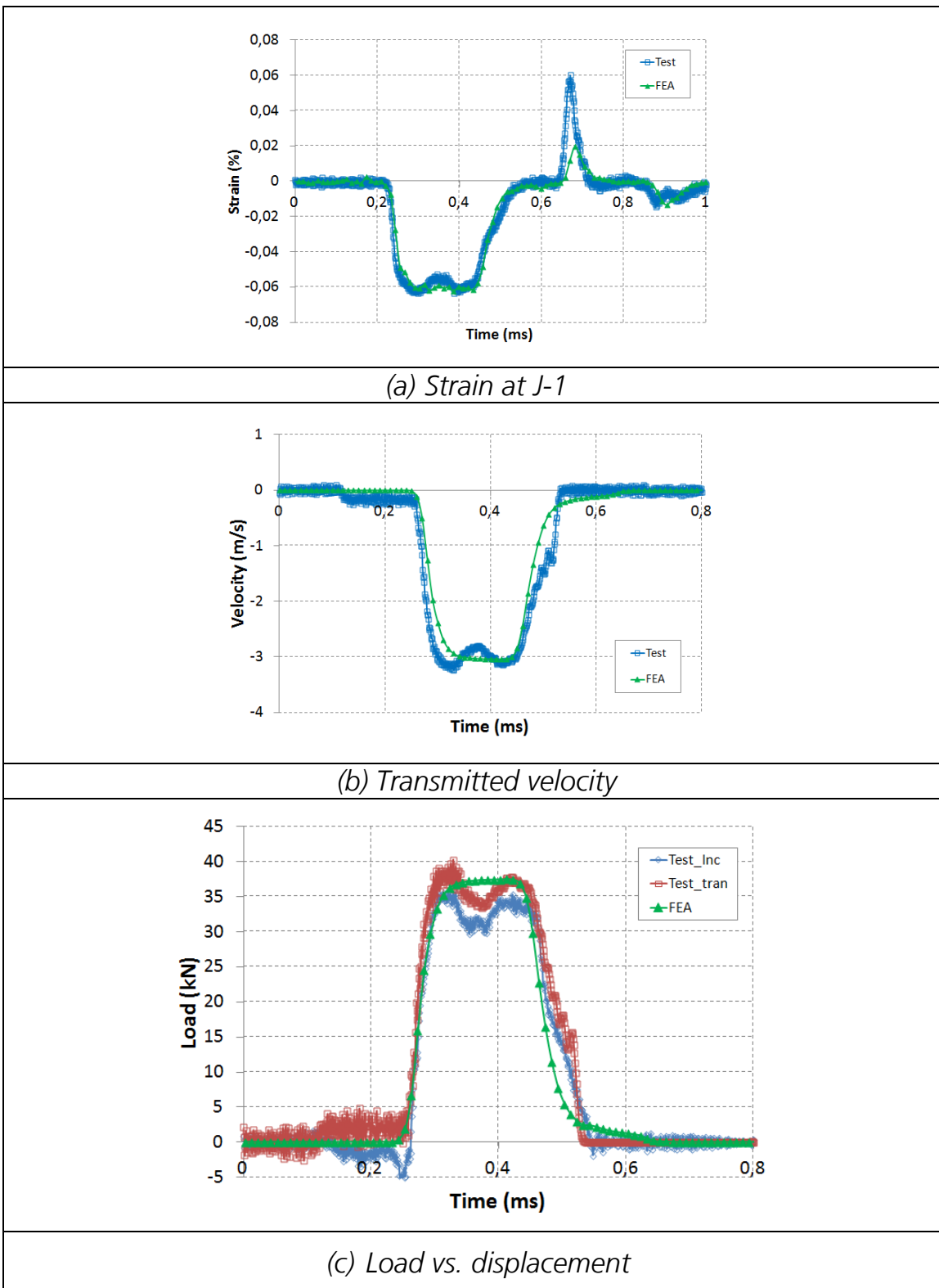


Fig. 6: Correlation experimental/numerical results, IP test [0]40, P = 0.5 bar.

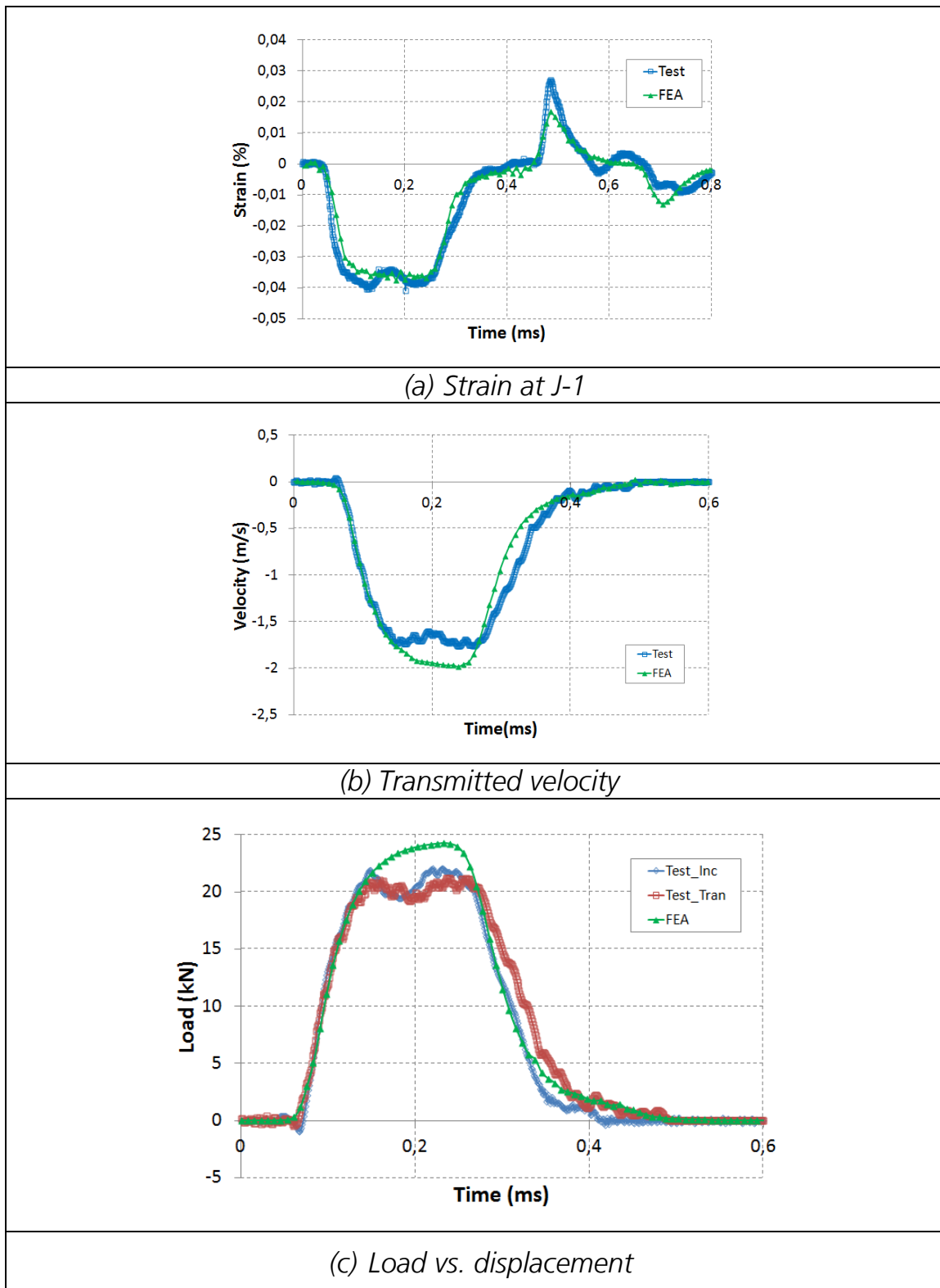


Fig. 7: Correlation experimental/numerical results, IP test $[\pm 30]_{20}$, $P = 0.5$ bar.

1.6 Conclusion

In this work, the high strain rate material response of $[0]_{40}$, $[\pm 20]_{20}$, $[\pm 30]_{20}$, $[\pm 45]_{20}$, $[\pm 60]_{20}$, $[\pm 70]_{20}$ and $[90]_{40}$ E-glass/epoxy composite material systems was investigated. A Split Hopkinson pressure bar was used to conduct high strain rate experiments. Maximum strain rates around 2000s^{-1} were achieved. Samples were subjected to IP tests. The first observation can be made, for in-plane tests, is that materials show a strength dependency on fibre orientation and impact pressure. Damage appears only for specific impact pressures: 1.2bar for $[0]_{40}$, 0.9-1bar for $([\pm 20/\pm 30]_{20})$, 0.9bar for $[\pm 45]_{20}$, 0.7-0.8bar for $([\pm 60/\pm 70]_{20})$ and 0.6bar for $[90]_{40}$. For this lower range of impact pressure there was no macroscopic damage but the existence of microscopic damage remains a possibility. It can also be noticed that the nature of the damage is strongly affected by the orientation of the laminates, a major parameter in improving dynamic compressive strength. The multiplication of the microscopic and macroscopic damage involves catastrophic failure. For these specimens a multiple fracture mode is determined and described. As the strain rate increases more damage mechanisms are involved; from matrix cracks to delamination with multiple paths to final fracture. The damage kinetics for in-plane loading is strongly conditioned by the specimen's fibre orientations. The initiation and propagation of failure mechanisms at different strain rates have been examined. Specimens fail due to fibre kinking at low strain rates, with delamination and interfacial separation dominating the high strain rate failure regime.

1.7 Acknowledgements

The Authors of this paper gratefully acknowledge the financial support of the DGA, France.

1.8 References

- [110] Tsai J., Sun C.T. Dynamic compressive strengths of polymeric composites. *International Journal of Solids and Structures*, Volume 41, Issues 11-12, June 2004, Pages 3211-3224.
- [111] Tsai J.L. and Sun C.T. Strain rate effect on in-plane shear strength of unidirectional polymeric composites. *Composites Science and Technology*, Volume 65, Issue 13, October 2005, Pages 1941-1947.
- [112] Gillespie J.W., Gama B.A., Cichanowski C.E., Xiao J.R. Interlaminar shear strength of plain weave S2-glass/SC79 composites subjected to out-of-plane high strain rate compressive loadings. *Composites Science and Technology*, Volume 65, Issues 11-12, September 2005, 1891-1908.
- [113] Brara A. and Klepaczko J.R. Fracture energy of concrete at high loading rates in tension. *International Journal of Impact Engineering*, Volume 34, Issue 3, March 2007, 424-435.
- [114] Harding J. The Effect of High Strain Rate on Material Properties. *Materials at High Strain Rate*, chapter 4, Ed. T. Z. Blazynski. Elsevier Applied Science, London & New York, 1987, 130-173.
- [115] Kumar P., A. Garg. and Argawal, B.D. Dynamic compressive behavior of unidirectional GFRP for various fiber orientations. *Material letters*, 1986, Volume 4, Issue 2, 111-116.
- [116] El-Habak A.M.A.. Mechanical behavior of woven glass fiber-reinforced composites under impact compression load. *Composites*, Volume 22, Issue 2, 1991, 129-134.
- [117] Ochola R. O., K. Marcus, G. N. Nurick and T. Franz. Mechanical behavior of glass and carbon fiber reinforced composites at varying strain rates. *Composite Structures*, Volume 63, Issues 3-4, February-March 2004, Pages 455-467.
- [118] Vinson J., E ; Woldesenbet. Fiber orientation effects on high strain rate properties of graphite/epoxy composites. *Journal of Composite Materials*, 2001, Vol. 35, 509–521.
- [119] Hosur MV, Alexander J, Vaidya UK, Jeslani S, Mayer A. Studies on the o.-axis high strain rate compression loading of satin weave carbon/epoxy composites. *Computer and Structure* 2004; 63: 75–85.
- [120] Gary G. and H. Zhao. Dynamic testing of fiber polymer matrix composite plates under in-plane compression.

Composites Part A: Applied Science and Manufacturing, Vol. 31, Issue 8, 2000, 835-840.

- [121] Gama B.A., Gillespie J.W., Mahfuz H., Raines R.P., Haque A., Jeelani S., Bogetti T.A., Fink B.K. High Strain-Rate Behavior of Plain-Weave S-2 Glass/Vinyl Ester Composite. *Journal of Composite Materials*.2001; 35: 1201-1228.
- [122] Haque A. and Ali M., High Strain Rate Responses and Failure Analysis in Polymer Matrix Composites – An Experimental and Finite Element Study. *Journal of Composite Materials*, 3 2005; vol. 39: pp. 423 - 450.
- [123] Kolsky H. An investigation of the mechanical properties of materials at very high rates of loading. *Proc. Phys. Soc. , 1949, Vol. 62B, 676-700.*
- [124] Bancroft D. The velocity of longitudinal waves in cylindrical bars. *Physical Review*, Volume 59, N° 59,1941, 588-593.
- [125] Tarfaoui M., Choukri S. and Neme A., Effect of fibre orientation on mechanical properties of the laminated polymer composites subjected to out-of-plane high strain rate compressive loadings. *Composite Science and Technology* 2007, Volume 68, Issue 2, 477-485, 2008.
- [126] Abaqus 6.11: Analysis User's Manual.